Novel Materials and Deposition Techniques for Solution Processed Solar Cells

Alexander Thomas Barrows

Department of Physics & Astronomy

University of Sheffield

Thesis submitted for the degree of Doctor of Philosophy

December 2015

Acknowledgements

Firstly, thanks go to my supervisor David Lidzey for giving me the opportunity to undertake this work, the freedom to pursue the aspects which I found interesting and for all the advice along the way. Particular thanks go to Andrew Pearson for assistance with experimental ideas, useful talks about data, teaching me how to use lab equipment and software packages and endless help with preparing manuscripts for papers and this thesis. I must also thank James Kingsley for endless help and advice in the lab and when discussing data. Thanks to Andrew Brook for all the help with laboratory equipment. I would also like to thank Samuele Lilliu for invaluable assistance with GIWAXS data collection and analysis, and saving me an inordinate amount of time by letting me use his software! In addition I would like to thank Andy Parnell for his assistance with learning the ropes of the DAWN software package for GISAXS data analysis.

Thanks also to the other PhD students and the post-docs of the EPMM group: Jon Griffin, Chris Bracher, Nick Scarratt, Ed Bovill, Tao Wang, Darren Watters and David Mohamad. Thanks to the Ossila staff for help and assistance, in particular Max Reinhardt, and to the technical staff in the III-V Centre for their help and training, and to Gordon for all the IPA.

Thanks to my family for family stuff, and to my friends for friend stuff. This thesis is dedicated to my nemeses, Eddie Barbour and Stu Littlefair. Thank you for letting me be better than you at climbing; maybe one day I'll be as good as you at physics. Finally to Ella, thanks for all the smiles.

Abstract

Whilst many advances have been made in the field of solution processed solar cells (SPSCs), there is still much work to be done if they are to fulfil their potential and reduce the cost of commercial photovoltaic devices. This thesis aims to assist in moving towards this objective by investigating ways to overcome some of the barriers to the commercialization of SPSCs. Such barriers include the costly and mechanically brittle electrode material of indium tin oxide, the use of solution deposition techniques which are not compatible with large-scale production, and a lack of understanding of the properties of promising new semiconducting materials such as organometal halide perovskites.

In this work a novel indium-free multilayer semi-transparent electrode has been fabricated and incorporated as the anode in polymer solar cells. Whilst molybdenum oxide is typically used as the 'seed layer' material in such trilayer structures, its replacement with tellurium dioxide has been found to lead to an enhanced transmittance in the optimised electrodes and to an increased short circuit current when such electrodes are employed in polymer solar cells.

The roll-to-roll compatible deposition technique of ultrasonic spray-coating has, for the first time, been successfully used for the fabrication of films of the organometal trihalide perovskite $CH_3NH_3PbI_{3-x}Cl_x$. Such films were subsequently successfully employed as the active layer in planar solar cells. This deposition technique is then extended to hole transporting and electron transporting materials in order to move towards a fully spray-deposited solar cell.

Finally, a combination of structural investigation techniques have been employed to monitor the formation of the perovskite $CH_3NH_3PbI_{3-x}Cl_x$ during thermal annealing of a precursor film. In-situ X-ray scattering measurements are used together with ex-situ scanning electron microscopy in order to correlate the evolution of the film during annealing to solar cell performance. In addition, the activation energy for the transition from precursor to perovskite has been calculated.

Publications

A. T. Barrows, A. J. Pearson, C. K. Kwak, A. D. F. Dunbar, A. R. Buckley and D. G. Lidzey, "Efficient planar heterojunction mixed-halide perovskite solar cells deposited via spray-deposition", *Energy & Environmental Science*, 7, 2944-2950 (2014)

A. T. Barrows, R. Masters, A. J. Pearson, C. Rodenburg and D. G. Lidzey, "Indium-free multilayer semi-transparent electrodes for polymer solar cells", *Solar Energy Materials & Solar Cells*, 144, 600-607 (2016)

A. T. Barrows, S. Lilliu, A. J. Pearson, D. Babonneau, J. E. Macdonald, A. D. F. Dunbar and D. G. Lidzey, "Monitoring the formation of a $CH_3NH_3PbI_{3-x}Cl_x$ perovskite during thermal annealing using X-ray scattering", submitted 2015

S. Lilliu, A. T. Barrows, M. Alsari, B. Curzadd, J. Griffin, O. Bikonda, J. E. Macdonald, D. G. Lidzey "Grain rotation and lattice deformation during perovskite spray coating and annealing probed in-situ by GI-WAXS", submitted 2015

L. Yang, A. T. Barrows, D. G. Lidzey and T. Wang, "Recent progress and challenges of organometal halide perovskite solar cells", *Reports of Progress in Physics*, 79, 026501 (2016)

C. K. Kwak, A. T. Barrows, A. J. Pearson, D. G. Lidzey, David and A. D. F. Dunbar, "An X-ray Scattering and Electron Microscopy Study of Bismuth Perovskites for Solar Cell Applications", submitted 2015

Conference Presentations

Solution Processed Semiconductor Solar Cells 2014, Oxford, September 2014 (Oral)

European Optical Society Annual Meeting 2014, Berlin, September 2014 (Oral)

Contents

Chapter 1: Introduction

Renewable resources – defined variously as resources which are not depleted when used or which are replenished on short timescales – are a vital part of the world's energy future. Whilst growth in energy generation since the industrial revolution has largely been driven by the utilization of fossil fuels, there is widespread recognition that this model is unsustainable. Perhaps the primary consideration in this regard is that of climate change. The 2014 report from the Intergovernmental Panel on Climate Change (IPCC) makes for stark reading, concluding that "Continued emission of greenhouse gases will cause further warming and long-lasting changes in all components of the climate system, including the likelihood of severe, pervasive and irreversible impacts for people and ecosystems" [1]. Even setting aside climate change, concerns around resource depletion and security of energy supply give some imperative to diversifying energy generation. Despite the moral imperative to reduce our use of hydrocarbon based energy sources, and despite the likely long-term necessity of doing so, economic and logistical considerations have thus far limited the widespread uptake of renewables. Indeed in 2012, excluding hydroelectricity, under 5% of global power production came from renewables (with around another 10% provided by hydroelectric installations) [2]. In this climate it is thus vital for researchers to work towards renewable energy solutions which are cheaper, more versatile and have lower embodied energy than those currently on the market.

Photovoltaic panels are not, at present, the cheapest option amongst the various players in the sustainable electricity market, being notably more expensive than both onshore wind and hydroelectricity[1]. They are, however, likely to be an essential component in future energy scenarios, being one of the few methods with the realistic potential to generate electricity on the scale required to achieve significant worldwide decarbonisation. The solar resource available to us is vast, with around 120 000 TW incident on the Earth's surface whilst average world energy usage is around 16 TW [3]. The solar resource is also rather more equitably distributed than known hydrocarbon

[1] Total system 'levelized cost of electricity' (LCOE) for new generation resources due to come online in the United States of America in 2019 are predicted to be 80, 85, 130 and 204 (2012$/MWh) for onshore wind, hydroelectric, utility scale solar PV and offshore wind respectively. These LCOE predictions represent the cost of building, connecting, maintaining and operating a plant over a 30 year time-frame, taking into account likely capacity factors. [8]

reserves, and so a transition to an economy driven by solar energy, rather than the burning of fossil fuels, could also act as a force for promoting an increase in worldwide equality. Solar PV generation capacity has increased rapidly over the last decade, with global installed capacity rising from 2.6 GW to 178.4 GW between 2003 and 2014 [4]. Despite this, photovoltaics still cover only slightly over 1% of electricity generation worldwide [4]. In order for solar power to achieve its potential in the near future, a significant reduction in the cost of photovoltaic modules is likely to be required.

Silicon panels currently dominate the PV market [5], accounting for around 90% of global production capacity [6]. Being an indirect band gap semiconductor, however, silicon has a poor absorption coefficient, requiring active layers hundreds of microns thick in order to produce an acceptably high optical density. There has thus been significant interest in the development of thin-film alternatives in order to reduce materials usage. Indeed, the thin-film market now includes First Solar, one of the largest PV producers in the world, and accounts for around 10% of global PV production capacity [7]. Within the thin-film 'genre' of devices, solution processed solar cells (SPSCs) offer a potential route to low cost, lightweight and mechanically flexible devices. Accordingly, the fields of solution processed organic photovoltaics and, more recently, perovskite photovoltaics have received extensive attention from the academic research community, resulting in huge improvements in the efficiency and lifetime of these devices as well as important advances in our understanding of these materials. Most research, however, has been undertaken using processing methods and materials which, whilst excellent for laboratory scale device fabrication, are of limited applicability when it comes to the commercialization and scale-up of these technologies.

1.1 Summary and Motivation

This thesis aims to play a role in moving solution processed solar cells towards the point of commercialization. Initial studies focused on organic solar cells based on polymer:fullerene bulk heterojunctions. During the course of the work, however, organometal halide perovskites emerged as an exciting new material in the world of solution processed solar cell research, and it seemed prudent for our research group to begin to explore these promising materials. Later studies thus focused on these

perovskite materials, which have seen rapid advances in device performance together with a vastly improved understanding of material properties over the past 2-3 years.

The requisite background knowledge and state of the current literature is detailed in **Chapter 2** which provides a general introduction to photovoltaics followed by a more specific discussion of solution processed solar cells, organic solar cells, perovskite solar cells and transparent electrodes. **Chapter 3** details the experimental methods used in this thesis.

In **Chapter 4** a new oxide/metal/oxide multilayer semi-transparent electrode is fabricated as a replacement for the widely used indium tin oxide (ITO) (the limitations of which are discussed in **Chapter 2**). This electrode has a structure TeO_2/Ag/MoO_3 (TAM) and is compared to an electrode with structure MoO_3/Ag/MoO_3 (MAM) which has been studied in a number of papers previously. The transmittance and sheet resistance measurements performed on these multilayer electrodes point to the formation of a more continuous silver film when deposited on TeO_2 as compared to MoO_3, and this is confirmed by scanning electron microscopy images. This lowering of the percolation threshold of the silver film leads to an increased transmittance for the TAM electrode in comparison to the MAM electrode, leading to an enhancement in the short circuit current and power conversion efficiency of PCDTBT:PCBM bulk heterojunction solar cells.

Chapter 5 details work on using ultrasonic spray-coating as a scalable deposition technique for the photoactive layer of planar perovskite solar cells with an inverted architecture. This is an important step forward in the replacement of the laboratory scale technique of spin-coating by roll-to-roll compatible processes. After an optimisation process in which deposition temperature, casting solvent, film thickness and thermal annealing protocol were investigated the spray-coated solar cells showed a maximum power conversion efficiency of over 11%, with an average efficiency equal to that of spin-coated reference devices. This work is believed to be the first published example of the fabrication of perovskite solar cells by a roll-to-roll compatible solution processing technique. In addition, the maximum efficiency achieved is believed to be the highest reported efficiency to that date for a solar cell employing a spray-coated photoactive layer. It is then shown that the PEDOT:PSS hole transport layer can also be successfully deposited using this method with no loss in average efficiency in

comparison to spin-coating. Finally, work on spray-coating of the PCBM electron transport layer and on 'two-step' fabrication of the perovskite films is presented.

Chapter 6 focuses on in-situ investigations of the crystallization of the $CH_3NH_3PbI_{3-x}Cl_x$ perovskite from a precursor film during a thermal annealing step. In-situ grazing incidence X-ray scattering is performed using both wide angle and small angle experimental arrangements (GIWAXS and GISAXS). These results are presented together with ex-situ scanning electron microscopy measurements and photovoltaic device results. The GIWAXS experiments show the formation of the perovskite from an unidentified precursor phase during the annealing step, followed by its degradation to products including lead iodide at longer annealing times. In addition, strong preferential out-of-plane orientation of the (110) plane of the perovskite is observed. The results also allow for the determination of the effective activation energy of the precursor to perovskite transition, which is found to be 85 kJ/mol. From the GISAXS measurements it can be seen that during a thermal anneal at 80°C there is an evolution of the length scales found in the film, with a large increase in the number of features with size in the range 30-400 nm and particularly around 100-150 nm. This evolution in length scales is observable in scanning electron microscopy measurements on ex-situ samples and is correlated to an increase in surface coverage of the perovskite film, a property which is known to be crucial for device performance. Results are correlated with the performance of spin-coated devices and average power conversion efficiencies of 12.2% are achieved.

1.2 References

[1] Intergovernmental Panel on Climate Change, "Climate Change 2014 Synthesis Report Summary Chapter for Policymakers," 2014.

[2] "BP Statistical Review of World Energy," 2013.

[3] D. J. C. Mackay, "Solar energy in the context of energy use , energy transportation and energy storage," *Phil. Trans. R. Soc. A*, vol. 371, p. 20110431, 2013.

[4] SolarPower Europe, "Global Market Ourlook For Solar Power 2015-2019," 2015.

[5] J. Nelson, C. J. M. Emmott, "Can solar power deliver?," *Phil. Trans. R. Soc. A*, vol. 371, p. 20120372, 2013.

[6] J. Jean, P. R. Brown, R. L. Jaffe, T. Buonassisi, and V. Bulovic, “Pathways for Solar Photovoltaics,” *Energy Environ. Sci.*, 2015.

[7] “International Technology Roadmap for Photovoltaic (ITPV),” 2013.

[8] U. S. Energy Information Administration, “Levelized Cost and Levelized Avoided Cost of New Generation Resources in the Annual Energy Outlook 2014,” 2014.

Chapter 2: Solution Processed Solar Cells – Organics and Perovskites

2.1 Introduction

Within this Chapter, relevant background information and underlying physical principles relating to the topics in this thesis are presented. **Section 2.2** introduces general concepts relating to the energy levels of electrons within atoms, molecules and crystals before going on to address the basic working principles of photovoltaic devices and the required background theory for understanding device characterisation measurements. **Section 2.3** then discusses the particular promises and pitfalls of solution processed solar cells together with a brief introduction to roll-to-roll film deposition techniques. **Section 2.4** and **Section 2.5** focus in greater detail on organic solar cells and perovskite solar cells respectively, whilst **Section 2.6** is concerned with transparent electrodes and in particular the replacement of the widely used indium tin oxide.

2.2 General Background

2.2.1 Atomic Orbitals

Within an atom, electrons are said to be in orbitals of differing energy. Unlike with the classical view of orbiting bodies, in which the location and movement of the body are well defined, the quantum mechanical nature of electrons dictates that these orbitals should be thought of as reflecting the probability of an electron being found within a particular region. The shape, properties and occupation of these orbitals are determined by the quantum numbers n (the principal quantum number, describing the potential energy of the electron), l (the azimuthal quantum number, describing the magnitude of the angular momentum of the electron and the shape of the orbital), m_l

(the magnetic quantum number, describing the direction of angular momentum of the electron and thus the orientation of the orbital) and m_s (the spin quantum number).

These four quantum numbers may take only specific values: n is an integer where $n \geq 1$, l is and integer where $0 \leq l \geq n\text{-}1$, m_l is an integer where $-l \leq m_l \geq l$ and m_s is equal to either +½ or -½. The principal quantum number defines the 'shell' in which the electrons reside. In order to avoid confusion, the l value of each orbital is typically denoted with a letter: 's' for $l = 0$, 'p' for $l = 1$, 'd' for $l = 2$, 'f' for $l = 3$ and alphabetically thence forth. Due to the Pauli exclusion principle, no two electrons can share all four quantum numbers and this, in combination with the rules for the allowed values of the four quantum numbers, limits the number of electrons which can reside within each orbital. **Table 2.1** demonstrates this for the first and second shells, which incorporate the orbitals 1s, 2s and 2p. Clearly, for higher energy shells there exist a larger number of orbitals. Whilst initially the relative energies of the orbitals are dominated by the principal quantum number (1s < 2s < 2p < 3s < 3p) beyond this it is found that the 4s orbital exists at a lower energy than the 3d orbital. At higher energies a pattern emerges in this regard, with the value of the azimuthal quantum number (l) coming to dominate over the principal quantum number (n) in determining the relative energy of orbitals, a situation which arises due to the dependence of the former on electron-electron interactions whilst the latter depends upon interactions between the electrons and the nucleus which become somewhat less important at higher orbital energies.

It should be noted that p orbitals can be subdivided into p_x, p_y and p_z orbitals with equal energy but differing orientation, with the orbitals considered as being orientated along x, y and z axes respectively.

n	l	m_l	m_s	Orbital Name		Total No. of Electrons
1	0	0	$m_s = ½$	1s		2
			$m_s = -½$			
2	0	0	$m_s = ½$	2s		8
			$m_s = -½$			
	1	-1	$m_s = ½$	$2p_x$	2p	
			$m_s = -½$			
		0	$m_s = ½$	$2p_y$		
			$m_s = -½$			
		1	$m_s = ½$	$2p_z$		
			$m_s = -½$			

Table 2.1 Quantum numbers, orbital names and the number of electrons which can occupy each shell. The first two shells only are shown.

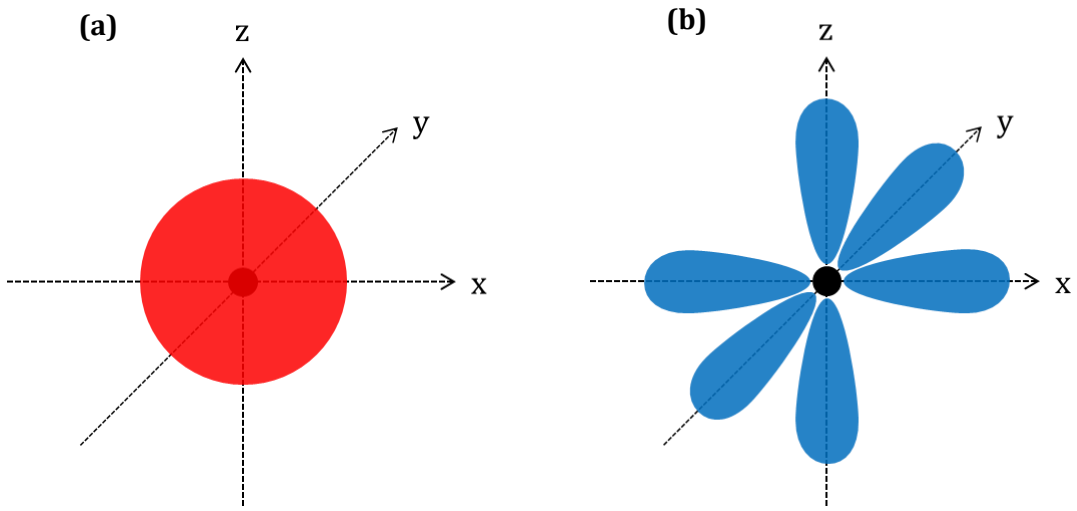

Figure 2.1 Simplified diagram showing the shape and orientation of s **(a)** and p **(b)** atomic orbitals about the nucleus.

2.2.2 Molecular Orbitals

When two atoms are brought close enough together their atomic orbitals will overlap to form molecular orbitals. These can be bonding orbitals or antibonding orbitals, respectively relating to constructive and destructive interactions between the atomic orbitals. Bonding orbitals have high electron density between the two nuclei, shielding their Coulombic repulsion and thus resulting in a lower energy system than that of the individual atomic orbitals. Conversely, antibonding orbitals have low electron density in the region between the nuclei leading to an unstable higher energy state. An example of these energy levels for 1s atomic orbitals, filled with one electron as in the case of hydrogen, is shown in **Figure 2.2(b)** where it can be seen that the electrons will fill the bonding orbital resulting in a covalent bond holding the atoms together. In the case of helium atoms, each containing 2 electrons in their 1s orbitals (denoted $1s^2$), both the bonding and antibonding orbitals would be filled, resulting in a total energy which is essentially the same as that of the individual atoms, thus explaining why hydrogen forms stable H_2 molecules but helium does not form He_2.

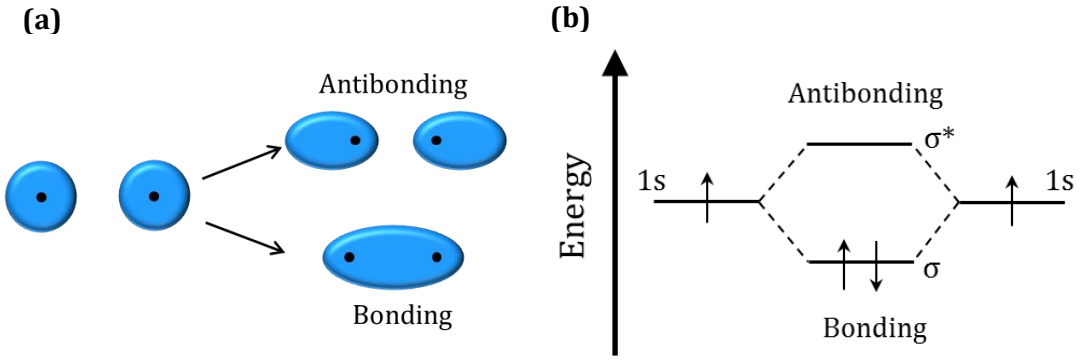

Figure 2.2 Schematic of electron density for bonding and antibonding orbitals when two hydrogen atoms are brought close together **(a)**. The energy levels of the atomic and molecular orbitals for this system are shown in **(b)**.

Molecular orbitals between two atoms that are symmetrical around the axis connecting the two nuclei are known as σ bonds and can, as discussed above, be either bonding (σ) or antibonding (σ*) in nature. Molecular orbitals which are not symmetrical about this axis are known as π bonds. Again these can be bonding or antibonding, and due to the location of their electron density away from the axis joining the two nuclei their strength is significantly lower than that of σ bonds [1].

2.2.3 Band Formation in Crystals

As discussed previously, when atoms are brought close together their electron orbitals overlap, leading to a splitting into bonding and antibonding molecular orbitals. As increasing numbers of atoms are brought close to each other, Pauli's exclusion principle forbids all overlapping orbitals from existing at the same energy. The resulting allowed states thus take slightly different energies, and as increasing numbers of atoms are brought into close proximity, the density (in energy) of these allowed states increases. Eventually, with close enough atomic spacing, for example that found in a crystal structure, the allowed energetic states can be considered to form a continuum, that is 'bands' of allowed energies are formed with energy gaps between them [2].

2.2.4 A Brief Introduction to Photovoltaics

In a typical inorganic semiconductor, the energy difference between the valence band (filled) and the conduction band (unfilled) is termed the band gap, denoted E_g. A photon with energy E_γ incident on this material can thus promote an electron from the valence band into the conduction band providing that $E_\gamma \geq E_g$. This process leaves behind a hole in the valence band, and the resulting electron-hole pair, bound together by Coulombic attraction, is termed an exciton. (**Figure 2.3(a)**). Lower energy (longer wavelength) photons, with energy less than E_g, cannot promote an electron across the band gap, and thus in a solar cell their energy is wasted (**Figure 2.3(b)**). For high energy (short wavelength) photons, with $E_\gamma > E_g$, there is enough energy to promote an electron across the band gap and also to impart additional energy to one or both of the charge carriers. The carrier(s) with excess energy will then relax to the edge of the band, giving up their energy primarily by the emission of phonons; the energy in excess of the band gap energy is thus simply converted into heat in the photoactive material and not useful electrical work (**Figure 2.3(c)**). Clearly there is thus a balance to be struck when considering the optimum band gap for a photoactive material – a low band gap material will absorb a high number of photons but will not extract the maximum possible useful energy from each photon. Conversely, a material with a large band gap will maximise utilisation of the energy carried by the short wavelength photons, but will not absorb those of longer wavelength. This balance can be thought of in terms of currents and voltages: in a solar cell the current is highly dependent upon the number of charge carriers generated whilst the voltage is closely related to the band gap

energy. This trade-off is reflected by the famous Shockley-Queisser limit, a calculation of the maximum theoretical efficiency for a single junction solar cell, which under the AM1.5 spectrum at 1 sun is around 33% for a band gap of just over 1.3 eV [3].

The binding energy of a photogenerated exciton is dependent upon the dielectric constant of the semiconducting material in which it exists. A small dielectric constant is indicative of limited screening of charge and will lead to an exciton with a high binding energy and a small separation between the charges. Depending upon the magnitude of its binding energy, the charges in an exciton may be separated ('exciton dissociation') either by thermal energy or by some other driving force such as a difference in electron affinity at an interface between two materials (see **Section 2.4.4**). If exciton dissociation does not occur, the electron and hole will recombine. Following successful charge separation, free carriers are swept from the device by an electric field and can perform work in an external circuit, allowing solar cells to fulfil their desired role of generating electrical power.

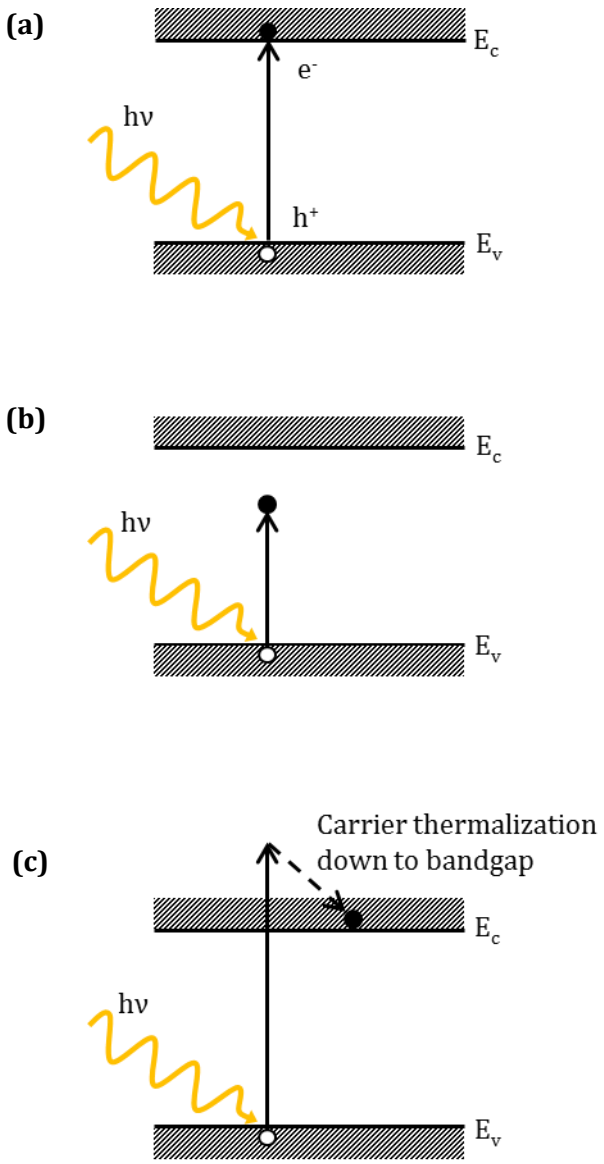

Figure 2.3 In **(a)** the incident photon has energy $E_\gamma = E_g$ and thus can promote an electron from the valence band to the conduction band. In **(b)** the incident photon has energy $E_\gamma < E_g$, and thus cannot promote an electron from the valence band to the conduction band. In **(c)** the incident photon has energy $E_\gamma > E_g$, the electron is thus promoted to the conduction band and receives some additional excess energy, this is given up primarily by non-radiative emission as the electron relaxes to the bottom of the conduction band.

2.2.5 Device Characterisation and Device Metrics

Photovoltaic devices are typically characterised by measuring their current-voltage response under illumination. A source-measure unit is used to apply a voltage across

the device and measure the resulting current flow whilst the device is illuminated with a known spectrum of light. Analysis of the relationship allows for the extraction of a number of metrics which give an insight into the workings of the device under test. A typical current density against voltage curve for a solar cell is shown in **Figure 2.4**.

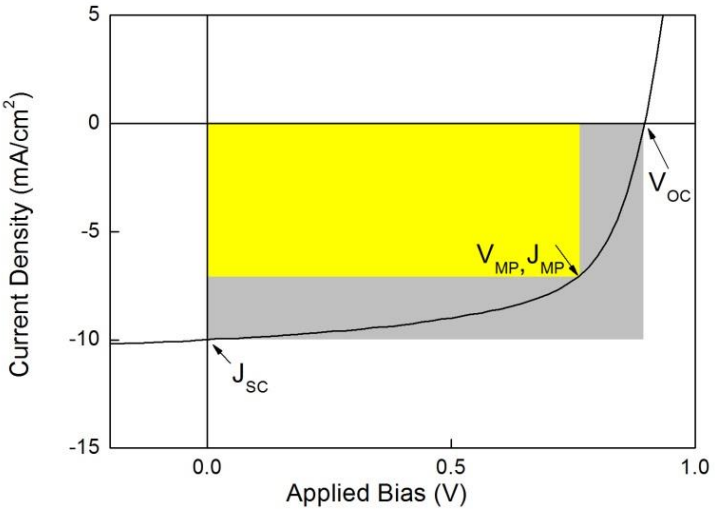

Figure 2.4 Typical current density against voltage characteristics of an illuminated solar cell showing the open circuit voltage (V_{OC}) and short circuit current density (J_{SC}) as well as the voltage and current at the maximum power point (V_{MP}, J_{MP}) .

The Solar Spectrum

The sun emits light with a spectrum approximately equal to that of a black body with a temperature of 5870 K, meaning that the largest proportion of the energy in the solar spectrum is in the visible region. Due to atmospheric absorption, however, the 'raw' solar spectrum is not used as the reference spectrum when testing photovoltaic devices. AM (air mass) spectra refer to the mass of air through which solar radiation has passed, with AM1 corresponding to light incident normal to the Earth's surface. The convention for characterising photovoltaics is to use the AM1.5 spectrum, with a total irradiance of 1000 Wm^{-2}, as shown in **Figure 2.5**, which corresponds to light incident at an angle of 48.2° relative to the normal to the Earth's surface. This spectrum is representative of the spectrum encountered terrestrially at mid-latitudes, for example much of Europe and North America.

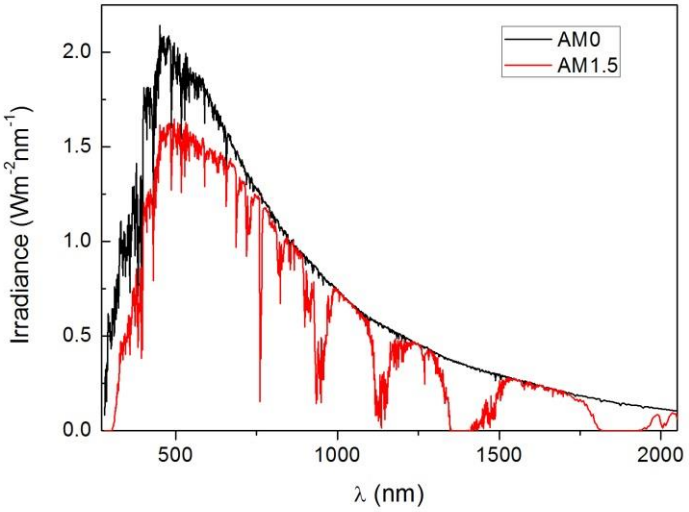

Figure 2.5 The AM0 and AM1.5 spectra [4].

Power Conversion Efficiency (PCE) & Maximum Power Point (MPP)

PCE is the overall efficiency of the solar cell at converting energy incident on the cell (in the form of electromagnetic radiation) into outputted electrical energy. Cell efficiency typically only refers to the efficiency of the active area, and does not take into account, for example, geometrical and aperture losses due to device design and geometry. These losses are more typically accounted for when 'module efficiency' is quoted. Efficiency is greatest where the product of voltage and current is maximised, termed the maximum power point. PCE can be defined as shown in **Equation 2.1** by using either the voltage and current at this maximum power point (V_{MP}, J_{MP}) or by using the short circuit current (J_{SC}), open circuit voltage (V_{OC}) and fill factor (FF), metrics which are common when discussing solar cell performance.

$$PCE = \frac{P_{out}}{P_{in}} = \frac{P_{MP}}{P_{in}} = \frac{V_{MP}J_{MP}}{P_{in}} = \frac{V_{OC}J_{SC}FF}{P_{in}} \quad \{2.1\}$$

Short Circuit Current (J_{SC})

This is the current which flows when there is no applied voltage. Charge is swept out of the device due to the built-in field which arises due to the difference in work functions between the electrodes. J_{SC} is highly dependent on the optical field intensity in the active layer, the absorbance of the photoactive materials and the efficiency of charge generation, transport and extraction within the device. Too thin an active layer or poor absorbance in the photoactive materials can be expected to result in a low J_{SC}.

Open Circuit Voltage (V_{OC})

The open circuit voltage is the applied voltage at which no current flows, that is, the point at which the applied voltage cancels out the built in voltage of the cell, leaving no driving force for the extraction of charges generated within the device.

Fill Factor (FF)

The fill factor is given by the ratio of the product of V and J at the maximum power point (V_{MP}, J_{MP}) to the product of V_{OC} and J_{SC} as shown in **Equation 2.2**.

$$FF = \frac{V_{MP}J_{MP}}{V_{OC}J_{SC}} \quad \{2.2\}$$

This is illustrated in **Figure 2.4** by the ratio of the yellow rectangle to the grey rectangle, and it can be seen to quantify the 'rectangularness' of the *JV* curve of the solar cell. An ideal device should have a high fill factor, indicative of few losses following charge generation. FF is strongly linked to charge transport and recombination as well as series and shunt resistances.

Series Resistance (R_s)

Series resistance arises due to resistance within the electrodes, resistance internal to the active layer itself and resistance at interfaces and contacts. It is a resistance to the extraction of electrons from the solar cell, and a good device should aim to have a very low series resistance. In well-functioning solar cells the chief contributor to this form of resistance is typically the sheet resistance of the semi-transparent window electrode – an electrode with high sheet resistance causes resistance to the lateral extraction of electrons to metal contacts, leading to an increased series resistance (see **Section 2.6** for a more detailed discussion of transparent electrodes). An estimate of series resistance can be obtained from the inverse of the slope of the *JV* curve at $V = V_{OC}$ [5].

Shunt Resistance (R_{sh})

Shunt resistance relates to current leakage paths in a device, and unlike series resistance in an ideal solar cell it should have a very high value. Low shunt resistance is indicative of pathways within the device which provide an alternative route for charges to travel through. This might occur if, for example, defects have allowed the hole transport material and electron transport material to come into contact with one

another. An estimate of a device's shunt resistance can be made as the inverse of the gradient of the *JV* curve at $V = 0$. By considering the shape of an ideal *JV* curve together with the slope of the curve for a non-ideal device at $V = 0$ and $V = V_{OC}$ we can clearly see that a high series resistance and/or low shunt resistance will manifest themselves as a low FF when considering device metrics.

External/Internal Quantum Efficiencies

The external quantum efficiency (EQE) of a solar cell at a particular wavelength is defined as the ratio of charges extracted from the device to photons of that wavelength incident on the device, whilst the internal quantum efficiency (IQE) is the ratio of charges extracted from the device to photons absorbed in the active layer of the device. IQE thus takes into account only loss mechanisms which occur after absorption of a photon whilst EQE also takes into account losses due to factors such as insufficient optical density of the active layer, reflection from the front face of the device and parasitic absorption by electrodes and interlayers.

Equivalent Circuit Model

A solar cell may be approximately modelled by the equivalent circuit shown in **Figure 2.6** in which a current source, a diode and a number of resistors allow reproduction of the *JV* behaviour of the device.

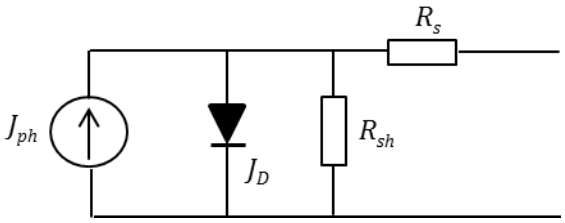

Figure 2.6 A basic equivalent circuit for a solar cell where J_{ph} and J_D are the photocurrent and diode current respectively, R_s is series resistance and R_{sh} is shunt resistance.

The current-voltage behaviour of an ideal solar cell ($R_s = 0$, $R_{sh} = \infty$, ideal diode) can be described by the Shockley equation for an ideal photodiode, given by

$$J = J_{ph} - J_D = J_{ph} - J_0 \left[\exp\left(\frac{eV}{kT}\right) - 1\right] \qquad \{2.3\}$$

When losses due to series resistance, shunt resistance and diode non-ideality are taken into account this becomes

$$J = J_{ph} - J_0 \left[\exp\left(\frac{e(V + JR_s)}{nkT} \right) - 1 \right] - \frac{V + JR_s}{R_{sh}} \quad \{2.4\}$$

where J_{ph} is the photogenerated current, R_s is the series resistance, R_{sh} is the shunt resistance, J_0 is the diode reverse saturation current density, n is the diode ideality factor, T is the temperature and k is Boltzmann's constant.

2.3 Solution Processed Solar Cells (SPSCs)

This class of solar cell has historically been dominated by organic and dye-sensitized solar cells, which have both risen to have record PCEs of over 11%. More recently perovskite solar cells have emerged as a major player in this area, achieving an unprecedented rise in PCE to over 20% [6].

2.3.1 Promises and Pitfalls

Arguably the greatest promise of solution processed solar cells (SPSCs) is in reducing the material and manufacturing costs of solar cell fabrication. The very low film thickness used for the photoactive layer of most SPSCs – typically a few tens or hundreds of nm, as opposed to tens or hundreds of microns for crystalline silicon – allows for a significant reduction in material usage per unit area, whilst in addition many of the materials are readily available at low cost. This is particularly the case for the emerging organometal halide perovskites, where materials synthesis is less complex than for the polymers typically used in high performance polymer solar cells. Compatibility with high throughput production methods is also vital in order to realise the potential for cost reductions offered by SPSCs. Continuous or semi-continuous processes such as roll-to-roll (R2R) processing are considered ideal for achieving these savings, and a fully roll-to-roll fabricated solar cell with high efficiency and long lifetime can be seen as the 'holy grail' of SPSC research. In roll-to-roll production a flexible substrate is transferred from an initial reel to a final reel with the solar cell

being deposited in the intervening space. This may involve numerous steps and a variety of deposition processes, although clearly the fewer the number of steps and the fewer different deposition systems required the simpler any production line can be. Such a high throughput system reduces the capital investment required to set up a production line with a given capacity, especially if it were to avoid the expense associated with vacuum systems commonly used for, for example, sputtering and evaporation. There is a caveat here, however: with the better established thin-film technologies such as cadmium telluride (CdTe) the majority of the module manufacturing costs now in fact arise not from the purchase and deposition of the semiconductor materials, but rather from the glass substrates, transparent electrodes, encapsulation materials and so forth [7]. In addition, 'balance of system' (BOS) costs for PV systems (mounting materials, installation labour, inverters, wiring and so forth) currently account for more than the module costs themselves in many markets [8]. In this economic environment, novel low cost materials and deposition processes for the semiconductor layers in a solar cell will likely not, in themselves, be enough to give the edge required to significantly disrupt the PV market. Since BOS costs increase with increasing area any novel solar cell should thus expect to need to match current technologies on efficiency and lifetime as well as providing lower material and processing costs. One hope for SPSCs is that since they should, ideally, allow for simple processing on flexible, lightweight substrates such as PET [9–12] or even metal foils [13,14] costs associated with glass substrates and bulky mounting equipment may be significantly reduced.

If SPSCs cannot reduce the overall cost of solar energy, then compatibility with lightweight and flexible designs may still ensure that they have a role to play in more niche applications, for example on clothes, tents or structures which cannot support the weight of traditional modules and their mounts.

Finally, building integrated photovoltaics (BIPVs) offer a potential application for semi-transparent polymer or perovskite solar cells. The idea behind BIPVs is to incorporate solar cells into materials which make up an integral part of a building, for example roofing materials or windows, thus offsetting many of the costs associated with the substrate, installation, transportation and so forth, significantly reducing the effective cost of the PV system. Semi-transparent cells are particularly interesting for application in windows within the BIPV concept, and have been explored with inorganic cells by utilising small holes or gaps in arrays of cells [15,16]. The resulting

modules, however, look quite different to a traditional window and struggle to obtain the neutral colouring which is desirable for most window applications. Semi-transparent polymer solar cells have been fabricated with quite some success in terms of both efficiency and achieving a neutral colour, with single junction cells achieving 4.2% PCE for 32% average visible transmittance (AVT)[17] and tandem cells reaching an impressive 8% PCE for 44% AVT whilst remaining close to neutral in colour [18]. Single junction neutral-coloured semi-transparent perovskite devices have also been fabricated with promising efficiencies (5.2% PCE for 28% AVT). In addition, these devices showed significantly improved performance at high angles of incidence in comparison to reference silicon devices, a property highly advantageous for BIPV scenarios, where such angles of incidence can be expected for much of the day [19].

As well as economic factors, it is worth considering the environmental impact of different solar cell technologies in relation to their energy payback time. Inorganic photovoltaics often require high temperature processing steps, and moving to low temperature, solution processed roll-to-roll fabrication methods should allow for significant reductions in the energy required for cell production. It has been suggested that a 5% efficient roll-to-roll fabricated organic solar cell (OSC) on a flexible substrate could have an energy payback time of as little as 0.2 years, around ten times less than multi-crystalline silicon was calculated to have under the same conditions [20].

2.3.2 Roll-to-Roll Compatible Processing Techniques

Various roll-to-roll (R2R) compatible film deposition techniques are available for solution processed materials, all having different requirements for ink formulations (viscosity, surface tension etc.) and all offering their own advantages and disadvantages. A number of the most common of these techniques are briefly summarized below; for further details on these and other techniques, interested readers are directed towards the following references [21–23].

Blade coating (as shown in **Figure 2.7(a)**, also known as doctor blading or knife coating) involves placing the ink in front of a fixed blade; movement of the substrate relative to the blade then leads to the spreading of a thin layer with the height of the blade and the solution concentration determining film thickness. One notable drawback of this technique is that it is not possible to easily pattern the film during deposition.

Slot-die coating (**Figure 2.7(b)**)deposits ink via a slot in a deposition head, with layer thickness being heavily dependent upon both the ink flow rate and the speed of movement of the head or substrate. This deposition technique is able to produce 1D patterns quite simply and has seen extensive development for R2R fabrication of OSCs, in particular by Frederik Krebs' research group at the Technical University of Denmark.

Rotary screen printing (**Figure 2.7(d)**) involves forcing ink through a mesh which is brought into contact with the substrate surface. This technique is capable of extensive patterning, however it requires high viscosity and low volatility inks which have proved difficult for the deposition of polymer solar cell active layers, although they have been quite successful in the deposition of silver electrodes [24].

Flexographic printing (**Figure 2.7(f)**) involves the transfer of ink from raised areas on a printing plate (commonly made of rubber or similar) which is affixed to a rotating cylinder. Capable of producing patterning, this technique has again been employed predominantly for the deposition of metal electrodes [25].

Inkjet printing (**Figure 2.7(e)**) typically employs piezoelectric transducers in order to force ink out of the nozzle once the pressure in the reservoir exceeds the surface tension of the ink at the nozzle exit. This technique offers the advantage of being capable of producing 2D patterns which can be changed without the requirement for new hardware. Its application in the deposition of large-area uniform films is highly complex however, requiring inks which are often a blend of up to 8 different solvents [21].

Spray-coating (**Figure 2.7(c)**), as has been used in **Chapter 5** of this work, is highly compatible with high throughput production of continuous films with low materials wastage. Due to the nature of the process, however, patterning is only possible through the use of masks which introduce both material wastage and the risk of edge effects in the final film. In all spray nozzles energy is used to break up the liquid bulk into droplets ('atomization'); in an airbrush nozzle this is achieved using high velocity gas, typically air or nitrogen. Spray-coating techniques using these simple airbrush nozzles have been employed in the deposition of the photoactive layer of OSCs since 2007, when a PCE of 2.8% was obtained [26]. More recent work has continued the application of this technology as well as exploring the application of ultrasonic spray-coating, a technique in which droplets are formed via high frequency vibrations and

subsequently directed to the substrate by a carrier gas. This technique has since been successfully employed for the deposition of PEDOT:PSS and molybdenum oxide hole transport layers, photoactive polymer:fullerene blends and silver electrodes [27–30]. Currently the highest published device efficiency for an OSC incorporating a spray-coated active layer appears to be 7.3% [31]. Further details on ultrasonic spray-coating are provided in **Chapter 3 Section 3.2.4**.

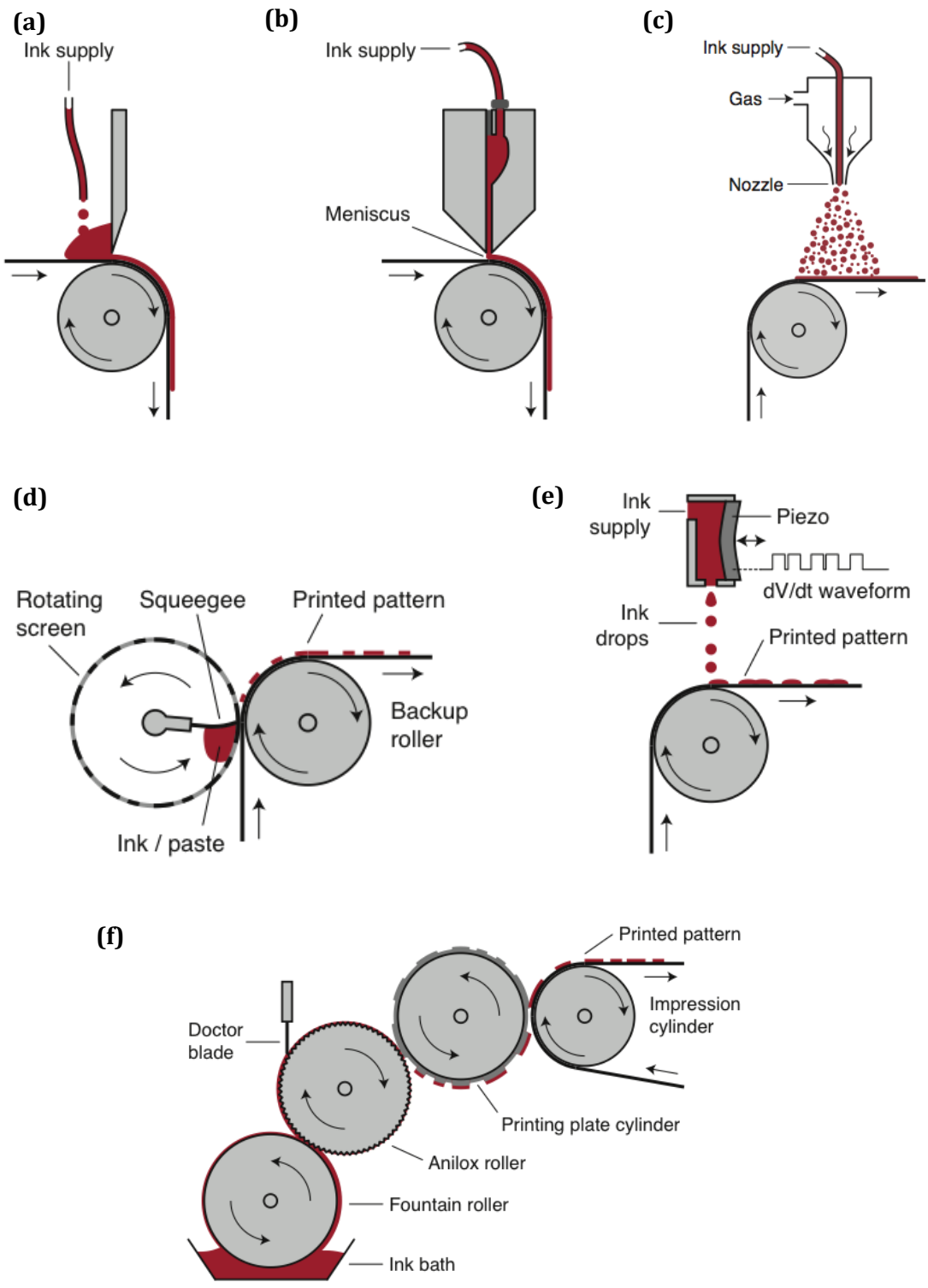

Figure 2.7 Schematics of printing and coating techniques: blade coating **(a)**, slot-die coating **(b)**, spray coating **(c)**, rotary screen printing **(d)**, inkjet printing **(e)**, flexographic printing **(f)**. Taken from Søndergaard et al. [23].

The work contained within **Chapter 5** is likely the first published demonstration of a solution processing, roll-to-roll compatible deposition method for the photoactive layer of a perovskite solar cell [32]. Since the publication of that work a number of other approaches have been successfully demonstrated for R2R compatible deposition of the perovskite layer of a solar cell; these are summarized in **Table 2.2**.

Deposition Technique	**Deposition Environment & Architecture**	**Other Layers Deposited Using R2R Compatible Solution Processing**	**Efficiency (%) (mean/max)**	**Ref.**
Ultrasonic spray-coating (Chapter 5)	Ambient Planar	None	7.8/11.1	[32]
Airbrush spray-coating	Ambient Planar	None	7.4/7.9	[33]
Airbrush spray-coating	N2 glovebox Planar	None	9.2/10.2	[34]
Inkjet printing	Ambient Mesoporous	None	11.2/12.3	[35]
Drop casting	Unclear Mesoporous	ZrO_2 (EBL/ scaffold) Carbon (electrode)	10.3/12.8	[36]
Slot-die coating*	Ambient Planar	ZnO (ETL) P3HT (HTL)	10.1/11.9	[37]
Slot-die coating	Ambient Planar	PEDOT:PSS (HTL) PCBM (ETL) Ag (electrode)	4.9/ no max. given	[38]

Table 2.2 Roll-to-roll compatible solution processing techniques used to deposit the perovskite layer of a solar cell. All perovskite layers have been fabricated via a 'one-step' process, apart from that marked with * in which a 'two-step' process was used; see **Section 2.5.7** for an explanation of one-step and two step fabrication.

2.4 Organic Solar Cells

2.4.1 Introduction

Whilst single layer organic solar cells (OSCs) were studied as far back as the 1950s [39], at that time they were unable to produce high efficiencies. This was largely due to the fact that absorbed light created a bound exciton in which the charges were far more likely to recombine than to dissociate and thence be collected at the electrodes. The solution to this problem lay in incorporating two materials rather than one into the photoactive layer, and so heterojunction devices consisting of electron donor and electron acceptor materials were born. The first 'donor-acceptor' OSC reported in the literature was a bi-layer device fabricated by Tang in 1986 which achieved an efficiency of around 1% [40]. OSCs have typically been divided up into two categories: polymer solar cells and small molecule solar cells. Whilst Tang's seminal work involved the use of small molecules, the first polymer solar cells were reported in the early 90s, and the now popular concept of 'bulk heterojunctions' emerged shortly afterwards [41,42]. Polymer devices have some innate disadvantages over their small molecule cousins, for example variations in molecular weight and polydispersity make batch-to-batch reproducibility a concern [43]. Unlike polymers however, small molecule based devices have often relied upon thermal evaporation for film deposition, and thus polymers have attracted the greater proportion of research efforts amongst those interested in solution processed electronics [44]. Within **Chapter 4** only polymer solar cells have been fabricated, and the following discussion is therefore devoted to this class of device only; from here onwards the term organic solar cell (OSC) is used to refer to this class of solar cell only.

2.4.2 Device Architecture

There are two possible device architectures for OSCs: 'normal' and 'inverted'. The normal architecture employs a transparent front electrode as the hole collecting anode with the reflective rear electrode acting as the electron collecting cathode. In the inverted structure these roles are reversed – the transparent front electrode acts as the cathode whilst the rear electrode acts as the anode. Appropriate materials selection for the rear electrode and intermediate layers allows many transparent electrode materials, such as the ubiquitous indium tin oxide (ITO), to be used as the front (transparent) electrode in either architecture. Simply exchanging the positions of the

interlayers can, for example, switch a device from normal to inverted architecture or vice-versa [45]. There is particular interest in inverted devices with respect to improving the lifetime of OSCs, since they typically replace low workfunction metals such as calcium and aluminium with a more stable metal such as silver. In addition they avoid the use of the hole transport material PEDOT:PSS, commonly used as an interlayer in devices with normal architecture, with which concerns about the impact of its hygroscopic and acidic nature on device lifetime have been raised, particularly in humid environments [46–49].

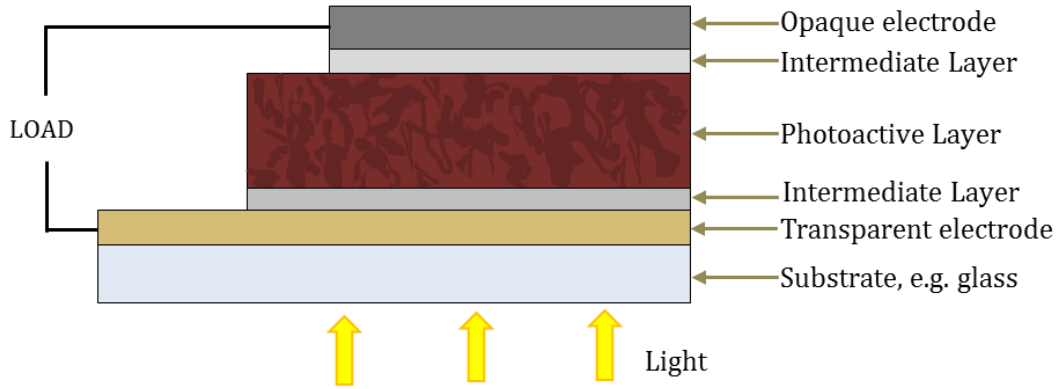

Figure 2.8 An overview of the typical structure of an organic solar cell, with light entering from the bottom.

Organic solar cells are typically built on a 'superstrate' or 'bottom illuminated' design, as shown in **Figure 2.8**, in which the device is fabricated on a transparent substrate (e.g. glass/ITO) but is then turned over in use, with light passing through the glass to reach the cell. The alternative is to build the device as it will be used, depositing the transparent electrode as the final layer in a 'substrate' ('top illuminated') design. This architecture offers the advantage of facilitating the production of devices on metal foil substrates which offer low cost, high mechanical flexibility and good thermal stability as well as providing a good barrier against moisture and oxygen ingress [14,50,51]. Building devices in this architecture, however, poses other challenges with regards to the roughness of the substrate, deposition of a conductive electrode without causing damage to underlying photoactive layers and requirements for encapsulation on the illuminated side. The traditional bottom illuminated design thus currently remains by far the most common architecture within academic research.

The intermediate charge extraction/blocking layers play a number of important roles in OSCs. Firstly they play a role in determining the polarity of the device, by determining the selectivity of the contact – whether holes or electrons will be able to reach the adjacent electrode. In this context they provide a 'blocking layer' to inhibit transfer of the undesired charges to the electrode. In addition they can assist in charge extraction for the charges which are to be collected at that electrode by providing an intermediate energy level between the relevant active layer material and the electrode. Charge extraction may also be enhanced by the formation of an interfacial dipole. This is believed to occur for certain interlayers such as the polymer PFN (poly [9,9-bis(3'-N,N-diethylamino)propyl)-2,7-fluorene)-alt-2,7-(9,9-dioctylfluorene)]), with the dipole aligning with the built-in potential which arises from the work function difference between the electrodes [52]. Finally, in OSCs intermediate layers often also act as an optical spacer in order to optimise light intensity within the active layer. By tuning the interference effects that occur due to reflection from the rear electrode it is possible to maximise the optical field intensity within the photoactive layer of the device [53].

2.4.3 Orbital Hybridization and Conjugation in Organic Semiconductors

Carbon provides the building block of organic molecules and is thus crucial in determining their optoelectronic properties. A neutral carbon atom contains 6 electrons in the orbitals $1s^2 2s^2 2p^2$, or more precisely $1s^2 2s^2 2p_x^1 2p_y^1$. Looking at this electronic structure it seems that carbon should form two covalent bonds since it has two electrons in unfilled orbitals. In fact, a process known as orbital hybridization allows for the electrons in the 2s orbital to play a role and explains why carbon is observed to form 4 bonds. This process occurs over two steps: firstly an electron is promoted from the 2s orbital to give the configuration $1s^2 2s^1 2p_x^1 2p_y^1 2p_z^1$ (a process which can occur due to electrostatic attraction from another atom being brought close to the carbon). Secondly the 2s orbital may combine with a number of the 2p orbitals in order to form 'hybrid' sp orbitals. This may occur with 1, 2 or all 3 of the p orbitals to form respectively two sp^1 orbitals, three sp^2 orbitals or four sp^3 orbitals [1].

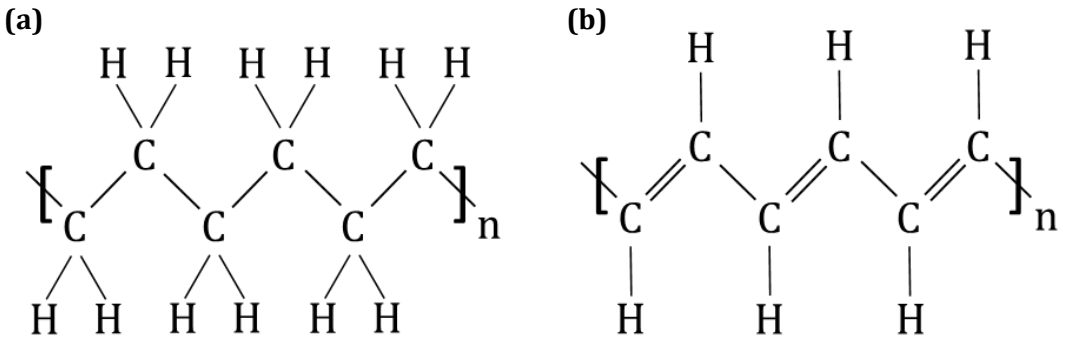

Figure 2.9 Chemical structures of polyethylene **(a)** and polyacetylene **(b)**.

An example of sp^3 hybridisation in action is polyethylene where each carbon atom bonds to two other carbons and two hydrogens (**Figure 2.9(a)**). Here all outer electrons are strongly bound in σ bonds, resulting in an insulating material. In contrast, the formation of a double bond between two carbon atoms involves sp^2 hybridization. Whilst one of the sp^2 orbitals forms a σ bond between the two carbon atoms, the unhybridized $2p_z$ orbital from each atom will overlap with its counterpart resulting in the formation of a π bond. Here the highest occupied molecular orbital (HOMO) corresponds to the π-bonding orbital as shown in **Figure 2.10** which depicts bond structure and energy levels for a C=C double bond structure. The energy level immediately above this is the lowest unoccupied molecular orbital (LUMO), corresponding to the π-antibonding orbital, denoted π*, and the difference between these two energy levels is the band gap of the material.

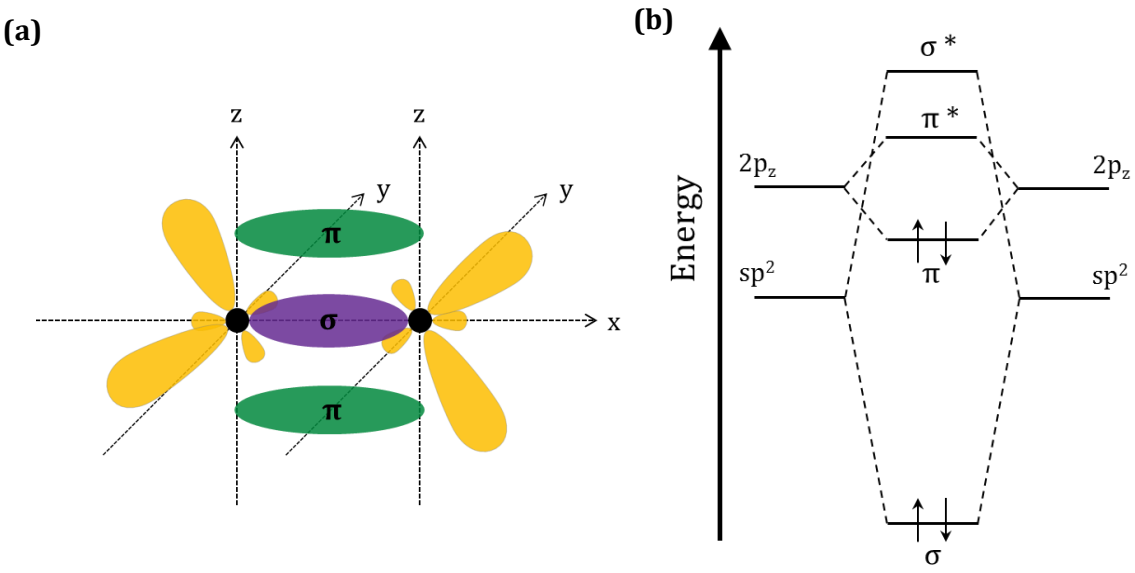

Figure 2.10 Bond structure **(a)** and energy levels **(b)** for a C=C double bond. Hybridized sp^2 orbitals (shown in yellow) will also form a σ bond between the carbon atoms (purple), whilst the unhybridized p_z orbital forms a π bond between the atoms (green).

In contrast to the tightly bound electrons in σ bonds, electrons in π bonds can be delocalised across a number of adjacent molecular units. Systems featuring alternating single-double (or single-triple) bonds along a carbon chain are referred to as being 'conjugated'; a common example of such a system is polyacetylene as shown in **Figure 2.9(b)**. If the carbon atoms in this structure were all equidistant from one another, the π bonds would become delocalised along the entire chain. This would result in the π and π* states being indistinguishable and such equivalence would lead to the absence of an energy gap, leading the material to behave as a metal since it would exhibit a half filled energy band. As it is, an effect known as Peierls' instability leads to alternating bond lengths and the formation of a band gap (i.e. π and π* are distinguishable and at different energies) [54,55]. The resulting electronic states are delocalised only over the space of a few atoms, an effect which leads to a requirement for electrons and holes to transfer between these states via a 'hopping' process in order for charge transport along the length of the chain to occur.

Fullerenes are currently the ubiquitous electron accepting material utilised in donor-acceptor polymer solar cells. Although they exhibit a caged structure rather than a chain as such, the bonding between their carbon atoms still occurs via sp^2

hybridization, and thus they can be considered to be conjugated materials as described above.

In **Chapter 4** the electron donating polymer PCDTBT (poly[[9-(1-octylnonyl)-9H-carbazole-2,7-diyl]-2,5-thiophenediyl-2,1,3-benzothiadiazole-4,7-diyl-2,5-thiophenediyl]) and the electron accepting fullerene $PC_{70}BM$ ([6,6]-phenyl-C71-butyric acid methyl ester) have been used for the fabrication of organic solar cells. Their structures are shown in **Figure 2.11**. PCDTBT is an example of a donor-acceptor copolymer, a group of polymers consisting of alternating electron rich (donor) and electron deficient (acceptor) moieties along the conjugated backbone. In these materials the HOMO is typically located on the donor unit whilst the LUMO is located on the acceptor unit, thus allowing for extensive manipulation of the bandgap of the material without unwanted knock on effects which may occur using other strategies for band gap engineering [56].

(a)

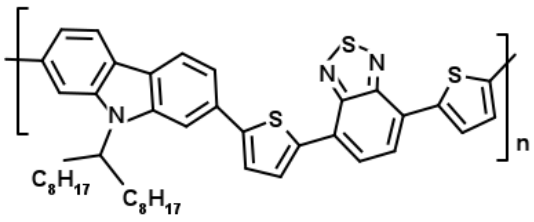

(b)

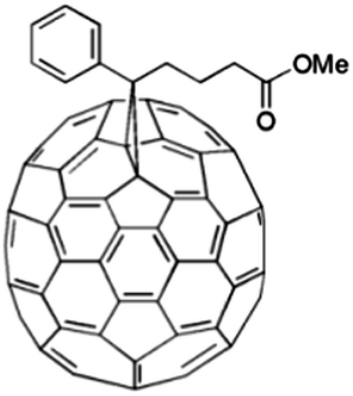

Figure 2.11 The chemical structures of the materials PCDTBT **(a)** and $PC_{70}BM$ **(b)**, both of which have been used in the photoactive layer of the OSCs fabricated in this work.

2.4.4 Operational Principles

Due to the low dielectric constant of organic semiconductors (typically ε_r = 3-4 [57]) excitons in these materials have a strong Coulombic attraction and thus a high binding energy – around 0.3 eV as opposed to only a few meV for inorganic semiconductors [58,59]. Excitons of this tightly bound type are typically referred to as Frenkel excitons, and unlike in their more weakly bound counterparts in inorganic semiconductors, they will not dissociate simply due to thermal energy (~26 meV) meaning that a driving force is needed in order to separate the bound charges. Solar cells of this type, in which exciton dissociation is not a spontaneous process at room temperature, are thus known as 'excitonic solar cells'. In donor-acceptor OSCs this driving force comes from the difference in electron affinity between the electron donating and electron accepting materials, typically a polymer and a fullerene respectively. Photocurrent generation in an illuminated organic solar cell involves five key stages: absorption of light to create an exciton, diffusion of the exciton to a donor/acceptor interface, separation of the exciton into free charges, transport of those free charges to the contacts of the device and finally charge extraction into the electrode materials and the external circuit. Each of these stages and their associated losses are covered in more detail below.

The morphology of the photoactive layer in high performance OSCs is nowadays that of a bulk heterojunction (BHJ). Here, donor and acceptor materials form an inter-penetrating mixture of domains which may be a pure donor phase, a pure acceptor phase or a mixed phase featuring both materials, as shown in **Figure 2.12**. In addition, within each of the pure phases there may be regions with varying levels of crystallinity [60]. In comparison to a bilayer structure, a BHJ offers a vastly increased interfacial area between donor and acceptor regions. The exact morphology of a BHJ can be tuned by altering parameters such as casting solvent, polymer:fullerene blend ratio, donor and acceptor material choice and post-deposition thermal and solvent annealing processes [61].

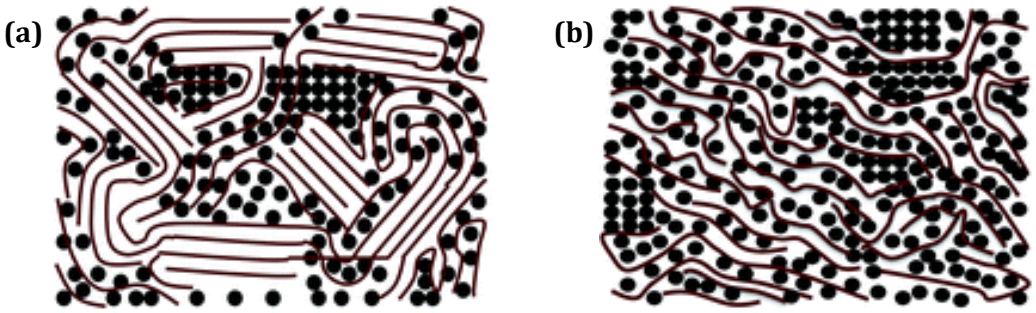

Figure 2.12 A schematic of the photoactive layer morphology of an OSC with bulk heterojunction design for a semi-crystalline polymer **(a)** and an amorphous polymer **(b)**. Red lines represent the donor polymer whilst black circles represent the acceptor fullerene. Taken from Wang et al. [60].

Absorption & Exciton Generation

A photon with energy greater than the bandgap energy, E_g, of the conjugated polymer in the photoactive layer of the device may be absorbed, resulting in the promotion of an electron from the HOMO level to LUMO level of the polymer and thus creating an exciton (**Figure 2.13(a)**). Whilst absorption occurs primarily in the donor polymer, which should thus be strongly absorbing, some absorption will also occur in the electron acceptor regions. In this case charge transfer would subsequently occur with the hole transferring to the 'donor' polymer, rather than the electron transferring *from* the 'donor' polymer. The use of $PC_{70}BM$ rather than $PC_{60}BM$ has been found to increase absorption in the electron accepting regions of the active layer [62].

Exciton Diffusion

A photogenerated exciton will undergo diffusion until it either reaches a donor/acceptor interface or the constituent electron and hole recombine via mono-molecular ('geminate') recombination. Exciton diffusion in OSCs is typically described as being a hopping process, both along individual molecular chains and between adjacent chains. For the majority of organic semiconductors the exciton diffusion length, L_D, is no more than around 10 nm [58,63] and therefore most excitons generated at a distance greater than this from a donor-acceptor interface will simply recombine. It is here that a bulk heterojunction (BHJ) morphology gives a great advantage over a bilayer structure: with suitable control of the morphology, the domains of donor/acceptor material can be engineered to be on a length scale similar to that of the exciton diffusion length, meaning that a large proportion of the excitons generated in a device will reach an interface and produce free charges. This is in

contrast to the bilayer device where only around a thin layer of the donor material close to the interface between the layers would be expected to generate excitons which will successfully dissociate. Here the intermixed phase in a BHJ is of particular importance in allowing excitons to easily reach a donor-acceptor interface.

Exciton Dissociation (Charge Separation)

When an exciton diffusing in a polymer domain reaches an interface with a fullerene domain, exciton dissociation will occur if it is energetically favourable for the bound electron to transfer to the fullerene due to its higher electron affinity, as shown in **Figure 2.13(c)**. In other words, if the energy offset between the higher lying LUMO of the polymer and lower lying LUMO of the fullerene is greater than the binding energy of the exciton then dissociation will occur. Note that for excitons generated within the fullerene, the charge transfer occurs via transfer of the hole in the exciton from the lower lying HOMO of the fullerene to the higher lying HOMO of the polymer. In a well-functioning OSC, once an exciton has reached a donor-acceptor interface this separation of the exciton into free charges occurs on a timescale of a few tens of femtoseconds and with a very high probability, since major loss mechanisms happen on slower timescales [59]. Once charge transfer has occurred the electron and hole are still bound in a so called charge transfer state and further separation is required to avoid geminate recombination. In OSCs the driving force for this separation arises due to the difference in work function between the electrodes/intermediate layers on either side of the device. This difference causes a built in electric field across the photoactive layer which causes free charges to move to opposite electrodes.

Whilst the offset between the energy levels of the acceptor and donor materials must be great enough to drive charge separation, it is worth noting that energy is lost in this process and that an excessive offset will result in a reduced V_{OC} in the solar cell. The exact reported HOMO and LUMO levels for PCDTBT and PCBM vary slightly in the literature, however the offset between the LUMO levels of these materials is around 0.6-0.8 eV, notably more than the ~0.3 eV required to drive exciton dissociation [59,64–66]. Due to the requirement for exciton dissociation, in a polymer solar cell utilising PCBM as the electron acceptor the optimum band gap for the donor polymer is slightly larger than in a traditional (non-excitonic) solar cell, being around 1.5 eV [67].

Charge Transport

Driven by the inbuilt field arising from the difference in work function between the cathode and the anode, free electrons travel through the acceptor domains to the cathode whilst free holes travel through the donor domains to the anode. (In fact, electrons in the LUMO level and holes in the HOMO level of an organic semiconductor will lead to some deformation of the molecule. The free charge carriers in organic semiconductors are thus not electrons and holes but rather electron polarons and hole polarons, these quasiparticles being the combination of the charge carrier and the deformation resulting from its presence. This deformation leads to a slight reduction in the energy of the LUMO level or slight increase in the energy of the HOMO level respectively in the case of electron and hole polarons.) In order for this process to occur successfully, continuous pathways are required in both the acceptor and donor materials to the respective electrodes, requiring an appropriate morphology of the bulk heterojunction. It is for this charge transport process that pure donor and acceptor domains are important in the morphology of a bulk heterojunction design. In organic semiconductor materials, electronic states are localised on polymer chains (as discussed in **Section 2.4.3**) and charge transport must thus occur via hopping between these states, rather than by transport within a conduction band as for inorganic semiconductors [58]. As a result of this, mobilities of free charges in the photoactive layer are generally poor: hole mobility in donor polymers is often of the order of 10^{-3} $cm^2V^{-1}s^{-1}$ or lower, whilst PCBM has electron mobility of a similar order of magnitude [64,68]. In comparison, silicon has charge carrier mobilities of the order of 10^2-10^3 $cm^2V^{-1}s^{-1}$. Drift length (L_{drift}), the average length which a charge carrier will drift under an electric field before it recombines, is given by

$$L_{drift} = \mu\tau E \qquad \{2.5\}$$

where μ is the carrier mobility, τ is the carrier lifetime and E is the electric field strength. It is thus clear that the low carrier mobilities typically found in organic semiconductors mean that the photoactive layer thickness must be very low in order to minimise bi-molecular recombination. For many material systems, including the PCDTBT:$PC_{70}BM$ blend used in this work, optimised active layer thickness is in the range of only 50-100 nm, and thus only a small proportion of incident light is absorbed on one pass through this layer. A reflective rear electrode is therefore important since reflection from this layer leads to the formation of standing waves within the device, meaning that layer thicknesses can be optimised in order to maximise the optical field

intensity within the active layer and thus ensure that light absorption in this layer is maximised. In this context, optical modelling techniques based upon the transfer matrix method, as utilised in **Chapter 4**, can be of assistance. In addition to the drift of charges due to the inbuilt field discussed above, there will also be a diffusion of carriers arising due to concentration gradients which arise as a result of the charge selective nature of the contacts.

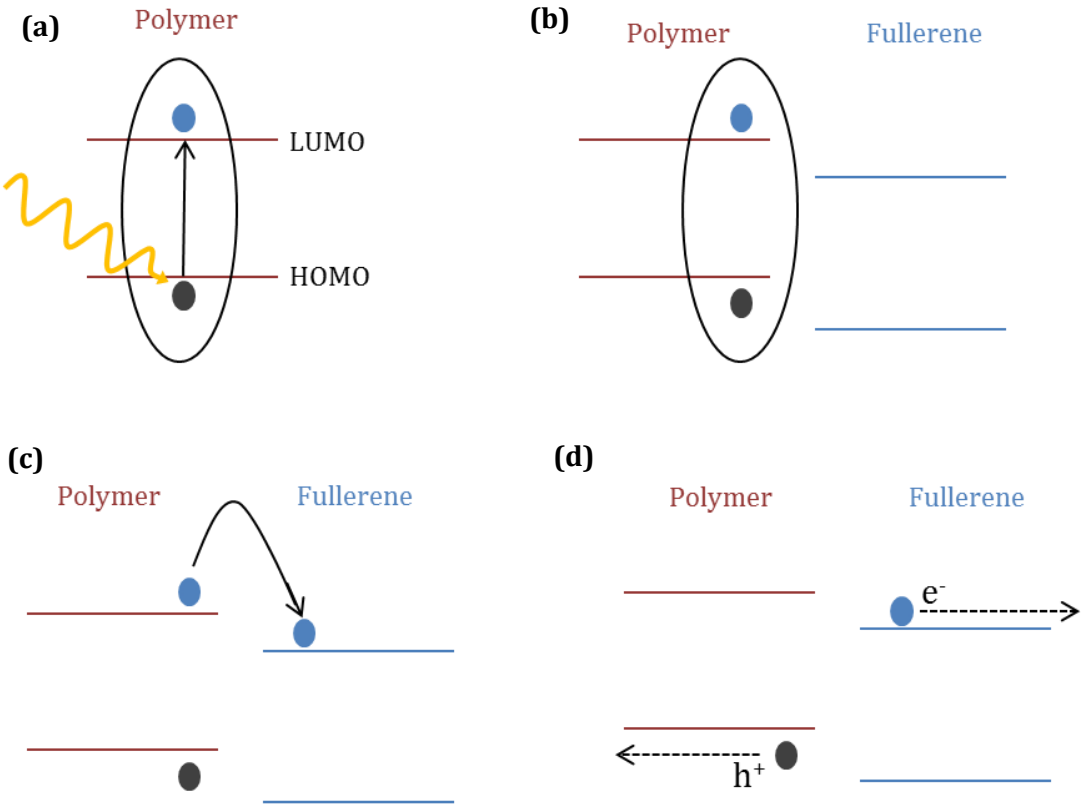

Figure 2.13 A basic schematic of the process of photocurrent generation in an organic solar cell. An incident photon of sufficient energy is absorbed by the polymer, generating an exciton **(a)**, which then diffuses until meeting a donor-acceptor interface **(b)** or recombining (not shown). At this interface the electron is transferred to the fullerene **(c)** and the resulting free charges are then separated by the inbuilt electric field **(d)**.

Charge Extraction

Charge extraction can occur once free carriers have successfully reached their respective electrodes. In order to ensure the high efficiency of this process it is important that the appropriate energy levels are well matched, that is, the work function of the anode to the HOMO level of the donor (for hole extraction) and the work

function of the cathode to the LUMO level of the acceptor (for electron extraction). In situations where this occurs, the contacts between the semiconductor and the electrodes have low resistance and are known as Ohmic contacts. Conversely, a mismatch in these energy levels will lead to poor charge transport across the interface which results in a charge build up and subsequent band banding, resulting in a further barrier to charge extraction. In the case of these non-Ohmic contacts, charge extraction can still take place but with significant losses due to the high resistance of this Schottky barrier.

For Ohmic contacts and efficient charge extraction to occur, Fermi level alignment, where the Fermi levels of the two materials equalize, is typically required at the metal-semiconductor interface. At a simple metal-metal interface, electrons will flow from the material with the higher Fermi energy to that with the lower Fermi energy, leading to Fermi level alignment as well as the establishment of an interfacial dipole (**Figure 2.14(a)**).

Similar alignment can occur at the interface between a metal contact and an organic semiconductor. If the work function of the metal is shallower than the LUMO of the organic material or is deeper than its HOMO then Fermi level alignment can be expected to occur due to the resulting charge transfer. In fact, states just within the band gap can exist due to the occurrence of structural as well as electronic relaxation when electrons are added to or removed from an organic semiconductor. It is between these states and the Fermi level of the metal that charge transfer and alignment occurs [69,70]. This process is shown in **Figure 2.14** parts **(b)** and **(c)** for LUMO and HOMO alignment respectively. Whilst interfaces between metal oxides and organic semiconductors might be expected to behave differently to this due to the band gap in the oxide, HOMO alignment has been found to occur in a remarkably similar manner [71].

In organic solar cells the factors determining the V_{OC} vary depending upon the type of contact formed at the electrodes. For ohmic contacts the V_{OC} is dependent on (but somewhat less than) the difference between the energy of the HOMO level of the donor material and the LUMO level of the acceptor material [69]. For non-ohmic contacts the V_{OC} is dependent on the difference between the work functions of the two electrodes. Recombination losses, and in particular non-radiative recombination losses, may further reduce the V_{OC} of a solar cell from its maximum potential value [72].

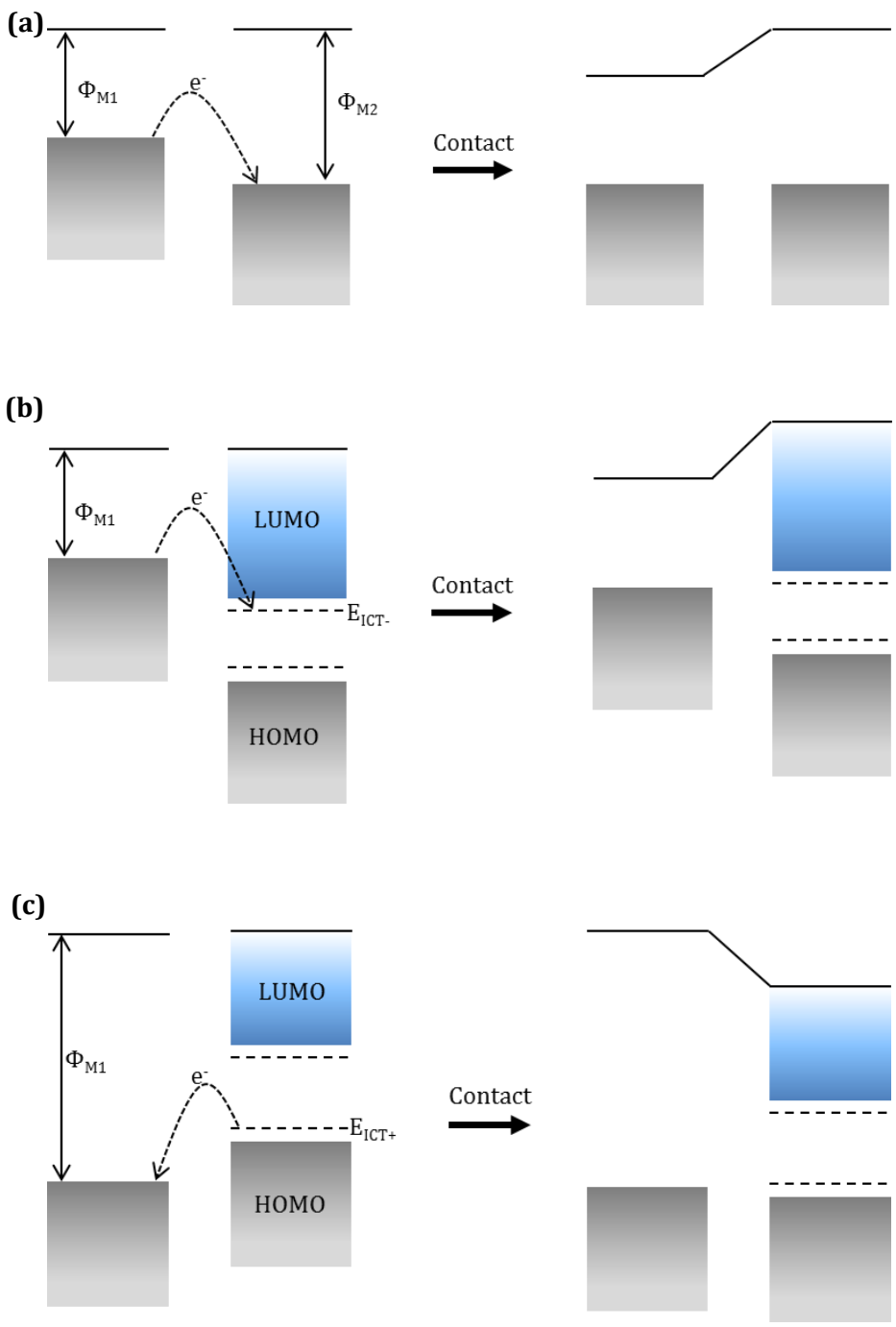

Figure 2.14 Energy level alignment before and after materials are brought into contact with each other for different interfaces: **(a)** metal-metal, **(b)** metal-organic semiconductor with LUMO alignment and **(c)** metal-organic semiconductor with HOMO alignment. Φ_M is the metal work function (Fermi level), E_{ICT-} and E_{ICT+} show so called 'integer charge transfer states' which exist close to the edges of the HOMO and LUMO of the organic material.

2.5 Perovskite Solar Cells

2.5.1 Introduction

The term perovskites refers to materials with a particular crystal structure, the name coming from Russian scientist Lev Perovski [73,74]. Whilst the word initially referred to the mineral $CaTiO_3$, it is now widely used to describe any material with the same crystal structure.

Most work on perovskite materials for photovoltaic applications has thus far been directed towards organometal trihalide perovskites, where, in an ABX_3 crystal structure, A is an organic cation, B is a metal cation (smaller in size than A) and X is a halide anion. Here BX_6 octahedra with halide anions at the corners and a metal cation in the centre form a 3D network, connected to other octahedra by shared corners. The organic cation can be thought of as fitting in the gaps between the octrahedra, neutralising the total charge. The size of the organic component must be such that it fits within these gaps, and indeed its precise size plays a key role in determining the optoelectronic properties of the material such as the bandgap. These are sensitive to any changes in the geometry of the 3D network arising due to small changes in the size of the constituent ions [74–76]. A simple illustration of the crystal structure is shown in **Figure 2.15**. The most commonly investigated organometal halide perovskites to date have been based on methylammonium ($CH_3NH_3^+$, also referred to as MA^+), and lead (Pb^{2+}) cations as part of either a 'tri-iodide' ($CH_3NH_3PbI_3$) or 'mixed-halide' ($CH_3NH_3PbI_{3-x}Cl_x$) perovskite. The likely crystal structure for different components can be determined via calculation of a 'tolerance factor' for the constituent ions, this being the ratio of the A-X and B-X bond lengths in a solid sphere model:

$$t = \frac{r_A + r_X}{\sqrt{2}(r_B + r_X)} \qquad \{2.6\}$$

where r_A, r_B and r_X are the ionic radii of atoms of A, B and X respectively. As a guide, if $0.7 < t < 1.1$ then 3D perovskite structures can be formed, with $t = 1$ giving a stable 3D cubic phase and distortion/deviation occurring for other values. For $0.81 < t < 1.0$ the cubic structure is likely to occur, with slightly lower values of t likely to produce a tetragonal or orthorhombic structure [7]. If t is below 0.7 or above 1.1 then formation of the 3D perovskite structure will become energetically unfavourable [7]. As a point of

reference, the commonly used perovskite $CH_3NH_3PbI_3$ gives a tolerance factor of 0.92 [77].

In a cubic structure the unit cell has sides *a*, *b* and *c* with lengths such that $a = b = c$. In a tetragonal structure this is stretched along one lattice vector meaning that $a = b \neq c$, whilst in an orthorhombic structure a cube is stretched along two of its lattice vectors by different proportions such that $a \neq b \neq c$. Transitions between the different phases often occur during temperature changes, for example $CH_3NH_3PbI_3$ undergoes a reversible transition from orthorhombic to tetragonal structure upon heating to ~160 K. This transition causes a slight (0.05 eV) reduction in band gap as well as a reduction in exciton binding energy [78]. Similarly, a tetragonal to cubic transition occurs at ~330 K (57°C) [79]. Whilst it has been shown that these phase transitions can lead to changes in band gap, exciton binding energy, charge carrier mobility and resistivity in the perovskite material [80,81], it is not clear precisely what effect these transitions have on the operation of complete devices. Lattice parameters for tetragonal $CH_3NH_3PbI_3$ are reported as $a \approx 8.8$ Å, $c \approx 12.6$ Å, whilst in the cubic phase exhibits $a \approx 6.3$ Å [82–84].

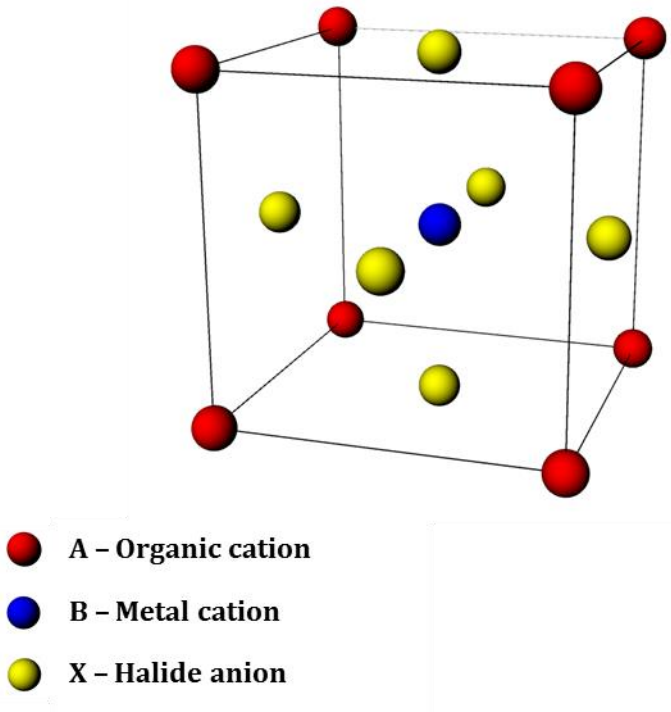

Figure 2.15 Unit cell for the cubic perovskite crystal structure, showing the metal cations (blue), organic cations (red), and halide anions (yellow).

Whilst organic-inorganic hybrid perovskites have been studied in some form since the late 1970s [85,86], and were investigated for use in thin film transistors and electroluminescent devices in the 1990s [87,88], the first solar cell featuring an organometal trihalide perovskite was not reported until 2006. At this time Miyasaka's group utilised $CH_3NH_3PbBr_3$ as a sensitizer on mesoporous TiO_2 and achieved a PCE of 2.2% in a device analogous to a liquid dye-sensitized solar cell [89]. In 2009 the same group increased the efficiency of their cells to 3.8%, partly through switching to a $CH_3NH_3PbI_3$ sensitizer [90], whilst 2 years later Park's group pushed the efficiency of this type of perovskite sensitized solar cell to 6.5% [91]. It is worth noting, however, that in these liquid electrolyte based devices the perovskite absorber suffered rapid dissolution or decomposition, meaning that performance degraded in a matter of minutes. In 2012 Grätzel and Park kicked off the current boom in solid state perovskite solar cell research, achieving a PCE of 9.7% with a cell utilising $CH_3NH_3PbI_3$ on a mesoporous TiO_2 scaffold [92]. Shortly afterwards, Snaith's group at Oxford demonstrated that $CH_3NH_3I_{3-x}Cl_x$ could produce efficient solid-state solar cells on both mesoporous TiO_2 and Al_2O_3, realising a PCE of up to 10.9% [84]. A flurry of papers quickly followed, with efficiencies rising rapidly, and by late 2013 perovskites had become the hot-topic of academic solar cell research, with Snaith being featured in Nature's '10 people who mattered this year' [93]. Around this time, many groups traditionally involved with DSSC cells or OPVs moved into the field and conferences began offering major sessions dedicated towards perovskite PV cells. By the end of 2014 perovskite devices had hit 20.1% on the NREL certified efficiency chart, establishing themselves as real contenders against more mature thin-film technologies such as CdTe and CIGS (respectively 21.5% and 21.7% as of May 2015) [6].

2.5.2 Lattice Planes and Miller Indices

The concept of lattice planes must briefly be introduced since such planes will be referred to in **Chapter 6**, where X-ray scattering measurements of perovskites have been made. Lattice planes are planes which have periodic interactions with a crystal lattice. They are described by 'Miller indices' which are the reciprocals of the intercepts which the plane makes with the three axes that define the edge of a unit cell (reduced to the smallest integers) [2]. By way of an example, **Figure 2.16** shows a simple cubic unit cell together with an illustration of the (110) lattice plane.

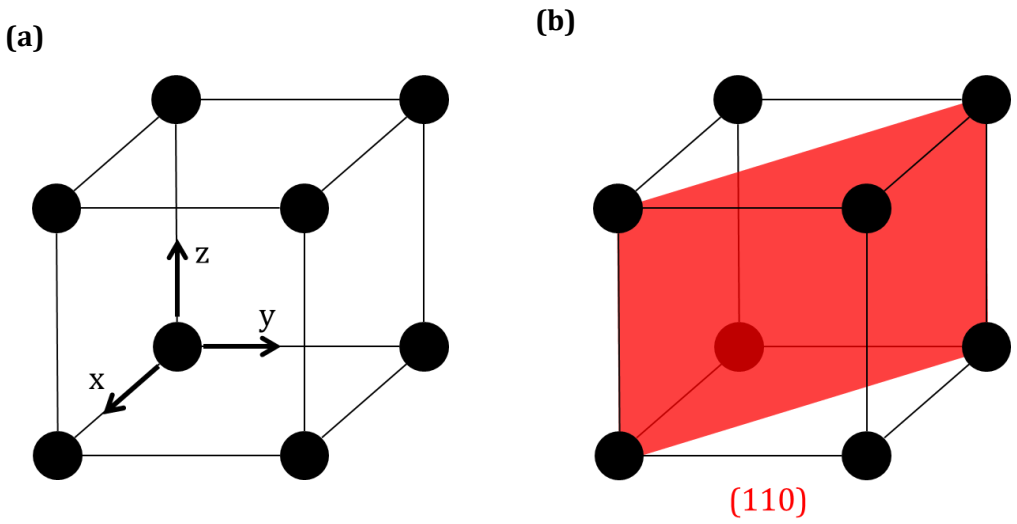

Figure 2.16 A unit cell for a simple cubic crystal **(a)** together with an illustration of the (110) plane of this crystal structure **(b)**.

2.5.3 Semiconducting Properties of Perovskites

A neutral lead (Pb) atom has an electronic configuration with outer orbitals $5d^{10}6s^{2}6p^{2}$, thus Pb^{2+}, as is present in organometal halide perovskites, has electronic configuration $5d^{10}6s^{2}\ 6p^{0}$ (lower energy orbitals are ignored for brevity). Similarly considering the outer orbitals only, iodine (I) has electronic configuration $4d^{10}5s^{2}5p^{5}$ whilst I^{-}, as is present in organometal halide perovskites, has electronic configuration $4d^{10}5s^{2}5p^{6}$.

For the common organometal halide perovskite $CH_3NH_3PbI_3$ the conduction band is formed of empty Pb 6p orbitals, whilst the upper valence band is formed by hybrid Pb 6s and I 5p antibonding orbitals [79,94–96]. This results in a direct band gap of energy ~1.5 eV, as shown in **Figure 2.17(a)**, leading to the semiconducting nature of the material [94,97]. Whilst computational studies predicting the electronic structure of these materials have typically been undertaken for the cubic phase of the perovskite, it has been shown that the band structures of the tetragonal and orthorhombic phases exhibit only small deviations from this [98].

Numerous studies simulating the electronic structure of $CH_3NH_3PbI_3$ have found that the organic cation (here MA^{+}) does not play a direct role in either the conduction or valence band orbitals, and is present in the structure in a charge balancing role [79,94,96]. It does, however, still play a role in determining the precise band structure

and band gap of the material due to the effect of its size on the geometry of the crystal lattice [74–76]. In addition, the orientation of the MA^+ cation can exert strain on the PbI_6 octahedra and thence slightly alter the band structure of the material. Since it has been shown that the MA^+ cation can rotate rapidly at room temperature [95,99], the band gap is thus actually a rapidly varying 'dynamical' band gap. Changes in the MA^+ orientation can in fact lead to the transition of the material to having an indirect band gap positioned slightly (~25 meV) below the direct band gap, as shown in **Figure 2.17(b)** [95]. This effect may help to explain the strong absorption (typical of direct band gap semiconductors) and long diffusion length (typical of indirect band gap semiconductors) observed in these materials. For the particular orientations of the MA^+ cation where an indirect band gap emerges, the absorption will be quite unaffected due to the existence of a direct band gap at only a slightly higher energy. At the same time, recombination of excited carriers is suppressed since they will thermalize to the band edge where they can benefit from longer lifetimes due to the indirect nature of the band gap for recombination.

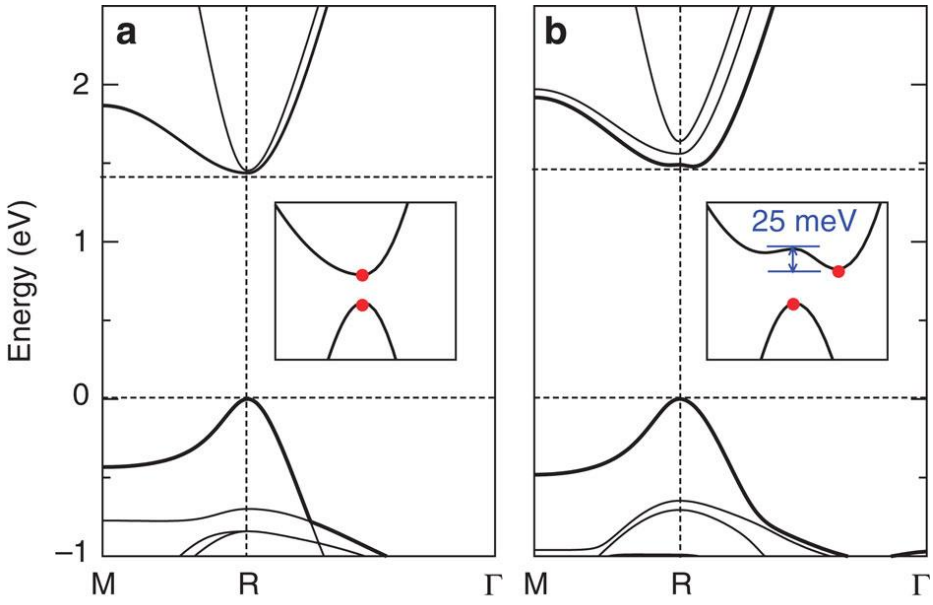

Figure 2.17 The band structure of $CH_3NH_3PbI_3$ as predicted by density functional theory calculations for orientation of the MA^+ cation along [111] **(a)** and [011] **(b)** directions, highlighting the change from direct gap to indirect gap. Zero energy is set at the valence band maximum. Taken from Motta et al. [95].

2.5.4 Operational Principles

Whilst the absorption coefficient of organometal halide perovskite films is not as high as that of many polymer:fullerene blends used in OPVs (around $6x10^4$ cm^{-1} at 600nm and $>10^5$ cm^{-1} respectively [61,100]), it compares favourably with those of traditional inorganic semiconductors, for example being up to an order of magnitude higher than that of GaAs in the visible region [101]. Band-gaps for the common perovskites $CH_3NH_3PbI_3$ and $CH_3NH_3I_{3-x}Cl_x$ are quite wide at 1.5-1.6 eV [75,76] which, when combined with low non-radiative recombination losses, leads to a V_{OC} as high as 1-1.1 V in the most efficient devices [72].

Charge separation is achieved significantly more easily in organometal halide perovskites than in organic solar cells, owing to a much smaller exciton binding energy (E_B). Initially there was some debate about whether these devices were excitonic in operating nature as binding energies were calculated to be in the region of 35-50 meV – a value greater than kT at room temperature (~26 meV) [102–105] although still far lower than the hundreds of meV observed for organic semiconductors [58,59]. It has since been suggested that the exciton binding energy in $CH_3NH_3PbI_3$ is in fact as low as 2 meV [106], with this considerably lower value calculated on the basis of ε'_{static} (ε' is the real part of the dielectric constant) rather than ε' determined at optical frequencies. There is some debate about the best approach in this regard (see [106] and references therein for further discussion), and it is an unusual situation since typical PV semiconductors like silicon do not exhibit such large changes in the value of ε' between low frequencies and optical frequencies. More recently, direct measurement of E_B at low temperature gave a value of 16 meV and the same team suggested that at room temperature the binding energy would be only a few millielectronvolts [107]. Theoretical investigations have recently suggested similar values of ~15 meV at low temperatures (orthorhombic phase) and ~5 meV at room temperature (tetragonal phase), with the drop at higher temperatures being related to the rotation of MA^+ ions [78]. Irrespective of the exact value for the exciton binding energy in these materials, a consensus is now emerging that it is below thermal energy at room temperature and thus unlike the tightly bound Frenkel excitons in organic semiconductors, excitons in organometal halide perovskites seem to be of a Wannier-Mott type with a large exciton radius [78]. Excitons in these materials can thus be expected to dissociate with high probability without the need for a donor-acceptor interface to drive this process, and

indeed they have been found to dissociate to free charges in a matter of picoseconds in perovskite films [105,108].

Once exciton dissociation has taken place, charge transport and extraction occur in a similar manner to in OSCs, with the exception that here charge carriers are able to move in the energy bands of the material rather than having to travel via a hopping process between localised electronic states. Charge carrier mobilities are thus significantly greater in both $CH_3NH_3PbI_3$ and $CH_3NH_3PbI_{3-x}Cl_x$ than in typical organic semiconductors and PCBM, being in the region of 10-20 $cm^2V^{-1}s^{-1}$ [108–110] as compared to 10^{-3} $cm^2V^{-1}s^{-1}$ [64,68], although this is still notably lower than for silicon where mobilities are of the order 10^2-10^3 $cm^2V^{-1}s^{-1}$. These high mobilities give a low monomolecular recombination since charges can move away from their point of creation rapidly [108] and when combined with an exceptionally low bimolecular recombination rate (i.e. long carrier lifetime) this leads to long charge diffusion lengths of over a micron in the mixed halide perovskite, and hundreds of nm in the triiodide version [100,109,111–113]. In fact, in large single crystals of $CH_3NH_3PbI_3$ diffusion lengths larger than 175 μm have been observed due to lower trap densities, greater mobilities and longer lifetimes than in polycrystalline films. This result implies that the enhanced diffusion length in the mixed halide perovskite may be related to film morphology rather than an effect intrinsic to the material [114]. The much longer diffusion lengths in the perovskite materials as compared to the materials systems used in OSCs allow for the use of a significantly thicker active layer, which provides for greater light absorption, as well as giving other advantages such as an increased tolerance to substrate roughness and less stringent processing and deposition requirements.

In addition to the above properties of perovskite films which make them highly suitable for the fabrication of high efficiency PV devices, the material also offers good ambipolar charge transport. That is, both electrons and holes are efficiently transported by perovskite layers, with well-balanced electron and hole mobilities and diffusion lengths [100,108,111,115]. Reasonably well-balanced mobilities are important for avoiding space charge limited photocurrent which can result in significantly degraded FF and PCE [116].

2.5.5 Perovskite Device Architectures

General device architecture for perovskite solar cells is similar to that of organic solar cells, consisting of a photoactive layer sandwiched by charge selective interlayers and electrodes, as shown in **Figure 2.18**. Their precise operating principles, meanwhile, vary somewhat depending upon the specific architecture used, which can be divided into two main classes: planar and mesoporous.

The planar device structure involves a simple flat layer of perovskite acting as the photoactive layer of the device. Mesoporous devices, on the other hand, involve infiltration of the perovskite material into a scaffold, and can be further divided into two distinct types, with differing principles of operation, which will here be termed 'sensitized' and 'meso-superstructured'. The sensitized device structure revolves around the use of a scaffold capable of electron transport (typically based on TiO_2 nanoparticles although other scaffolds such as ZnO nanorods have been investigated [117]), with the perovskite material filling the voids within this structure. During photovoltaic operation, electron transfer occurs from the perovskite to the scaffold material and subsequent electron transport to the cathode occurs through the scaffold itself [84,118]. In the case of a 'meso-superstructured' device, the scaffold material is insulating, typically alumina (Al_2O_3), and provides a structural component of the cell only, playing no part in the electronic operation. Charge transport thus occurs through the perovskite itself for both electrons and holes, with the perovskite again filling the pores in the mesoporous scaffold.

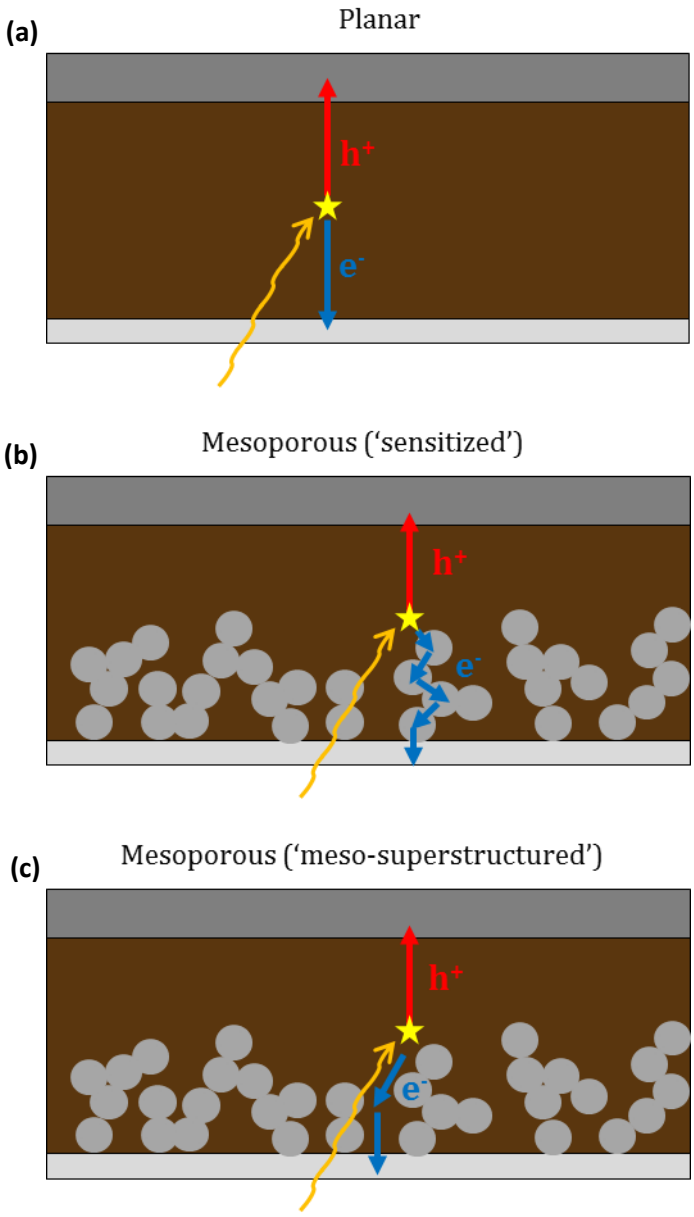

Figure 2.18 Schematics of device architecture and charge transport mechanisms following charge generation at the point marked by the yellow star. Devices with planar **(a)**, sensitized **(b)** and meso-superstructured **(c)** architectures are shown. In both **(b)** and **(c)** a capping layer is shown covering the scaffold. All devices are shown with standard architecture, i.e. the light enters through the cathode (see below).

For devices with mesoporous structure, consideration must be given to whether the deposition process produces a 'capping layer' of perovskite. The presence of a dense, uniform layer of this kind covering the scaffold has been found to be beneficial in the case of sensitized cells since it reduces the probability of contact between the electron transporting scaffold and the hole transporting material; such a contact would provide an easy recombination pathway [110,119]. In addition, a capping layer can reduce the

surface roughness of the photoactive layer, thus reducing the probability of shorts where the perovskite material directly contacts the electrode in regions where the HTM has not fully covered the perovskite [120]. It has also been proposed that a significant and surprisingly large proportion of charge-carrier generation occurs within the capping layer [121]. A thicker capping layer of perovskite does, however, seem to lead to an increased level of hysteresis in JV measurements (hysteresis is discussed further in **Section 2.5.9**) [121,122].

In addition to the distinctions between planar and mesostructured architectures, perovskite devices also come in 'standard' and 'inverted' forms, similarly to organic solar cells. Perovskite solar cells have however, somewhat confusingly, come to use different terminology to their organic cousins in this regard due to their emergence from the field of dye sensitised solar cells (DSSCs). When discussing perovskite solar cells, 'standard' or 'normal' architecture thus refers to a device with a transparent electron collecting cathode and an opaque hole collecting rear anode. In these devices the most commonly used electron transport material (ETM) is compact TiO_2 whilst the most commonly used hole transporting material (HTM) is spiro-MeOTAD. 'Inverted' perovskite solar cells typically involve a PEDOT:PSS hole transport/electron blocking layer adjacent to their semi-transparent electrode. The choice of PEDOT:PSS as the HTM is in part due to poor film coverage when perovskite films have been deposited onto metal oxides such as vanadium oxide [123]. Indeed, attempts by the author to use spin-coating and ultrasonic spray-coating of $CH_3NH_3PbI_{3-x}Cl_x$ onto a molybdenum oxide layer were unsuccessful due to significant dewetting leading to very low film coverage. PCBM is widely used in inverted devices as the ETM separating the photoactive perovskite layer from the rear electrode (typically Au, Ag or Al). Typical device structures for the standard and inverted devices are thus respectively FTO/TiO_2/perovskite/spiro-OMeTAD/Au and ITO/PEDOT:PSS/perovskite/PCBM/Au, although it should be noted that extra charge transport interlayers are often used.

2.5.6 The Importance of Film Morphology

Perhaps the primary concern in the fabrication of solution processed organometal halide perovskite solar cells is ensuring the formation of a dense, uniform perovskite film with few gaps and pinholes. **Figure 2.19** shows three perovskite films with differing levels of surface coverage in order to provide the reader with an illustration of how these voids and pinholes can manifest themselves. The morphology of the

perovskite film is key in determining all device metrics in a solar cell, since poor coverage will have a multitude of effects detrimental to device performance. If coverage is low enough then the device will not operate, although even with enough coverage to ensure a working solar cell, PCE can be significantly reduced by two key factors. Firstly, reduced absorption in regions without the perovskite will result in a reduced J_{SC}. Secondly, leakage paths where the hole transport and electron transport materials come into contact with each other will result in a reduction in shunt resistance and will reduce both the V_{OC} and FF of the device [123,124].

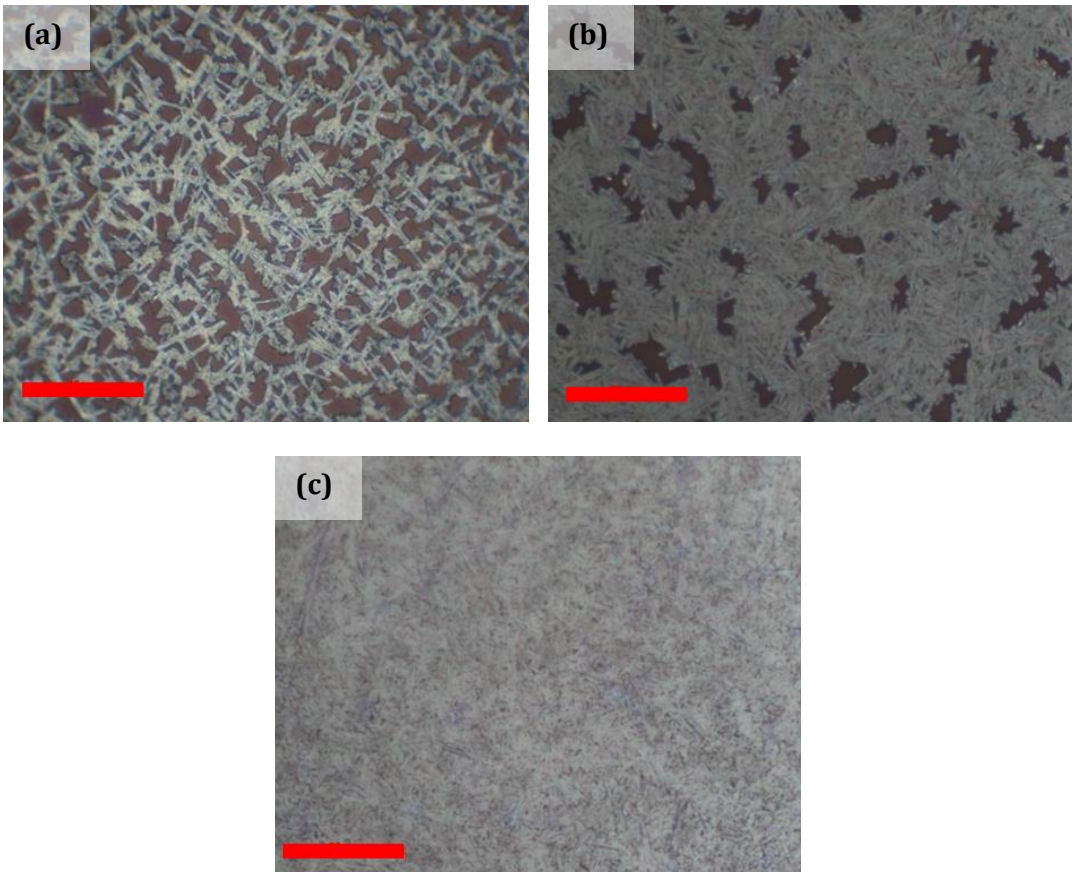

Figure 2.19 Optical micrographs of $CH_3NH_3PbI_{3-x}Cl_x$ films on ITO/PEDOT:PSS substrates showing increasing film coverage from **(a)** to **(c)**. Red scale bars correspond to 20 μm.

2.5.7 Perovskite Fabrication

Fabrication of perovskite films from solution is predominantly achieved via two approaches, commonly known as the 'one-step' and 'two-step' processes. The one-step process involves the dissolution of both the lead salt and organic halide in a common solvent – typically lead iodide (PbI_2) or lead chloride ($PbCl_2$) together with methylammonium iodide (MAI) in the solvent dimethylformamide (DMF) or dimethyl sulphoxide (DMSO). This single solution is deposited onto the substrate via a suitable technique such as spin-coating, and a thermal annealing step is then used to convert the precursors into the final perovskite film. The transition from precursor to perovskite is typically very obvious to the eye, since it involves a transformation from a bright yellow film to one with a dark brown/black colour. Whilst there are numerous variations upon this theme, including the use of additives [125,126] or 'freezing out' a particular crystal structure using a solvent engineering process [127,128] the key idea in the one-step process is that both the lead halide and the organic component are deposited from a single solution and in a single step.

In the two-step method a film of PbI_2 is first deposited by, for example, spin-coating, and subsequently exposed to the organic halide. This method was first developed by Grätzel's group using a process in which the PbI_2 layer was dipped into a solution of MAI dissolved in isopropyl alcohol (IPA) and held there briefly, resulting in its conversion to the $MAPbI_3$ perovskite [129]. Alternatives include deposition of an organic halide layer onto the PbI_2 by spin-coating or spray-coating, followed by interdiffusion between the two layers. This results in perovskite formation, although it is interesting that in some studies this interdiffusion step requires a thermal anneal to drive the process whilst in others it does not; it is not clear as to why this discrepancy arises [130,131]. Finally, exposing the PbI_2 layer to MAI vapour has been used successfully to fabricate perovskite layers [132]. In addition to these most commonly employed solution processing methods, perovskite films can be deposited by alternative means, for example co-evaporation of PbI_2 and MAI [124].

2.5.8 The Role and Importance of Chlorine (and other precursors)

Whilst perovskite films prepared using $PbCl_2$ and MAI were initially thought to form a perovskite structure incorporating both iodine and chlorine into the crystal lattice, denoted by the formula $CH_3NH_3PbI_{3-x}Cl_x$ [84,133] this conclusion was put in doubt by

later results which failed to detect any chlorine in the final film [134]. Indeed, there have more recently still been conflicting results emerging on this topic, with some studies concluding that there is indeed some Cl present in some capacity [135,136] and others finding no traces of chlorine in their films and no change to the band-gap and X-ray diffraction peak positions following chlorine incorporation [137,138]. It is worth noting at this point that finding a signal from chlorine in the final film does not necessarily mean that Cl is incorporated into the crystal structure, since it could be present as residual MACl, as $MAPbCl_3$, or as unconverted $PbCl_2$ from a two-step process [138,139]. Where chlorine has been detected there is some evidence to show that it is preferentially located close to the interface with the metal oxide layer onto which the perovskite has been deposited [136]. Despite the conflicting results, the consensus does seem to be that the 'mixed halide' perovskite commonly fabricated using $PbCl_2$ and MAI precursors (and more rarely PbI_2 and MACl) does in fact form the same material as the triiodide version, that is, it forms the perovskite $CH_3NH_3PbI_3$. Despite this, the use of the differing notations to refer to different preparation methods has generally continued in the literature, partly for continuity and also to make clear distinctions between processing routes until questions on this subject are more conclusively answered. For these reasons this notation has been adopted in the experimental Chapters of this thesis. Given the emerging consensus, the differences which arise in the properties of the films fabricated using chlorine precursors are thought to be due to their effect on the crystallization of the perovskite, resulting in changes to the morphology and crystalline properties of the resultant films. Indeed, this proposal is commensurate with results mentioned briefly in **Section 2.5.4**, where charge diffusion lengths >175 μm were measured in single crystals of $MAPbI_3$. Any differences in charge diffusion lengths between 'triiodide' and 'mixed halide' perovskite films thus appear to arise due to the different properties of the polycrystalline films rather than properties of the materials themselves.

The use of $PbCl_2$ instead of PbI_2 as a precursor in the one-step process has been shown in numerous studies to result in increased grain size, increased preferential crystallographic orientation, increased film coverage and smoother films [137,138,140–144]. The reason for this appears to be to do with the organic component which is formed in the solution or precursor film but released during perovskite formation, and which should be completely removed from the final film in order to avoid increased series resistance [144]. This organic component, MACl in the case of a $PbCl_2$ precursor and MAI in the case of a PbI_2 precursor, initially remains in

the film, retarding crystallization as the solvent evaporates. It is then removed during the thermal annealing step, allowing for the crystallization of the perovskite itself. MACl is more easily removed than MAI at a low temperatures, and the reduced temperature required for the annealing process (typically 90-100°C rather than 130-150°C) avoids coarsening of the film, ensuring a smooth and uniform final layer [123,137,143–145]. Indeed, the use of lead acetate ($PbAc_2$), resulting in the formation of the more volatile organic component MAAc, has been found to further reduce the difficulty of removing this component allowing for a very short anneal (5 minutes at 100°C) which resulted in very smooth and uniform films [143]. In addition, it has also been proposed that $PbCl_2$ nanocrystals may act as nucleation sites [141] and may be involved in an important intermediate phase during crystallization [140].

It should be noted that not all studies are in agreement over the proposed sublimation of the organic component (MACl, MAI, MAAc etc.) from the film during the thermal annealing step and concurrent perovskite formation. Whilst results from TGA (thermogravimetric analysis) and DSC (differential scanning calorimetry) experiments on MACl and MAI imply that they should be thermally stable until >200°C it has been proposed that the increased surface area to volume ratio in thin films can explain their removal at a lower temperature [143,145]. A number of studies have observed evidence for the sublimation of MACl or MAI during the thermal annealing step [137,145,146], however others have found evidence that it does not appear to be removed from the films in this way [135,139].

2.5.9 Hysteresis

Hysteresis in the current-voltage characteristics of perovskite solar cells was first reported in Spring 2014 and has since been widely observed [147,148]. Whilst studies relating to this phenomenon make up a significant fraction of recently published work on organometal halide perovskites, no definite consensus has been reached on the mechanism behind it. The observed hysteretic behaviour manifests itself in an improvement in apparent device performance on the 'reverse' (forward bias to reverse bias) sweep of a *JV* curve as compared to the 'forward' sweep (reverse bias to forward bias). The difference is predominantly in the fill factor of the device, giving an increased current in the region close to the maximum power point of the device on the reverse sweep (see **Figure 2.20(a)**). Looking more closely at the current-voltage response of a device, it has been shown that on the reverse scan, when the applied bias is decreased

the current from the device 'overshoots' its steady-state value before slowly settling back to a stable level. Similarly, on the forward scan, when the voltage is increased the photocurrent 'undershoots' its steady-state value (see **Figure 2.20(b)**). The true steady-state maximum power point lies between the overestimate made by the reverse sweep *JV* curve and the underestimate made by the forward sweep *JV* curve.

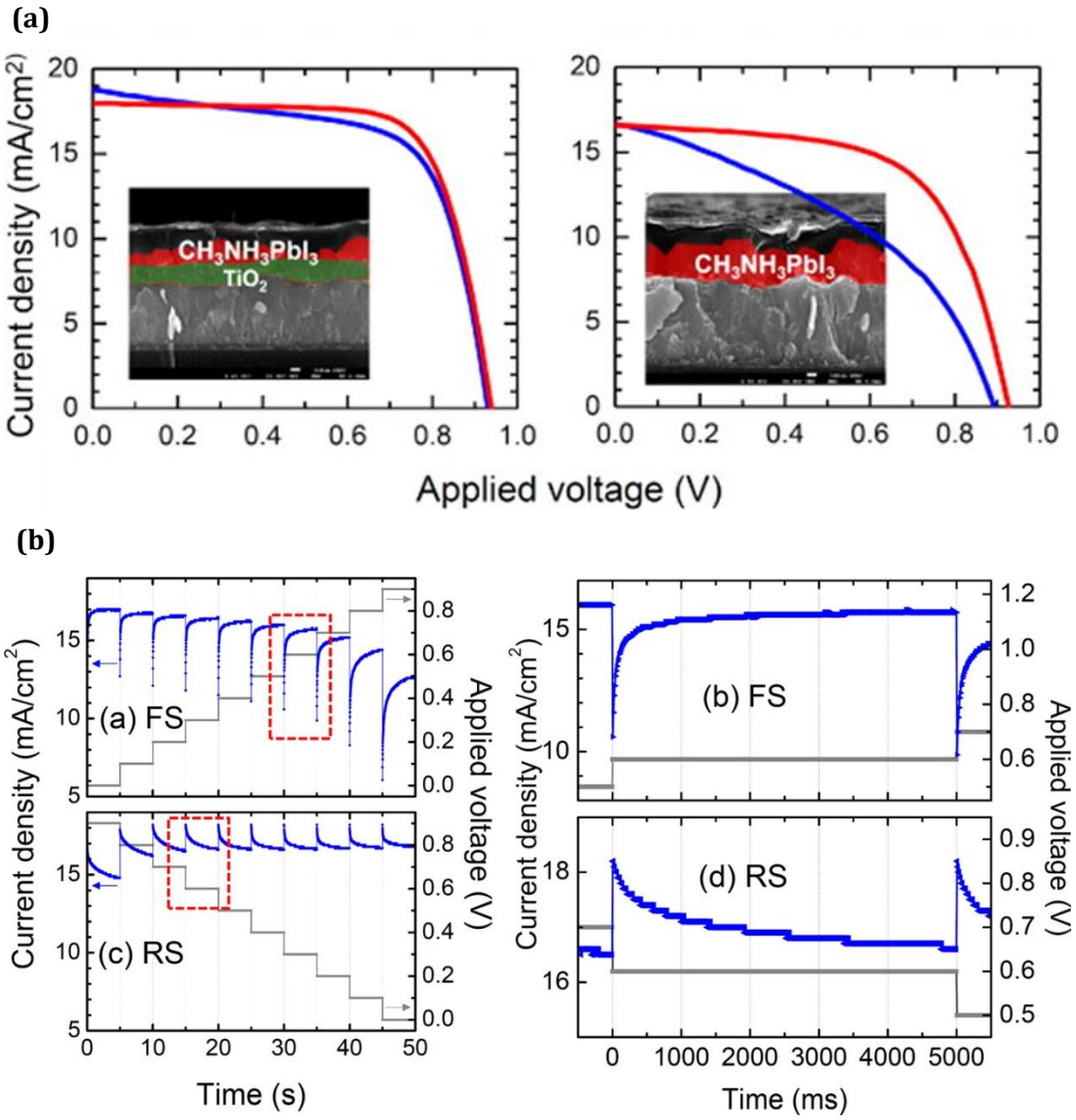

Figure 2.20 Part **(a)** shows the hysteresis commonly observed in the current-voltage characteristics of perovskite solar cells. For devices based on a compact-TiO_2 ETL, an increased hysteresis is observed for a planar device when compared to its sensitised counterpart. Part **(b)** demonstrates 'undershoot' and 'overshoot' of the photocurrent response under forward scan (FS) and reverse scan (RS) conditions. Taken from Kim et al. [149].

A number of mechanisms have been proposed to explain the hysteresis observed in perovskite solar cells, and it is of course possible that these occur concurrently. The three most commonly discussed processes are:

1. The filling and emptying of trap states under different applied biases[150].
2. Effects relating to the polarization and ferroelectricity of the material. Typical explanations involve the alignment of dipoles on the methylammonium cations due to rotation of these ions. This may also induce structural changes and distortion of the crystal lattice, changing the electronic properties and band structure of the material, as well as a leading to a potential increase in capacitance [122,149,151–153].
3. Ion migration, which has in particular been attributed to migration of iodide ion vacancies. This ion migration would allow build-up of charge at the interfaces, causing band bending which would either oppose or enhance charge extraction for reverse bias or forward bias polling respectively [154–161].

The magnitude of hysteresis varies depending upon the scan rate used whilst performing a *JV* sweep, although the precise interplay between the two is not always agreed upon [147,148,152]. The consensus currently seems to be that hysteresis is observed most at moderate scan speeds [155,162]. This can be rationalised as follows: at very low scan rates the dynamic processes (e.g. ion diffusion or lattice distortion) which follow a voltage change will have time to complete before the current is measured, and results will thus be quasi-steady-state. This may require a delay of seconds to tens of seconds between applying a bias and taking the current measurement [156,157,162]. As scan rate increases the dynamic processes will not have time to complete before the current measurement is taken, and thus the recent history of the bias applied to the device will influence the result of the measurement. At exceptionally high scan rates the entire scan will be completed before dynamic processes have had a significant effect; in this scenario hysteresis will be minimal however the measurements will not be a true reflection of the steady-state response of the device under test.

The observed hysteresis appears to be intrinsic to the material, but is also influenced by the interfaces and architecture of the device and the resulting charge extraction efficiency. Devices incorporating a compact TiO_2 ETL exhibit greater hysteresis when they are planar in architecture than when they incorporate a mesoporous (mp) TiO_2 scaffold, whilst switching to an mp-Al_2O_3 scaffold increases the hysteresis still further

[122,147,151,162]. Planar devices using PEDOT:PSS and PCBM HTL and ETLs respectively tend to exhibit only small hysteresis [151].

2.5.10 Toxicity

One possible barrier to the commercialization of the current generation of organometal halide perovskite solar cells lies in concerns about the toxicity of the lead incorporated into the material. Even quite low levels of lead exposure can lead to neurological, cardiovascular, renal, developmental and reproductive problems, with the nervous system being particularly prone to damage, especially amongst children and babies [163]. One of the chief concerns is that organo-lead halide perovskite can be decomposed to products including lead iodide, which is partially soluble in water. A solar panel which is exposed to the environment through broken or faulty encapsulation thus provides a route for rain water to dissolve small amounts of PbI_2, which can then leach into the soil and groundwater. It has, however, been calculated that even if 1 in every 300 panels were to break (in a 20 year operating period) and leach its entire content of lead into the environment, this would still be a reduction in the amount of lead released in comparison to producing the equivalent amount of energy through a coal burning power station [164]. With regards to the production of the lead required, it has also been shown that using lead from recycled lead-acid batteries produces solar cells with the same efficiency as those using pristine material purchased from commercial suppliers (Sigma), an encouraging result from a recycling and lifecycle perspective [165]. In any case, eliminating or reducing the lead used in these materials is still a highly worthwhile goal. To date, lead free alternatives have largely focused on the replacement of the lead cation (Pb^{2+}) by a tin cation (Sn^{2+}). These devices have had some limited success, achieving PCEs of up to around 6%, however they have struggled with extremely poor lifetime due to the susceptibility of the Sn^{2+} ions to oxidise to Sn^{4+} in the presence of oxygen or moisture, leading to the decomposition of the perovskite structure [166,167].

2.6 Transparent Electrodes

Transparent conducting electrodes (TCEs), also commonly known as 'window electrodes' are an important part of any organic or perovskite solar cell such as those studied in this thesis.

2.6.1 Key Electrode Properties

There are a number of factors which determine the suitability of an electrode for use in a given solar cell design, including:

- Transmittance
- Sheet resistance
- Work function
- Costs of materials and deposition techniques
- Mechanical flexibility
- Degradation rates and mechanisms
- Compatibility with substrates, interlayers, photoactive layers and deposition processes. These may be influenced by properties like surface roughness, wettability, resistance to solvents, required deposition temperature and so forth.

A high transmittance over the range of wavelengths at which the photoactive layer absorbs is clearly a key requirement for a TCE in order to maximise the optical field intensity within the photoactive material. A second vital concern is the ability of the electrode to conduct charges laterally, allowing them to reach metallic contacts and thus enter an external electrical circuit. The most commonly used metric for comparing electrodes in this regard is sheet resistance. Resistance is commonly expressed as

$$R = \rho \frac{l}{wt} = R_{\square} \frac{l}{w} \qquad \{2.7\}$$

Where t, l and w are the thickness, length and width of the sample respectively and sheet resistance, $R_{\square}$, is defined by

$$R_{\square} = \frac{\rho}{t} \quad \{2.8\}$$

Sheet resistance is thus defined as the resistance when l=w , i.e. when we have a square geometry, and has units of Ohms, although for clarity it is generally expressed in Ohms per square (Ω/□). A high sheet resistance will lead to a high series resistance, R_s, in the device, degrading power output by

$$P_{loss} = I^2 R_s \quad \{2.9\}$$

This form of power loss becomes increasingly important as the length over which charges are extracted through the electrode increases (i.e. as device size increases) [168]. The ideal transparent electrode, as well as maintaining compatibility with a wide variety of substrate, interlayer and active layer materials, would both maximise transmittance and minimise sheet resistance. These typically, however, are competing properties, for example increasing the thickness of a transparent conducting oxide leads to a lower sheet resistance but a reduced transmittance. It can therefore be useful to combine these two variables into a single value in order to facilitate comparison between electrodes. The most commonly used metric for this is the figure of merit (FOM) proposed by Haacke, defined as

$$FOM = \frac{T^{10}}{R_{\square}} \quad \{2.10\}$$

where T is the average transmittance and $R_{\square}$ the sheet resistance [169]. T is taken over the range of wavelengths relevant for the device under consideration, which is typically similar to the visible region of the electromagnetic spectrum (~400-700nm).

It is worth emphasising that the FOM gives only a rough guide as to the quality of a particular TCE. Haacke's definition maximises FOM at approximately T=0.9 [169], however depending on the specifics of the application this may be considered to place too great or too little importance on transmittance as compared to the sheet resistance. The relative importance of these two characteristics depends, amongst other things, on the absolute area and the geometry of the device, neither of which are accounted for in the calculation of Haacke's FOM. In addition, optical cavity and interference effects can be important in thin film organic devices but are not incorporated in the FOM.

2.6.2 The Need for New Electrode Materials

Due to its combination of exceptionally high transmittance, high conductivity and low surface roughness indium tin oxide (ITO) is currently the ubiquitous material for the transparent front electrode in OSCs and is widely used in perovskite solar cells. Whilst ITO fulfils the role of TCE very well in the rigid, small devices typical of a research environment, it has a number of limitations meaning that the development of novel TCE material systems is of interest.

Cost and Scarcity of Materials

The greatest demand for indium is for the production of ITO which is used in a variety of applications, most notably LCDs and touchscreens [170]. With an increasing market for both these and other ITO-containing devices such as OLEDs, OSCs and thin film CIGS solar cells, there are concerns about the scarcity of indium and rising prices [171]. It has been shown that a flexible substrate with ITO could account for around 30% of the cost of a flexible OSC module, with the vast majority of this contribution coming from the material and deposition costs of the ITO [11]. In addition, if the dream of high throughput roll-to-roll production of solution processed solar cells (SPSCs) is realised and these systems began to be produced on a large scale, considerations of indium scarcity and rising prices would be of increasing importance.

Embodied Energy

If solution processed solar cells are to play a significant role in displacing fossil fuels it is vital that their energy payback time – the time taken for the total energy produced by a module to match the energy used in its production and installation – is minimised. With this in mind it is necessary to ensure that the energy embodied in both the constituent materials of a solar cell and their deposition processes is minimised. One lifecycle analysis of a P3HT:PCBM solar cell on a PET substrate (using all roll-to-roll techniques apart for the deposition of the ITO electrode) found that the sputtered ITO layer accounted for 69% of the equivalent primary energy embedded in the final device [172]. Another found that the sputtered ITO accounted for 47% of the total energy used the production of an OPV module on PET. In this analysis the embodied energy of the material itself was separated out from that attributable to the sputtering process used in its deposition, showing that the sputtering accounted for the majority of the energy involved due to the vacuum and high substrate temperature employed [20,173].

Compatibility with Flexible Substrates

A key selling point for SPSCs is the promise of lightweight, flexible devices. ITO is unsuitable for use in flexible devices since it is brittle and has been demonstrated to experience a significant increase in sheet resistance upon bending, as shown in **Figure 2.21** [174,175].

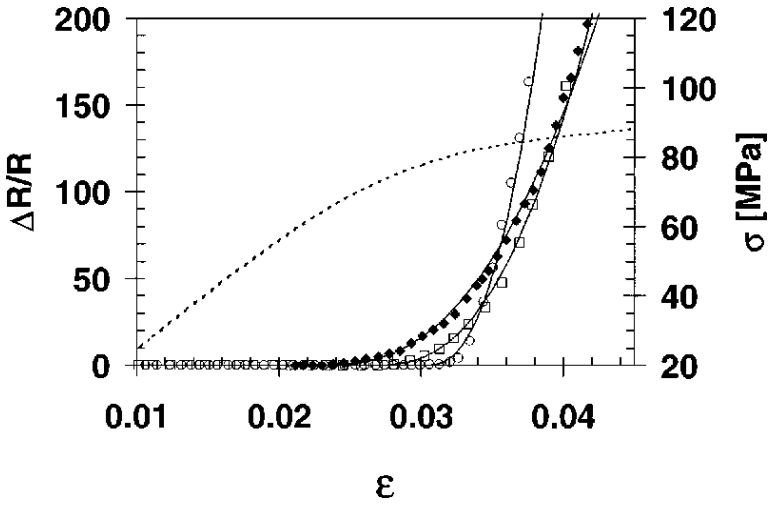

Figure 2.21 Fractional change in resistance with as a function of strain, *ε*, for ITO on PET for ITO thickness 105 (filled diamonds), 42 (empty squares) and 17 (empty circles) nm. The dotted line is the stress-strain curve (right axis). Taken from Cairns et al. [175].

In addition, plastic substrates cannot withstand the temperatures typically used in the sputtering of ITO. The use of lower substrate temperatures during deposition leads to the formation of an amorphous or low quality crystalline structure with many dislocations, leading to significant degradation of the electrical properties of the film. ITO deposited on a flexible PET substrate thus typically has a sheet resistance of around five times higher than for a comparable film thickness on glass [9,176–178]. In addition, ITO on PEN has in some cases been shown to have a very rough surface with a number of large spikes up to 50nm in size which could easily cause current leakage or short circuits in a device with a thin active layer [9].

2.6.3 Indium Free Alternatives

A variety of indium free electrodes have previously been developed and incorporated into both OSCs and perovskite solar cells. Due to their higher active layer thickness, perovskite solar cells have a less stringent requirement for low surface roughness than

do OSCs. For this reason fluorine doped tin oxide (FTO), a cheaper but rougher alternative to ITO, has been widely used in their fabrication. FTO, however, retains the requirement for an expensive and energy intensive sputtering process as well as exhibiting poor performance and durability when employed on flexible substrates [179–181]. Beyond FTO, indium free alternatives which have been successfully employed in OSCs include:

- Other transparent conducting oxides, for example aluminium doped or gallium doped zinc oxide (AZO and GZO) [182,183]. As with FTO, however, these materials are typically deposited by sputtering and also fail to resolve the issue of compatibility with flexible substrates due to a reliance on high temperature processing and/or a brittle nature [184,185].
- Highly conductive PEDOT:PSS [186]. A number of modifications to standard PEDOT:PSS exist in order to improve conductivity. These electrodes are solution processable, however they struggle with poor conductivity, often having sheet resistance of hundreds of Ω/□. Incorporation of metal current collecting grids into the highly conductive PEDOT:PSS film is significantly more promising [187]. There are concerns, however, about the long-term stability of devices incorporating PEDOT:PSS, particularly in humid environments, due to its hygroscopic and acidic nature [46–48].
- Carbon nanosheets [188], although these struggle to achieve a good sheet resistance.
- Silver nanowires, either as a standalone electrode or sandwiched between layers of, for example, PEDOT or ITO [189–191].
- Oxide/Metal/Oxide (O/M/O) stacks in which a thin metal film provides high lateral conductivity whilst the two oxide layers serve as a seed layer for metal film growth and a charge transport layer, as well as acting to suppress reflection (see **Chapter 4**). It is worth noting that even if oxides containing indium are to be used, a stack design involving ITO/thin metal film/ITO offers improved compatibility with flexible substrates in comparison to a simple ITO electrode, since the use of a thin and flexible metal film to allow lateral conduction both reduces the degradation of sheet resistance upon bending and the requirement for such high quality ITO allowing a lower processing temperature to be used [192].

2.6.4 Growth Modes of Metal Films

The different growth modes of thin metal films are important in determining the morphology of the final film and thus its optoelectronic properties. In oxide/metal/oxide multilayer electrodes this can have great influence on the performance of the electrode. Growth modes depend upon the properties of both the film material and the underlying layer, as well as deposition parameters such as substrate temperature and deposition rate.

The Frank-van der Merwe growth mode is a layer-by-layer process which occurs in situations where the deposited atoms are more strongly bound to the substrate than to each other. In this process a complete layer is formed before the next layer begins to grow, as shown in **Figure 2.22(a)**.

The Volmer-Weber growth mode involves the growth of individual island-like features and occurs when the deposited atoms are more strongly bound to each other than to the substrate, meaning that they have the tendency to agglomerate. This is shown in **Figure 2.22(b)**. Islands may then coalesce by a number of processes, for example Ostwald ripening in which atoms leave a small island more readily than a large one due to the more convex curvature, leading to a net flow of atoms from small islands to large islands.

Stranski-Krastanov growth initially involves layer by layer growth, however above a critical thickness the growth continues via island formation, as shown in **Figure 2.22(c)**.

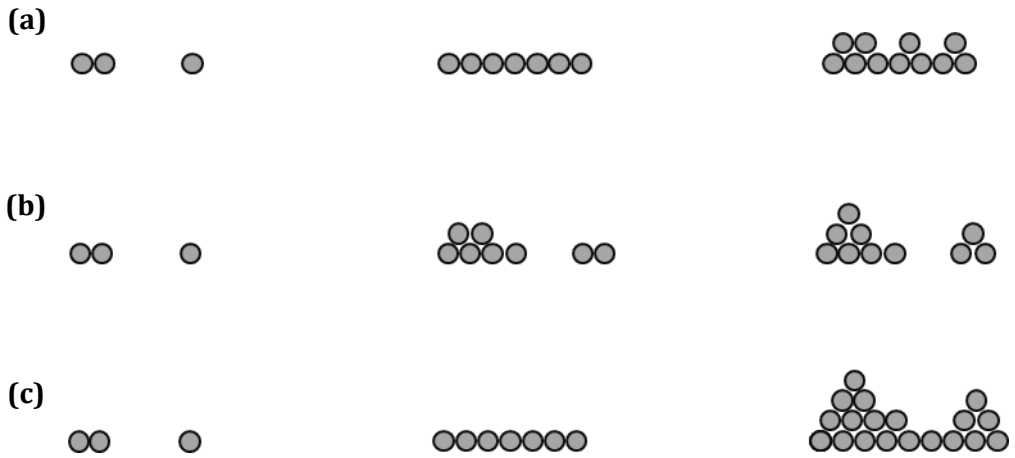

Figure 2.22 A schematic of Frank-van der Merwe **(a)**, Volmer-Weber **(b)** and Stranski-Krastanov **(c)** growth modes.

2.7 Conclusions

Within this Chapter, relevant background information and underlying physical principles relating to the topics covered in this thesis have been presented. **Section 2.2** introduced concepts important for understanding both photovoltaic devices in general and the materials which constitute the photoactive layer of organic and perovskite photovoltaics. **Section 2.3** then discussed the particular promises and pitfalls of solution processed solar cells as well as providing an overview of roll-to-roll film deposition techniques and a brief summary of how these have been applied in the fabrication of perovskite solar cells. This section is particularly relevant to the work presented in **Chapter 5**. **Section 2.4** and **Section 2.5** focused in greater detail on organic solar cells and perovskite solar cells respectively. Organic devices have been used in **Chapter 4** whilst perovskite solar cells have been explored in **Chapter 5** and **Chapter 6**. Finally **Section 2.6**, particularly relevant to the work in **Chapter 4**, covered important information relating to transparent electrodes and in particular the replacement of the widely used indium tin oxide.

2.8 References

[1] J. Clayden, N. Greeves, S. Warren, P. Wothers, Organic Chemistry, Oxford University Press, 2001.

[2] C. Kittel, Introduction to solid state physics, 8th ed., Wiley, 2004.

[3] W. Shockley, H.J. Queisser, Detailed Balance Limit of Efficiency of p-n Junction Solar Cells, J. Appl. Phys. 32 (1961) 510.

[4] NREL Reference Solar Spectral Irradiance, (n.d.). http://rredc.nrel.gov/solar/spectra/am1.5/ASTMG173/ASTMG173.html (accessed September 25, 2015).

[5] M.W. Denhoff, N. Drolet, The effect of the front contact sheet resistance on solar cell performance, Sol. Energy Mater. Sol. Cells. 93 (2009) 1499–1506.

[6] M.A. Green, K. Emery, Y. Hishikawa, W. Warta, E.D. Dunlop, Solar cell efficiency tables (version 46), Prog. Photovoltaics Res. Appl. 23 (2015) 805–812.

[7] M.A. Green, A. Ho-Baillie, H.J. Snaith, The emergence of perovskite solar cells, Nat. Photonics. 8 (2014) 506–514.

[8] J. Jean, P.R. Brown, R.L. Jaffe, T. Buonassisi, V. Bulovic, Pathways for Solar Photovoltaics, Energy Environ. Sci. (2015).

[9] Y. Galagan, I.G. de Vries, A.P. Langen, R. Andriessen, W.J.H. Verhees, S.C. Veenstra, et al., Technology development for roll-to-roll production of organic photovoltaics, Chem. Eng. Process. Process Intensif. 50 (2011) 454–461.

[10] M. Kaltenbrunner, M.S. White, E.D. Głowacki, T. Sekitani, T. Someya, N.S. Sariciftci, et al., Ultrathin and lightweight organic solar cells with high flexibility., Nat. Commun. 3 (2012) 770.

[11] F.C. Krebs, M. Jørgensen, K. Norrman, O. Hagemann, J. Alstrup, T.D. Nielsen, et al., A complete process for production of flexible large area polymer solar cells entirely using screen printing—First public demonstration, Sol. Energy Mater. Sol. Cells. 93 (2009) 422–441.

[12] P. Docampo, J. Ball, M. Darwich, G. Eperon, H.J. Snaith, Efficient organometal trihalide perovskite planar-heterojunction solar cells for flexible polymer substrates, Nat. Commun. 4 (2013) 2761.

[13] Y. Galagan, D.J.D. Moet, D.C. Hermes, P.W.M. Blom, R. Andriessen, Large area ITO-free organic solar cells on steel substrate, Org. Electron. 13 (2012) 3310–3314.

[14] F.-C. Chen, J.-L. Wu, W.-C. Huang, H.-M.P. Chen, W.-C. Chen, Flexible Polymer Photovoltaic Devices Prepared With Inverted Structures on Metal Foils, IEEE Electron Device Lett. 30 (2009) 727–729.

[15] P. Fath, H. Nussbaumer, R. Burkhardt, Industrial manufacturing of semitransparent crystalline silicon POWER solar cells, Sol. Energy Mater. Sol. Cells. 74 (2002) 127–131.

[16] B. Petter Jelle, C. Breivik, H. Drolsum Røkenes, Building integrated photovoltaic products: A state-of-the-art review and future research opportunities, Sol. Energy Mater. Sol. Cells. 100 (2012) 69–96.

[17] C.C. Chueh, S.C. Chien, H.L. Yip, J.F. Salinas, C.Z. Li, K.S. Chen, et al., Toward high-performance semi-transparent polymer solar cells: Optimization of ultra-thin light absorbing layer and transparent cathode architecture, Adv. Energy Mater. 3 (2013) 417–423.

[18] A.R.B.M. Yusoff, S.J. Lee, F.K. Shneider, W.J. da Silva, J. Jang, High-Performance Semitransparent Tandem Solar Cell of 8.02% Conversion Efficiency with Solution-Processed Graphene Mesh and Laminated Ag Nanowire Top Electrodes, Adv. Energy Mater. 4 (2014) 1301989.

[19] G.E. Eperon, D. Bryant, J. Troughton, S.D. Stranks, M.B. Johnston, T. Watson, et al., Efficient, Semitransparent Neutral-Colored Solar Cells Based on Microstructured Formamidinium Lead Trihalide Perovskite, J. Phys. Chem. Lett. 6 (2015) 129–138.

[20] A.L. Roes, E.A. Alsema, K. Blok, M.K. Patel, Ex-ante Environmental and Economic Evaluation of Polymer Photovoltaics, Prog. Photovoltaics Res. Appl. 17 (2009) 372–393.

[21] F.C. Krebs, Fabrication and processing of polymer solar cells: A review of printing and coating techniques, Sol. Energy Mater. Sol. Cells. 93 (2009) 394–412.

[22] R. Sondergaard, M. Hosel, D. Angmo, T.T. Larsen-olsen, F.C. Krebs, Roll-to-roll fabrication of polymer solar cells, Mater. Today. 15 (2012) 36–49.

[23] R.R. Søndergaard, M. Hösel, F.C. Krebs, Roll-to-Roll fabrication of large area functional organic materials, J. Polym. Sci. Part B Polym. Phys. 51 (2013) 16–34.

[24] F.C. Krebs, R. Søndergaard, M. Jørgensen, Printed metal back electrodes for R2R fabricated polymer solar cells studied using the LBIC technique, Sol. Energy Mater. Sol. Cells. 95 (2011) 1348–1353.

[25] F.C. Krebs, N. Espinosa, M. Hösel, R.R. Søndergaard, M. Jørgensen, 25th anniversary article: Rise to power - OPV-based solar parks, Adv. Mater. 26 (2014) 29–39.

[26] D. Vak, S.-S. Kim, J. Jo, S.-H. Oh, S.-I. Na, J. Kim, et al., Fabrication of organic bulk heterojunction solar cells by a spray deposition method for low-cost power generation, Appl. Phys. Lett. 91 (2007) 081102.

[27] C. Girotto, D. Moia, B.P. Rand, P. Heremans, High-Performance Organic Solar Cells with Spray-Coated Hole-Transport and Active Layers, Adv. Funct. Mater. 21 (2011) 64–72.

[28] T. Wang, N.W. Scarratt, H. Yi, A.D.F. Dunbar, A.J. Pearson, D.C. Watters, et al., Fabricating High Performance, Donor-Acceptor Copolymer Solar Cells by Spray-Coating in Air, Adv. Energy Mater. 3 (2013) 505–512.

[29] J. Griffin, A.J. Pearson, N.W. Scarratt, T. Wang, D.G. Lidzey, A.R. Buckley, Organic photovoltaic devices incorporating a molybdenum oxide hole-extraction layer deposited by spray-coating from an ammonium molybdate tetrahydrate precursor, Org. Electron. 15 (2014) 692–700.

[30] C. Girotto, B.P. Rand, S. Steudel, J. Genoe, P. Heremans, Nanoparticle-based, spray-coated silver top contacts for efficient polymer solar cells, Org. Electron. 10 (2009) 735–740.

[31] D. Zheng, J. Huang, Y. Zheng, J. Yu, High performance airbrush spray coated organic solar cells via tuning the surface tension and saturated vapor pressure of different ternary solvent systems, Org. Electron. 25 (2015) 275–282.

[32] A. Barrows, A. Pearson, C. Kwak, A. Dunbar, A. Buckley, D. Lidzey, Efficient planar heterojunction mixed-halide perovskite solar cells deposited via spray-deposition, Energy Environ. Sci. 7 (2014) 2944–2950.

[33] Z. Liang, J. Ding, S.-H. Zhang, X. Xu, N. Wang, J. Wang, et al., A large grain size perovskite thin film with dense structure for planar heterojunction solar cells

via spray deposition under ambient conditions, RSC Adv. 5 (2015) 60562–60569.

[34] M. Ramesh, K.M. Boopathi, T.-Y. Huang, Y.-C. Huang, C.-S. Tsao, C.-W. Chu, Using an airbrush pen for layer-by-layer growth of continuous perovskite thin films for hybrid solar cells, ACS Appl. Mater. Interfaces. 7 (2015) 2359–2366.

[35] K. Jiang, S.-G. Li, M. Su, X. Cui, J.-H. Huang, Q.-Q. Zhang, et al., Inkjet Printing CH3NH3PbI3 on Mesoscopic TiO2 Film for Highly Efficient Perovskite Solar Cells, J. Mater. Chem. A. 3 (2015) 9092–9097.

[36] A. Mei, X. Li, L. Liu, Z. Ku, T. Liu, Y. Rong, et al., A hole-conductor-free, fully printable mesoscopic perovskite solar cell with high stability, Science. 345 (2014) 295–298.

[37] D. Vak, K. Hwang, A. Faulks, Y.-S. Jung, N. Clark, D.-Y. Kim, et al., 3D Printer Based Slot-Die Coater as a Lab-to-Fab Translation Tool for Solution-Processed Solar Cells, Adv. Energy Mater. 5 (2015) 1401539.

[38] T.M. Schmidt, T.T. Larsen-olsen, J.E. Carlé, D. Angmo, F.C. Krebs, Upscaling of Perovskite Solar Cells : Fully Ambient Roll Processing of Flexible Perovskite Solar Cells with Printed Back Electrodes, Adv. Energy Mater. (2015) 1500569.

[39] G.A. Chamberlain, Organic solar cells: A review, Sol. Cells. 8 (1983) 47–83.

[40] C.W. Tang, Two-layer organic photovoltaic cell, Appl. Phys. Lett. 48 (1986) 183.

[41] J.J.M. Halls, C.A. Walsh, N.C. Greenham, E.A. Marseglia, R.H. Friend, S.C. Moratti, et al., Efficient photodiodes from interpenetrating polymer networks, Nature. 376 (1995) 498–500.

[42] G. Yu, J. Gao, C. Hummelen, F. Wudl, A.J. Heeger, Polymer Photovoltaic Cells: Enhanced Efficiencies via a Network of Internal Donor-Acceptor Heterojunctions, Science. 270 (1995) 1789–1791.

[43] A. Mishra, P. Bäuerle, Small molecule organic semiconductors on the move: Promises for future solar energy technology, Angew. Chemie - Int. Ed. 51 (2012) 2020–2067.

[44] G. Li, R. Zhu, Y. Yang, Polymer solar cells, Nat. Photonics. 6 (2012) 153–161.

[45] G. Li, C.-W. Chu, V. Shrotriya, J. Huang, Y. Yang, Efficient inverted polymer solar cells, Appl. Phys. Lett. 88 (2006) 253503.

[46] M. Jørgensen, K. Norrman, S. a Gevorgyan, T. Tromholt, B. Andreasen, F.C. Krebs, Stability of polymer solar cells., Adv. Mater. 24 (2012) 580–612.

[47] K.H. Wong, K. Ananthanarayanan, M.D. Heinemann, J. Luther, P. Balaya, Enhanced photocurrent and stability of organic solar cells using solution-based NiO interfacial layer, Sol. Energy. 86 (2012) 3190–3195.

[48] E. Voroshazi, B. Verreet, A. Buri, R. Müller, D. Di Nuzzo, P. Heremans, Influence of cathode oxidation via the hole extraction layer in polymer:fullerene solar cells, Org. Electron. 12 (2011) 736–744.

[49] S. Kundu, S.R. Gollu, R. Sharma, S. G, A. Ashok, A.R. Kulkarni, et al., Device stability of inverted and conventional bulk heterojunction solar cells with MoO3 and ZnO nanoparticles as charge transport layers, Org. Electron. 14 (2013) 3083–3088.

[50] X. Tong, R.F. Bailey-Salzman, G. Wei, S.R. Forrest, Inverted small molecule organic photovoltaic cells on reflective substrates, Appl. Phys. Lett. 93 (2008) 2006–2009.

[51] E.-C. Chen, P.-T. Tsai, C.-Y. Tsai, J.-H. Chang, Z.-Y. Huang, H.-F. Meng, et al., ITO-free inverted polymer solar cell on metal substrate with top-illumination, Synth. Met. 187 (2014) 172–177.

[52] Z. He, C. Zhong, X. Huang, W.-Y. Wong, H. Wu, L. Chen, et al., Simultaneous enhancement of open-circuit voltage, short-circuit current density, and fill factor in polymer solar cells., Adv. Mater. 23 (2011) 4636–4643.

[53] R. Po, C. Carbonera, A. Bernardi, N. Camaioni, The role of buffer layers in polymer solar cells, Energy Environ. Sci. 4 (2011) 285.

[54] R.E. Peierls, Quantum theroy of solids, Clarendon Press, Oxford, 1955.

[55] C.S. Yannoni, T.C. Clarke, Molecular Geometry of cis - and trans -Polyacetylene by Nutation NMR Spectroscopy, Phys. Rev. Lett. 51 (1983) 1191–1193.

[56] Z. Zhang, J. Wang, Structures and properties of conjugated Donor–Acceptor copolymers for solar cell applications, J. Mater. Chem. 22 (2012) 4178–4187.

[57] J.-L. Brédas, J.-L. Brédas, D. Beljonne, D. Beljonne, V. Coropceanu, V. Coropceanu, et al., Charge-Transfer and Energy-Transfer Processes in π-Conjugated Oligomers and Polymers: A Molecular Picture, Chem. Rev. 104 (2004) 4971.

[58] J. Nelson, Organic photovoltaic films, Curr. Opin. Solid State Mater. Sci. 6 (2002)

87–95.

[59] P. Kumar, S. Chand, Recent progress and future aspects of organic solar cells, Prog. Photovoltaics Res. Appl. 20 (2012) 377–415.

[60] T. Wang, A.J. Pearson, D.G. Lidzey, Correlating molecular morphology with optoelectronic function in solar cells based on low band-gap copolymer:fullerene blends, J. Mater. Chem. C. 1 (2013) 7266–7293.

[61] H. Hoppe, N.S. Sariciftci, Organic solar cells : An overview, J. Mater. Res. 19 (2004) 1924–1945.

[62] M.M. Wienk, J.M. Kroon, W.J.H. Verhees, J. Knol, J.C. Hummelen, P. a van Hal, et al., Efficient methano[70]fullerene/MDMO-PPV bulk heterojunction photovoltaic cells., Angew. Chem. Int. Ed. Engl. 42 (2003) 3371–3375.

[63] P.E. Shaw, A. Ruseckas, I.D.W. Samuel, Exciton diffusion measurements in poly(3-hexylthiophene), Adv. Mater. 20 (2008) 3516–3520.

[64] B.C. Thompson, J.M.J. Fréchet, Polymer-fullerene composite solar cells., Angew. Chem. Int. Ed. Engl. 47 (2008) 58–77.

[65] N. Blouin, A. Michaud, M. Leclerc, A low-bandgap poly(2,7-carbazole) derivative for use in high-performance solar cells, Adv. Mater. 19 (2007) 2295–2300.

[66] A.A.B. Alghamdi, D.C. Watters, H. Yi, S. Al-Faifi, M.S. Almeataq, D. Coles, et al., Selenophene vs. thophene in benzothiadiazole-based low energy gap donor-acceptor polymers for photovoltaic applications, J. Mater. Chem. A. 1 (2013) 5165–5171.

[67] C. Soci, I.-W. Hwang, D. Moses, Z. Zhu, D. Waller, R. Gaudiana, et al., Photoconductivity of a Low-Bandgap Conjugated Polymer, Adv. Funct. Mater. 17 (2007) 632–636.

[68] D.C. Watters, H. Yi, A.J. Pearson, J. Kingsley, A. Iraqi, D. Lidzey, Fluorene-based co-polymer with high hole mobility and device performance in bulk heterojunction organic solar cells., Macromol. Rapid Commun. 34 (2013) 1157–1162.

[69] R. Steim, F.R. Kogler, C.J. Brabec, Interface materials for organic solar cells, J. Mater. Chem. 20 (2010) 2499–2512.

[70] S. Braun, W.R. Salaneck, M. Fahlman, Energy-Level Alignment at Organic/Metal and Organic/Organic Interfaces, Adv. Mater. 21 (2009) 1450–1472.

[71] M.T. Greiner, M.G. Helander, W. Tang, Z. Wang, J. Qiu, Z. Lu, Universal energy-level alignment of molecules on metal oxides, Nat. Mater. 11 (2011) 76–81.

[72] K. Tvingstedt, O. Malinkiewicz, A. Baumann, C. Deibel, H.J. Snaith, V. Dyakonov, et al., Radiative efficiency of lead iodide based perovskite solar cells, Sci. Rep. 4 (2014) 6071.

[73] M.D. Graef, M. McHenry, Structure of Materials: An Introduction to Crystallography, Diffraction and Symmetry, Cambridge University Press, 2007.

[74] S. Kazim, M.K. Nazeeruddin, M. Grätzel, S. Ahmad, Perovskite as light harvester: a game changer in photovoltaics., Angew. Chem. Int. Ed. Engl. 53 (2014) 2812–2824.

[75] G.E. Eperon, S.D. Stranks, C. Menelaou, M.B. Johnston, L.M. Herz, H.J. Snaith, Formamidinium lead trihalide: a broadly tunable perovskite for efficient planar heterojunction solar cells, Energy Environ. Sci. 7 (2014) 982.

[76] S. Pang, H. Hu, J. Zhang, S. Lv, Y. Yu, F. Wei, et al., $NH_2CHNH_2PbI_3$: An Alternative Organolead Iodide Perovskite Sensitizer for Mesoscopic Solar Cells, Chem. Mater. 26 (2014) 1485–1491.

[77] G.H. Imler, X. Li, B. Xu, G.E. Dobereiner, H.-L. Dai, Y. Rao, et al., Solid state transformation of the crystalline monohydrate $(CH_3NH_3)PbI_3(H_2O)$ to the $(CH_3NH_3)PbI_3$ perovskite, Chem. Commun. 51 (2015) 11290–11292.

[78] J. Even, L. Pedesseau, C. Katan, Analysis of multivalley and multibandgap absorption and enhancement of free carriers related to exciton screening in hybrid perovskites, J. Phys. Chem. C. 118 (2014) 11566–11572.

[79] J.M. Frost, K.T. Butler, F. Brivio, C.H. Hendon, M. van Schilfgaarde, A. Walsh, Atomistic origins of high-performance in hybrid halide perovskite solar cells., Nano Lett. 14 (2014) 2584–2590.

[80] C.C. Stoumpos, C.D. Malliakas, M.G. Kanatzidis, Semiconducting tin and lead iodide perovskites with organic cations: Phase transitions, high mobilities, and near-infrared photoluminescent properties, Inorg. Chem. 52 (2013) 9019–9038.

[81] X.Y. Chin, D. Cortecchia, J. Yin, A. Bruno, C. Soci, Lead Iodide Perovskite Light-Emitting Field-Effect Transistor, Nat. Commun. 6 (2015) 7383.

[82] T. Baikie, Y. Fang, J.M. Kadro, M. Schreyer, F. Wei, S.G. Mhaisalkar, et al., Synthesis and crystal chemistry of the hybrid perovskite $(CH_3NH_3)PbI_3$ for solid-

state sensitised solar cell applications, J. Mater. Chem. A. 1 (2013) 5628.

[83] A. Poglitsch, D. Weber, Dynamic disorder in methylammoniumtrihalogenoplumbates (II) observed by millimeter-wave spectroscopy, J. Chem. Phys. 87 (1987) 6373.

[84] M.M. Lee, J. Teuscher, T. Miyasaka, T.N. Murakami, H.J. Snaith, Efficient hybrid solar cells based on meso-superstructured organometal halide perovskites, Science. 338 (2012) 643–647.

[85] D. Weber, $CH_3NH_3PbX_3$, ein Pb(II)-System mit kubischer Perowskitstruktur, Z. Naturforsch. 33b (1978) 1443–1445.

[86] D. Weber, CH3NH3SnBrxI3-x (x=0-3), ein Sn(II)-System mit kubischer Perowskitstruktur, Z. Naturforsch. 33b (1978) 862–865.

[87] C.R. Kagan, D.B. Mitzi, C.D. Dimitrakopoulos, Organic-Inorganic Hybrid Materials as Semiconducting Channels in Thin-Film Field-Effect Transistors, Science. 286 (1999) 945–947.

[88] M. Era, S. Morimoto, T. Tsutsui, S. Saito, Organic-inorganic heterostructure electroluminescent device using a layered perovskite semiconductor $(C_6H_5C_2H_4NH_3)_2PbI_4$, Appl. Phys. Lett. 65 (1994) 676–678.

[89] A. Kojima, K. Teshima, T. Miyasaka, Y. Shirai, Novel Photoelectrochemical Cell with Mesoscopic Electrodes Sensitized by Lead-halide Compounds, in: Proc. 210th Electrochem. Soc. Meet., 2006.

[90] A. Kojima, K. Teshima, Y. Shirai, T. Miyasaka, Organometal halide perovskites as visible-light sensitizers for photovoltaic cells., J. Am. Chem. Soc. 131 (2009) 6050–6051.

[91] J.-H. Im, C.-R. Lee, J.-W. Lee, S.-W. Park, N.-G. Park, 6.5% Efficient Perovskite Quantum-Dot-Sensitized Solar Cell., Nanoscale. 3 (2011) 4088–4093.

[92] H.-S. Kim, C.-R. Lee, J.-H. Im, K.-B. Lee, T. Moehl, A. Marchioro, et al., Lead iodide perovskite sensitized all-solid-state submicron thin film mesoscopic solar cell with efficiency exceeding 9%, Sci. Rep. 2 (2012) 591.

[93] Nature, Nature's Ten People Who Mattered this year, Nature. 504 (2013) 357–365.

[94] F. Brivio, A.B. Walker, A. Walsh, Structural and electronic properties of hybrid perovskites for high-efficiency thin-film photovoltaics from first-principles, APL

Mater. 1 (2013) 042111.

[95] C. Motta, F. El Mellouhi, S. Kais, N. Tabet, F. Alharbi, S. Sanvito, Revealing the role of organic cations in hybrid halide perovskite $CH_3NH_3PbI_3$, Nat. Commun. 6 (2015) 7026.

[96] F. Brivio, K.T. Butler, A. Walsh, M. van Schilfgaarde, Relativistic quasiparticle self-consistent electronic structure of hybrid halide perovskite photovoltaic absorbers, (2014) 1–6.

[97] J.H. Noh, S.H. Im, J.H. Heo, T.N. Mandal, S. Il Seok, Chemical management for colorful, efficient, and stable inorganic-organic hybrid nanostructured solar cells, Nano Lett. 13 (2013) 1764–1769.

[98] W. Yin, J. Yang, J. Kang, Y. Yan, S.-H. Wei, Halide Perovskite Materials for Solar Cells: A Theoretical Review, J. Mater. Chem. A. 3 (2015) 8926–8942.

[99] R.E. Wasylishen, O. Knop, J.B. Macdonald, Cation Rotation in Methylammonium Lead Halides, Solid State Commun. 56 (1985) 581–582.

[100] G. Xing, N. Mathews, S. Sun, S.S. Lim, Y.M. Lam, M. Grätzel, et al., Long-range balanced electron- and hole-transport lengths in organic-inorganic $CH_3NH_3PbI_3$, Science. 342 (2013) 344–347.

[101] W.-J. Yin, T. Shi, Y. Yan, Unique Properties of Halide Perovskites as Possible Origins of the Superior Solar Cell Performance, Adv. Mater. 26 (2014) 4653–4658.

[102] M. Hirasawa, T. Ishihara, T. Goto, K. Uchida, N. Miura, Magnetoabsorption of the lowest exciton in perovskite-type compound (CH3NH3)PbI3, Phys. B. 201 (1994) 427–430.

[103] T. Ishiharat, Optical properties of PbI-based perovskite structures, J. Lumin. 60&61 (1994) 269–274.

[104] K. Tanaka, T. Takahashi, T. Ban, T. Kondo, K. Uchida, N. Miura, Comparative study on the excitons in lead-halide-based perovskite-type crystals CH3NH3PbBr3 CH3NH3PbI3, Solid State Commun. 127 (2003) 619–623.

[105] V.D. Innocenzo, G. Grancini, M.J.P. Alcocer, A. Ram, S. Kandada, S.D. Stranks, et al., Excitons versus free charges in organo-lead tri-halide perovskites, Nat. Commun. 5 (2014) 3586.

[106] Q. Lin, A. Armin, R.C.R. Nagiri, P.L. Burn, P. Meredith, Electro-optics of

perovskite solar cells, Nat. Photonics. 9 (2014) 106–112.

[107] A. Miyata, A. Mitioglu, P. Plochocka, O. Portugall, J.T. Wang, S.D. Stranks, et al., Direct measurement of the exciton binding energy and effective masses for charge carriers in organic-inorganic tri-halide perovksites, Nat. Phys. 11 (2015) 582–588.

[108] C.S. Ponseca, T.J. Savenije, M. Abdellah, K. Zheng, A. Yartsev, T. Pascher, et al., Organometal halide perovskite solar cell materials rationalized: ultrafast charge generation, high and microsecond-long balanced mobilities, and slow recombination., J. Am. Chem. Soc. 136 (2014) 5189–5192.

[109] C. Wehrenfennig, G.E. Eperon, M.B. Johnston, H.J. Snaith, L.M. Herz, High Charge Carrier Mobilities and Lifetimes in Organolead Trihalide Perovskites, Adv. Mater. 26 (2013) 1584–1589.

[110] T. Leijtens, S.D. Stranks, G.E. Eperon, R. Lindblad, E.M.J. Johansson, J.M. Ball, et al., Electronic Properties of Meso-Superstructured and Planar Organometal Halide Perovskite Films: Charge Trapping, Photodoping, and Carrier Mobility, ACS Appl. Mater. Interfaces. 8 (2014) 7147–7155.

[111] S.D. Stranks, G.E. Eperon, G. Grancini, C. Menelaou, M.J.P. Alcocer, T. Leijtens, et al., Electron-hole diffusion lengths exceeding 1 micrometer in an organometal trihalide perovskite absorber, Science. 342 (2013) 341–344.

[112] E. Edri, S. Kirmayer, S. Mukhopadhyay, K. Gartsman, G. Hodes, D. Cahen, Elucidating the charge carrier separation and working mechanism of CH3NH3Pb3-xClx perovskite solar cells, Nat. Commun. 5 (2014) 3461.

[113] V. Gonzalez-Pedro, E.J. Juarez-Perez, W.-S. Arsyad, E.M. Barea, F. Fabregat-Santiago, I. Mora-Sero, et al., General Working Principles of $CH_3NH_3PbX_3$ Perovskite Solar Cells., Nano Lett. 14 (2014) 888–893.

[114] Q. Dong, Y. Fang, Y. Shao, P. Mulligan, J. Qiu, L. Cao, et al., Electron-hole diffusion lengths > 175 mm in solution-grown $CH_3NH_3PbI_3$ single crystals, Science. 347 (2015) 967–970.

[115] Y. Chen, J. Peng, D. Su, X. Chen, Z. Liang, Efficient and Balanced Charge Transport Revealed in Planar Perovskite Solar Cells, ACS Appl. Mater. Interfaces. 7 (2015) 4471–4475.

[116] P.W.M. Blom, V.D. Mihailetchi, L.J.A. Koster, D.E. Markov, Device physics of

polymer:Fullerene bulk heterojunction solar cells, Adv. Mater. 19 (2007) 1551–1566.

[117] D.-Y. Son, J.-H. Im, H.-S. Kim, N.-G. Park, 11% Efficient Perovskite Solar Cell Based on ZnO Nanorods: An Effective Charge Collection System, J. Phys. Chem. C. 118 (2014) 16567–16573.

[118] A. Marchioro, J. Teuscher, D. Friedrich, M. Kunst, R. van de Krol, T. Moehl, et al., Unravelling the mechanism of photoinduced charge transfer processes in lead iodide perovskite solar cells, Nat. Photonics. 8 (2014) 250–255.

[119] P. Qin, S. Tanaka, S. Ito, N. Tetreault, K. Manabe, H. Nishino, et al., Inorganic hole conductor-based lead halide perovskite solar cells with 12.4% conversion efficiency, Nat. Commun. 5 (2014) 3834.

[120] G. Li, K.L. Ching, J.Y.L. Ho, M. Wong, H.-S. Kwok, Identifying the Optimum Morphology in High-Performance Perovskite Solar Cells, Adv. Energy Mater. 5 (2015) 1401775.

[121] V.W. Bergmann, S. a. L. Weber, F. Javier Ramos, M.K. Nazeeruddin, M. Grätzel, D. Li, et al., Real-space observation of unbalanced charge distribution inside a perovskite-sensitized solar cell, Nat. Commun. 5 (2014) 5001.

[122] H. Chen, N. Sakai, M. Ikegami, T. Miyasaka, Emergence of Hysteresis and Transient Ferroelectric Response in Organo-Lead Halide Perovskite Solar Cells, J. Phys. Chem. Lett. 6 (2015) 164–169.

[123] G.E. Eperon, V.M. Burlakov, P. Docampo, A. Goriely, H.J. Snaith, Morphological Control for High Performance, Solution-Processed Planar Heterojunction Perovskite Solar Cells, Adv. Funct. Mater. 24 (2014) 151–157.

[124] M. Liu, M.B. Johnston, H.J. Snaith, Efficient planar heterojunction perovskite solar cells by vapour deposition, Nature. 501 (2013) 395–398.

[125] P.-W. Liang, C.-Y. Liao, C.-C. Chueh, F. Zuo, S.T. Williams, X.-K. Xin, et al., Additive Enhanced Crystallization of Solution-Processed Perovskite for Highly Efficient Planar-Heterojunction Solar Cells, Adv. Mater. 26 (2014) 3748–3754.

[126] Y.-J. Jeon, S. Lee, R. Kang, J.-E. Kim, J.-S. Yeo, S.-H. Lee, et al., Planar heterojunction perovskite solar cells with superior reproducibility, Sci. Rep. 4 (2014) 6953.

[127] N.J. Jeon, J.H. Noh, Y.C. Kim, W.S. Yang, S. Ryu, S. Il Seok, Solvent engineering for

high-performance inorganic-organic hybrid perovskite solar cells, Nat. Mater. 13 (2014) 897–903.

[128] M. Xiao, F. Huang, W. Huang, Y. Dkhissi, Y. Zhu, J. Etheridge, et al., A Fast Deposition-Crystallization Procedure for Highly Efficient Lead Iodide Perovskite Thin-Film Solar Cells, Angew. Chemie Int. Ed. 126 (2014) 10056–10061.

[129] J. Burschka, N. Pellet, S.-J. Moon, R. Humphry-Baker, P. Gao, M.K. Nazeeruddin, et al., Sequential deposition as a route to high-performance perovskite-sensitized solar cells, Nature. 499 (2013) 316–319.

[130] Z. Xiao, B. Cheng, Y. Shao, Q. Dong, Q. Wang, Y. Yongbo, et al., Efficient, High Yield Perovskite Photovoltaic Devices Grown by Interdiffusion of Solution-Processed Precursor Stacking Layers, Energy Environ. Sci. 7 (2014) 2619–2623.

[131] C.-G. Wu, C.-H. Chiang, Z.-L. Tseng, Planar Heterojunction Perovskite/$PC_{71}BM$ Solar Cells with enhanced open-circuit voltage via (2/1)-step Spin-coating Process, J. Mater. Chem. A. 2 (2014) 15897–15903.

[132] F. Hao, C.C. Stoumpos, Z. Liu, R.P.H. Chang, M.G. Kanatzidis, Controllable Perovskite Crystallization at a Gas-Solid Interface for Hole Conductor-Free Solar Cells with Steady Power Conversion Efficiency over 10%, J. Am. Chem. Soc. 136 (2014) 16411–16419.

[133] S. Colella, E. Mosconi, P. Fedeli, A. Listorti, F. Gazza, F. Orlandi, et al., $MAPbI_{3-x}Cl_x$ Mixed Halide Perovskite for Hybrid Solar Cells : The Role of Chloride as Dopant on the Transport and Structural Properties, Chem. Mater. 25 (2013) 4613–4618.

[134] P. Docampo, F. Hanusch, S.D. Stranks, M. Döblinger, J.M. Feckl, M. Ehrensperger, et al., Solution Deposition-Conversion for Planar Heterojunction Mixed Halide Perovskite Solar Cells, Adv. Energy Mater. 4 (2014) 1400355.

[135] A.E. Williams, P.J. Holliman, M.J. Carnie, M.L. Davies, D.A. Worsley, T.M. Watson, Perovskite Processing for Photovoltaics: a Spectro-Thermal Evaluation, J. Mater. Chem. A. 2 (2014) 19338–19346.

[136] S. Colella, E. Mosconi, G. Pellegrino, A. Alberti, V.L.P. Guerra, S. Masi, et al., The Elusive Presence of Chloride in Mixed Halide Perovskite Solar Cells, J. Phys. Chem. Lett. 5 (2014) 3532–3538.

[137] H. Yu, F. Wang, F. Xie, W. Li, J. Chen, N. Zhao, The Role of Chlorine in the Formation Process of "$CH_3NH_3PbI_{3-x}Cl_x$" Perovskite, Adv. Funct. Mater. 24 (2014)

7102–7108.

[138] M.I. Dar, N. Arora, P. Gao, S. Ahmad, M. Grätzel, M.K. Nazeeruddin, Investigation Regarding the Role of Chloride in Organic-Inorganic Halide Perovskites Obtained from Chloride Containing Precursors, Nano Lett. 14 (2014) 6991–6996.

[139] A. Dualeh, P. Gao, S. Il Seok, M.K. Nazeeruddin, M. Grätzel, Thermal Behavior of Methylammonium Lead-trihalide Perovskite Photovoltaic Light Harvesters, Chem. Mater. 26 (2014) 6160–6164.

[140] S.T. Williams, F. Zuo, C.-C. Chueh, C.-Y. Liao, P.-W. Liang, A.K.-Y. Jen, Role of chloride in the morphological evolution of organo-lead halide perovskite thin films, ACS Nano. 8 (2014) 10640–10654.

[141] Y. Tidhar, E. Edri, H. Weissman, D. Zohar, G. Hodes, D. Cahen, et al., Crystallization of methyl ammonium lead halide perovskites: implications for photovoltaic applications., J. Am. Chem. Soc. 136 (2014) 13249–13256.

[142] G. Grancini, S. Marras, M. Prato, C. Giannini, C. Quarti, F. De Angelis, et al., The Impact of the Crystallization Processes on the Structural and Optical Properties of Hybrid Perovskite Films for Photovoltaics, J. Phys. Chem. Lett. 5 (2014) 3836–3842.

[143] W. Zhang, M. Saliba, D.T. Moore, S. Pathak, M. Horantner, T. Stergiopoulos, et al., Ultra-smooth organic-inorganic perovskite thin-film formation and crystallization for Efficient Planar Heterojunction Solar Cells, Nat. Commun. 6 (2015) 6142.

[144] N. Yantara, Y. Fang, S. Chen, H.A. Dewi, P.P. Boix, S.G. Mhaisalkar, et al., Unravelling the Effects of Cl Addition in Single Step $CH_3NH_3PbI_3$ Perovskite Solar Cells, Chem. Mater. 27 (2015) 2309–2314.

[145] E.L. Unger, A.R. Bowring, C.J. Tassone, V.L. Pool, A. Gold-parker, R. Cheacharoen, et al., Chloride in Lead Chloride-Derived Organo-Metal Halides for Perovskite-Absorber Solar Cells, Chem. Mater. 26 (2014) 7158–7165.

[146] L.Q. Zhang, X.W. Zhang, Z.G. Yin, Q. Jiang, X. Liu, J.H. Meng, et al., Highly efficient and stable planar heterojunction perovskite solar cells via a low temperature solution process, J. Mater. Chem. A. 3 (2015) 12133–12138.

[147] H.J. Snaith, A. Abate, J.M. Ball, G.E. Eperon, T. Leijtens, N. Kimberly, et al.,

Anomalous Hysteresis in Perovskite Solar Cells, J. Phys. Chem. Lett. 5 (2014) 1511–1515.

[148] A. Dualeh, T. Moehl, N. Tetreult, J. Teuscher, P. Gao, M.K. Nazeeruddin, et al., Impednce Spectroscopic Analysis of Lead Iodide Perovskite-Sensitized Solid-State Solar Cells, ACS Nano. 8 (2014) 362–373.

[149] H. Kim, N. Park, Parameters Affecting I–V Hysteresis of $CH_3NH_3PbI_3$ Perovskite Solar Cells: Effects of Perovskite Crystal Size and Mesoporous TiO2 Layer, J. Phys. Chem. Lett. 5 (2014) 2927–2934.

[150] Y. Shao, Z. Xiao, C. Bi, Y. Yuan, J. Huang, Origin and elimination of photocurrent hysteresis by fullerene passivation in $CH_3NH_3PbI_3$ planar heterojunction solar cells, Nat. Commun. 5 (2014) 5784.

[151] B. Wu, K. Fu, N. Yantara, G. Xing, S. Sun, T.C. Sum, et al., Charge Accumulation and Hysteresis in Perovskite-Based Solar Cells: An Electro-Optical Analysis, Adv. Energy Mater. 5 (2015) 1500829.

[152] R.S. Sanchez, V. Gonzalez-Pedro, J.-W. Lee, N.-G. Park, Y.S. Kang, I. Mora-Sero, et al., Slow Dynamic Processes in Lead Halide Perovskite Solar Cells. Characteristic Times and Hysteresis, J. Phys. Chem. Lett. 5 (2014) 2357–2363.

[153] R. Gottesman, E. Haltzi, L. Gouda, S. Tirosh, Y. Bouhadana, A. Zaban, et al., Extremely Slow Photoconductivity Response of $CH_3NH_3PbI_3$ Perovskites Suggesting Structural Changes under Working Conditions, J. Phys. Chem. Lett. 5 (2014) 2662–2669.

[154] C. Eames, J.M. Frost, P.R.F. Barnes, B.C. O'Regan, A. Walsh, M.S. Islam, Ionic transport in hybrid lead iodide perovskite solar cells, Nat. Commun. 6 (2015) 7497.

[155] W. Tress, N. Marinova, T. Moehl, S.M. Zakeeruddin, M.K. Nazeeruddin, M. Graetzel, Understanding the rate-dependent J–V hysteresis, slow time component, and aging in $CH_3NH_3PbI_3$ perovskite solar cells: the role of a compensated electric field, Energy Environ. Sci. 8 (2015) 995–1004.

[156] Y. Zhao, C. Liang, H.M. Zhang, D. Li, D. Tian, G. Li, et al., Anomalously large interface charge in polarity-switchable photovoltaic devices: an indication of mobile ions in organic-inorganic halide perovskites, Energy Environ. Sci. 8 (2015) 1256–1260.

[157] H.M. Zhang, C. Liang, Y. Zhao, M. Sun, H. Liu, J. Liang, et al., Dynamic interface charge governing the current-voltage hysteresis in perovskite solar cells, Phys. Chem. Chem. Phys. 17 (2015) 9613–9618.

[158] T.-Y. Yang, G. Gregori, N. Pellet, M. Grätzel, J. Maier, The Significance of Ion Conduction in a Hybrid Organic-Inorganic Lead-Iodide-Based Perovskite Photosensitizer, Angew. Chemie Int. Ed. 54 (2015) 7905–7910.

[159] L.K. Ono, S.R. Raga, S. Wang, Y. Kato, Y. Qi, Temperature-dependent hysteresis effects on perovskite-based solar cells, J. Mater. Chem. A. 3 (2015) 9074–9080.

[160] X. Li, X. Wang, W. Zhang, Y. Wu, F. Gao, J. Fang, The effect of external electric field on the performance of perovskite solar cells, Org. Electron. 18 (2015) 1–6.

[161] Z. Xiao, Y. Yuan, Y. Shao, Q. Wang, Q. Dong, C. Bi, et al., Giant switchable photovoltaic effect in organometal trihalide perovskite devices, Nat. Mater. (2014) 1–6.

[162] E.L. Unger, E.T. Hoke, C.D. Bailie, W.H. Nguyen, A.R. Bowring, T. Heumuller, et al., Hysteresis and transient behavior in current-voltage measurements of hybrid-perovskite absorber solar cells, Energy Environ. Sci. (2014) 3690–3698.

[163] G. Flora, D. Gupta, A. Tiwari, Toxicity of lead: A review with recent updates., Interdiscip. Toxicol. 5 (2012) 47–58.

[164] B. Hailegnaw, S. Kirmayer, E. Edri, G. Hodes, D. Cahen, Rain on Methyl-Ammonium-Lead-Iodide Based Perovskites: Possible Environmental Effects of Perovskite Solar Cells, J. Phys. Chem. Lett. 6 (2015) 1543–1547.

[165] P.-Y. Chen, J. Qi, M.T. Klug, X. Dang, P.T. Hammond, A. Belcher, Environmentally-responsible fabrication of efficient perovskite solar cells from recycled car batteries, Energy Environ. Sci. 7 (2014) 3659–3665.

[166] F. Hao, C.C. Stoumpos, D.H. Cao, R.P.H. Chang, M.G. Kanatzidis, Lead-free solid-state organic–inorganic halide perovskite solar cells, Nat. Photonics. 8 (2014) 489–494.

[167] N.K. Noel, S.D. Strnaks, E. Al, Lead-Free Organic-Inorganic Tin Halide Perovskites for Photovoltaic Applications, Energy Environ. Sci. (2014).

[168] S. Choi, W.J. Potscavage, B. Kippelen, Area-scaling of organic solar cells, J. Appl. Phys. 106 (2009) 054507.

[169] G. Haacke, New figure of merit for transparent conductors, J. Appl. Phys. 47

(1976) 4086.

[170] A.C. Tolcin, U.S. Geological Survey, 2010 Minerals Yearbook: Indium, 2010.

[171] A. Chipman, A commodity no more, Nature. 449 (2007) 131.

[172] N. Espinosa, R. García-Valverde, A. Urbina, F.C. Krebs, A life cycle analysis of polymer solar cell modules prepared using roll-to-roll methods under ambient conditions, Sol. Energy Mater. Sol. Cells. 95 (2011) 1293–1302.

[173] C.J.M. Emmott, A. Urbina, J. Nelson, Environmental and economic assessment of ITO-free electrodes for organic solar cells, Sol. Energy Mater. Sol. Cells. 97 (2012) 14–21.

[174] R. Paetzold, K. Heuser, D. Henseler, S. Roeger, G. Wittmann, A. Winnacker, Performance of flexible polymeric light-emitting diodes under bending conditions, Appl. Phys. Lett. 82 (2003) 3342.

[175] D.R. Cairns, R.P. Witte, D.K. Sparacin, S.M. Sachsman, D.C. Paine, G.P. Crawford, et al., Strain-dependent electrical resistance of tin-doped indium oxide on polymer substrates, Appl. Phys. Lett. 76 (2000) 1425.

[176] E. Terzini, G. Nobile, T. Polichetti, P. Thilakan, Development and Application of Low Temperature RF Magnetron Sputtered ITO Thin Films for a-Si:H based p/i/n Junction Solar Cells, in: Proc. 26th IEEE Photovoltaics Spec. Conf., 1997: pp. 667–670.

[177] J.A. Thornton, High Rate Thick Film Growth, Ann. Rev. Mater. Sci. 7 (1977) 239–260.

[178] R. Bel Hadj Tahar, T. Ban, Y. Ohya, Y. Takahashi, Tin doped indium oxide thin films: Electrical properties, J. Appl. Phys. 83 (1998) 2631.

[179] Y. Wang, M. Wu, X. Lin, Z. Shi, A. Hagfeldt, T. Ma, Several highly efficient catalysts for Pt-free and FTO-free counter electrodes of dye-sensitized solar cells, J. Mater. Chem. 22 (2012) 4009.

[180] X. Huang, S. Huang, Q. Zhang, X. Guo, D. Li, Y. Luo, et al., A flexible photoelectrode for CdS/CdSe quantum dot-sensitized solar cells (QDSSCs), Chem. Commun. 47 (2011) 2664–2666.

[181] L. Zhang, H.K. Mulmudi, S.K. Batabyal, Y.M. Lam, S.G. Mhaisalkar, Metal/metal sulfide functionalized single-walled carbon nanotubes: FTO-free counter electrodes for dye sensitized solar cells, Phys. Chem. Chem. Phys. 14 (2012)

9906.

[182] S.-G. Ihn, K.-S. Shin, M.-J. Jin, X. Bulliard, S. Yun, Y. Suk Choi, et al., ITO-free inverted polymer solar cells using a GZO cathode modified by ZnO, Sol. Energy Mater. Sol. Cells. 95 (2011) 1610–1614.

[183] N. Formica, D.S. Ghosh, A. Martinez-Otero, T.L. Chen, J. Martorell, V. Pruneri, Ultrathin oxidized Ti to increase stability and smoothness of Al doped ZnO transparent conductors for high efficiency indium-free polymer solar cells, Appl. Phys. Lett. 103 (2013) 183304.

[184] H. Hagendorfer, K. Lienau, S. Nishiwaki, C.M. Fella, L. Kranz, A.R. Uhl, et al., Highly Transparent and Conductive ZnO: Al Thin Films from a Low Temperature Aqueous Solution Approach, Adv. Mater. 26 (2013) 632–636.

[185] C. Peng, M.M. Hamasha, D. Vanhart, S. Lu, C.R. Westgate, Electrical and Optical Degradation Studies on AZO Thin Films Under Cyclic Bending Conditions, IEEE Trans. Device Mater. Reliab. 13 (2013) 236–244.

[186] W. Zhang, High-Efficiency ITO-Free Polymer Solar Cells Using Highly Conductive PEDOT:PSS/Surfactant Bilayer Transparent Anodes, Energy Environ. Sci. 6 (2013) 1956–1964.

[187] Y. Galagan, B. Zimmermann, E.W.C. Coenen, M. Jørgensen, D.M. Tanenbaum, F.C. Krebs, et al., Current Collecting Grids for ITO-Free Solar Cells, Adv. Energy Mater. 2 (2012) 103–110.

[188] S.I. Na, J.S. Lee, Y.J. Noh, T.W. Kim, S.S. Kim, H.I. Joh, et al., Efficient ITO-free polymer solar cells with pitch-converted carbon nanosheets as novel solution-processable transparent electrodes, Sol. Energy Mater. Sol. Cells. 115 (2013) 1–6.

[189] K.H. Choi, J. Kim, Y.J. Noh, S.I. Na, H.K. Kim, Ag nanowire-embedded ITO films as a near-infrared transparent and flexible anode for flexible organic solar cells, Sol. Energy Mater. Sol. Cells. 110 (2013) 147–153.

[190] J.H. Lee, H.S. Shin, Y.J. Noh, S.I. Na, H.K. Kim, Brush painting of transparent PEDOT/Ag nanowire/PEDOT multilayer electrodes for flexible organic solar cells, Sol. Energy Mater. Sol. Cells. 114 (2013) 15–23.

[191] J.W. Lim, D.Y. Cho, S.I. Na, H.K. Kim, Simple brush-painting of flexible and transparent Ag nanowire network electrodes as an alternative ITO anode for

cost-efficient flexible organic solar cells, Sol. Energy Mater. Sol. Cells. 107 (2012) 348–354.

[192] S.H. Choa, C.K. Cho, W.J. Hwang, K. Tae Eun, H.K. Kim, Mechanical integrity of flexible InZnO/Ag/InZnO multilayer electrodes grown by continuous roll-to-roll sputtering, Sol. Energy Mater. Sol. Cells. 95 (2011) 3442–3449.

Chapter 3: Experimental Methods

3.1 Introduction

This chapter introduces the various experimental methods used throughout this thesis. In **Section 3.2** the techniques used in the fabrication of thin-film samples and solar cells are detailed. **Section 3.3** describes the methods used in the characterisation of thin-film samples whilst **Section 3.4** details the characterisation of completed photovoltaic devices. **Section 3.5** is devoted to discussion of the X-ray scattering techniques used heavily in **Chapter 6**. Finally, in **Section 3.6** details are presented of the optical model which is used in **Chapter 4**.

3.2 Fabrication Techniques

3.2.1 Materials Synthesis and Solution Preparation

Organic Solar Cell Preparation

Organic solar cells based on a PCDTBT:PCBM bulk heterojunction have been fabricated in **Chapter 4** of this work. PCDTBT (chlorobenzene fraction, M_w = 38800), $PC_{60}BM$ (99%) and $PC_{70}BM$ (99%) were purchased from Ossila Ltd. Polymer solutions were prepared by adding dry PCDTBT to chlorobenzene and stirring the resulting solution for 24 hours at 70°C. This solution was then added to $PC_{70}BM$ to produce a 1:4 blend of PCDTBT:$PC_{70}BM$ at a concentration of 20 mg/ml, before being stirred for a further 24 hours at 70°C. The solution was cooled to room temperature and filtered with a 0.45 μm PTFE filter before use.

Perovskite Solar Cell Preparation

Perovskite solar cells have been fabricated in **Chapter 5** and **Chapter 6** of this thesis. Perovskite solutions were prepared by dissolving lead chloride ($PbCl_2$) and methylammonium iodide (MAI) in the solvent dimethylformamide (DMF) at a 1:3 ($PbCl_2$:MAI) molar ratio. Solution concentrations for spray-coating are discussed in the

main text where relevant, for spin-coating a solution concentration of 629 mg/ml (40 wt%) was used. Solutions were stirred overnight at 70°C, cooled to room temperature and filtered with a 0.45 μm PTFE filter before use. PCBM solutions for deposition of the electron transport layer in perovskite devices were made by dissolving PCBM in chlorobenzene at 50 mg/ml. Both $PC_{60}BM$ and $PC_{70}BM$ have been used; the exact fullerene used is stated in the relevant text. Solutions were stirred overnight at 70°C, cooled to room temperature and filtered with a 0.45 μm PTFE filter before use.

In **Chapter 5**, $PbCl_2$ (98%) was purchased from Sigma whilst MAI was synthesised as described in the literature [1]. Briefly, methylamine (CH_3NH_2, 33 wt% solution in ethanol) was reacted under constant stirring with stabilized hydroiodic acid (57 wt% in water) in ethanol at room temperature. Quantities used were in the proportions of 2.4 mL methylamine solution to 1 mL hydroiodic acid solution to 10 mL ethanol. Crystallization of MAI was achieved by evaporation to produce a white coloured powder which was subsequently dried for 24 hours in a vacuum oven at 60°C. For the work in **Chapter 6**, perovskite precursor solutions were provided by Ossila Ltd. Blend details are the same as provided above. The MAI used in the preparation of these solutions has been synthesised using a slightly adjusted method: the reaction was performed in an ice bath to avoid HI decomposition, crystallization was achieved using a rotary evaporator and the resulting powder was then dissolved in ethanol and recrystallized using diethyl ether in order to enhance material purity.

All materials were stored in a nitrogen glovebox in order to avoid moisture absorption and degradation. Solids were stored in opaque containers whilst solutions and solvents were stored in amber vials.

3.2.2 Device Fabrication Procedure

Glass substrates with pre-patterned ITO were purchased from Ossila Ltd; where an electrode has been fabricated 'in house' (**Chapter 4**) a blank glass substrate of the same thickness (1.1mm) has been used. All substrates had dimensions 20 mm x 15 mm and once completed into devices incorporate 6 individual regions in which both the front and rear electrodes overlap (see **Figure 3.1(d)**). These regions are termed devices (or pixels) and each have an area of 0.04 cm^2, although during testing the exposed area is reduced to 0.025 cm^2 by use of an aperture mask (see **Section 3.4.1**). Before use all substrates were cleaned via sequential sonication for 5 minutes each

time in warm (60-70°C) Helmanex solution, isopropyl alcohol and deionised (DI) water. After each step the substrates were rinsed with hot DI water. Finally substrates were dried with compressed nitrogen.

Where PEDOT:PSS has been used as a hole transport material it was filtered using a 0.45 μm PVDF filter and deposited via spin-coating at 5000rpm in air, producing a layer approximately 30 nm thick as measured by surface profilometry. Immediately following film deposition, substrates were annealed at 130°C for 30 minutes in order to remove residual moisture. Where MoO_3 has been employed as a hole transport material it was deposited by evaporation at a rate of 0.3 $Å s^{-1}$ (see **Section 3.2.5**).

Following deposition of the hole transport material, the photoactive layer was deposited (**Figure 3.1(c)**). In **Chapter 4** the photoactive layer has been deposited via spin-coating of the polymer:fullerene blend solution. Details of perovskite film fabrication are discussed in **Chapter 5**. For perovskite solar cells, following deposition of the perovskite film an electron transport layer of PCBM is deposited via spin-coating of a PCBM solution.

Once fabrication of the above layers was completed the rear electrode was deposited by thermal evaporation through a shadow mask. Devices were then sealed by affixing a glass cover slip to the device using an epoxy which is cured under a UV lamp for 30 minutes. All device testing was then undertaken in air.

It should be noted that in **Chapter 4** all organic solar cell fabrication after substrate cleaning was performed in a nitrogen glovebox. In **Chapter 5** and **Chapter 6** all perovskite films were fabricated in air whilst PCBM deposition occurred in a nitrogen glovebox.

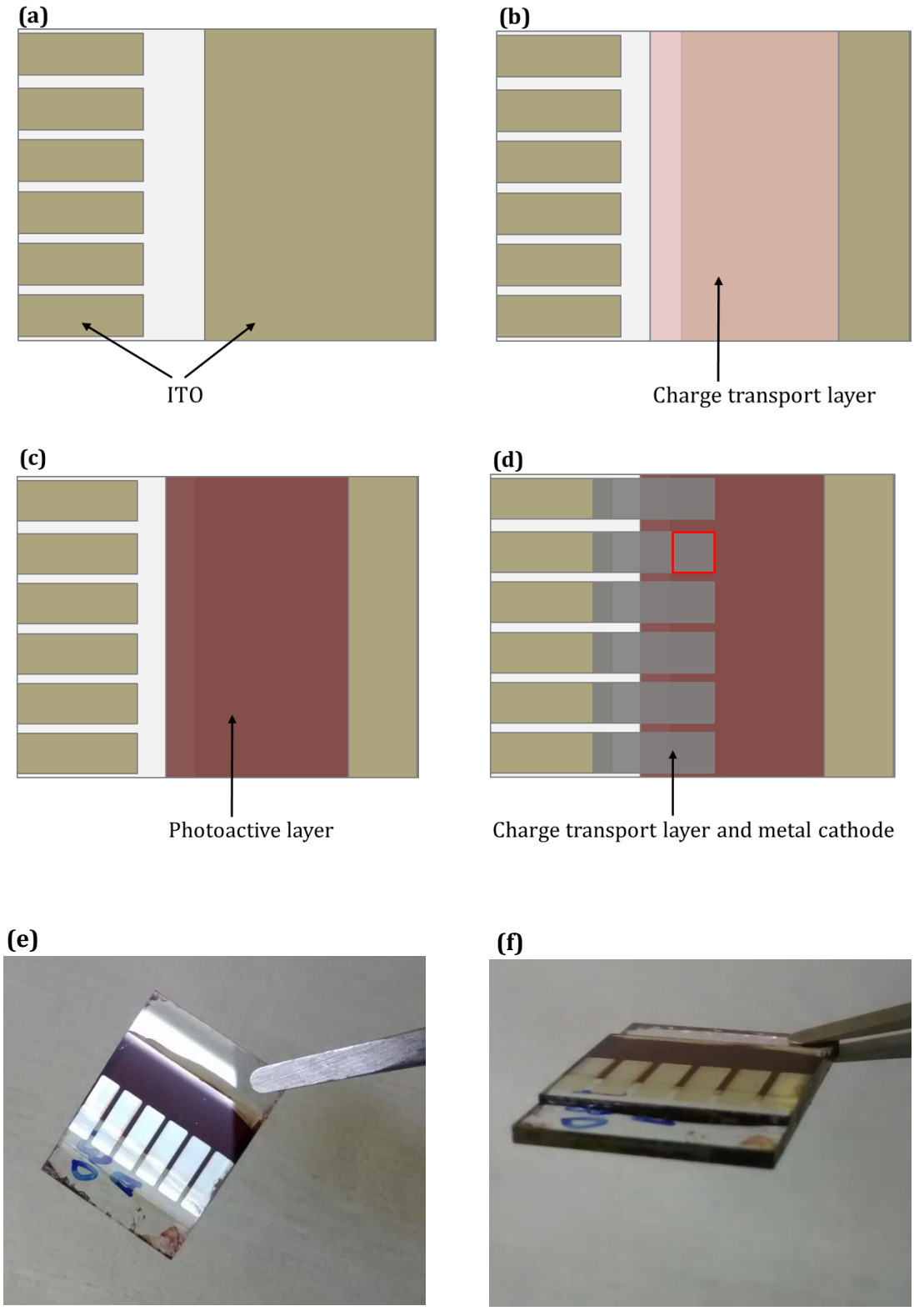

Figure 3.1 An illustration of solar cell device geometry, showing the sequential steps in device fabrication (**(a)** to **(d)**). The red square in **(d)** shows one of the six devices on the substrate. Parts **(e)** and **(f)** show photographs of a finished perovskite solar cell.

3.2.3 Spin-Coating

Spin-coating is currently the standard laboratory technique for deposition of thin films from solution, due to high repeatability and excellent film uniformity as well as the simplicity of the process. The film materials (or suitable precursors) are dissolved in an appropriate solvent and the resulting solution is dispensed onto the substrate whilst it rotates, typically at speed of around 500-5000rpm.* The rotation of the substrate throws off a large quantity of the solution, with that remaining drying via evaporation, typically over a period of 5-30s, to form a film whose thickness t is determined chiefly by solution concentration (c), viscosity (η) and the speed of substrate rotation (ω) according to the relation

$$t \propto \frac{c\eta}{\sqrt{\omega}} \qquad \{3.1\}$$

Film thickness can thus be tuned both through solution concentration (within solubility limits) and spin speed. Whilst spin-coating is an excellent tool in a research setting, the low material utilisation and inherently batch-to-batch nature of the process mean that it is important to consider alternative film deposition techniques when looking towards the industrialisation and commercialisation of solution processed solar cells.

3.2.4 Ultrasonic Spray-Coating

Spray-coating is a solution deposition method which is far more suitable than spin-coating for industrial scale thin-film fabrication. Of particular appeal is its compatibility with roll-to-roll production techniques, which could allow for significant reductions in production costs. Unlike sputtering or evaporation, no energy intensive and costly high-vacuum is required. In addition, the solutions used in spray-coating are typically of a much lower concentration (around 5 times lower in many cases [2,3]) than those required for spin-coating which can be advantageous for materials with limited solubility.

* This is known as a 'dynamic dispense', it is also possible to use a static dispense, in which the solution is dispensed onto a static substrate, which is then accelerated to the desired rotation speed, however this tends to lead to inferior repeatability in film thickness.

A Prism ultrasonic spray coating system from Ultrasonic Systems Inc. has been used in this work, with a transducer vibrating frequency of 35 kHz. The solution to be deposited is stored in a syringe and transferred to the spray nozzle through a pipe. Piezoelectric transducers have a rapidly switching voltage applied across them, causing them to expand and contract at high frequency. This results in a vibration being transferred to the solution as it flows past the vibrating head, resulting in the atomisation of the liquid as droplets are ejected from the top of the resultant standing wave. These droplets are then directed to the target surface by a nitrogen flow (see **Figure 3.2(b)**). Film thickness is dependent upon both the concentration of the solution and the quantity of solution deposited, which itself can be controlled by the solution flow rate (determined by the nitrogen pressure on the solution reservoir), the height of the spray head and the speed of the spray head.

In comparison to a simple pneumatic nozzle an ultrasonic nozzle produces smaller droplets, typically of the order of tens of microns in diameter, and a smaller spread in droplet size which should allow for improved film uniformity and repeatability. Droplet size is determined by the vibration frequency of the head and the properties of the solution. Ultrasonic spray-coating also decouples droplet size, droplet energy and rate of material deposition, which are interconnected with pressure nozzles. This allows, for example, for a large flow rate without a resulting increase in droplet energy (velocity) which could result in bounce-back and thus an increased likelihood of non-uniformities and poor repeatability. Finally, the nozzle aperture can be wider than for a pressure nozzle, reducing the probability of clogs occurring.

(a)

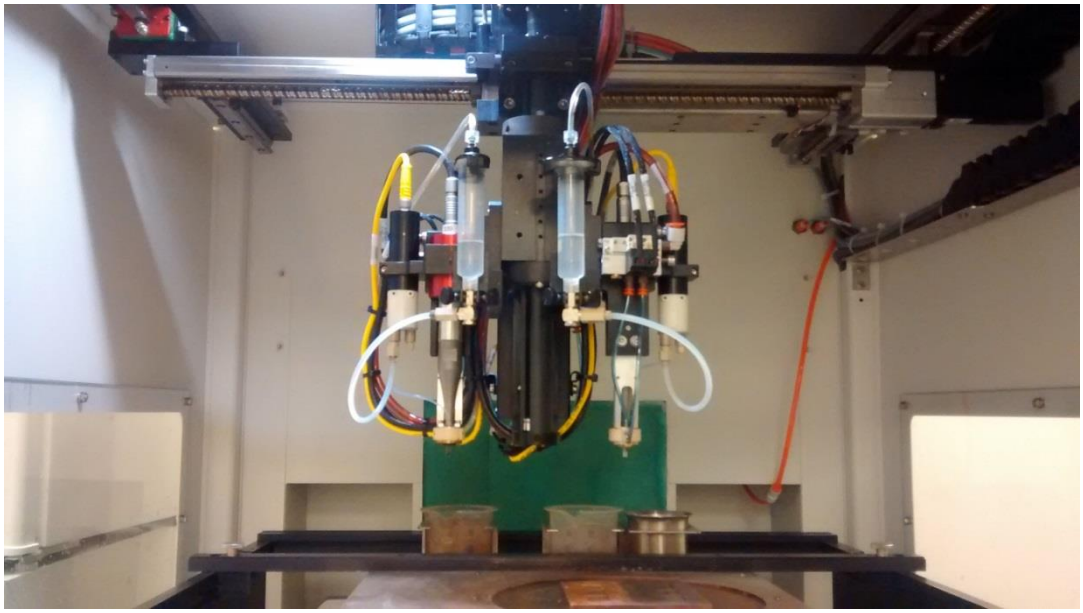

(b)

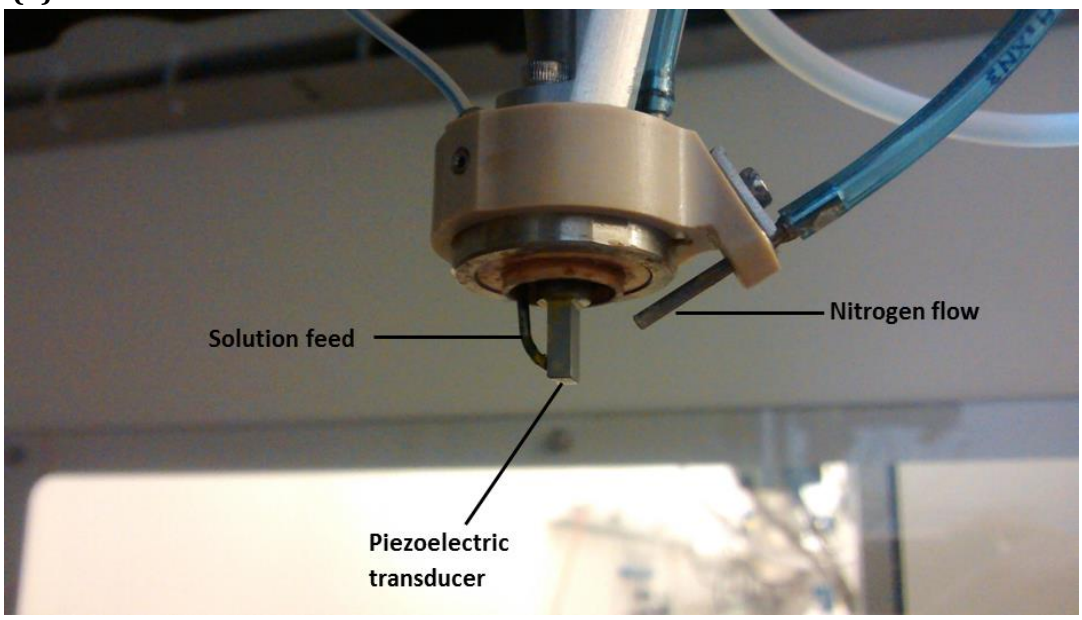

Figure 3.2 A photograph of the ultrasonic spray heads mounted on a gantry which allows movement in all three dimensions, controlled by computer **(a)**, together with a close-up of the spray head **(b)**.

The spray-heads are mounted on a computer controlled gantry which can move in all three dimensions ensuring a repeatable spraying process, as shown in **Figure 3.2(a)**. A hot plate was installed beneath the spray heads, allowing for control of the substrate temperature during the deposition process. This is crucial in order to allow control of the drying rate of the film, which is key in ensuring good film uniformity. Upon

impacting the substrate surface, droplets should ideally coalesce to form a continuous layer of solution which then dries evenly, leaving behind a thin film. If the solution dries too quickly then the individual droplets will not be able to coalesce, whilst if the drying occurs too slowly a number of non-uniform drying effects are likely (see **Figure 3.3**). In this process the wettability of the solvent on the surface is highly important in determining the quality of the resultant film, whilst the boiling point, solubility and viscosity are also important considerations.

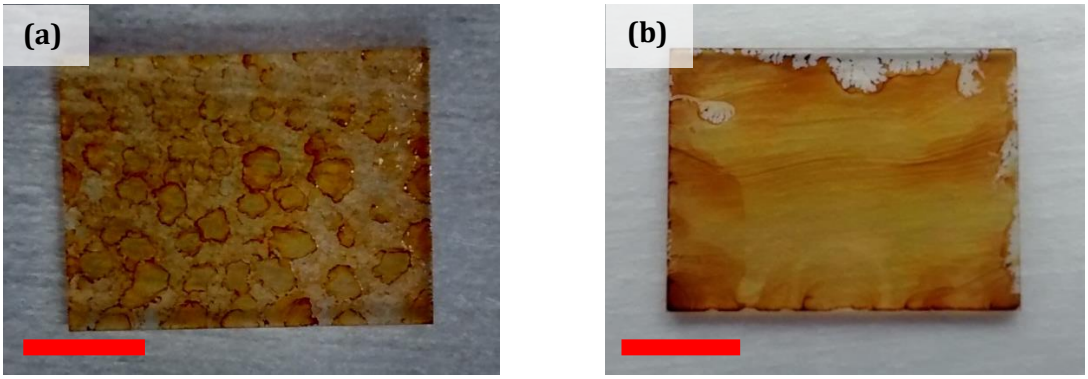

Figure 3.3 Photographs showing films of $PC_{60}BM$ spray-coated from a solution in chlorobenzene. Part **(a)** shows a film which has dried much too rapidly (substrate at 85°C) Part **(b)** shows a film which has dried too slowly (substrate at room temperature). Red scale bars correspond to 5 mm.

3.2.5 Evaporation

In this widely used deposition technique the source material is placed within an appropriate crucible and positioned within a wire heater (usually tungsten). By passing a current through the wire, resistive heating raises the temperature of the material to the desired level where evaporation or sublimation occurs. Evaporations were performed at under vacuum (< 5 x 10^{-5} mbar). For the opaque rear electrode of devices a deposition rate of 0.4 $Ås^{-1}$ was used for calcium deposition and 1.0 $Ås^{-1}$ for aluminium deposition. For layers employed in the multilayer electrodes fabricated in **Chapter 4**, metal oxides were deposited at a rate of 0.3 $Ås^{-1}$ whilst silver was deposited at a rate of 5.0 $Ås^{-1}$ unless otherwise stated.

The thickness of the deposited layer was monitored in-situ by a quartz crystal, excited by an oscillator at just under 6 MHz. As material is deposited onto the crystal the

frequency of oscillation decreases, and this can be used to calculate the mass of material deposited. Through knowledge of the density of the material being evaporated, the thickness of the deposited layer can thus be established. A tooling factor is included in order to allow for the geometrical difference between the location of the crystal sensor and the substrates in the evaporator setup. Calibration of this tooling factor is performed by depositing test films with thickness of a few hundred nanometres and measuring their precise thickness using surface profilometry.

3.3 Film Characterization Techniques

3.3.1 Surface Profilometry

Veeco Dektak profilometers (various models) have been used for measurement of layer thicknesses. Samples were scored with a scalpel and subsequently cleaned with compressed nitrogen in order to remove any loose debris. The stylus of the Dektak was then passed over the sample, crossing over a scratch in the film, allowing a thickness measurement to be taken as shown in **Figure 3.4(a)**. At least 3 readings from separate scratches were taken for each sample and the mean value used. In the case of rough films the height was averaged over a range in position in order to ensure a more accurate reading (see **Figure 3.4(b)**).

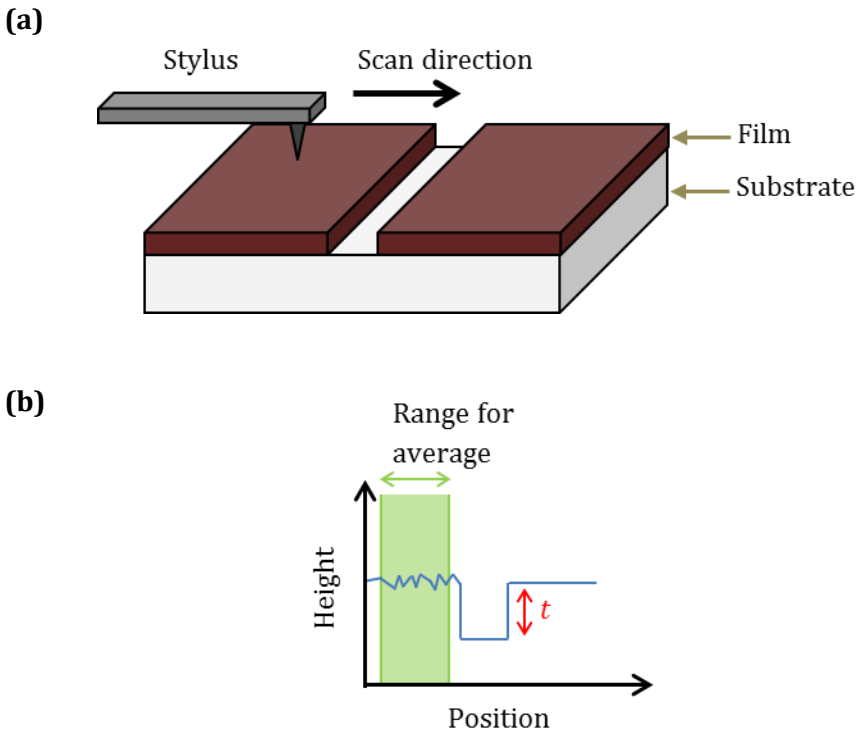

Figure 3.4 A schematic of the profilometry equipment **(a)** and an example scan showing the use of a range in order to ensure a more accurate height reading when measuring rough films **(b)**.

3.3.2 Resistance Measurements

A 4 point probe, developed in conjunction with Ossila Ltd., was used for measurement of the sheet resistance of various samples during the work presented in **Chapter 4**. The probe has linear spring-loaded tips with an equal tip spacing of 1.27 mm and was driven by a Keithley 2602 two channel source-measure unit.

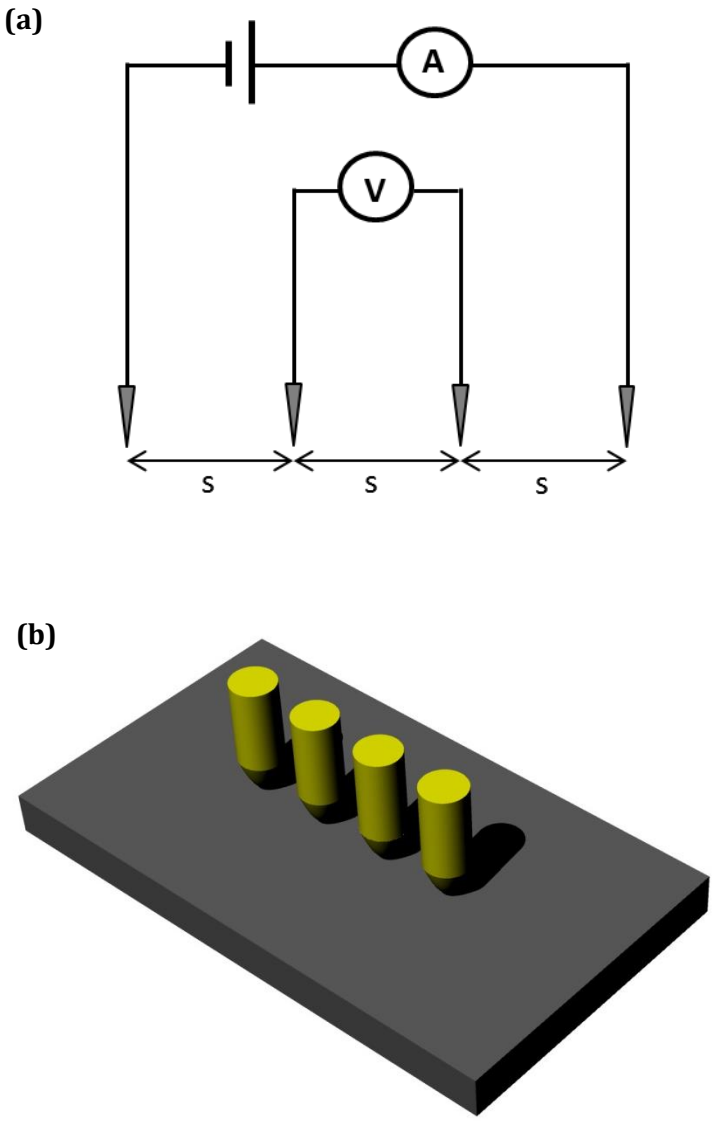

Figure 3.5 Circuit diagram of a 4 point probe **(a)**, and illustration of the arrangement of pins on a sample for a system with a linear arrangement of probes **(b)**.

In a 4 point probe the outer probes deliver a current to the sample whilst the inner probes measure the resulting voltage drop (see **Figure 3.5(a)**). This design greatly reduces inaccuracies in the measurement due to contact resistance, which is defined as the resistance from the contacts between the probes and the sample as well as that due to components such as the leads and so forth. In a 2 point probe set up – in which one pair of probes both delivers current and measures voltage – the full current flows in the probes and thus by V = IR a notable voltage drop will be caused by any contact resistance, and this cannot be distinguished from that caused by the sample itself. In a 4 point probe system a high impedance voltmeter is used with the sensing probes, ensuring that very little current flows in these probes and any voltage drop due to their

contact resistance is thus negligible compared to that across the sample being measured, which has the full applied current flowing through it.

Calculation of resistance using a 4 point probe is achieved as follows. Resistivity (ρ) and resistance (R) are related by

$$\rho = R\frac{A}{l} \qquad \{3.2\}$$

where A is the cross sectional area of the sample through which the current is flowing and l the length along which it flows. Thus differential resistance is

$$dR = \frac{\rho}{A}dl \qquad \{3.3\}$$

In a bulk sample the current travels outwards from the current injecting probe in spheres, thus A is half the surface area of a sphere, $2\pi r^2$. In a thin film sample of thickness t, this current can then be approximated to be travelling in rings giving an area, A, of $2\pi rt$ where t is the thickness of the sample.

We set l = 0 at the tip from which current emanates and integrate between the inner probe tips where the voltage measurement is taken. With a uniform probe spacing of s we find

$$R = \int_s^{2s} \frac{\rho}{2\pi lt}dl = \left[\frac{\rho}{2\pi t}\ln(l)\right]_s^{2s} = \frac{\rho}{2\pi t}\ln(2) \qquad \{3.4\}$$

For a linear four point probe setup as used in this work, due to superposition of current at the outer (current carrying) tips

$$R = \frac{V}{2I} \qquad \{3.5\}$$

thus

$$\rho = \frac{\pi t}{\ln(2)}\left(\frac{V}{I}\right) \qquad \{3.6\}$$

Since sheet resistance ($R_{\square}$) is commonly defined as

$$R_{\square} = \frac{\rho}{t} \qquad \{3.7\}$$

we find that

$$R_{\square} = \frac{\pi}{\ln(2)}\left(\frac{V}{I}\right) \qquad \{3.8\}$$

Whilst the above equation is correction for a semi-infinite and thin sheet, deviation from either of these characteristics requires the use of a correction factor. All samples investigated in this thesis have thickness $t \ll s$, and thus can be treated as a thin film. A correction factor for the finite size of the samples is, however, required and can be looked up in tables from the following references [4,5]. Where the data did not cover the exact geometry fabricated, cubic spline interpolation has been used in order to estimate the correction factor for that geometry.

3.3.3 Hall Effect Measurements

Hall effect measurements have been used in order to measure the carrier mobility of transparent electrodes fabricated in **Chapter 4**. A square 4 point probe set-up is used, with the probes contacting a square sample at its corners. In this system current and voltage are measured between opposite corners (see **Figure 3.6**). A uniform magnetic field is applied perpendicular to the substrate which causes a Lorentz force on moving electrons within the sample. Electrons thus accumulate on one side of the sample and the resulting build-up of charge leads to a potential difference ('Hall voltage') and an electric field which opposes and balances the Lorentz force due to the external magnetic field.

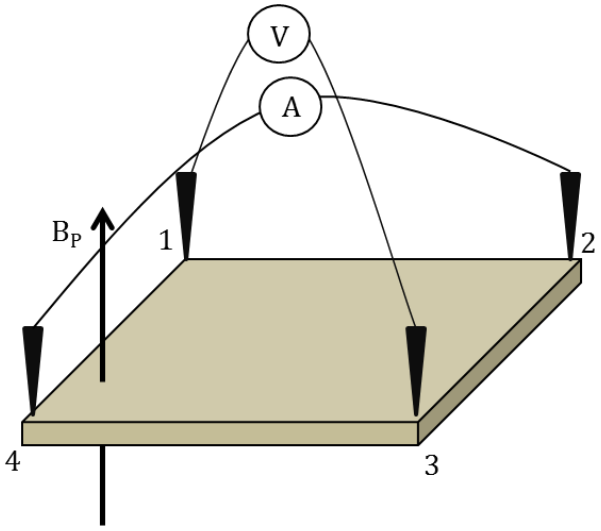

Figure 3.6 An example of one possible contact set-up for Hall effect measurements on a square thin-film sample.

This technique involves the measurement of 8 different voltages. Notation V_{13} denotes voltage measured across corners 1 and 3 whilst current flows from corner 2 to 4; likewise V_{31} denotes the same measurement but with current flowing from corner 4 to 2. The subscripts *P* and *N* refer to the magnetic field pointing in the positive *z* direction (as shown in **Figure 3.6**) or the negative *z* direction respectively. These 8 voltage measurements can be combined as follows

$$V_A = V_{13P} - V_{13N} \quad \{3.9\}$$

$$V_B = V_{31P} - V_{31N} \quad \{3.10\}$$

$$V_C = V_{24P} - V_{24N} \quad \{3.11\}$$

$$V_D = V_{42P} - V_{42N} \quad \{3.12\}$$

It can then be shown that sheet carrier density ($n_{\square}$) with units cm^{-2}, is given by

$$n_{\square} = \frac{8 \times 10^{-8} IB}{e(V_A + V_B + V_C + V_D)} \quad \{3.13\}$$

where I is the applied current and B is the magnetic field strength in Gauss. Carrier mobility, μ, is subsequently calculated by

$$\mu = \frac{1}{q n_{\square} R_{\square}} \quad \{3.14\}$$

Hall effect measurements were carried out by Dr Patrick Isherwood at Loughborough University. An Ecopia HMS 3000 device with a 2 mA current and magnetic field strength of 0.55 T was used in combination with 1 cm x 1 cm electrode samples.

3.3.4 Atomic Force Microscopy

Atomic force microscopy (AFM) is a surface sensitive technique in which a very fine tip (radius of curvature < 10 nm) is mounted on a cantilever and scanned across the surface of the sample. By measuring the reflection of a laser from the back of the cantilever the deflection can be measured; a simple schematic of an AFM is shown in **Figure 3.7**. The main modes of operation of an AFM are 'contact mode', in which the tip stays in contact with the surface and its deflection correlates directly with sample height and 'tapping mode', also known as 'intermittent contact mode'. In this mode the cantilever is oscillated close to its resonant frequency. As the tip is brought close to, and finally in contact with, the surface a repulsive force occurs, decreasing the amplitude of oscillation. A feedback loop can be used to control a piezoelectric actuator in order to maintain a constant amplitude of oscillation, allowing a map of surface topography to be built up. Lateral resolution is typically of the order of a few nm (limited by tip size), whilst vertical resolution is of the order of 0.1nm (limited by thermal and electrical noise) [6].

Within this thesis tapping mode has been used for all samples in order to reduce the probability of damaging soft films. A Veeco Dimension 3100 AFM has been used together with Budget Sensors Tap300-G tips with a resonant frequency of 300kHz and a spring constant of $40 Nm^{-1}$. Data analysis was performed using the Gwyddion software package.

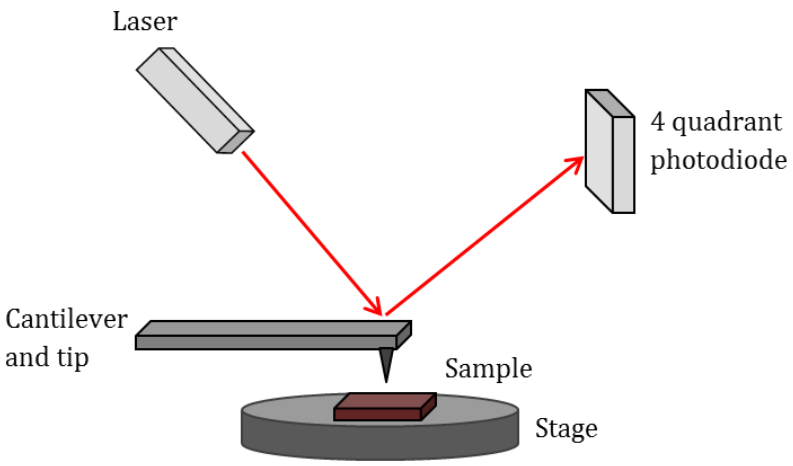

Figure 3.7 Simple schematic of an atomic force microscope

3.3.5 Scanning Electron Microscopy

Scanning electron microscopy (SEM) utilises electrons to probe the sample surface in order to facilitate imaging at higher resolution than is possible with optical microscopy. From the well-known equation

$$E = \frac{hc}{\lambda} \qquad \{3.15\}$$

it is clear that a higher energy probe will have a shorter wavelength. Since resolution is limited to around half the wavelength of the probe, it is possible to obtain much higher resolution with electron microscopy than optical microscopy. In addition, SEMs provide a more '3D' image than optical microscopes due to a larger depth of focus arising from a lower aperture angle.

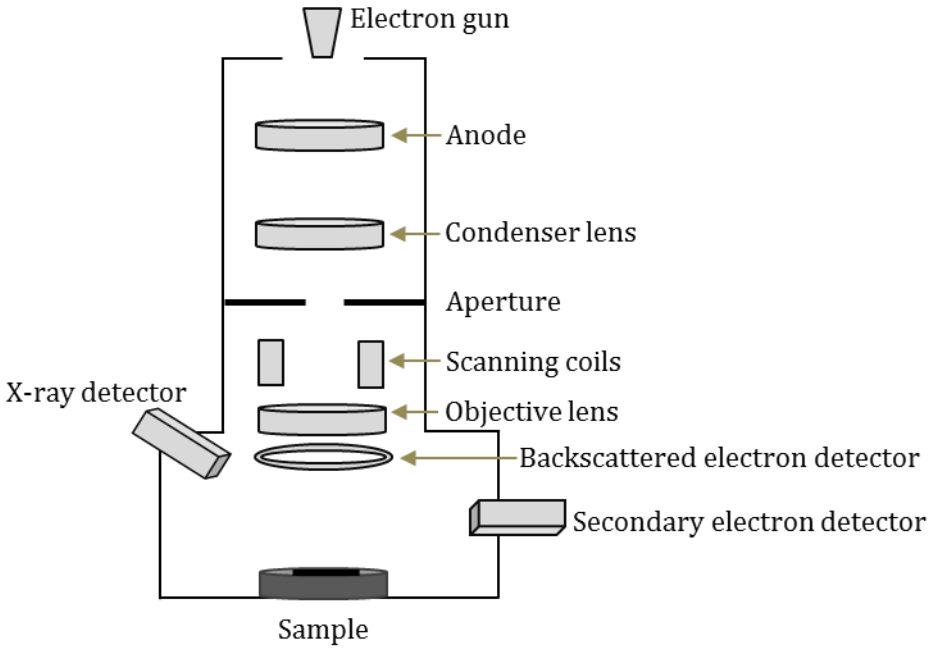

Figure 3.8 A basic schematic of a scanning electron microscope.

A simple schematic for an SEM is shown in **Figure 3.8**. The electron gun, optics and sample chamber are held under vacuum in order to avoid interactions between the electron beam and the air, which would reduce image quality and could cause sample damage. The generation of the electron beam in an SEM is by either a thermionic emission gun (heating a filament to release electrons) or field emission gun (using a strong electric field to extract electrons from a tungsten crystal). A field emission gun SEM (FEGSEM or FESEM) provides better resolution than its thermionic counterpart due to producing a narrower beam of electrons with a smaller spread in energy. In this work both thermionic and field emission gun SEMs have been used. Emitted electrons travel in a helical path down the microscope column under the influence of magnetic fields from the electromagnetic lenses. The condenser lens(es) and aperture(s) act in tandem to control the spot size of the beam on the sample. A reduced spot size will increase resolution but reduce the clarity of the image and result in 'graininess' as fewer electrons impinge on the sample. Scanning coils are used to raster the electron beam across the sample in order to build up an image, whilst the objective lens focuses the electron beam onto the sample. A higher accelerating voltage decreases the diameter of electron probe, thus improving resolution. It also, however, reduces the clarity of surface structures, since the penetration of the beam into the sample is increased. In addition charging is increased along with any sample damage which may occur.

When the electron beam strikes the sample it will cause both electrons and X-rays to be ejected from the material. The ejected electrons are typically divided into two types – secondary and backscattered, with imaging generally achieved using the secondary electrons (SEs). These have a shallow generation region (~10 nm) since those generated deeper in the sample will be unable to escape due to their fairly low energy (~50 eV or less). Secondary electron detectors have a scintillator (fluorescent material) over which a voltage is applied. In front of the detector there is also a collector, across which a high voltage is applied in order to attract the secondary electrons released from the sample. These will impact on the scintillator and generate light which is passed through a photomultiplier before being converted to an electrical signal. When the electron beam impinges on the sample at an angle, more secondary electrons are produced than when it is normal to the surface, meaning that SE images appear particularly topographical. Backscattered electrons have a higher energy than secondary electrons, having a range of energies up to that of the incident beam. Their increased energy means that they are less affected by charging and specimen contamination than SEs, and that their generation region is significantly larger. Whilst this reduces resolution, it does allow for detection of electrons from deeper into the sample. Backscattered electron intensity is dependent on atomic number, and thus backscattered images can provide a composition contrast as well as a topographic one.

It is important that the sample under examination is suitably conductive, or coated and stuck to the sample stub with a conductive material in order to avoid charging. This occurs when electrons from the probe beam build up on the specimen, interfering with secondary electron emission and thus adversely affects image quality and resolution.

In **Chapter 4** an FEI Nova NanoSEM 450 FESEM has been used with a 3 kV primary beam and a backscatter detector; data was acquired by Mr Rob Masters. In **Chapter 5** a JEOL JSM6010LA SEM (thermionic emission gun) has been used with a beam energy of 4 kV and a secondary electron detector; data was acquired by the author. In **Chapter 6** an FEI Inspect F50 FESEM has been used with 5 kV beam energy and a secondary electron detector; data was acquired by the author.

3.3.6 UV-Vis Spectrometry

Transmittance measurements for the electrodes fabricated in **Chapter 4** have been obtained using a Jobin Yvon Horiba Fluoromax-4, a basic schematic of which is shown in **Figure 3.9**. Light from a xenon arc lamp is focused into a Czerny-Turner monochromator, featuring a blazed grating. Rotation of this grating selects the wavelength of light incident upon the second slit, the width of which determines the intensity of light falling upon the sample as well as affecting resolution (a smaller slit size giving higher resolution). The beam is then split, allowing for measurement of both the light intensity after passing through the sample and, as a reference, the light intensity falling upon the sample.

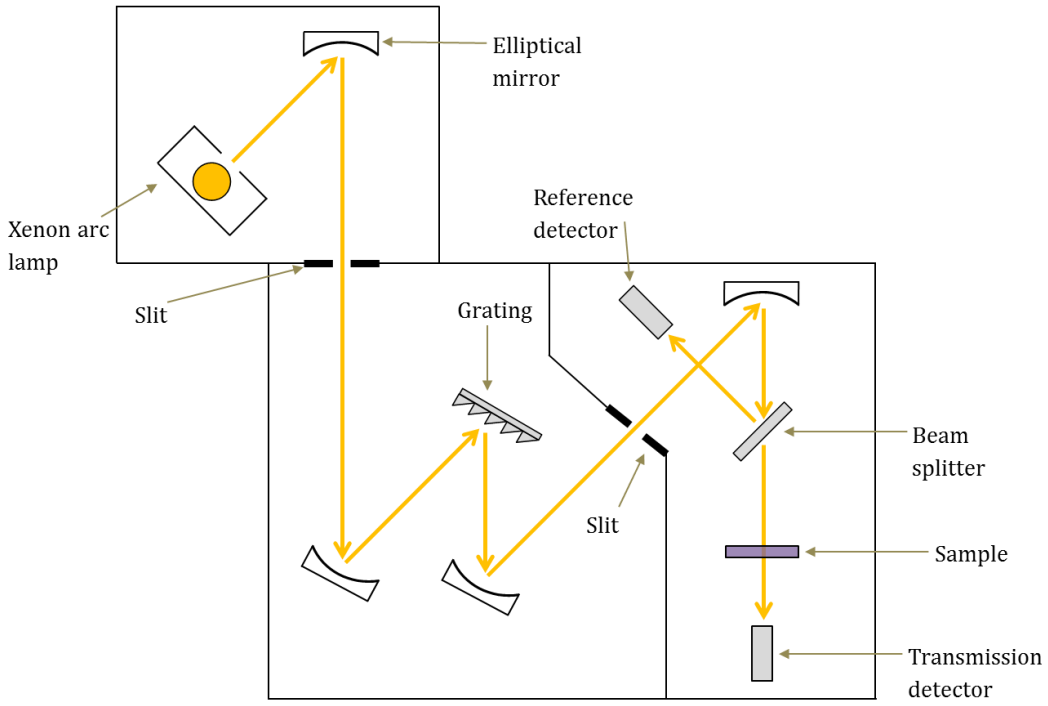

Figure 3.9 A schematic of the spectrometer used in this work.

The transmittance of the sample is calculated using the following equation

$$T_{sample}(\lambda) = \frac{I(\lambda)}{I_0(\lambda)} \qquad \{3.16\}$$

where $I(\lambda)$ is the intensity of light transmitted by the sample, and $I_0(\lambda)$ is the amount of light incident on the sample (as measured by the reference photodiode). Electrode

transmittance spectra have been referenced to either air or a glass slide, allowing the transmittance of the electrodes to be calculated using

$$T(\lambda) = \frac{T_{electrode\ on\ glass}(\lambda)}{T_{reference}(\lambda)} \quad \{3.17\}$$

Transmittance measurements were taken over the range 300-900 nm using a 1 nm step size with a slit width of 4 nm.

3.3.7 Spectroscopic Ellipsometry

Spectroscopic ellipsometry involves measuring changes in the polarisation of light reflected from a sample in order to determine a number of properties of the sample layer. Changes to the light are dependent upon layer thickness and roughness as well as the refractive index (n) and extinction coefficient (k) of the material. Ellipsometry does not measure these parameters directly, but rather extracted data is used to measure the goodness of fit of a model which incorporates these parameters. The optical constants n and k are important inputs to the transfer matrix model discussed in **Section 3.6** and utilised in **Chapter 4**. In this work a Woolam M-2000V ellipsometer with a wavelength range of 370-1000 nm has been used to determine the optical constants of a number of material systems.

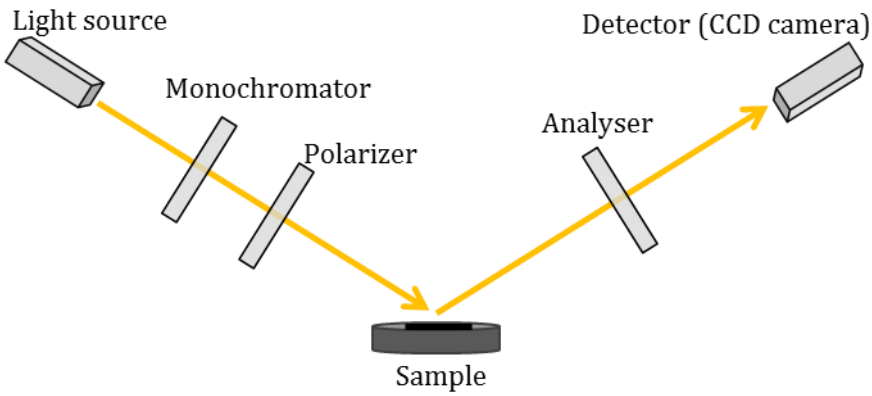

Figure 3.10 Schematic of the key components of a spectroscopic ellipsometer.

A schematic of the key components of a spectroscopic ellipsometer is shown in **Figure 3.10**. Light from a xenon lamp is first passed through a monochromator and a

polarizer. The resulting monochromatic light, linearly polarised with known s- and p-polarised components (light polarised perpendicular to and parallel to the plane of incidence respectively) is then incident upon the sample. Upon reflection the light undergoes both amplitude and phase changes and the reflected light will be elliptically polarised. A rotating polariser ('analyser') is placed in front of a CCD camera, and this set-up is used to measure r_s and r_p, respectively the amplitudes of the s- and p-polarised components of the light after interaction with the sample, normalized to their values before interaction with the sample. This allows for calculation of ψ and Δ, respectively the amplitude ratio and phase difference between the two components upon reflection, via the reflectance ratio (ρ):

$$\rho = \frac{r_s}{r_p} = tan(\psi)e^{i\Delta} \qquad \{3.18\}$$

It is then ψ and Δ that are the outputs from ellipsometry measurements. A model of the sample, incorporating layer thickness, layer roughness and the optical constants of the material is then developed and used to predict ψ and Δ. In order to avoid having to adjust the values of the optical constants at every individual wavelength a dispersion relationship is typically used. A Cauchy model has been used in order to establish layer thickness and roughness. Here the real part of the refractive index (n) is given by

$$n(\lambda) = A + \frac{B}{\lambda^2} + \frac{C}{\lambda^4} \ldots \qquad \{3.19\}$$

where A, B and C are positive constants. Since the model does not consider the extinction coefficient of the material it can only be applied in wavelength ranges where transmittance is high, for example below the band gap of a semiconductor. Once layer thickness and roughness have been established using an appropriate wavelength range these values are used as inputs for a B-spline model [7]. This has then been used to model the refractive index and extinction coefficient of the sample over the full wavelength range of the ellipsometry data. Once a model has been generated the predicted and measured ψ and Δ are then compared, the free parameters in the model are adjusted according to the results of this comparison, new values for ψ and Δ are generated and the process repeats until the mean squared error (MSE) between the measured and modelled values is minimised. It should be noted that care must be taken to ensure that the model is a realistic fit and not the result of a 'local minimum' in

MSE. In this work the software package CompleteVASE has been used for modelling and data processing.

Data acquisition and subsequent modelling for PCDTBT:$PC_{70}BM$ blends was performed by Dr Tao Wang. Data acquisition and modelling for MoO_3 and TeO_2 was undertaken by the author.

3.4 Device Characterization

3.4.1 Current-Voltage Measurements

Photovoltaic performance has been measured using a Newport 92251A-1000 solar simulator producing an AM1.5 spectrum at an intensity of 100 $mWcm^{-2}$, calibrated against an NREL certified reference silicon photovoltaic device. The ITO at the edges of the device substrate was contacted by spring-loaded metal pins in order to make an electrical connection between the test rig and the device under test. The active area of the device is defined using a metal aperture mask with an area of 0.025 cm^2 per device, with the mask defining 6 devicess per substrate as discussed in **Section 3.2.2**. Edge pixels, however, are disregarded from the final results due to the high likelihood of edge effects undermining confidence in their being representative of the rest of the device. In all cases average efficiencies reported are from the best 50% of pixels, thus excluding pixels containing a significant defect whilst avoiding the use of a statistical method that is open to user bias. Separate masks defining only one single pixel have also been used in order to check that there is no 'cross-talk' between pixels. The use of an aperture mask, rather than simply relying on active area being defined by the region in which all layers of the cell overlap, is essential in order to ensure accurate measurement of the device photocurrent [8]. A Keithly 237 source-measure unit was used to sweep voltage from -1 V to 1 V, typically in 0.02 V steps at a scan rate of 0.5 V/s, whilst output current is measured. Device parameters such as FF, J_{SC}, V_{OC} and PCE are then determined from the resulting *JV* curve, as discussed in **Chapter 2**. In some parts of **Chapter 5** and **Chapter 6** alternative parameters have been used for the voltage sweep in order to investigate hysteresis in the current density against voltage characteristics of perovskite solar cells. This is discussed in detail at the appropriate

points within those Chapters. It should be noted that no spectral mismatch correction has been used in this work.

3.4.2 External Quantum Efficiency

External quantum efficiency (EQE) is a measurement of the proportion of incident photons at a given wavelength from which free carriers are successful generated and extracted. Light from a tungsten lamp is passed through a monochromator before being focused onto the target area. An infrared (IR) filter is typically installed between the lamp and the monochromator in order to avoid sample heating. Calibration measurements are undertaken using a silicon photodiode with a known spectral response. Measurements can then be taken for a small area of the device under test at all desired wavelengths.

The system used in this thesis has a start wavelength of 380 nm. Since the monochromator cannot distinguish between, for example, 800 nm light and harmonics of 400 nm light, when a spectrum is required beyond 760 nm a filter must be used. A 600 nm long pass filter was used for this purpose, with the IR filter briefly removed, and two overlapping spectra were taken: 380-700 nm with the IR filter in place and 600-900 nm with the 600 nm long pass filter in place. The overlap region was used to confirm that no significant mismatch between the two spectra was present. The spectra were then stitched in this region using a weighted average which varied linearly across the 100 nm overlap.

The measured EQE spectrum can be used to calculate a J_{SC} value for the device under test using the following equation:

$$J_{SC} = \int (EQE \times photon\ flux \times e)\ d\lambda \qquad \{3.20\}$$

where the photon flux at a given wavelength is calculated from the AM1.5 spectrum and e is the charge of an electron. In the system used here, the AM1.5 spectrum is divided up into 2 nm 'bins' for the purpose of this calculation.

Minor differences between the J_{SC} found from the JV curve of a device and that calculated from its EQE spectrum can be expected since the later uses only a single

wavelength at a time and involves taking measurement at a much lower light intensity, both of which may affect the recombination processes in a device [9].

3.5 X-Ray Scattering Techniques

X-ray scattering experiments are an important tool for the investigation of the structure of crystalline materials. Here, an incident X-ray beam undergoes elastic scattering from atoms in the sample and is diffracted by periodic structures, for example atoms in a crystal lattice. The angle of the scattered (diffracted) beam gives information about the sample crystal structure whilst the intensity of the received signal at each angle provides information about how much of the sampled volume has that periodicity. Grazing incidence wide angle X-ray scattering (GIWAXS) has been used briefly in **Chapter 5** in order to make a comparison of crystal structure between spray-coated and spin-coated perovskite films. Both GIWAXS and its counterpart, grazing incidence small angle X-ray scattering (GISAXS), have been employed extensively in **Chapter 6** where in-situ experiments have been performed in order to monitor perovskite film formation.

3.5.1 Grazing Incidence Wide Angle X-Ray Scattering

Grazing incidence wide angle X-ray scattering (GIWAXS) experiments were performed on the XMaS beamline at the European Synchrotron Radiation Facility (ESRF), Grenoble, France using a 2D Pilatus detector. The beam energy was 10 keV and the incident angle was 0.24°. In-situ experiments were performed in air (relative humidity 40-45%) so as to reproduce, as best as possible, the conditions under which the perovskite solar cells studied elsewhere in this work have been fabricated. Performing the experiments in air rather than helium (as is commonly used) increases X-ray scattering from the environment, however the highly crystalline nature of the perovskite samples means that signal to noise ratios remained high. Samples were placed on a hotplate which was tilted to a very low angle of incidence with respect to an incoming X-ray beam. Reflected and transmitted X-rays were blocked by a lead beam-stop, leaving only the scattered (diffracted) X-rays incident on the detector. A 2D detector is used, allowing for characterization of crystal orientation whilst the use of a synchrotron source to provide the X-rays ensures a high signal-to-noise ratio.

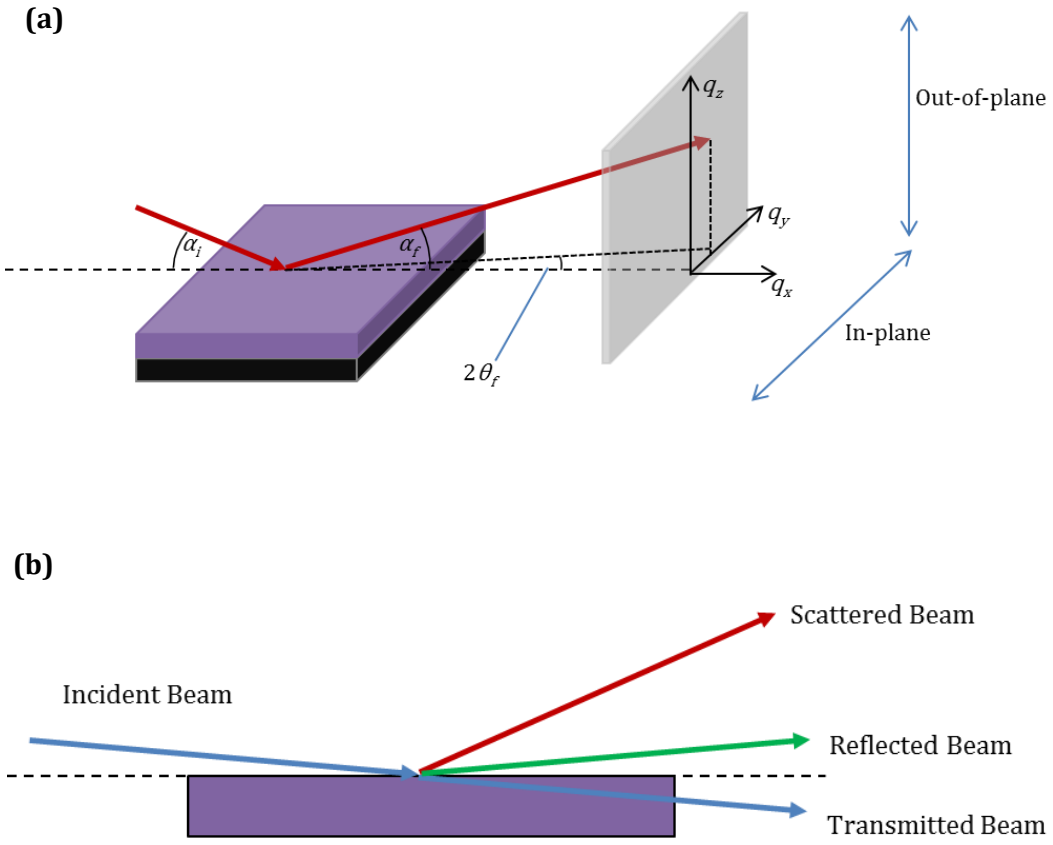

Figure 3.11 Part **(a)** presents a schematic of an X-ray scattering experiment. Part **(b)** shows an X-ray beam incident on a thin film sample which will be transmitted, reflected and scattered (as well as absorbed) in various proportions.

X-rays incident upon a crystalline sample will undergo Bragg diffraction, governed by Bragg's law

$$n\lambda = 2d\sin\theta \qquad \{3.21\}$$

where d is the distance between lattice planes, θ is the incident angle with respect to the lattice planes, λ is the wavelength of the X-rays and n is an integer referring to the order of reflection. X-ray diffraction experiments produce results in reciprocal space,

with periodic structures in real space give rise to a sharp peak in reciprocal space. Typically the reciprocal space parameter q is used in grazing incidence X-ray work, which is related to real space quantities by

$$q = \frac{2\pi}{d} = \frac{4\pi \sin\theta}{\lambda} \quad \{3.22\}$$

The length scales probed by GIWAXS are of the order of Angstroms and nanometres, i.e. periodicity on at atomic scale. This technique is thus useful for determination of the constituent crystalline materials in a sample by providing information on unit cell dimensions as well as the relative quantities of different crystalline materials or phases present in a sample.

In grazing incidence X-ray scattering experiments the critical angle, α_c, of the material under investigation is crucial. Below the critical angle the incoming X-rays undergo total external reflection, leaving only exponentially decaying waves in the sample surface. At these low angles only the top few tens of nanometres will thus be probed (see section 2.1.1 of [10] for a more complete discussion). Above the critical angle the X-rays will probe the bulk of the sample. It should be noted that for rough samples, such as the perovskite films investigated in this thesis, the angle of incidence on the material becomes somewhat notional. Using a freely available program for calculating X-ray attenuation length [11] and a density of 4.29 g/cm^3 for $CH_3NH_3PbI_3$ [12] the critical angle for this material is predicted to be between 0.1° and 0.2° at the X-ray energies used herein (10 keV and 12.4 keV). For the perovskite films studied in this thesis it was found that the transition from below to above the critical angle could be clearly observed by changes in the measured diffraction patterns. Below the critical angle the diffraction rings are narrow, as shown in **Figure 3.12(a)** (α_i = 0.02°). As the incident angle increases beyond the critical angle these rings become broad, as can be seen in **Figure 3.12(b)** (α_i = 0.24°). This broadening of the diffraction peaks likely arises due to multiple lattice constants being present in the perovskite film. As the critical angle is exceeded the sample volume probed increases dramatically, meaning that a greater number of these different lattice constants are sampled and thus the diffraction peak broadens.

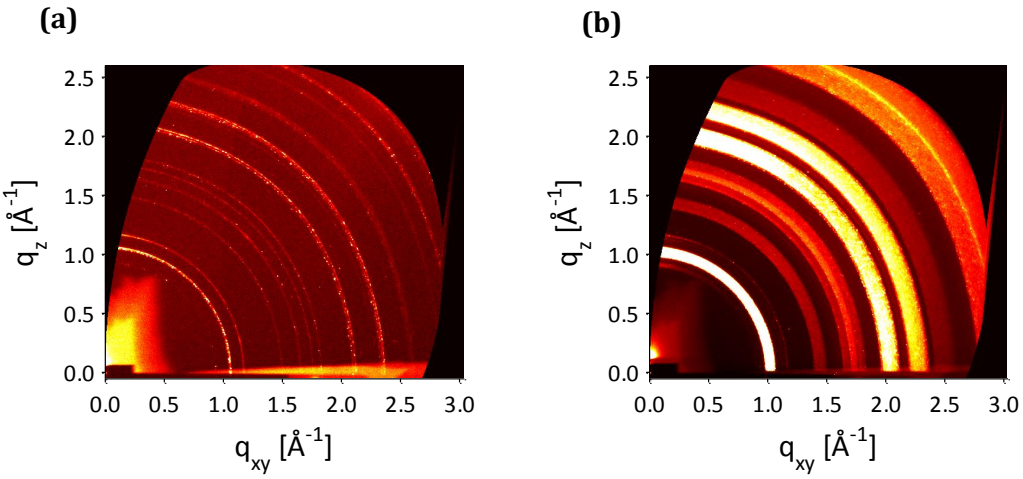

Figure 3.12 GIWAXS data for the same perovskite film probed with an incident angle of 0.02° (< α_c) **(a)** and 0.24° (> α_c) **(b)**.

Data processing and analysis of GIWAXS data has been performed using the GI-XRD-GUI software developed by Samuele Lilliu [13]. Calibration was performed by scanning the detector vertically and horizontally and tracking the direct beam position [13]. Incorporated in the software is mapping into q space (i.e. from pixels to scattering vectors) which takes account of the fact that the detector is a 2D plane, but it is probing the curved surface of the 'Ewald sphere' which relates to scattering from the sample. At large distances from the sample (e.g. in the GISAXS experiments discussed in **Section 3.5.2**, below) this curvature is minimal and can be ignored. At the small sample-detector distances used in GIWAXS, however, it must be accounted for. Thus whilst GISAXS data is presented with axes of q_z and q_y, GIWAXS data is presented with axes q_z and q_{xy} (sometimes written q_r). Line profiles are taken from the 2D scattering data in either radial or azimuthal directions in order to present GIWAXS data in graphical format (intensity against either q or χ), as shown in **Figure 3.13**.

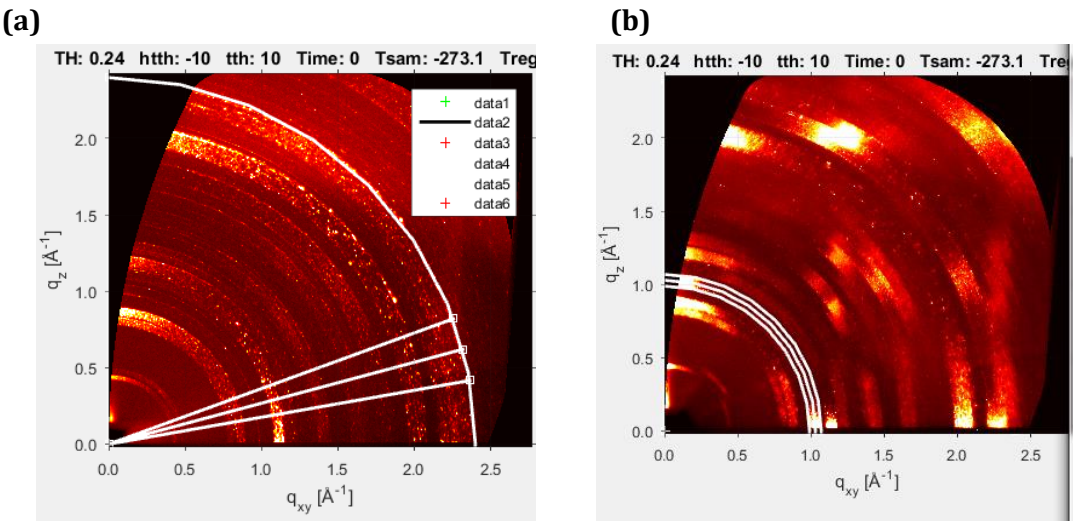

Figure 3.13 Screenshots of the GI-XRD-GUI data analysis program. Part **(a)** shows an out-of-plane radial profile; a number of radial line profiles are taken in the cake slice defined by the outer radial lines and are subsequently averaged. Part **(b)** shows an azimuthal profile, again a number of profiles are taken in the region between the outer rings shown and these are then averaged.

3.5.2 Grazing Incidence Small Angle X-Ray Scattering

Grazing incidence small angle X-ray scattering (GISAXS) experiments use a very similar experimental set-up to GIWAXS experiments, however a larger distance between the sample and the detector means that only very small scattering angles are probed. Photographs of GIWAXS and GISAXS experimental set-ups at Diamond Light Source are shown in **Figure 3.14**, where the much larger sample-detector distance for the GISAXS set-up can be seen. This technique thus allows investigation of structure in the size range of nanometres to hundreds of nanometres, so whilst GIWAXS is a useful technique for determining which type of crystals are present, GISAXS is more suited to investigating grain sizes and morphology in the sample films [14]. The size range probed is quite comparable to that which can be probed by techniques like atomic force microscopy, however unlike with AFM measurements, GIWAXS is able to probe the bulk of the sample as well as the surface; in addition, in-situ studies can be undertaken, as have been performed in **Chapter 6**. GISAXS experiments were performed in air (relative humidity 45-50%) on beamline I22 at the Diamond Light Source, Rutherford Appleton Laboratory, Didcot, UK. A 2D Pilatus P3-2M detector was used with a beam energy of 12.4 keV and an incident angle equal to 0.2°. Data processing and analysis has been undertaken using the DAWN software package [15]

with calibration performed using silver behenate and dry collagen samples with well-known peak spacing.

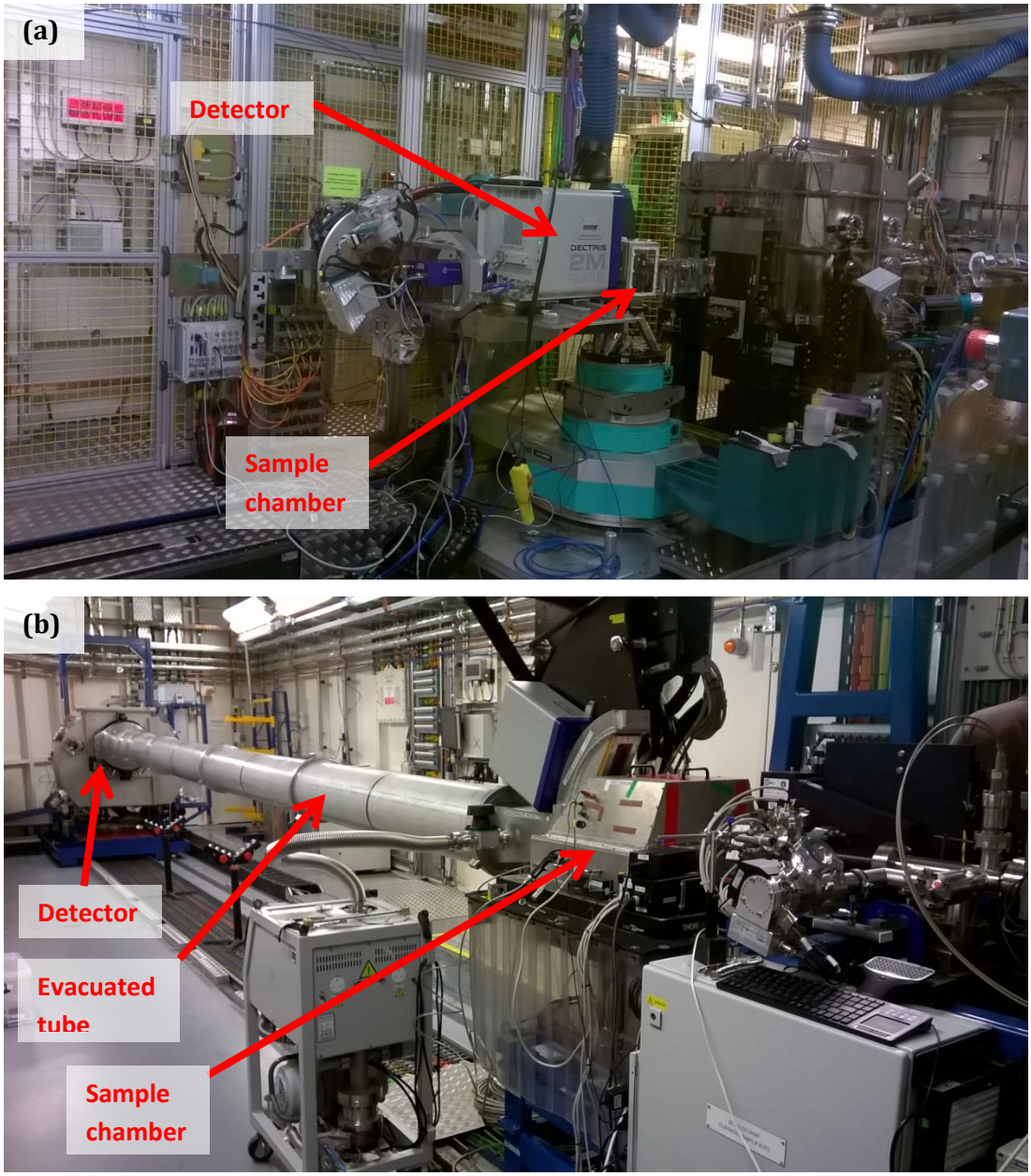

Figure 3.14 Photographs of beamline set-ups for GIWAXS **(a)** and GISAXS **(b)** measurements at Diamond Light Source. Photographs courtesy of David Lidzey.

Data slices are taken using box profiles 9 pixels high in q_z, centred on the Yoneda peak (see below). These profiles run from $q_y = 1.54 \times 10^{-3}$ Å^{-1} to $q_y = 3.608 \times 10^{-2}$ Å^{-1} on the left hand side of the obtained GISAXS images. The decision to take data from the left hand side of the images was taken as some datasets had issues with the beam-stop in

the experimental set-up shading the right hand side of the image slightly. In any case, this should only lose a small amount of high q value data, and, as is shown in **Chapter 6**, it is the lower q values which prove more interesting. The lower limit of the q_y range is due to the central shadowed region of the image which arises due to the detector.

The Yoneda peak is a maximum in scattering intensity which occurs when the scattering angle is equal to the critical angle of the material, that is $\alpha_f = \alpha_c$ (see **Figure 3.11(a)**) [16]. In order to locate the Yoneda peak for each image, a box profile is taken in q_z from 0 to 1500 pixels; this box profile is 5 pixels wide in q_y and positioned immediately to the left of the central shadowed region; the maximum scattering occurs at the Yoneda peak which was clearly identifiable in the case of perovskite samples , as shown in **Figure 3.15**

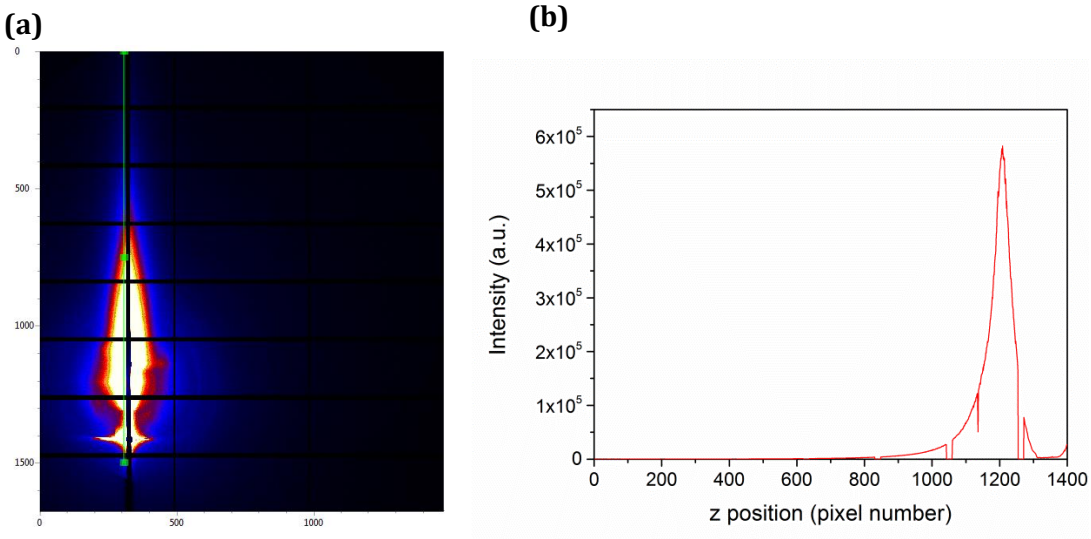

Figure 3.15 An example of the box profile taken in order to determine the location of the the Yoneda peak in *z* for this image. In part **(a)** the thin green box shows the area used for the box profile presented in **(b)** where the Yoneda peak can clearly be seen at 1209 pixels.

3.6 Optical Modelling Using the Transfer Matrix Method

In **Chapter 4**, a freely available model based on the Transfer Matrix Method has been used to calculate electromagnetic field intensity within the various layers of an organic solar cell [17]. Using this information, the model then gives a maximum possible short circuit current for the device which we term $J_{SC\_100\%}$. This is calculated by assuming an internal quantum efficiency of 100% and thus ignoring all loses after exciton generation. The model requires inputs of real and imaginary refractive indices (*n* and *k*) for all layers as well as layer thicknesses to be set by the user. Refractive indices for ITO, Al, Ag and Ca were taken from the library associated with this model whilst those for MoO_3, TeO_2 and PCDTBT:$PC_{70}BM$ films were determined using spectroscopic ellipsometry as discussed in **Section 3.3.7** above. It should be noted that the model assumes isotropic, homogeneous media, optically flat interfaces and light at normal incidence.

At any interface between different materials, light will undergo a certain amount of reflection and transmission. In a series of layers, reflected and transmitted light will repeatedly meet further interfaces and undergo further reflection and transmission. A huge (technically infinite) number of calculations would then need to be performed in order to calculate the electromagnetic field intensity within any layer of the structure. The transfer matrix method (TMM) is a more elegant solution to the problem of making these calculations. The TMM relies on the boundary conditions for electric and magnetic fields, namely that the tangential component of the E-field must be continuous across any boundary (interface) and the normal component of the B-field (that is, the tangential component of the H-field) must be continuous across any boundary (interface). In addition, if a field is known at the start of a layer it can be derived at the end of that layer by a simple matrix operation.

A stack of layers (j = 1, 2…. m) are sandwiched between two semi-infinite layers (j = 0 and j = m+1), with light entering from the layer j = 0, as shown in **Figure 3.16**.

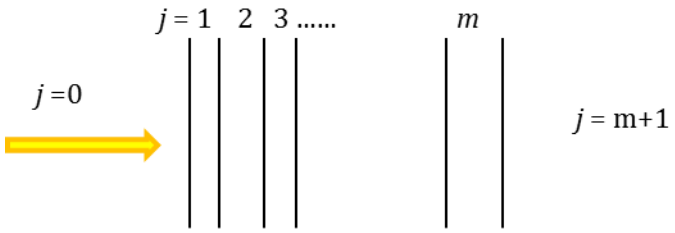

Figure 3.16 Light entering a multi-layer stack to be modelled using the transfer matrix method.

Propagation of an electric field $\boldsymbol{E}$ at an interface between layers j and k, where $k = j+1$ is defined by

$$\begin{bmatrix} \boldsymbol{E}_j^+ \\ \boldsymbol{E}_j^- \end{bmatrix} = I_{jk} \begin{bmatrix} \boldsymbol{E}_k^+ \\ \boldsymbol{E}_k^- \end{bmatrix} \quad \{3.23\}$$

where the superscripts + and – refers to a wave moving in the forward and backward directions respectively, the total field being the superposition of these two waves. The interface matrix between the layers j and k is defined as

$$I_{jk} = \frac{1}{t_{jk}} \begin{bmatrix} 1 & r_{jk} \\ r_{jk} & 1 \end{bmatrix} \quad \{3.24\}$$

where r_{jk} and t_{jk} are respectively the Fresnel complex reflection and transmission coefficients at interface jk, given by

$$r_{jk} = \frac{\tilde{n}_j - \tilde{n}_k}{\tilde{n}_j + \tilde{n}_k} \quad \{3.25\}$$

$$t_{jk} = \frac{2\tilde{n}_j}{\tilde{n}_j + \tilde{n}_k} \quad \{3.26\}$$

(for a derivation please see [18].) Propagation of the field though a layer is described by

$$\begin{bmatrix} \boldsymbol{E}'^+_j \\ \boldsymbol{E}'^-_j \end{bmatrix} = L_j \begin{bmatrix} \boldsymbol{E}_j^+(x) \\ \boldsymbol{E}_j^-(x) \end{bmatrix} \quad \{3.27\}$$

where the layer matrix L_j is given by

$$L_j = \begin{bmatrix} e^{-i\xi_j d_j} & 0 \\ 0 & e^{i\xi_j d_j} \end{bmatrix} \quad \{3.28\}$$

and

$$\xi_j = \frac{2\pi}{\lambda}\tilde{n}_j \quad \{3.29\}$$

where d_j is the thickness of layer j and $\tilde{n}_j$ is the complex refractive index of the layer j, i.e. $\tilde{n}_j = n_j + ik_j$. For the total system we thus have a 'scattering matrix', S, which relates the field in the first semi-infinite layer (layer 0) to the field in the final semi-infinite layer (layer $m+1$) via

$$\begin{bmatrix} \boldsymbol{E}_0^+ \\ \boldsymbol{E}_0^- \end{bmatrix} = S \begin{bmatrix} \boldsymbol{E}_{m+1}^+ \\ \boldsymbol{E}_{m+1}^- \end{bmatrix} \quad \{3.30\}$$

where

$$S = \begin{bmatrix} S_{11} & S_{12} \\ S_{21} & S_{22} \end{bmatrix} = \left(\prod_{n=1}^{m} I_{(n-1)n} L_n \right) I_{m(m+1)} \quad \{3.31\}$$

Thus S is the product of all the interface and layer matrices separating layer 0 and layer $m+1$, as one would expect.

By noting that since the final layer $m+1$ is semi-infinite then

$$\boldsymbol{E}_{m+1}^- = 0 \quad \{3.32\}$$

and by dividing the system into two subsets separated by the layer j, it becomes possible to find the electromagnetic field strength at any point in the device by

$$E_j(x) = (t_j^+ e^z + t_j^- e^{-z}) E_0^+ \quad \{3.33\}$$

where $z = i\xi_j d_j$ and

$$t_j^+ = \frac{1}{S'_{j11} + \frac{S'_{j12}S''_{j21}e^{2z}}{S''_{j11}}} \quad \{3.34\}$$

and

$$t_j^- = \frac{1}{S'_{j12} + \frac{S'_{j11}S''_{j11}e^{-2z}}{S''_{j21}}} \quad \{3.35\}$$

Since knowledge of the thicknesses and optical properties of the layers allows for calculation of the scattering matrices, and we can set the incoming light E_0^+ to the AM1.5 spectrum, the electromagnetic field strength at any point within the layer stack (solar cell) can now be calculated.

The model then calculates absorbed power at position *x* in layer *j* at a given wavelength λ by

$$Q_j(x) = \frac{4\pi c\varepsilon_0 k_j n_j}{2\lambda}\left|\bar{E}_j(x)\right|^2 \quad \{3.36\}$$

where ε_0 is the permittivity of free space and *c* the speed of light in vacuum. By integrating in *x* across the photoactive layer we thus obtain an absorbed power at each wavelength, which can easily be converted into the number of photons absorbed per second. Integrating across a wavelength range and assuming an IQE of 100% we thus find the maximum possible current from the device, $J_{SC\_100\%}$.

3.7 Conclusions

The experimental methods outlined in **Section 3.2 Fabrication Techniques** have been applied for the fabrication of solar cells throughout this thesis. With regards to film deposition techniques, ultrasonic spray-coating has been used extensively in **Chapter 5** whilst spin-coating has been used in all Chapters. Throughout this work device characterization has been performed as detailed in **Section 3.4 Device Characterization**. Where device testing parameters have been varied in order to investigate hysteresis in the current density against voltage response of a device this is

stated clearly in the text, as in **Chapter 5** and **Chapter 6**. The film characterization techniques of atomic force microscopy, scanning electron microscopy and surface profilometry have been used in all Chapters within this thesis.

In **Chapter 4**, the electrical characterisation techniques discussed in **Section 3.3.2 Resistance Measurements** and **Section 3.3.3 Hall Effect Measurements** are employed in in order to characterise semi-transparent electrodes. Similarly, **Section 3.3.6 UV-Vis Spectrometry** details techniques utilised extensively to characterise the transmittance of the electrodes fabricated within that Chapter. Finally in **Chapter 4** the optical model described in **Section 3.6 Optical Modelling Using the Transfer Matrix Method** has been applied, and the techniques described in **Section 3.3.7 Spectroscopic Ellipsometry** have been used to establish the optical constants of a number of materials systems as inputs to this model.

Chapter 6 is concerned with the application of the techniques described in **Section 3.5.1 Grazing Incidence Wide Angle X-Ray Scattering** and **Section 3.5.2 Grazing Incidence Small Angle X-Ray Scattering**. Wide angle X-Ray scattering measurements are also briefly presented in **Chapter 5** in order to make a comparison between spray-coated and spin-coated perovskite films.

3.8 References

[1] P. Docampo, F. Hanusch, S.D. Stranks, M. Döblinger, J.M. Feckl, M. Ehrensperger, et al., Solution Deposition-Conversion for Planar Heterojunction Mixed Halide Perovskite Solar Cells, Adv. Energy Mater. 4 (2014) 1400355.

[2] T. Wang, N.W. Scarratt, H. Yi, A.D.F. Dunbar, A.J. Pearson, D.C. Watters, et al., Fabricating High Performance, Donor-Acceptor Copolymer Solar Cells by Spray-Coating in Air, Adv. Energy Mater. 3 (2013) 505–512.

[3] A. Barrows, A. Pearson, C. Kwak, A. Dunbar, A. Buckley, D. Lidzey, Efficient planar heterojunction mixed-halide perovskite solar cells deposited via spray-deposition, Energy Environ. Sci. 7 (2014) 2944–2950.

[4] Haldor Topsoe, Geometric Factors in Four Point Resistivity Measurement, 1966.

[5] F.M. Smits, Measurement of Sheet Resistivities with the Four-Point Probe, Bell

Syst. Tech. J. May 1958 (1958) 711.

[6] N. A. Geisse, AFM and combined optical techniques, Mater. Today. 12 (2009) 40–45.

[7] B. Johs, J.S. Hale, Dielectric function representation by B-splines, Phys. Status Solidi. 205 (2008) 715–719.

[8] E. Zimmermann, P. Ehrenreich, T. Pfadler, J. A. Dorman, J. Weickert, L. Schmidt-Mende, Erroneous efficiency reports harm organic solar cell research, Nat. Photonics. 8 (2014) 669–672.

[9] J. A. Christians, J.S. Manser, P. V. Kamat, Best Practices in Perovskite Solar Cell Efficiency Measurements. Avoiding the Error of Making Bad Cells Look Good, J. Phys. Chem. Lett. 6 (2015) 852–857.

[10] G. Renaud, R. Lazzari, F. Leroy, Probing surface and interface morphology with Grazing Incidence Small Angle X-Ray Scattering, Surf. Sci. Rep. 64 (2009) 255–380.

[11] B.L. Henke, E.M. Gullikson, J.C. Davis, X-ray interactions: photoabsorption, scattering, transmission and reflection at E = 50-30,000 eV, Z = 1-92, At. Data Nucl. Data Tables. 54 (1993) 181–342.

[12] T. Baikie, Y. Fang, J.M. Kadro, M. Schreyer, F. Wei, S.G. Mhaisalkar, et al., Synthesis and crystal chemistry of the hybrid perovskite $(CH_3NH_3)PbI_3$ for solid-state sensitised solar cell applications, J. Mater. Chem. A. 1 (2013) 5628.

[13] S. Lilliu, T. Agostinelli, E. Pires, M. Hampton, J. Nelson, J.E. Macdonald, Dynamics of Crystallization and Disorder during Annealing of P3HT PCBM Bulk Heterojunctions, Macromolecules. 44 (2011) 2725–2734.

[14] P. Muller-Buschbaum, Grazing incidence small-angle x-ray scattering: an advanced scattering technique for the investigation of nanostructured polymer films, Anal. Bioanal. Chem. 376 (2003) 3–10.

[15] M. Basham, J. Filik, M.T. Wharmby, P.C.Y. Chang, B. El Kassaby, M. Gerring, et al., Data Analysis WorkbeNch (DAWN), J. Synchrotron Radiat. 22 (2015) 853–858.

[16] D. Altamura, T. Sibillano, Assembled Nanostructured Architectures Studied By Grazing Incidence X-Ray Scattering, Nanomater. Nanotechnol. 2 (2012) 16:2012.

[17] G.F. Burkhard, E.T. Hoke, M.D. McGehee, Accounting for interference, scattering, and electrode absorption to make accurate internal quantum efficiency

measurements in organic and other thin solar cells., Adv. Mater. 22 (2010) 3293–3297.

[18] E. Hecht, Optics, 4th Edition, Addison-Wesley, 2001.

Chapter 4: Indium-Free Multilayer Semi-Transparent Electrodes for Polymer Solar Cells

4.1 Introduction and Theory

In **Chapter 2** the key features of transparent conducting electrodes were introduced, together with the motivation for investigating alternatives to the ubiquitous indium tin oxide (ITO). In addition, a brief introduction was given to oxide/metal/oxide (O/M/O) multilayer electrodes as one possible ITO replacement. In these multilayer structures the initial oxide layer acts as a 'seed layer' for the subsequent growth of an ultrathin metal film (UTMF). When such an electrode is employed in an organic solar cell (OSC), the metal film provides high lateral conductivity ensuring a suitably low series resistance. The second oxide layer meanwhile acts as an intermediate layer (as shown in **Figure 4.1(a)**), facilitating appropriate charge extraction and charge blocking in the device, for example assisting with hole extraction and electron blocking at the anode [1,2]. In addition to their electronic functionality, such oxide layers also suppress reflection from the metal film and maximise optical transmittance [3,4]. In comparison to these trilayer structures, bilayer electrodes, which incorporate only one of the metal oxide layers, have been shown to give worse transmission and lower device efficiencies for a variety of material combinations including V_2O_5/Ag [5], WO_3/Ag [6], AZO/Au [7], AZO/Ag [8], AZO/Al [9], ZnO/Ag [10] and graphene/Ag [11]. Previously both silver and gold have both been found to offer good performance when used as the UTMF in O/M/O electrodes [12,13]. Ideally a less expensive metal than silver or gold would be employed, and to this end copper has been investigated as a replacement, however this has been found to diffuse easily into the oxide layers leading to a reduction in device performance, and hence silver remains the most widely utilised metal for this application [12,14].

Whilst the transmittance of indium free O/M/O electrodes is typically notably lower than for an ITO electrode, this can be somewhat compensated for by optimisation of optical interference effects. These can be particularly important due to the cavity established between the metal films compromising both the front (semi-transparent)

and rear (opaque) electrodes. This cavity leads to the pinning of antinodes in electric field intensity at both metal layers, an effect which can clearly be seen in field intensity simulations performed using a Transfer Matrix Model. One such simulation is shown in **Figure 4.1(b)** where the field intensity (summed over the wavelength range 380–600 nm, corresponding to the range over which the photoactive PCDTBT:$PC_{70}BM$ layer absorbs most strongly) is plotted for each position in the device (where 0 is defined at the edge of the glass substrate, i.e. the point at which the seed layer begins).

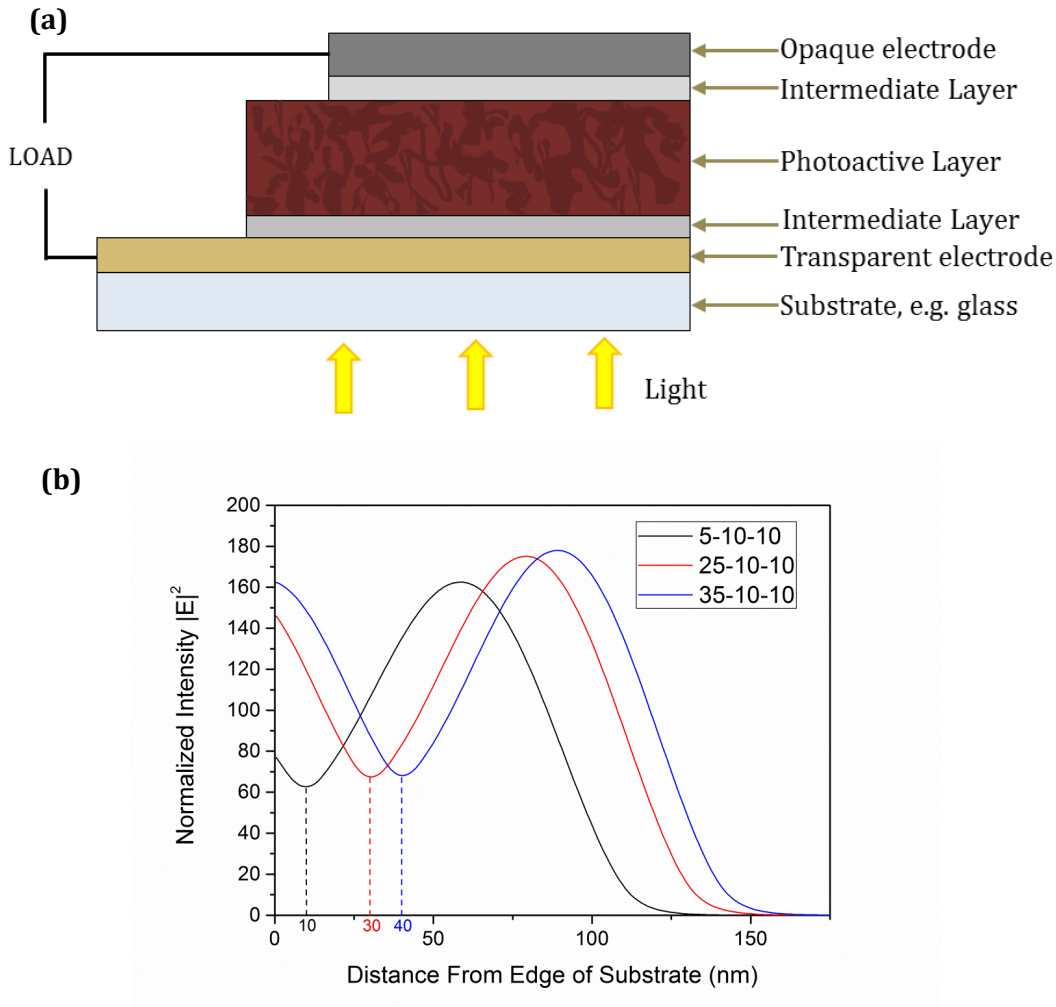

Figure 4.1 Part **(a)** shows a schematic of an OSC. The trilayer electrodes investigated within this Chapter act as both the transparent electrode and the adjacent intermediate layer. Part **(b)** shows simulated electric field intensity within devices with MoO_3/Ag/MoO_3 electrodes with layer thicknesses shown in the key; 5-10-10, for example, refers to a 5 nm seed layer, a 10 nm silver layer and a 10 nm final oxide layer. All 3 devices shown here are simulated with an 80nm thick active layer in order to make comparison by eye simpler. The dashed lines show the midpoints of the thin silver films, clearly showing the pinning of an antinode in intensity.

In this Chapter two different oxide/metal/oxide electrodes have been investigated, having the structures MoO_3/Ag/MoO_3 (MAM) and TeO_2/Ag/MoO_3 (TAM). The difference between these two structures is thus the material which is employed as the seed layer. Following their characterisation and optimisation, these electrodes have been utilised as the anode (hole collecting electrode) in polymer solar cells based on the polymer:fullerene blend PCDTBT:$PC_{70}BM$. Whilst MAM electrodes have previously been investigated for use in OPVs [6,13,15,16], TAM electrodes have not. One study which investigated a TeO_2/Ag/PEDOT:PSS electrode [11] suggested that a tellurium dioxide seed layer should lead to an enhanced short circuit current (J_{SC}) in comparison with an equivalent MoO_3/Ag/PEDOT:PSS structure, resulting from the larger real part of the refractive index of TeO_2 [4]. Whilst devices fabricated with such electrodes achieved promising efficiencies, the expected enhancement in J_{SC} was not verified by experimental comparison between the different seed layer materials.

In this work a direct comparison between MAM and TAM structures has it has been made for the first time. It has been found that replacement of the MoO_3 seed layer by TeO_2 results in a significantly enhanced transmittance at low silver film thickness, attributable to the formation of a more continuous silver layer as confirmed by scanning electron microscopy (SEM) images. When applied as the transparent front electrode in polymer solar cells based upon a PCDTBT:$PC_{70}BM$ bulk heterojunction, the higher transmittance of the TAM electrode leads to an increased J_{SC} and hence a higher power conversion efficiency (PCE) when compared to devices utilising a MAM electrode.

At this early stage it is worth defining certain notation for simplicity – a multilayer structure with, for example, layer thicknesses of 2 nm for the seed layer, 12 nm for the silver layer and 10 nm for the final oxide layer will herein be denoted as having layer thicknesses of 2-12-10 nm.

4.2 The Effect of Silver Film Thickness

4.2.1 Optical and Electrical Properties

Metal film thickness is crucial for determining the optical and electrical properties of oxide/metal/oxide electrodes. In order to explore this effect a series of structures were fabricated in which the thickness of the metal (silver) film was varied whilst both oxide layers were kept to a thickness of 10 nm. The thickness of all films was determined by the film thickness monitor in the evaporation chamber. Note that such thicknesses should be considered as average values since the films are highly structured at nanometre length-scales, as shall be discussed below. Transmittance spectra for MAM electrodes with silver thickness varying from 4–10 nm and 10–16 nm are presented in **Figures 4.2(a)** and **(b)** respectively. Similarly, transmittance spectra for TAM electrodes with silver thickness varying from 4–8 nm and 8–16 nm are presented in **Figures 4.2(c)** and **(d)** respectively.

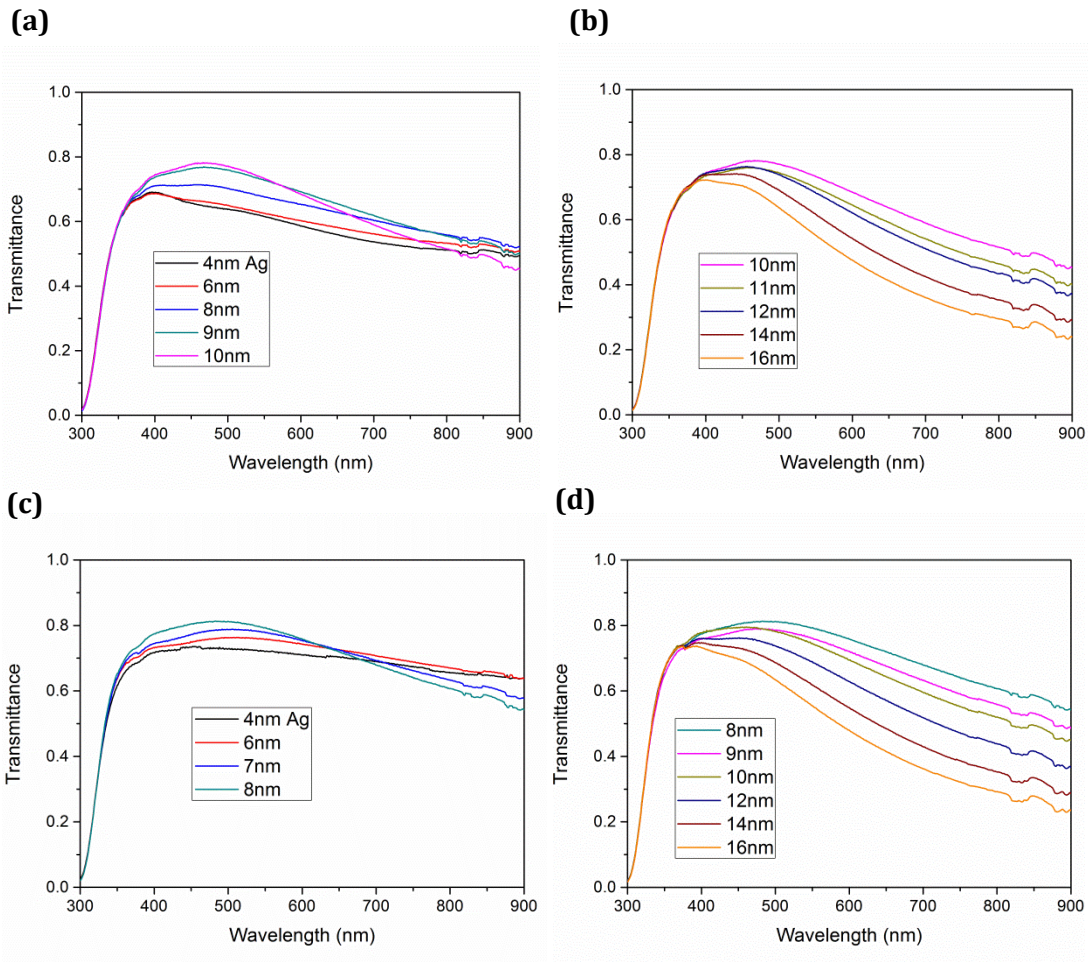

Figure 4.2 Transmittance spectra for multilayer MAM (**(a)** and **(b)**) and TAM (**(c)** and **(d)**) electrodes on glass with varying thickness of the silver film. All spectra are referenced to air, meaning that the spectra presented herein include reflection and absorption by the glass substrate.

Counter-intuitively, but in line with other reports on oxide/metal/oxide structures, the transmittance of the structures initially increases with increasing thickness of the silver layer, before reaching a maximum at a thickness termed the percolation threshold. The origin of this effect is discussed in **Section 4.2.2**. Above this thickness the transmittance of the multilayer reduces, an effect particularly pronounced at longer wavelengths as a result of the silver film acting as a mirror. It can be seen that for the MAM electrodes the maximum transmittance occurs at a silver thickness of 10 nm, a result comparable to other literature values for the percolation threshold of Ag on MoO_3 (being between 10 and 11 nm [6,15,16]). For the TAM electrodes the maximum transmittance occurs at a reduced silver thickness of 8 nm. The average transmittance of the MAM and TAM electrodes over the wavelength range 350–700 nm is shown in

Figure 4.3(a). The sheet resistance of the films as a function of the thickness of the silver layer has also been measured, with data presented in **Figure 4.3(b)**. It can be seen that for both the MAM and TAM electrodes there is a rapid decrease in sheet resistance as the thickness of the silver layer increases, however this decrease saturates as the film thickness exceeds the percolation threshold.

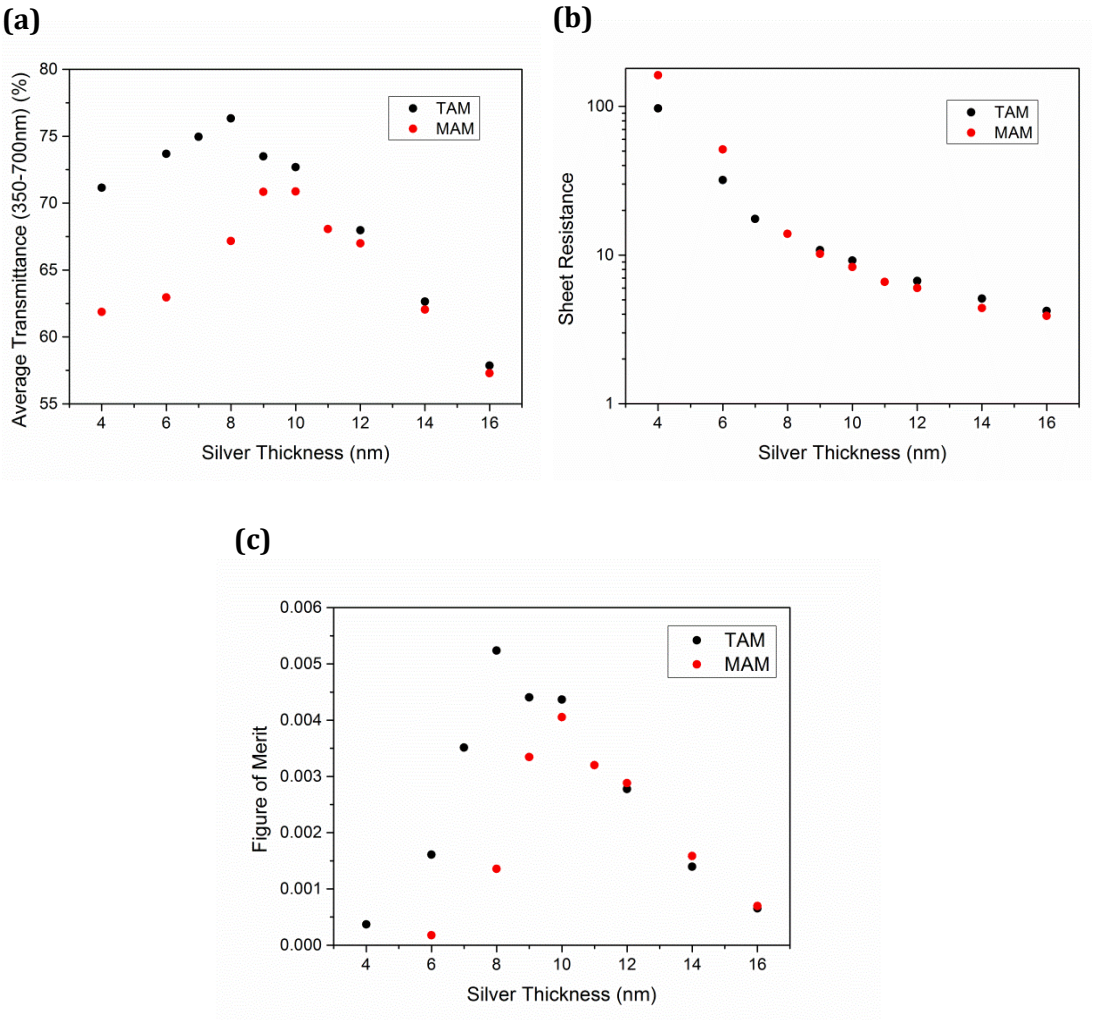

Figure 4.3 Average transmittance in the 350–700 nm range **(a)**, sheet resistance **(b)** and figure of merit **(c)** for MAM and TAM electrodes with varying silver film thickness.

Figures 4.3(a) and **(b)** clearly show that for low thickness of the silver film, the TAM electrode has a significantly higher transmittance and somewhat lower sheet resistance than the corresponding MAM electrode. As the thickness of the silver film increases, the relative improvement in transmittance afforded by the use of a TAM structure is reduced, with the transmission of the TAM electrode being only slightly greater than that of the MAM electrode at and above the percolation threshold. Whilst

at low silver thickness the sheet resistance of the TAM electrodes is notably less than that of the MAM electrodes, above an Ag thickness of 8 nm the sheet resistances of the TAM and MAM electrodes are similar. Finally, **Figure 4.3(c)** plots Haacke's figure of merit (FOM), as described earlier in **Section 2.6.1**, for both multilayer electrode structures. At low thickness of the silver film, the FOMs of TAM electrodes notably exceed those of the equivalent MAM electrodes, whilst above the MAM percolation threshold (10 nm Ag thickness) their FOMs are similar. The maximum FOM for the TAM electrodes is 5.24×10^{-3}, occurring for a silver film thickness of 8 nm. MAM electrodes, by comparison, exhibit a lower maximum FOM value of 4.05×10^{-3}, a value which occurs at a silver film thickness of 10 nm.

The potential benefit of the use of the TAM structure as a transparent front electrode in an organic solar cell is illustrated in **Figure 4.4**, by plotting the relative transmission of the MAM and TAM electrodes at their percolation threshold (point of maximum optical transmittance). The TAM electrode having an 8 nm thick silver layer exhibits a maximum transmittance of 81.3%, an average transmittance (350–700 nm) of 76.3% and a sheet resistance of 13.9 Ω/□. In contrast the MAM electrode having a 10 nm thick silver layer has a reduced maximum transmittance of 78.2% and an average transmittance (350–700 nm) of only 70.9%, with the sheet resistance being slightly lower at 8.3 Ω/□. For comparison, the reference ITO electrode (150nm) coated with a 10 nm thick MoO_3 layer is also shown and exhibits a maximum transmittance of 89.8%, an average transmittance (350 to 700 nm) of 83.8% and a sheet resistance of 15.9 Ω/□.

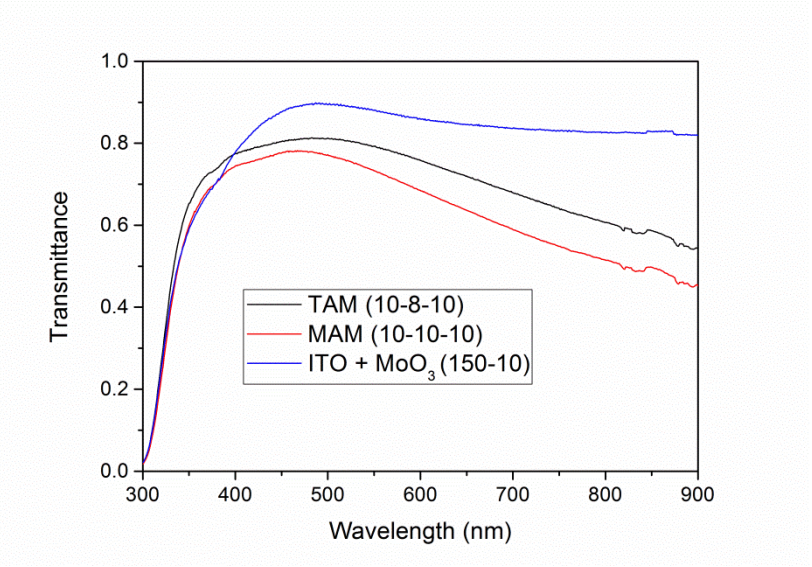

Figure 4.4 Transmittance spectra for the TAM and MAM multilayer electrodes with silver film thickness equal to the percolation threshold for that structure, i.e. layer thicknesses of 10-8-10 nm and 10-10-10 nm respectively. The transmittance spectrum of the ITO/MoO_3 electrode used in reference polymer solar cells is also presented.

4.2.2 Origin of Enhanced Transmittance in TeO_2 Based Electrodes

The trends observed in transmittance and sheet resistance as the silver layer thickness increases result from the growth characteristics of the metal film. As silver is deposited, it initially forms isolated islands and chains (so-called Volmer-Weber growth), resulting in poor lateral conductivity due to a lack of continuous conduction pathways. As the film thickness increases, the silver particles coalesce to form an increasingly uniform and continuous layer. The formation of continuous conduction pathways then results in a rapid reduction in sheet resistance, a process that slows once a uniform and well-connected film has been created. Whilst a number of studies have observed these same trends for a variety of oxide/metal/oxide structures, there is some disagreement as to the exact source of the initial increase in transmittance as the layer is deposited. Some studies attribute it simply to light scattering by the unconnected islands, with this scattering effect being reduced as the layer becomes more connected and uniform [11,18,19]. Others attribute it to surface plasmon resonance at the optimum thickness, with excitation of the surface plasmon only being achieved effectively for the structure which obtains maximum transmittance (due to the different sizes and spacing of metallic chains in films with different thickness)

[14,20,21]. It should be noted that the percolation threshold occurs for a layer with continuous conduction pathways but which is not entirely uniform and homogenous, rather retaining a number of holes which can act like a 2D grating or array, allowing light to excite surface plasmons. Indeed, one recent study observed that as the film thickness increased, the film structure changed from one characterised by narrow cracks between metal islands and chains (usually unconnected) to a continuous structure with a random collection of nanoholes. It was proposed that the nanoholes allow for the formation of surface plasmon polaritons which propagate through the holes, with light then being re-radiated, thus increasing transmission. At higher thicknesses, such nanoholes become covered by the silver layer, and transmittance again drops [22].

The results presented above can be explained by the formation of a more continuous silver layer at low thickness on a tellurium dioxide seed layer in comparison to silver films grown on a molybdenum oxide seed layer. The formation of a more continuous Ag layer on TeO_2 is consistent with the observed improvement in transmittance due to reduced scatter from unconnected islands, whilst the reduced sheet resistance at low silver thickness is similarly explained by the more continuous silver film. Overall, this effect allows the optimised TAM electrode to have a notably higher transmittance than can be obtained using a MAM electrode. This explanation is also consistent with the percolation threshold being reached at a comparatively reduced silver thickness on the TeO_2 seed layer compared to that observed on the MoO_3 seed layer (8 nm and 10 nm respectively). Clearly for Ag thicknesses above the percolation threshold for both types of electrode, the silver films formed are quasi-continuous and no large differences in transmittance are observed. The formation of a more continuous silver film on TeO_2 is commensurate with previous work in which liquid Ag was found to have a slightly lower contact angle on TeO_2 than on MoO_3 [23]. This is indicative of stronger interactions between the silver and the TeO_2, which could be expected to assist with the formation of a more continuous silver layer by encouraging growth to occur in a layer-by-layer manner (Frank-van der Merwe growth) and reducing the favourability of island formation. Indeed, modification of the seed layer to achieve a higher surface energy (again giving stronger substrate-silver interactions) has previously been found to lead to the formation of a more continuous silver film in MAM electrodes [24].

Modelling of the optical properties of the multilayer structures has been undertaken in order to explore whether differences in the refractive index (real and imaginary parts)

of the seed layers play a significant role in modifying the transmittance of the electrodes. A Transfer Matrix Model (TMM) has been used, which assumes that all layers are uniform and continuous, and thus does not take into account the reduction in transmittance which occurs for discontinuous silver films with thickness below the percolation threshold for a given oxide/metal/oxide structure [25]. As inputs into this model, *n* and *k* for TeO_2 and MoO_3 have been established using spectroscopic ellipsometry, and their spectra are shown in **Figures 4.5(a)** and **(b)**. Note that data acquisition and subsequent modelling for PCDTBT:$PC_{70}BM$ blends was performed by Dr Tao Wang. Data acquisition and modelling for MoO_3 and TeO_2 was undertaken by the author. The calculated transmittance of MAM and TAM multilayer electrodes, both having layer thickness of 10–8–10 nm, is shown in **Figure 4.5(c)**. It can be seen that the model suggests that the MAM and TAM electrodes have similar transmittance values, with an average transmittance over the wavelength range 380–800 nm of 81.2% and 82.1% respectively. The measured transmittance for these structures on the other hand is 71.5% and 81.0% respectively over the same range. These measured transmittance spectra are presented in **Figure 4.5(d)**. (Note that the TMM model does not account for reflection and absorption losses arising from the glass substrate. For ease of comparison the measured transmittance values stated above and the spectra presented in **Figure 4.5(d)** are thus referenced to a glass substrate rather than to air unlike elsewhere in this work.) In the model the small enhancement in transmittance for the TAM electrode results from the lower extinction coefficient of TeO_2 as compared to MoO_3, as well as its favourable refractive index (see below). The much larger enhancement in measured transmittance strongly suggests that this notable enhancement, observed for silver thickness less than 10 nm, can be attributed to an effect not taken into account in the model, namely the formation of a more continuous silver film. This is as opposed to any optical effects resulting from the differing optical constants (*n* and *k*) of the seed layer materials themselves.

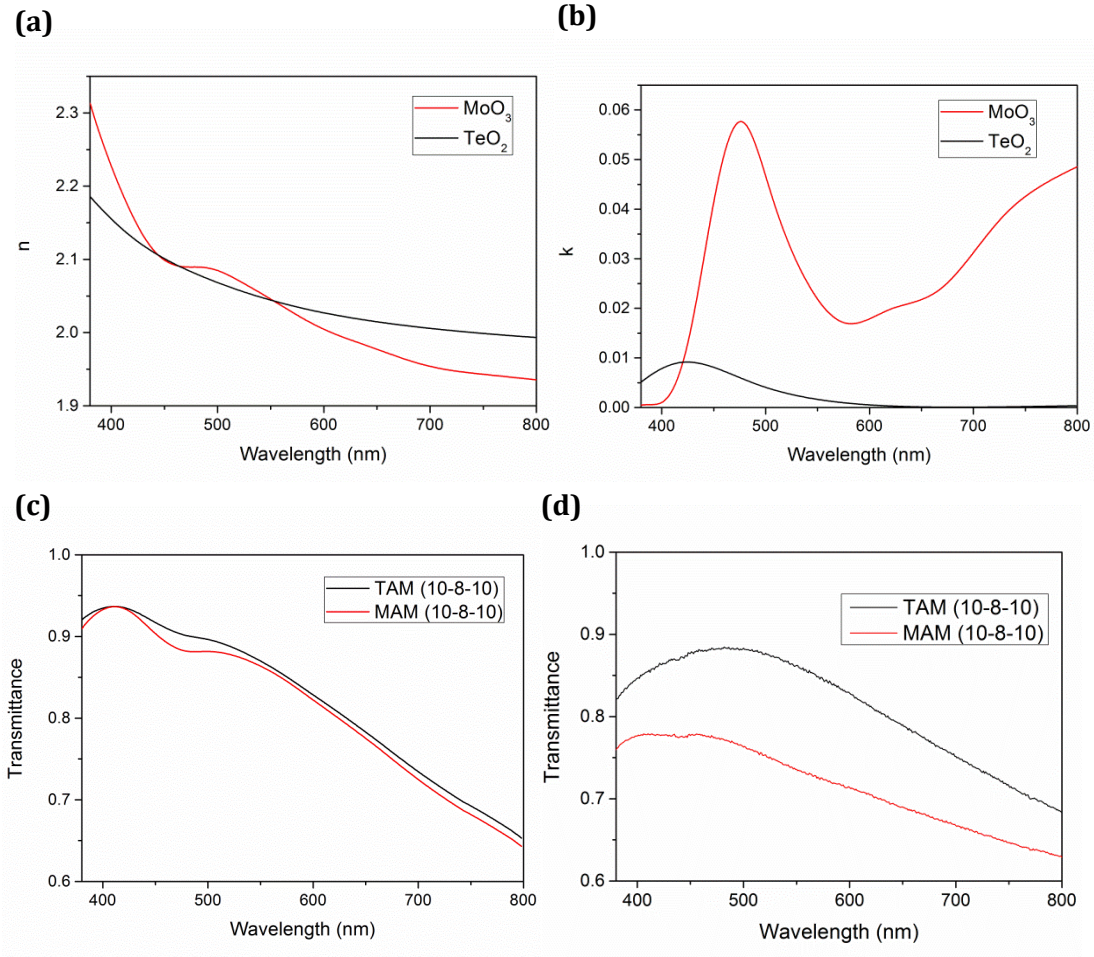

Figure 4.5 Parts **(a)** and **(b)** show optical contstants for thin MoO_3 and TeO_2 layers as determined by spectroscopic ellipsometry. Modelled transmittance spectra for MAM and TAM electrodes with layer thickness 10-8-10 nm are shown in **(c)** whilst **(d)** presents measured spectra for the same structures. Note that here the transmittance spectra do not include reflection and absorption losses due to the glass substrate, unlike in previously presented spectra.

As stated above, at high silver film thickness the small enhancement in transmittance for the TAM electrode, observed in both modelling and measurement, results from the favourable optical constants of TeO_2 as compared to MoO_3. This is largely attributable to the higher extinction coefficient (k) of MoO_3 at most wavelengths, but also in part to the refractive index (n) which is favourable for TeO_2 being higher at longer wavelengths and lower at shorter wavelengths. The advantageous effect of this refractive index is shown in **Figure 4.6**.

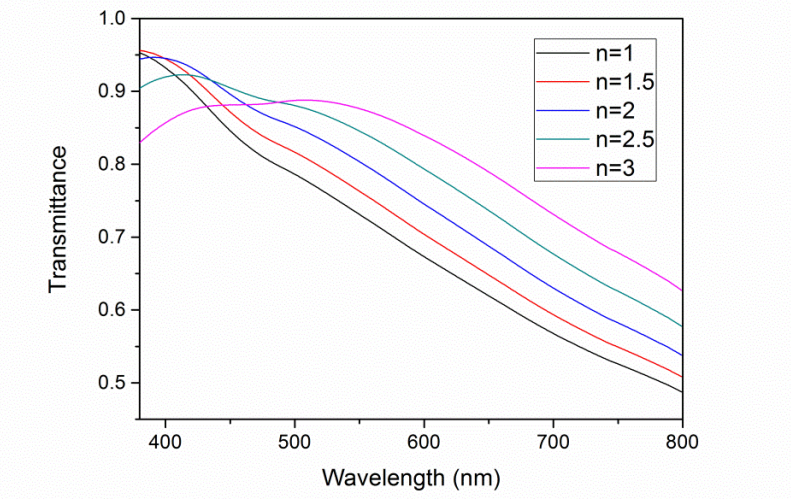

Figure 4.6 Modelled transmittance spectra for various multilayer structures in which the refractive index of the seed layer was set to a given value, shown in the key, whilst the other two layers were set to Ag and MoO_3, as used experimentally. Layer thicknesses are 10-10-10 nm. Note that modelled transmittance spectra do not include reflection and absorption losses due to the glass substrate.

To further confirm the origin of the improved transmittance of the TAM electrodes at low Ag thickness, scanning electron microscopy (SEM) images were taken of bilayer structures consisting of the metal oxide seed layer and an Ag layer. Images for Ag films having a thickness of 6 nm and 8 nm, deposited on 10 nm thick seed layers of TeO_2 and MoO_3 are shown in **Figure 4.7**. It can be seen that the 6 nm thick silver film deposited on MoO_3, shown in part **(a)**, is characterised by a series of thin "chains" having a typical width in the range 10–30 nm. Such structures presumably result in a non-continuous pathway for charge-carrier extraction. In contrast, the 6 nm thick silver film deposited on TeO_2 (part **(b)**) appears to be more continuous in nature and consists of a film which is broken up by a series of holes having a diameter of around 5–20 nm. Importantly, such films contain fewer isolated (unconnected) features. When the silver thickness is increased to 8 nm, the film on MoO_3 (part **(c)**) appears to have formed a more connected structure, whilst the film on TeO_2 (part **(d)**) exhibits fewer holes than with the 6 nm thick film. In fact, the magnified images of an 8 nm Ag film on MoO_3 (part **(c)**) and a 6 nm Ag film on TeO_2 (part **(b)**) appear very similar in terms of morphology. This finding is commensurate with the measurements of the electrodes' optical properties presented earlier, in which the percolation threshold was found to occur with 2 nm thinner silver films for a TeO_2 seed layer compared to an MoO_3 seed layer. Estimates of the surface coverage of the silver films from these SEM images are presented in **Table 4.1** and also support the proposed hypothesis.

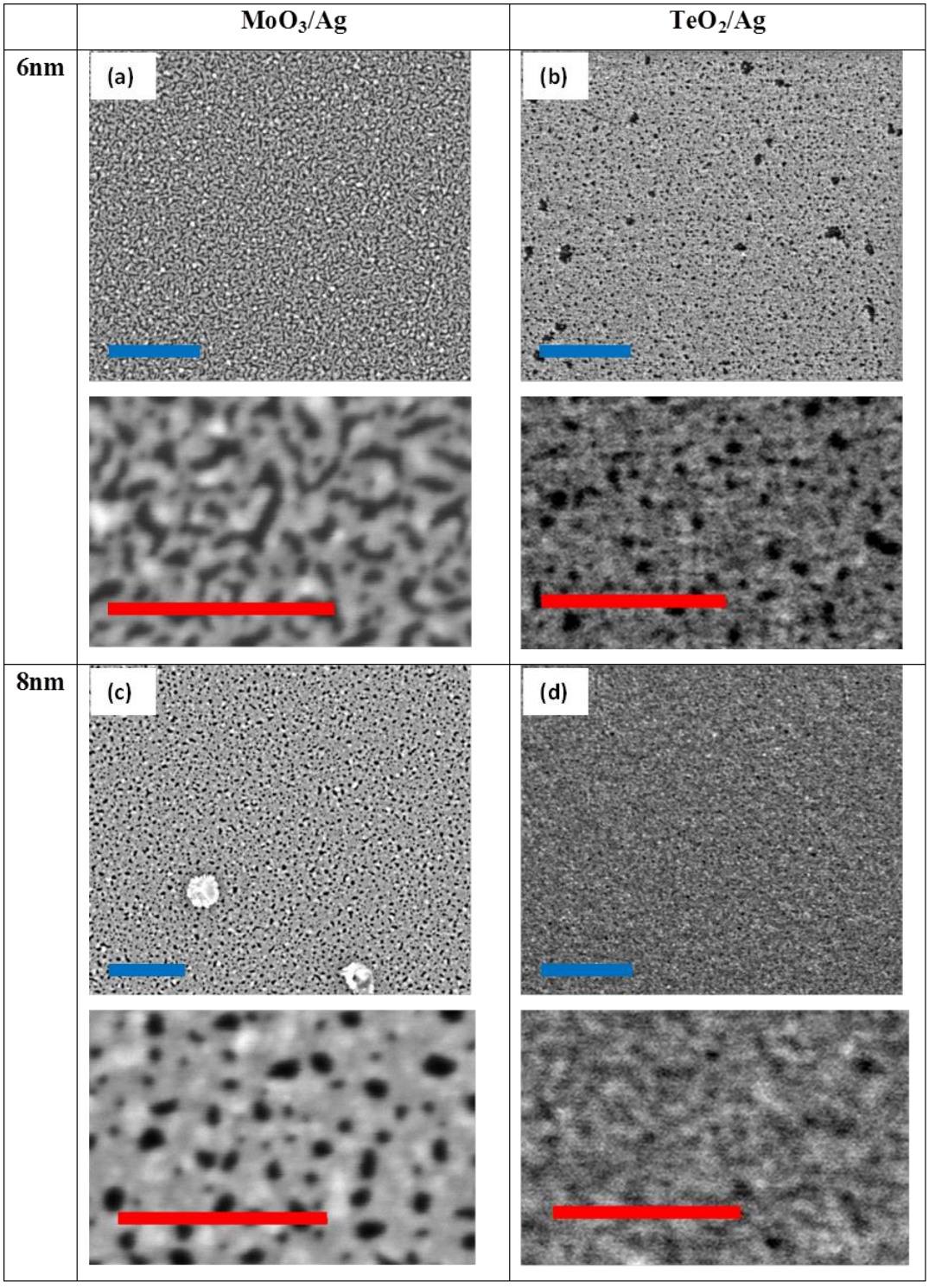

Figure 4.7 SEM images of MoO_3/Ag and TeO_2/Ag bilayers in which the oxide layer thickness is fixed at 10 nm. Parts **(a)** and **(c)** show an MoO_3/Ag bilayer for a silver thickness of 6 nm and 8 nm respectively. Parts **(b)** and **(d)** similarly show a TeO_2/Ag bilayer again utilising a silver layer having a thickness of 6 nm and 8 nm respectively. Blue scale bars correspond to 500 nm. In each case a magnified image of the film is shown with red scale bars corresponding to 200 nm.

	MoO_3	TeO_2
6nm	66	84
8nm	82	94
10nm	96	98
12nm	98	-

Table 4.1 Percentage surface coverage of the silver film at different thicknesses on the MoO_3 and TeO_2 seed layers. Coverage was estimated using the Image J software package with manual thresholding and is the average of the values obtained from three separate SEM images in each case.

4.3 Silver Deposition Rate & Film Repeatability

Whilst the optoelectronic properties of O/M/O multilayer electrodes are highly dependent upon the materials that constitute each layer and the thickness of those layers, they also depend upon the conditions under which these materials are deposited. Initial work undertaken on MAM structures found that the deposition rate of the silver UTMF was crucial in determining both the transmittance and sheet resistance of the resulting electrode. As the silver deposition rate increased from 0.3 Å/s to 5.6 Å/s there was a significant increase in transmittance alongside a reduction in sheet resistance, as shown in **Figure 4.8**. The effect is particularly notable as the rate increases from 0.3 to 2.0 Å/s, with subsequent improvements with increased deposition rate dropping off as the rate increases further. Around the time that this work was underway, a number of other studies were published on this topic, concluding that the optimum deposition rate was in the region of 4–6 Å/s [13,26]. Since maintaining a stable deposition rate above 5 Å/s proved difficult, and looking at the results of this initial work and the recently published literature, a deposition rate of 5 Å/s was chosen for all further experiments, such as those presented above in **Section 4.2**.

The improved performance of the multilayer electrodes observed for higher silver deposition rates can be rationalised by considering the growth of the metal film. A high deposition rate will cause silver atoms landing on the surface to be trapped in place before they can diffuse to lower energy positions, resulting in the formation of a more

continuous film rather than the growth of individual islands (i.e. encouraging Frank-van der Merwe growth rather than Volmer-Weber growth).

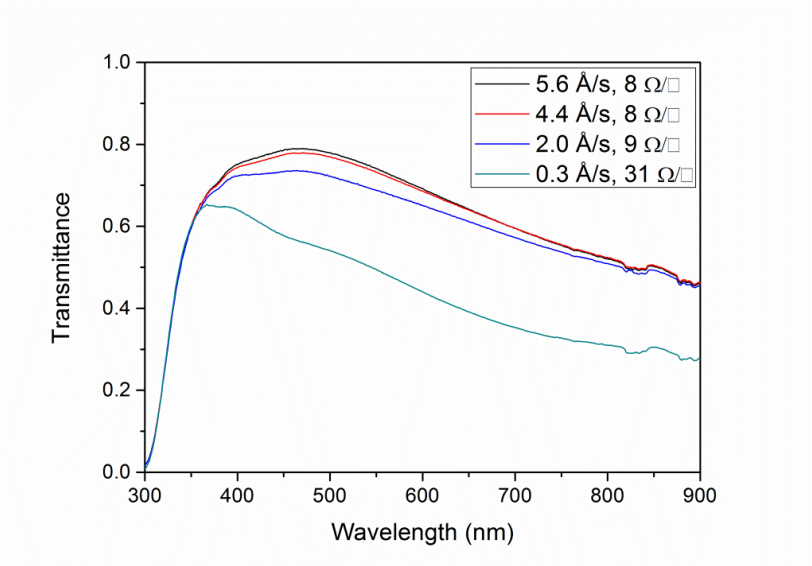

Figure 4.8 Transmittance and sheet resistance of MAM electrodes with different silver deposition rates. All layers in the electrodes had thickness 10 nm. All spectra are referenced to air, meaning that the spectra presented here include reflection and absorption by the glass substrate.

In order to gauge the repeatability and errors involved in electrode fabrication, three MAM electrodes with thickness 10-10-10 nm were fabricated on three different days. As can be seen in **Figure 4.9** their transmittance shows only very slight variation. Maximum transmittance for each of the three samples was 78.2%, 78.5% and 77.6% whilst sheet resistance was 8.4, 8.5 and 8.0 Ω/□ respectively. The minor variations in electrode transmittance and sheet resistance give confidence in the repeatability of the electrode fabrication process.

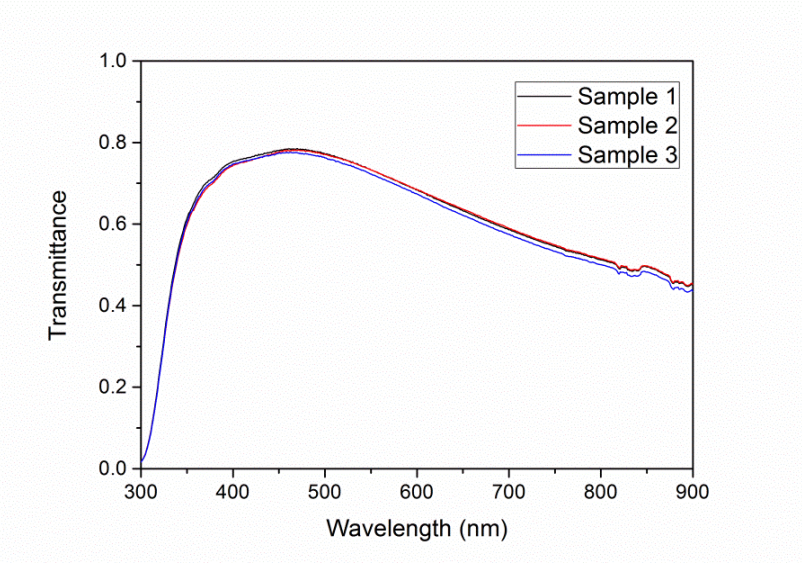

Figure 4.9 Transmittance spectra for three MAM electrodes fabricated on different days, all with layer thicknesses 10-10-10 nm.

4.4 Incorporation into Indium-Free Polymer Solar Cells

In order to demonstrate the practical use of these electrodes, bulk heterojunction polymer solar cells have been fabricated based on a PCDTBT:$PC_{70}BM$ photoactive layer using MAM, TAM and ITO/MoO_3 anodes. In each case the multilayer electrode having the maximum transmittance (also the maximum figure of merit) was used; the MAM electrode thus utilised a 10 nm Ag layer whilst the TAM electrode incorporated a slightly thinner 8 nm Ag layer. This choice was made in order to maximise the short circuit current of the polymer solar cells, and whilst the sheet resistance of the optimised TAM electrode (13.9 Ω/□) is slightly larger than that of the optimised MAM electrode (8.3 Ω/□), it is still lower than that of the reference ITO electrode (15.9 Ω/□) and perfectly adequate for the solar cells fabricated here.

4.4.1 Device Optimisation – Oxide Layer Thickness & Active Layer Thickness

Transfer Matrix Modelling has been used to predict the optimum thickness of the two oxide layers in the multilayer electrode as well as the thickness of the PCDTBT:$PC_{70}BM$ active-layer [25]. The model predicts the electric field strength throughout the device and thus can give a prediction of the device's short-circuit current by assuming an

internal quantum efficiency of 100% (i.e. by assuming each photon absorbed in the active layer generates an exciton which then successfully dissociates and the resulting charges are all extracted). This photocurrent is here termed $J_{SC\_100\%}$. In the model the thickness of the metal oxide seed layer, the thickness of the hole-extraction layer (the metal oxide layer placed adjacent to the active layer) and the thickness of the active semiconductor layer have been varied in order to maximise $J_{SC\_100\%}$. The model predicts that $J_{SC\_100\%}$ is maximized for seed layers having a thickness ≥ 30nm, however this photocurrent is only marginally larger than that predicted when using a 5 nm seed layer. In fact, we find that by adjusting the thickness of the active layer appropriately, $J_{SC\_100\%}$ varies only very slightly from 11.50 to 11.59 mA/cm^2 as the seed layer thickness varies between 5 and 40 nm. Thicker seed layers, however, are predicted to require slightly thicker active layers (by around 10 nm) in order to maximise $J_{SC\_100\%}$. Experimentally, increasing the thickness of the active layer is known to increase losses within the device as a result of increased non-geminate charge recombination. In addition, a thinner seed layer was found experimentally to lead to a marginally lower sheet resistance and a better correspondence to the modelled transmittance (see **Figure 4.10** and **Table 4.2**). For this reason, a relatively thin (5 nm) seed layer was used for the MAM and TAM electrodes – an approach that has also been taken in other studies [27]. With this seed layer thickness of 5 nm the measured average transmittance in the 350–700nm range rises slightly from 70.9% to 71.7% for the optimised MAM electrode and from 76.3% to 77.1% for the optimised TAM electrode. For clarity, it should be noted that the transfer matrix model for transmittance of electrodes assumes that the final layer of the electrode is adjacent to air, as in measured transmittance spectra. The full device modelling, meanwhile, models the entire device structure.

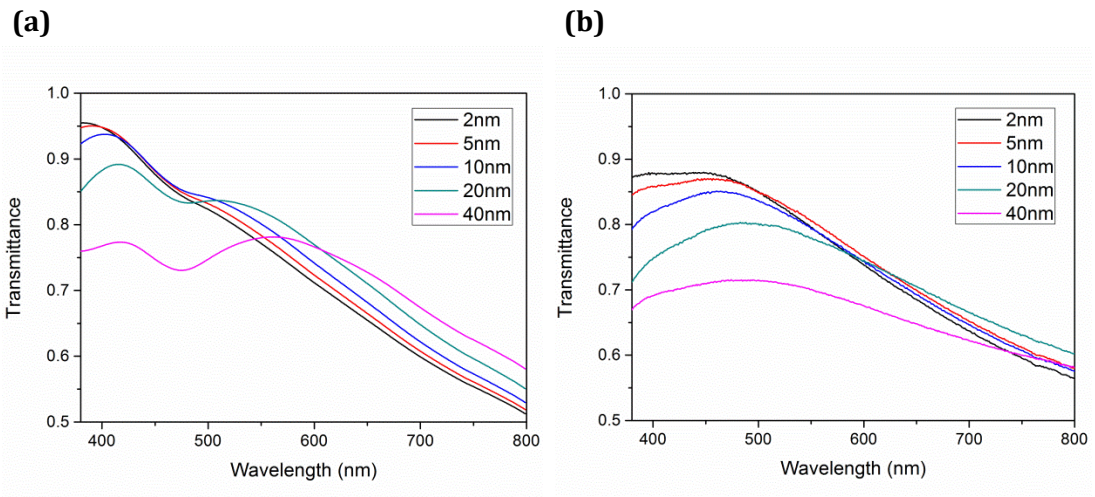

Figure 4.10 Modelled **(a)** and measured **(b)** transmittance with increasing seed layer thickness for MAM electrodes. Note that here the spectra are referenced to glass and thus reflection and absorption losses due to the glass substrate are not included in either the modelled or measured spectra. It can be seen that for the modelled electrodes, a thicker seed layer leads to a significantly increased transmittance at longer wavelengths. Notably, however, this is not observed experimentally.

Seed Layer Thickness (nm)	Sheet Resistance (Ω/□)
2	8.3
5	7.9
10	8.3
20	9.7
40	10.3

Table 4.2 Sheet resistance of MAM electrodes with increasing seed layer thickness (layer thickness x-10-10)

The model predicts that for both oxide/metal/oxide electrodes the maximum value of $J_{SC\_100\%}$ occurs for a metal oxide HTL having a thickness of 10 nm, with the active layer having a thickness of 70 nm. Experimentally it was found that the optimum device efficiency occurred when the active layer was slightly thinner (60 nm thickness) than predicted by the model for both types of multilayer electrode. For devices utilising an ITO/MoO_3 electrode, the model similarly predicted an optimum HTL thickness of 10 nm and an optimum active layer thickness of 85 nm, however experimental measurements determined that the highest device efficiency was realised for an active

layer thickness of 75 nm. Device metrics for different active layer thicknesses are shown in **Table 4.3** (ITO/MoO_3 anode), **Table 4.4** (MAM anode) and **Table 4.5** (TAM anode). In order to aid visualization of this data the PCE and J_{SC} values from the thickness optimisation experiments are presented graphically in **Figure 4.11**. For each variable 4 substrates were fabricated, resulting in 16 pixels (devices) per variable once edge pixels are discounted. In all cases, the discrepancy between the modelled and experimental optimisation results likely results from imperfect charge extraction through the active layer, an effect not considered by the model.

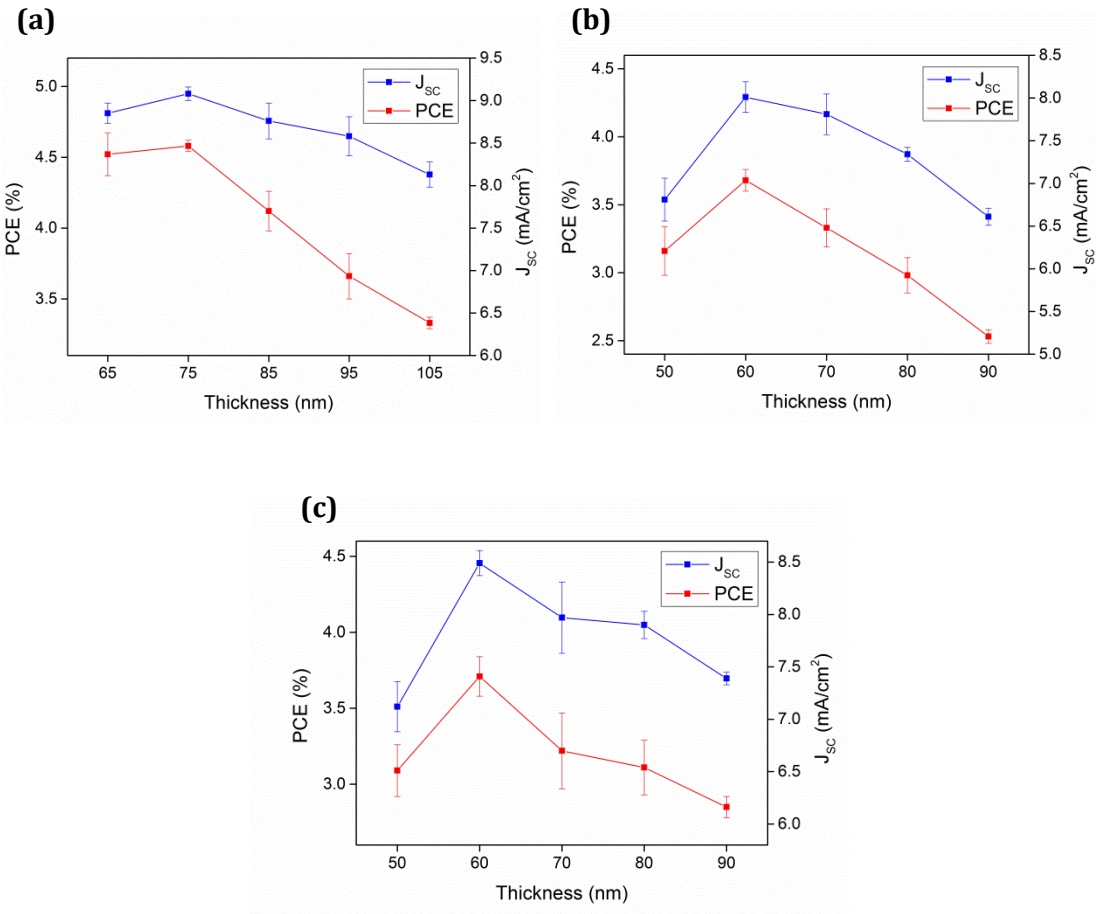

Figure 4.11 Power conversion efficiency (PCE) and short circuit current density (J_{SC}) as a function of active layer thickness for polymer solar cells based on ITO/MoO_3 **(a)**, MAM **(b)** and TAM **(c)** anodes.

Active Layer Thickness (nm)	PCE (%)	J_{SC} (mA/cm²)	V_{OC} (V)	FF (%)
65	4.52	8.85	0.86	60
75	4.58	9.08	0.85	59
85	4.12	8.76	0.85	56
95	3.66	8.58	0.83	52
105	3.33	8.13	0.82	50

Table 4.3 Device metrics for polymer solar cells based on ITO/MoO_3 anodes with varying thickness of the PCDTBT:$PC_{70}BM$ active layer.

Active Layer Thickness (nm)	PCE (%)	J_{SC} (mA/cm²)	V_{OC} (V)	FF (%)
50	3.16	6.81	0.78	60
60	3.68	8.01	0.77	59
70	3.33	7.81	0.74	58
80	2.98	7.34	0.75	54
90	2.53	6.61	0.75	51

Table 4.4 Device metrics for polymer solar cells based on MoO_3/Ag/MoO_3 anodes with varying thickness of the PCDTBT:$PC_{70}BM$ active layer.

Thickness (nm)	PCE (%)	J_{SC} (mA/cm²)	V_{OC} (V)	FF (%)
50	3.09	7.12	0.75	58
60	3.71	8.49	0.76	58
70	3.22	7.97	0.75	54
80	3.11	7.90	0.75	52
90	2.85	7.39	0.75	51

Table 4.5 Device metrics for polymer solar cells based on TeO_2/Ag/MoO_3 anodes with varying thickness of the PCDTBT:$PC_{70}BM$ active layer.

4.4.2 Final Electrode Properties

As detailed above, the MAM and TAM electrodes that were incorporated into PCDTBT:$PC_{70}BM$ polymer solar cells had layer thicknesses of 5-10-10 nm and 5-8-10 nm respectively. The transmittance spectra of these electrodes are presented in **Figure 4.12**.

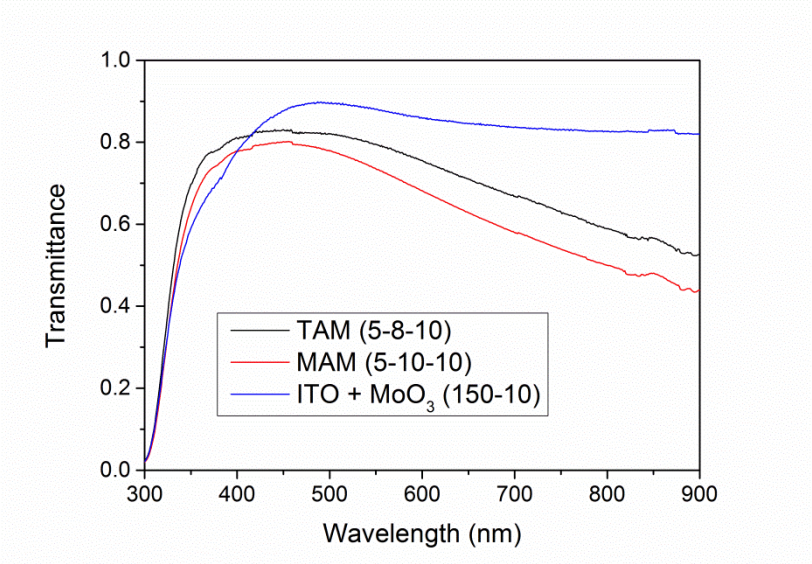

Figure 4.12 Transmittance spectra for the optimised MAM and TAM electrodes with layer thicknesses 5-10-10 nm and 5-8-10 nm respectively. The spectrum for the ITO/MoO_3 reference electrode is also presented.

The surface roughness of the optimised MAM (5-10-10) and TAM (5-8-10) electrodes was studied using atomic force microscopy (AFM). AFM data for a 10 μm x 10 μm area of the surface of each electrode is shown in **Figure 4.13**. Root mean squared surface roughness for the MAM, TAM and ITO/MoO_3 electrodes is 1.42 nm, 0.48 nm and 1.90 nm respectively. These low and comparable values show that all electrodes should be compatible with solar cells requiring a low active layer thickness and that differences in surface roughness between these electrodes are unlikely to significantly influence device performance.

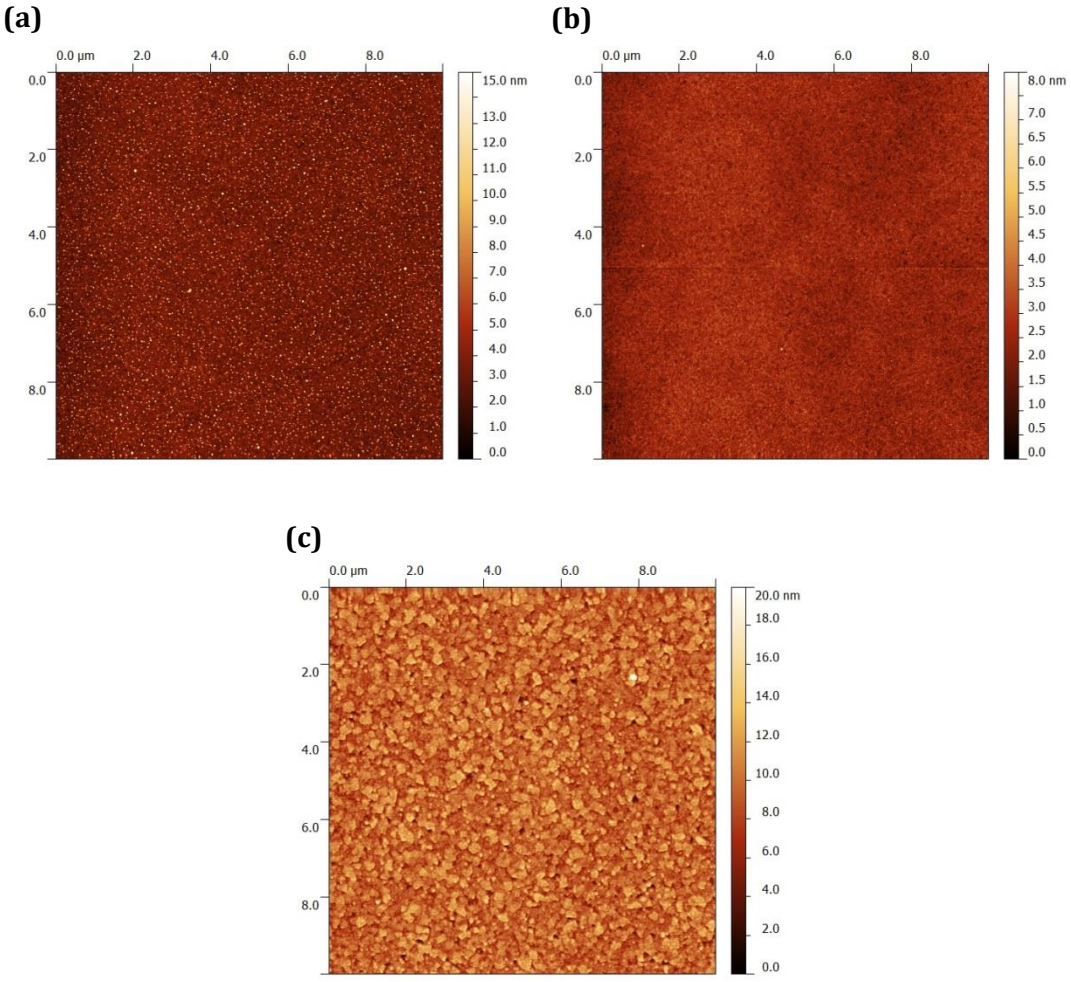

Figure 4.13 Atomic force microscopy images of the optimised electrodes. Part **(a)** shows the MAM electrode with layer thickesses 5-10-10 nm, part **(b)** shows the TAM electrode with layer thicknesses 5-8-10 nm, part **(c)** shows the ITO/MoO_3 electrode with layer thicknesses 150-10 nm. RMS roughness values are 1.42 nm, 0.48 nm and 1.90 nm respectively.

Mobility and resistivity data for the optimised electrodes were taken using a Hall Effect measurement system and are presented in **Table 4.6**. As could be expected the optimised MAM electrode, which has a lower sheet resistance, also has a higher mobility and lower resistivity than the optimised TAM electrode.

Electrode	Sheet Resistance (Ω/□)	Mobility ($cm^2/V{\cdot}s$)	Resistivity (Ω·cm)
$TeO_2/Ag/MoO_3$	13.7	11.6	3.42×10^{-5}
$MoO_3/Ag/MoO_3$	8.1	17.2	1.66×10^{-5}

Table 4.6 Sheet resistance, resistivity and mobility data for the optimised TAM (5-8-10) and MAM (5-10-10) electrodes. Values are the average of two measurements on separate samples.

4.4.3 Final Device Results

For each different anode structure 4 different substrates were fabricated, resulting in 16 devices per anode once edge pixels have been discounted. Average device parameters are tabulated in **Table 4.7**. *JV* curves for a typical device with each type of anode are shown in **Figure 4.14**. The optimised devices using a TAM electrode had an average PCE of (4.22 ± 0.08)% whilst the optimised MAM electrode devices had a slightly lower average PCE of (3.94 ± 0.12)%. The improvement in efficiency for devices incorporating the TAM electrode arises due to a relative enhancement in J_{SC} by 7% from (8.11 ± 0.14) mA/cm² to (8.70 ± 0.12) mA/cm², an effect attributable to the higher transmittance of the TAM electrode. The optimised ITO/MoO_3 reference device had the highest average PCE of (4.81 ± 0.09)%, again resulting from an enhanced J_{SC} of (9.12 ± 0.12) mA/cm². It is worth noting that ITO/MoO_3 devices having an active layer thickness identical to that used in the TAM and MAM devices had a slightly lower PCE of 4.49%, with a comparable J_{SC} to the TAM devices (8.54 ± 0.23) mA/cm².

The ITO/MoO_3 based devices were also characterised by a larger V_{OC} than were the devices utilising a MAM or TAM anode. This effect has been observed previously in MAM based devices [26,28] and has been attributed to diffusion of Ag through the charge extracting metal oxide layer, although such reductions in V_{OC} are not always observed. It is not clear why such reductions in V_{OC} are not uniformly reported; it is possible that, for example, variations in substrate temperature during the evaporation could result in differences in Ag diffusion. We note, however, that if such a reduction in V_{OC} could be eliminated, then devices utilising the TAM electrode would outperform those based on ITO in which a comparable thickness of active layer has been used.

Anode	Electrode Average Transmittance 350–700 nm (%)	Electrode Sheet Resistance (Ω/□)	FF (%)	V_{OC} (V)	J_{SC} (mA/cm²)	PCE (%)
MoO_3/Ag/MoO_3 (60nm active)	71.8 (71.6/72.1)	8.3 (8.2/8.4)	60.7 (1.1)	0.801 (0.006)	8.11 (0.14)	3.94 (0.12)
TeO_2/Ag/MoO_3 (60nm active)	77.2 (77.0/77.4)	13.7 (13.6/13.9)	60.5 (1.0)	0.802 (0.007)	8.70 (0.12)	4.22 (0.08)
ITO/MoO_3 (60nm active)	83.9 (83.7/84.0)	16.0 (15.8/16.3)	59.6 (0.7)	0.882 (0.003)	8.54 (0.23)	4.49 (0.16)
ITO/MoO_3 (75nm active)	83.9 (83.7/84.0)	16.0 (15.8/16.3)	59.7 (0.7)	0.885 (0.003)	9.12 (0.24)	4.81 (0.09)

Table 4.7 Electrode properties and solar cell performance for MAM (5-10-10), TAM (5-8-10) and ITO/MoO_3 (150-10) electrodes. The ITO electrode was tested with active layer thickness of both 60nm and 75nm. Standard deviations for device parameters are shown in brackets. Electrode properties are the mean (max/min) of three values.

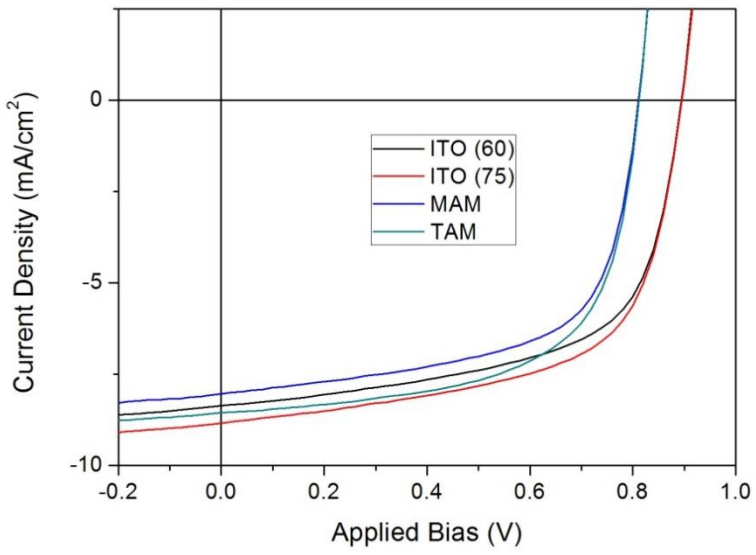

Figure 4.14 Current-density against voltage curves for typical devices fabricated using the different anodes. ITO (60) refers to the ITO based devices with a 60 nm thick active layer; ITO (75) refers to the ITO based devices with a 75 nm thick active layer.

4.5 Conclusions

In conclusion, TeO_2/Ag/MoO_3 (TAM) and MoO_3/Ag/MoO_3 (MAM) multilayer electrodes have been fabricated. The optimised TAM electrodes have an average transmittance of 77.1% over the wavelength range 350–700 nm whilst the optimised MAM electrodes have a reduced average transmittance of 71.7% over the same range. The enhanced transmittance of the TAM electrodes is attributable to the lower percolation threshold of the silver film on the TeO_2 seed layer than on the MoO_3 seed layer (8 nm vs 10 nm). When applied as the transparent front electrode in PCDTBT:$PC_{70}BM$ polymer solar cells the higher transmittance of the TAM electrode leads to an enhanced J_{SC} and thus an enhanced PCE. These efficiencies are, however, generally smaller than those of devices based on conventional ITO electrodes. In conclusion, TeO_2 appears to be a promising replacement for MoO_3 as the seed layer material in oxide/metal/oxide indium-free electrodes.

4.6 References

[1] V. Shrotriya, G. Li, Y. Yao, C.-W. Chu, Y. Yang, Transition metal oxides as the buffer layer for polymer photovoltaic cells, Appl. Phys. Lett. 88 (2006) 073508.

[2] R. Steim, F.R. Kogler, C.J. Brabec, Interface materials for organic solar cells, J. Mater. Chem. 20 (2010) 2499–2512.

[3] J.C.C. Fan, Transparent heat-mirror films of TiO_2/Ag/TiO_2 for solar energy collection and radiation insulation, Appl. Phys. Lett. 25 (1974) 693.

[4] C. Guillén, J. Herrero, TCO/metal/TCO structures for energy and flexible electronics, Thin Solid Films. 520 (2011) 1–17.

[5] L. Shen, S. Ruan, W. Guo, F. Meng, W. Chen, Semitransparent inverted polymer solar cells using MoO_3/Ag/V_2O_5 as transparent anodes, Sol. Energy Mater. Sol. Cells. 97 (2012) 59–63.

[6] F. Li, S. Ruan, Y. Xu, F. Meng, J. Wang, W. Chen, et al., Semitransparent inverted polymer solar cells using MoO_3/Ag/WO_3 as highly transparent anodes, Sol. Energy Mater. Sol. Cells. 95 (2011) 877–880.

[7] T. Dimopoulos, G.Z. Radnoczi, B. Pécz, H. Brückl, Characterization of

ZnO:Al/Au/ZnO:Al trilayers for high performance transparent conducting electrodes, Thin Solid Films. 519 (2010) 1470–1474.

[8] D.S. Ghosh, T.L. Chen, N. Formica, J. Hwang, I. Bruder, V. Pruneri, High figure-of-merit Ag/Al:ZnO nano-thick transparent electrodes for indium-free flexible photovoltaics, Sol. Energy Mater. Sol. Cells. 107 (2012) 338–343.

[9] Y.-S. Lin, W.-C. Tseng, Effect of Al Nanoparticles on the Microstructure, Electrical, and Optical Properties of AZO/Al/AZO Trilayer Thin Film, J. Electron. Mater. 41 (2011) 437–441.

[10] S.H. Mohamed, Effects of Ag layer and ZnO top layer thicknesses on the physical properties of ZnO/Ag/Zno multilayer system, J. Phys. Chem. Solids. 69 (2008) 2378–2384.

[11] F. Li, Z. Lin, B. Zhang, Y. Zhang, C. Wu, T. Guo, Fabrication of flexible conductive graphene/Ag/Al-doped zinc oxide multilayer films for application in flexible organic light-emitting diodes, Org. Electron. 14 (2013) 2139–2143.

[12] H.M. Stec, R.A. Hatton, Widely applicable coinage metal window electrodes on flexible polyester substrates applied to organic photovoltaics, ACS Appl. Mater. Interfaces. 4 (2012) 6013–6020.

[13] N.P. Sergeant, A. Hadipour, B. Niesen, D. Cheyns, P. Heremans, P. Peumans, et al., Design of transparent anodes for resonant cavity enhanced light harvesting in organic solar cells, Adv. Mater. 24 (2012) 728–732.

[14] I.P. Lopéz, L. Cattin, D.-T. Nguyen, M. Morsli, J.C. Bernède, Dielectric/metal/dielectric structures using copper as metal and MoO3 as dielectric for use as transparent electrode, Thin Solid Films. 520 (2012) 6419–6423.

[15] D.-T. Nguyen, S. Vedraine, L. Cattin, P. Torchio, M. Morsli, F. Flory, et al., Effect of the thickness of the MoO3 layers on optical properties of MoO3/Ag/MoO3 multilayer structures, J. Appl. Phys. 112 (2012) 063505. doi:10.1063/1.4751334.

[16] L. Cattin, M. Morsli, F. Dahou, S.Y. Abe, A. Khelil, J.C. Bernède, Investigation of low resistance transparent MoO3/Ag/MoO3 multilayer and application as anode in organic solar cells, Thin Solid Films. 518 (2010) 4560–4563.

[17] J.-F. Salinas, H.-L. Yip, C.-C. Chueh, C.-Z. Li, J.-L. Maldonado, A.K.-Y. Jen, Optical

Design of Transparent Thin Metal Electrodes to Enhance In-Coupling and Trapping of Light in Flexible Polymer Solar Cells, Adv. Mater. 24 (2012) 6362–6367.

[18] F. Nehm, S. Schubert, L. Müller-Meskamp, K. Leo, Observation of feature ripening inversion effect at the percolation threshold for the growth of thin silver films, Thin Solid Films. 556 (2014) 381–384.

[19] H.-K. Park, J.-W. Kang, S.-I. Na, D.-Y. Kim, H.-K. Kim, Characteristics of indium-free GZO/Ag/GZO and AZO/Ag/AZO multilayer electrode grown by dual target DC sputtering at room temperature for low-cost organic photovoltaics, Sol. Energy Mater. Sol. Cells. 93 (2009) 1994–2002.

[20] D. Zhang, H. Yabe, E. Akita, P. Wang, R. Murakami, X. Song, Effect of silver evolution on conductivity and transmittance of ZnO/Ag thin films, J. Appl. Phys. 109 (2011) 104318.

[21] K.-H. Choi, H.-J. Nam, J.-A. Jeong, S.-W. Cho, H.-K. Kim, J.-W. Kang, et al., Highly flexible and transparent $InZnSnO_x$/Ag/$InZnSnO_x$ multilayer electrode for flexible organic light emitting diodes, Appl. Phys. Lett. 92 (2008) 223302.

[22] W.-F. Xu, C.-C. Chin, D.-W. Hung, P.-K. Wei, Transparent electrode for organic solar cells using multilayer structures with nanoporous silver film, Sol. Energy Mater. Sol. Cells. 118 (2013) 81–89.

[23] D. Jeannot, J. Pinard, P. Ramoni, E.M. Jost, Physical and Chemical Properties of Metal Oxide Additions to Ag-SnO_2 Contact Materials and Predictions of Electrical Performance, IEEE Trans. Components, Packag. Manuf. Technol. 17 (1994) 17–23.

[24] S. Schubert, J. Meiss, L. Müller-Meskamp, K. Leo, Improvement of Transparent Metal Top Electrodes for Organic Solar Cells by Introducing a High Surface Energy Seed Layer, Adv. Energy Mater. 3 (2013) 438–443.

[25] G.F. Burkhard, E.T. Hoke, M.D. McGehee, Accounting for interference, scattering, and electrode absorption to make accurate internal quantum efficiency measurements in organic and other thin solar cells., Adv. Mater. 22 (2010) 3293–3297.

[26] L. Cattin, Y. Lare, M. Makha, M. Fleury, F. Chandezon, T. Abachi, et al., Effect of the Ag deposition rate on the properties of conductive transparent MoO_3/Ag/MoO_3 multilayers, Sol. Energy Mater. Sol. Cells. 117 (2013) 103–109.

[27] Z. Wang, C. Zhang, R. Gao, D. Chen, S. Tang, J. Zhang, et al., Improvement of transparent silver thin film anodes for organic solar cells with a decreased percolation threshold of silver, Sol. Energy Mater. Sol. Cells. 127 (2014) 193–200.

[28] T. Abachi, L. Cattin, G. Louarn, Y. Lare, A. Bou, M. Makha, et al., Highly flexible, conductive and transparent MoO_3/Ag/MoO_3 multilayer electrode for organic photovoltaic cells, Thin Solid Films. 545 (2013) 438–444.

Chapter 5: Spray-Deposited Planar Heterojunction Perovskite Solar Cells

5.1 Introduction

In order for solution processed solar cells to realise their potential in bringing cost savings to large-scale solar cell fabrication it is necessary to demonstrate their compatibility with industrially applicable film deposition techniques. With this goal in mind the roll-to-roll compatible deposition method of ultrasonic spray-coating was introduced in **Chapter 2**. Having previously been employed in the fabrication of polymer solar cells [1,2], this technique is here applied to the fabrication of the photoactive layer of solar cells based on the perovskite $CH_3NH_3PbI_{3-x}Cl_x$. At the time of publication of this work in *Energy & Environmental Science*, this was the first report of the application of a roll-to-roll compatible solution processing technique to the deposition of the perovskite layer of a solar cell. In addition, at this time it was the highest reported efficiency for a solar cell employing a spray-deposited photoactive layer. The technique of ultrasonic spray-coating is then extended to the both interlayers of the device: the hole transport layer PEDOT:PSS and the electron transport layer $PC_{70}BM$.

5.1.1 Materials and Architecture Choice

A planar device architecture has been chosen for the solar cells fabricated in this work, together with the 'one-step' process for fabrication of the perovskite layer. This device architecture and processing route were selected for their simplicity and small number of processing steps, both of which would be likely to prove advantageous in a commercial setting as well as facilitating the fabrication of a proof of concept device in this work. An inverted architecture (transparent front anode) was chosen in order to allow simple fabrication of charge transport layers without the necessity for high temperature sintering (~500°C) which is typically required for perovskite solar cells with normal architecture due to their use of TiO_2.

The greater diffusion length of perovskite films based on the mixed halide perovskite ($CH_3NH_3PbI_{3-x}Cl_x$) in comparison to the tri-iodide perovskite ($CH_3NH_3PbI_3$), as discussed in **Sections 2.5.4** and **2.5.8**, makes this material particularly suitable for planar heterojunction devices. Charge diffusion lengths of >1 μm allow for the use of planar perovskite layers many hundreds of nanometres thick without incurring high recombination losses. It has, indeed, been suggested in the literature that the triiodide perovskite may be better suited to being used in a sensitized device as opposed to planar or meso-superstructred devices, due to its shorter diffusion length [3]. In addition, the mixed halide perovskite has been shown to have more balanced charge transport than its triiodide counterpart and has typically proved more resistant to processing in ambient conditions [4–6]. For these reasons, and in particular since all spray-coating was carried out in air, the mixed halide perovskite has been employed in this work. It is noteworthy that despite the above issues, planar devices based on the triiodide perovskite have now reached PCEs in excess of 15% [7–9].

5.2 Process Optimisation

An optimisation procedure for spray-deposition of the $CH_3NH_3PbI_{3-x}Cl_x$ perovskite layer has been undertaken in order to allow fabrication of a high efficiency 'proof of concept' spray-coated perovskite solar cell. In line with early literature reports, a precursor solution of methylammonium iodide (MAI) and lead (II) chloride ($PbCl_2$) in a 3:1 molar ratio was used. This solution was deposited via ultrasonic spray-coating onto glass/ITO/PEDOT:PSS substrates onto which the PEDOT:PSS hole transport layer (thickness ~30 nm) had been deposited via spin-coating. After initial trials with a solution concentration for the MAI:$PbCl_2$ blend of 50 mg/ml, this was increased to 100 mg/ml in order to allow deposition of perovskite films with an appropriate thickness (hundreds of nm) without excessive drying times due to high solvent volumes. A detailed optimisation of solution concentration was not undertaken.

It is worth noting that in early experiments no record of relative humidity was taken. It has since emerged that this parameter can have a significant impact on device performance and indeed anecdotally in this research group it has been observed that high humidity often leads to poor device performance. The group's spin-out company, Ossila Ltd, have also observed this for devices based on spin-coated perovskite layers

in a more rigorous experiment. This agrees with published work where, when film deposition and annealing take place within the same environment, higher humidity was found to lead to a reduced solar cell efficiency [6]. For completeness, in later experiments where relative humidity has been measured during film fabrication this information has been included in the relevant Figure and Table captions.

5.2.1 Substrate Temperature

Given that the drying dynamics of a spray-deposited film can have a strong influence on film formation, substrate temperature during the spray-coating process can be expected to have an effect on the quality of the resulting perovskite films. In order to investigate this process perovskite films were fabricated via ultrasonic spray-coating with substrates held at temperatures varying from 28–103°C. The solvent dimethylformamide (DMF) was used for the perovskite precursor solution. Following film deposition, a 90 minute thermal anneal at 90°C was applied in order to convert the precursor films (bright yellow in colour) into the desired perovskite material (black/dark brown in colour). Optical microscopy images of the resultant films, with thickness (250 ± 20) nm, are shown in **Figure 5.1**. Whilst all films provided reasonable uniformity to the eye, at low substrate temperatures, corresponding to relatively long drying times (minutes), the optical micrographs show relatively large crystalline regions separated by large voids, leading to a low overall surface coverage. The film deposited at 28°C, for example, exhibits a surface coverage of only around 65%. With increasing substrate temperature the surface coverage increases significantly, reaching a maximum at 75°C. Increased surface coverage is known to lead to improved solar cell performance due to enhanced absorption (resulting in an increased J_{SC}) and reduced leakage paths (resulting in an increased V_{OC} and FF) [10,11]. Concurrent with the increase in surface coverage at higher substrate temperatures, the needle-like crystalline regions become significantly smaller (micron sized). Above 75°C the size of these needle-like features begins to increase again, accompanied by a reduction in overall surface coverage. On the basis of this investigation it was decided that a substrate temperature of 75°C would be used during film deposition in order to maximise the surface coverage of the perovskite film on the underlying ITO/PEDOT:PSS electrode.

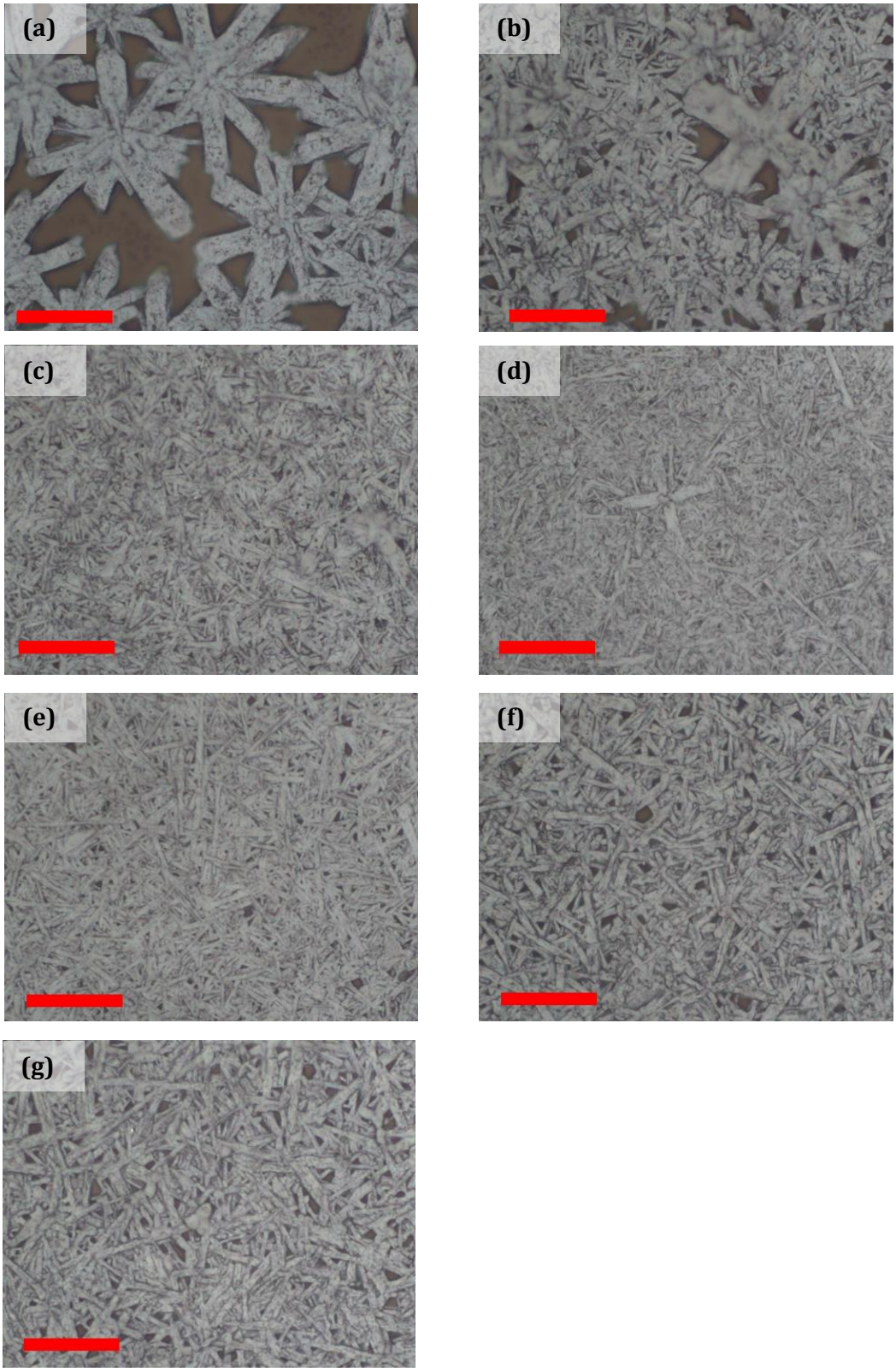

Figure 5.1 Optical microscopy images of perovskite films deposited via spray-coating from the solvent DMF and subsequently annealed for 90 minutes at 90°C. Substrates were held at a range of different temperatures: **(a)** 28°C, **(b)** 38°C, **(c)** 55°C, **(d)** 75°C, **(e)** 80°C, **(f)** 87°C, **(g)** 103°C. Red scale bars correspond to 20 μm.

5.2.2 Annealing Protocol

Spray-coated MAI:$PbCl_2$ films, deposited at a substrate temperature of 75°C, have been subjected to different thermal annealing procedures in order to investigate the effect of annealing temperature on film surface coverage. Optical microscopy images of the resultant films of thickness (300 ± 30) nm are shown in **Figure 5.2**. When an annealing temperature of 90°C is used the resulting perovskite film shows good surface coverage (**Figures 5.2(a)–(c)**). After an anneal time of 30 minutes, shown in **Figure 5.2(a)**, the precursor to perovskite transition does not appear to be complete as can be observed by the dark regions in the image. In parts **(b)** and **(c)**, corresponding to annealing times of 60 and 90 minutes respectively, these regions are not observed; the 90 minute anneal does, however, appear to give a slightly improved surface coverage over the 60 minute anneal. At the lower annealing temperature of 70°C, even after an extended 2 hour anneal time the film retains a significant yellow hue whilst exhibiting colour variation across its surface, indicative of an extremely slow transformation to the perovskite material. A film annealed for 90 minutes at 70°C is shown in **Figure 5.2(d)** where it can be observed that film coverage at this point is also notably inferior to those films annealed at 90°C. If the annealing temperature is increased above 90°C the morphology of the resultant film changes to show larger crystalline features with significant voids between them and surface coverage is reduced. This effect can be seen in **Figure 5.2(e)** which shows a film annealed at 110°C for 30 minutes; longer annealing times at this temperature lead to a slow colour change of the film back to yellow, as can be observed in **Figure 5.2(f)**, an effect which can be attributed to the degradation of the perovskite into products including yellow lead (II) iodide (PbI_2) [12–14]. Annealing the precursor film at 130°C (**Figure 5.2(g)**) was seen to also cause an increase in size of the crystalline regions of the film and lead to a poor surface coverage. As a consequence of these observations, a 90 minute thermal anneal at 90°C was chosen for the continuation of this work, in line with other early reports which typically found optimum annealing temperatures of 90–100°C for periods of 45–120 minutes. In these reports lower temperatures were observed to result in incomplete conversion of the precursor film and/or inferior surface coverage whilst higher temperatures significantly reduced surface coverage [10,13]. Whilst a rigorous optimisation of annealing time based on device performance was not undertaken at this time, a later optimisation of spin-coated devices with a similar perovskite film thickness of (370 ± 10) nm found an optimum annealing time of 90 minutes. Device metrics from this later experiment are presented in **Table 5.1**.

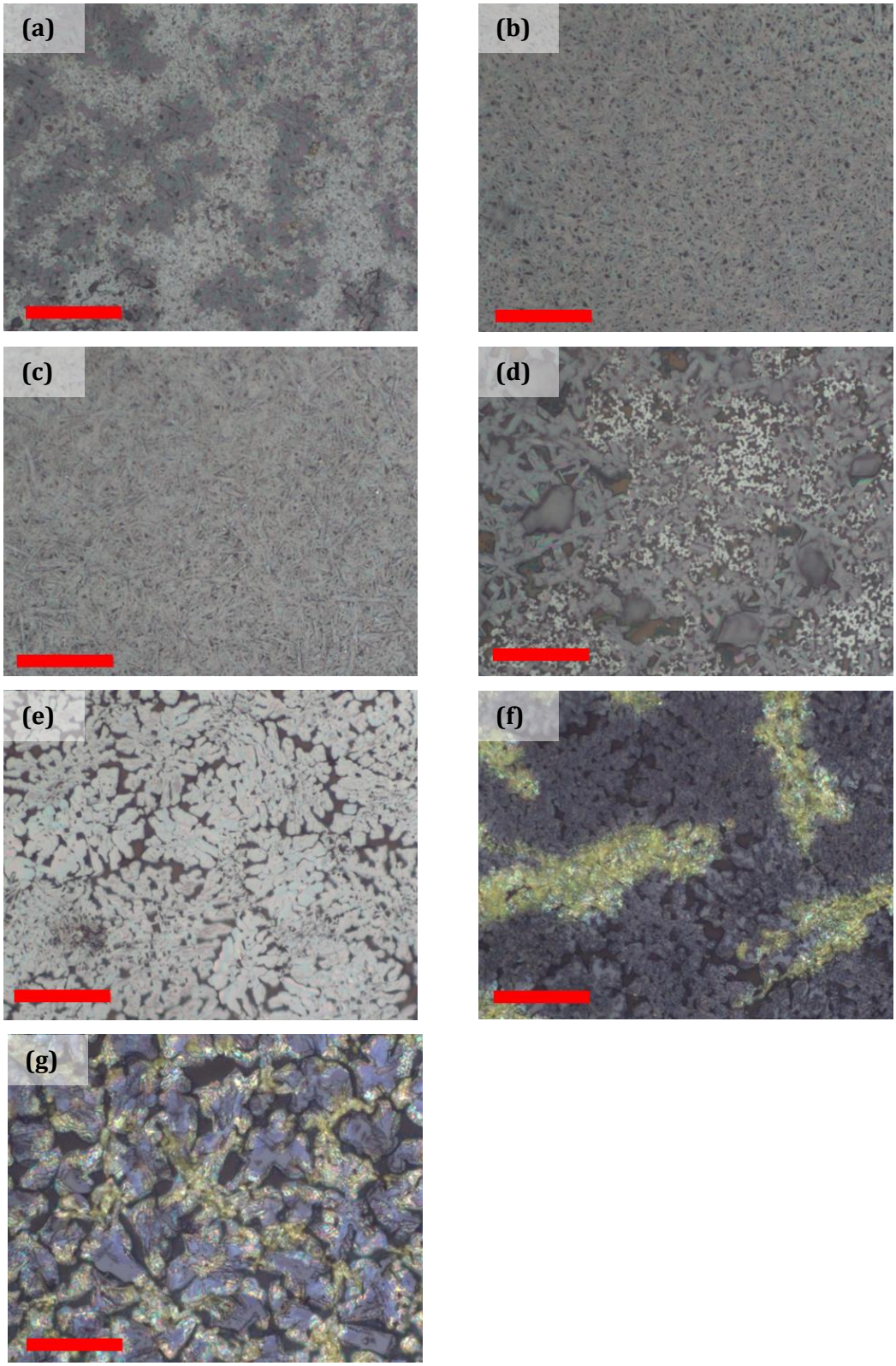

Figure 5.2 Optical microscopy images of perovskite films deposited via spray-coating at a substrate temperature of 75°C and subsequently annealed at 90°C for 30 minutes **(a)**, 60 minutes **(b)** and 90 minutes **(c)**; 70°C for 90 minutes **(d)**; 110°C for 30 minutes **(e)** and 90 minutes **(f)** and 130°C for 30 minutes **(g)**. Red scale bars correspond to 20 μm.

Anneal Time (min)	PCE (%) (max)	J_{SC} (mA/cm^2)	V_{OC} (V)	FF (%)
50	8.7 ± 1.0 (10.9)	15.0 ± 0.7	0.965 ± 0.008	59.9 ± 4.7
70	10.7 ± 0.2 (11.1)	17.5 ± 0.2	0.892 ± 0.004	68.6 ± 1.0
90	11.4 ± 0.4 (11.8)	16.9 ± 0.6	0.929 ± 0.022	72.4 ± 1.5
110	9.8 ± 0.2 (10.1)	16.7 ± 0.4	0.874 ± 0.010	66.9 ± 1.5
130	10.0 ± 0.1 (10.2)	16.5 ± 0.2	0.878 ± 0.009	69.4 ± 1.0

Table 5.1 Device metrics for different annealing times for spin-coated perovskite films annealed at 90°C. Note that devices were fabricated in a relative humidity of ~30% and with a different batch of materials to those employed in this chapter. Errors given are standard deviations. For PCE the maximum value is also given in brackets.

5.2.3 Perovskite Layer Thickness

A number of solar cell devices were fabricated in order to optimise the thickness of the spray-coated photoactive perovskite layer. Solar cells with a device architecture ITO/PEDOT:PSS/$CH_3NH_3PbI_{3-x}Cl_x$/$PC_{60}BM$/Ca/Al were fabricated with perovskite layer thickness varying from 290–1150 nm; for each thickness 5 substrates (containing a total of 20 devices) were fabricated. Device metrics for the fabricated solar cells are tabulated in **Table 5.2** with power conversion efficiency against perovskite layer thickness presented in **Figure 5.3**. PCE is highest (6.5% average) for an active layer thickness of 340 nm, a value comparable to the layer thickness typically used in early literature reports as well as the recent high efficiency devices [8,15–18]. Films as thick as 670 nm are still, however, able to produce a high average efficiency of 6.0%. This unusually broad tolerance of PCE to film thickness is likely due to the long charge diffusion lengths observed in mixed halide perovskite films [19,20]; indeed in early literature reports PCEs in excess of 11% were obtained using planar perovskite layers with a wide range of thicknesses from 140–500 nm [10,21].

Perovskite Layer Thickness (nm)	PCE (%)	J_{SC} (mA/cm²)	V_{OC} (V)	FF (%)
290 ± 30	3.3 ± 0.5	10.8 ± 0.8	0.73 ± 0.05	42 ± 3.4
340 ± 30	6.5 ± 0.8	15.2 ± 0.7	0.78 ± 0.10	55 ± 3.6
450 ± 40	5.0 ± 0.5	10.4 ± 0.9	0.86 ± 0.03	56 ± 2.1
670 ± 200	6.0 ± 0.3	12.2 ± 0.5	0.87 ± 0.03	57 ± 1.5
1150 ± 250	3.7 ± 2.1	10.8 ± 4.1	0.72 ± 0.22	42.1 ± 6.5

Table 5.2 Device metrics for perovskite solar cells with varying thickness of the spray-cast $CH_3NH_3PbI_{3-x}Cl_x$ active layer. Errors given are standard deviations.

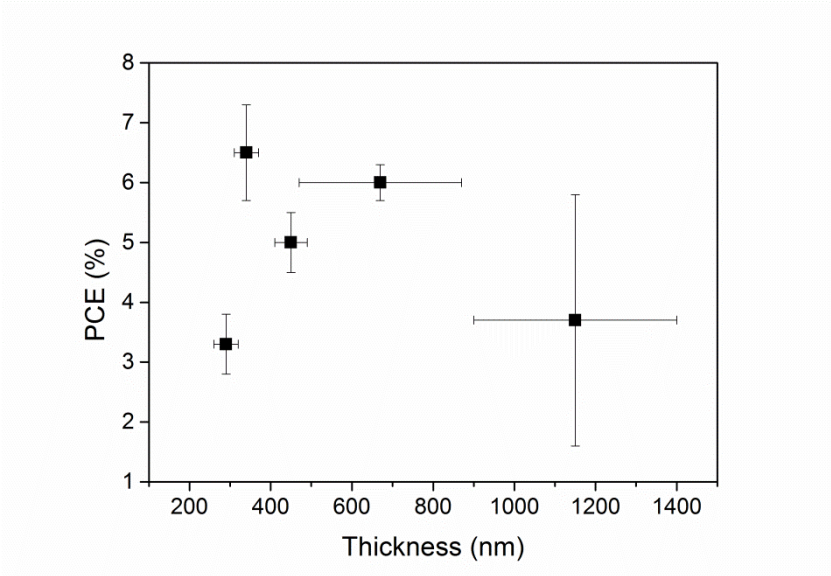

Figure 5.3 Power conversion efficiency (PCE) against active layer thickness for spray-cast perovskite solar cells.

5.2.4 Casting Solvent: DMSO

In order to investigate the effect of casting solvent on perovskite film formation, the precursor solution was spray-coated from the solvent dimethyl sulphoxide (DMSO) in replacement for the solvent dimethylformamide (DMF). Films deposited from DMSO can be expected to exhibit differences to those deposited from DMF due to its higher boiling point (189°C for DMSO as compared to 153°C for DMF). Substrate temperature during the deposition process was varied, as for the films spray-cast from DMF, and following the drying of the films a 90 minute thermal anneal at 90°C was again applied in order to convert the precursor films to perovskite. Final perovskite films had thickness of (370 ± 30) nm. Optical microscopy images for the resulting films are presented in **Figure 5.4.** As can be seen in the insets in **Figures 5.4(a)** and **(b)**, at substrate temperatures of 28°C and 38°C there is significant de-wetting of the film due to the extended drying time (20 minutes or more), leading to incomplete coverage of the substrate. As the temperature is increased to 55°C, 75°C and 80°C macroscopically uniform films are formed, however on inspection of the optical micrographs it can be seen that these films consist of large perovskite crystals which are separated by significant voids. At 87°C and above (**Figures 5.4(f)** and **(g)**), the crystal size is notably reduced although surface coverage is not detrimentally affected. At all temperatures surface coverage can be seen to be significantly lower than for counterpart films deposited from DMF (presented above in **Figure 5.1**).

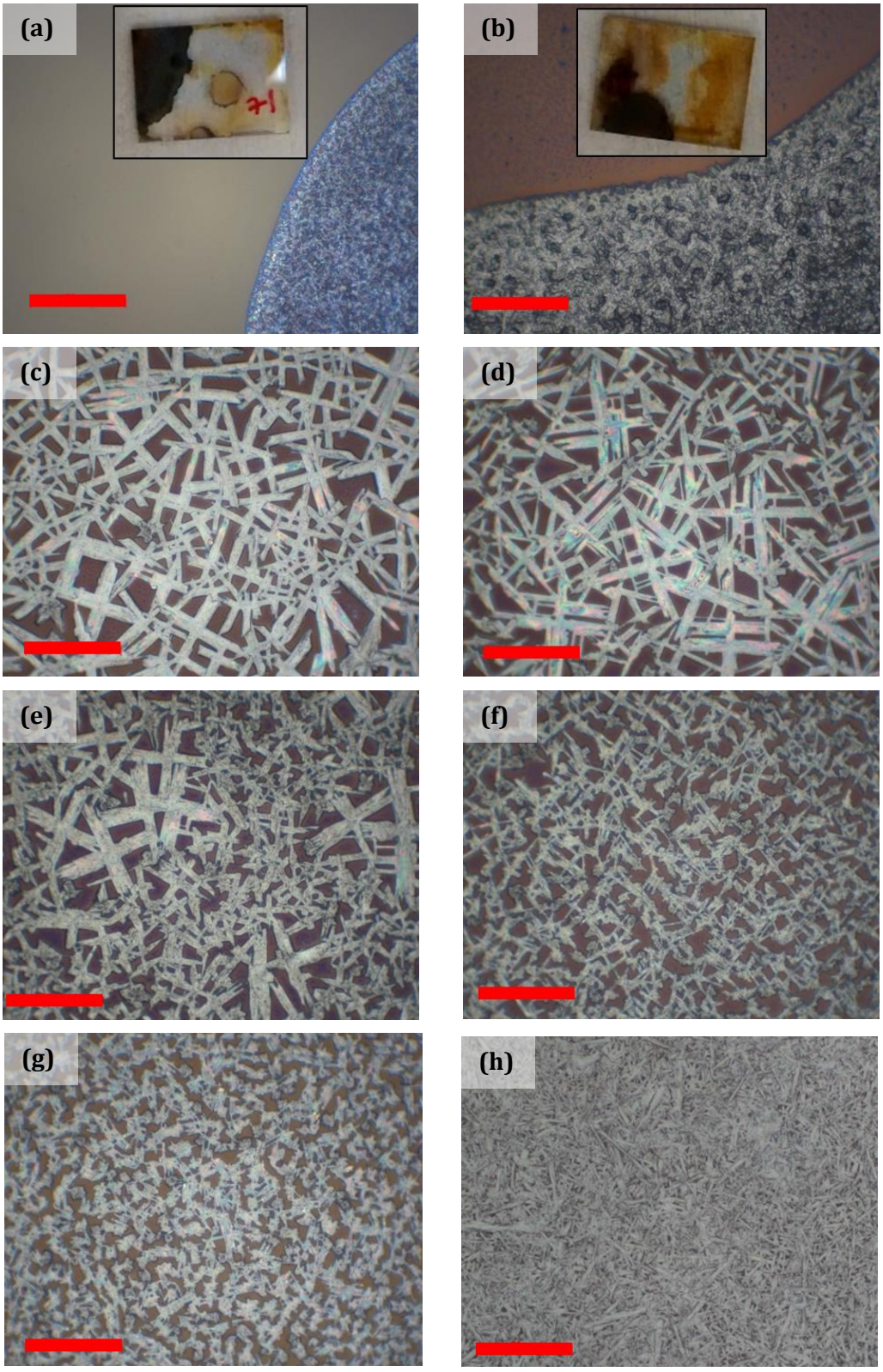

Figure 5.4 Optical microscopy images of perovskite films deposited via spray-coating from the solvent DMSO and subsequently annealed for 90 minutes at 90°C. Substrates were held at a range of different temperatures: **(a)** 28°C, **(b)** 38°C, **(c)** 55°C, **(d)** 75°C, **(e)** 80°C, **(f)** 87°C, **(g)** 103°C. Part **(h)** shows a reference film spray-cast from DMF onto a substrate held at 75°C. Red scale bars correspond to 20 μm.

In order to confirm how the observed changes affect device performance, perovskite solar cells were fabricated employing films deposited at each substrate temperature. 3 substrates (containing a total of 12 devices) were fabricated per deposition temperature. Average device metrics are presented in **Table 5.3** with power conversion efficiency against deposition temperature presented in **Figure 5.5**. Devices fabricated with deposition temperatures of 28°C and 38°C exhibit very low efficiencies due to significant de-wetting from large areas of the substrate, as detailed above. PCEs for devices fabricated using deposition temperatures of 55–80°C are higher, although efficiencies still remain quite poor due to the low surface coverage. At 87°C and 103°C photovoltaic performance is reduced, although from the optical micrographs presented in **Figures 5.4(f)** and **(g)** this does not appear to be due to surface coverage effects.

Deposition Temperature (°C)	**PCE (%) (max)**	**J_{SC} (mA/cm²)**	**V_{OC} (V)**	**FF (%)**
28	0.21 ± 0.13 (0.38)	1.81 ± 0.77	0.28 ± 0.14	32.7 ± 6.2
38	0.04 ± 0.03 (0.07)	0.67 ± 0.31	0.20 ± 0.07	25.5 ± 1.9
55	2.52 ± 1.77 (4.81)	9.95 ± 0.63	0.47 ± 0.27	47.6 ± 9.6
75	2.47 ± 0.54 (3.52)	9.28 ± 1.27	0.51 ± 0.06	53.2 ± 8.8
80	3.05 ± 0.45 (3.88)	9.62 ± 0.54	0.56 ± 0.06	56.8 ± 2.8
87	0.84 ± 0.40 (1.43)	8.20 ± 0.57	0.25 ± 0.07	38.5 ± 9.9
103	0.64 ± 0.13 (0.82)	4.67 ± 0.71	0.38 ± 0.03	35.9 ± 1.1

Table 5.3 Average device metrics for solar cells fabricated using a spray-cast perovskite film, deposited from a DMSO solution onto substrates at different temperatures. Errors given are standard deviations. For PCE the maximum value is also given in brackets.

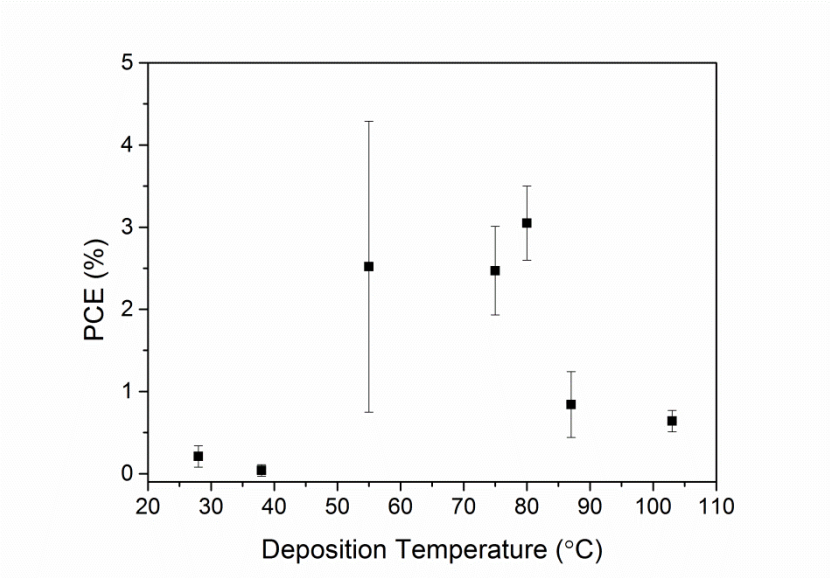

Figure 5.5 Power conversion efficiency (PCE) against substrate temperature during deposition for perovskite solar cells in which the photoactive layer was deposited by spray-coating from a solution in DMSO.

Overall it can be seen that the slow drying dynamics of the films deposited from DMSO appear to lead to a reduced surface coverage and hence a low solar cell efficiency. It was thus decided that precursor solutions utilising DMF as the solvent would be used in the fabrication of future devices.

5.3 Film Characterization

The 2D GIWAXS patterns for spray-coated and spin-coated perovskite films following a thermal anneal for 90 minutes at 90°C are shown in **Figure 5.6(a)** and **(b)** respectively. The observation of scattering rings indicates a polycrystalline film in which crystal grains take various orientations; further discussion on detailed analysis of X-ray scattering data for perovskite samples is presented in **Chapter 6**. **Figure 5.6(c)** presents azimuthally integrated radial line profiles for each measurement, from which it is clear that both deposition methods produce films with very similar crystal structures. The strong peak at q ≈ 1 $Å^{-1}$ is widely attributed to the (110) plane of the tetragonal $CH_3NH_3PbI_{3-x}Cl_x$ perovskite structure, although the (002) plane, having scattering peak at q = 0.99 $Å^{-1}$, may also provide a contribution to this feature [22,23]. Similarly the peak at q ≈ 2 $Å^{-1}$ can be attributed to the (220) and (004) planes of the

same structure. Further peak positions for this crystal structure have been predicted by simulation by Dr. Samuele Lilliu (data unpublished) using crystallographic information files from ref [24]. The planes contributing to the peaks observed in the GIWAXS data have been noted in **Figure 5.6(c)**.

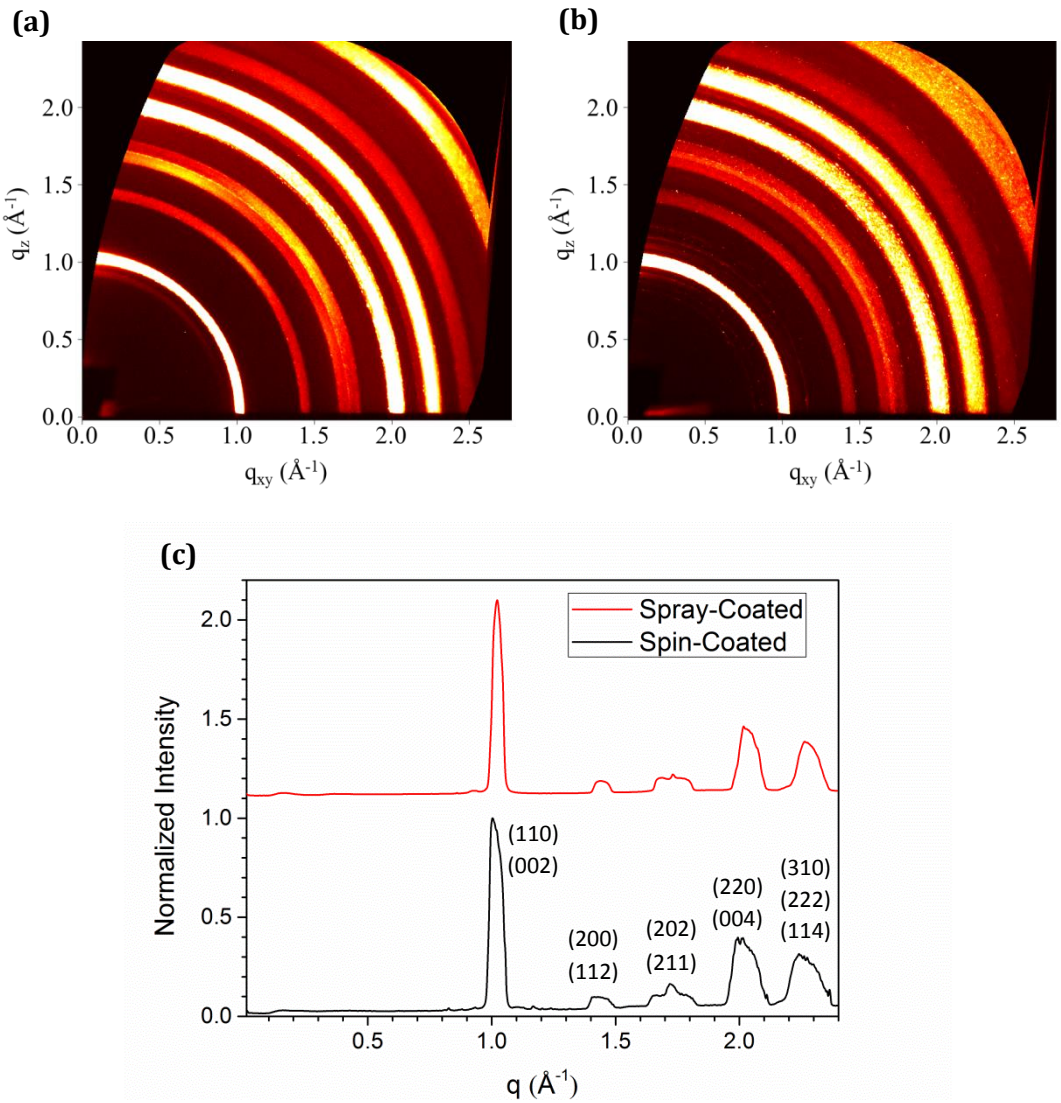

Figure 5.6 2D GIWAXS images of a spray-coated perovskite film **(a)** and a spin-coated perovskite film **(b)**, together with azimuthally integrated radial line profiles for both samples **(c)**. Each sample has been annealed for 90 minutes at 90°C.

Atomic force microscopy (AFM) has been performed on a spray-coated perovskite film in order to further investigate its morphology and surface roughness; an AFM image is presented in **Figure 5.7**. The root mean squared surface roughness for the film is 56 nm, a figure that is large for a film having a thickness of (270 ± 40) nm. In addition, the

largest height variations are hundreds of nm in magnitude. A relatively thick (~120 nm) electron transport layer of $PC_{60}BM$ has thus been employed in the solar cells fabricated herein in order to planarize the rough perovskite film as far as possible, thereby minimizing direct contact between the perovskite and the metal cathode.

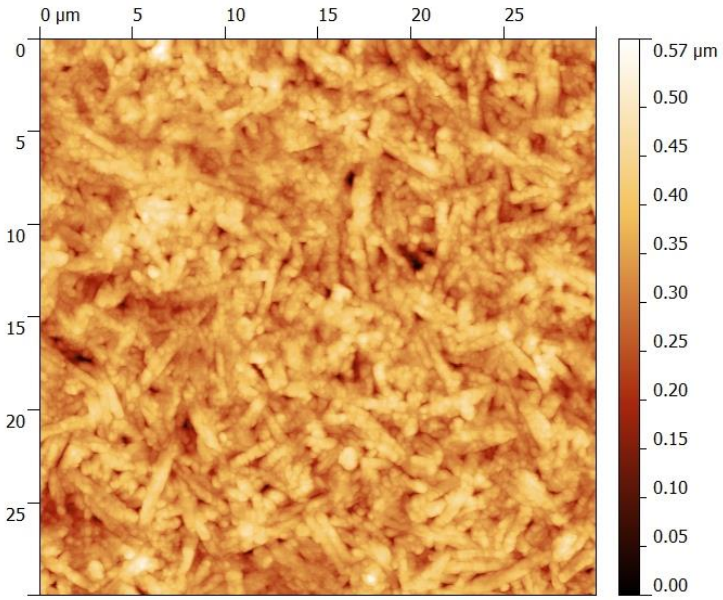

Figure 5.7 Atomic force microscopy image of a spray-coated perovskite film. RMS surface roughness is 56 nm.

5.4 Solar Cell Characterization

5.4.1 Final Device Results

A final device fabrication experiment was performed in which 11 substrates were fabricated, resulting in 44 solar cell devices. Perovskite layer thickness for this batch of solar cells was (330 ± 40) nm. Average (mean) device metrics, together with the metrics for the champion device are presented in **Table 5.4**. **Figure 5.8(a)** shows a histogram of PCE for all devices fabricated in this batch whilst **Figure 5.8(b)** presents the champion device *JV* curve.

	PCE (%)	J_{SC} (mA/cm^2)	V_{OC} (V)	FF (%)
Average	7.82 ± 1.62	14.9 ± 1.5	0.842 ± 0.051	63.4 ± 4.1
Champion device	11.1	16.8	0.924	71.6

Table 5.4 Device metrics for average and champion spray-coated perovskite solar cells. Errors given are standard deviations.

Average power conversion efficiency (PCE) for this batch of devices, incorporating a spray-coated perovskite layer, was 7.8% whilst the maximum PCE reached 11.1%. At the time of publication of the work [25] this maximum efficiency is believed to have been the highest ever reported PCE for a solar cell employing a spray-coated photoactive layer. This value has now been raised to 13% by a report which undertook a similar process to that described here for a device structure of ITO/TiO_2/$CH_3NH_3PbI_{3-x}Cl_x$/Spiro-OMeTAD/Ag [26]. In that work a similar optimisation procedure was undertaken with similar outcomes – the maximum efficiency was found to occur for a substrate temperature during deposition of 75°C, a perovskite layer thickness of 300 nm and with use of the solvent DMF.

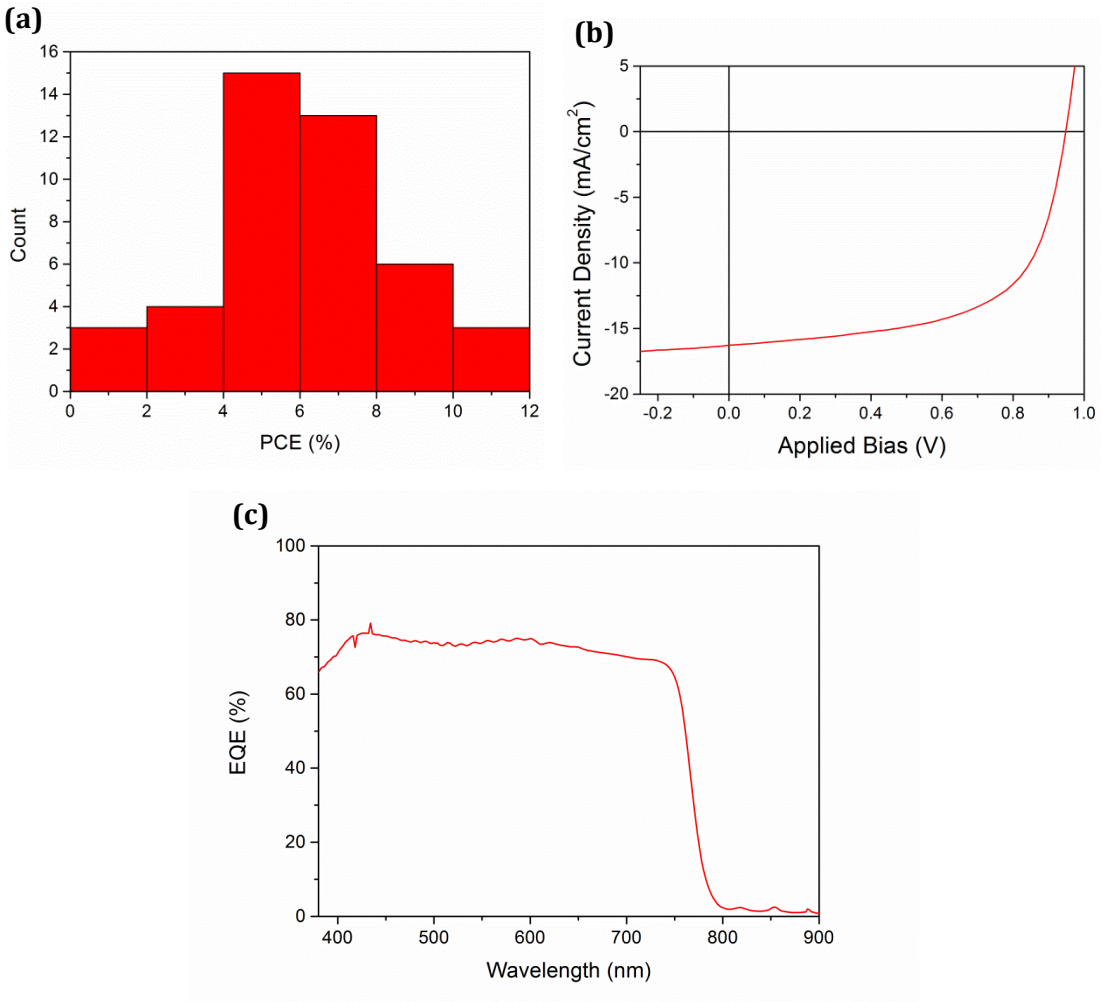

Figure 5.8 Histogram showing the distribution of power conversion efficiencies for all devices within the final fabrication run **(a)**. Current density against voltage characteristics for the champion spray-coated perovskite solar cell **(b)**. External quantum efficiency spectrum of a typical spray-coated perovskite solar cell **(c)**.

The external quantum efficiency spectrum for a typical spray-coated perovskite solar cell (PCE = 7.8%) is plotted in **Figure 5.8(c)**. From this spectrum the short circuit current density of the device under test is calculated to be 17.7 mA/cm^2, a value 10% larger than the 16.1 mA/cm^2 obtained from the *JV* curve of the device under AM1.5 illumination. The discrepancy between these values is within the range generally considered acceptable. In addition, it should be noted that the experimental method used in the EQE experiment selects the best performing part of the device (at 550 nm), and since the laser spot size in the EQE experiment is somewhat smaller that the device size tested under the solar simulator, this could cause an overestimate of the value of J_{SC} by the EQE measurement if the active area of the device is non-uniform in nature.

5.4.2 Light Soaking Effects

Unless otherwise stated, all device results presented in this Chapter are for solar cells which have undergone 20 minutes light soaking under AM1.5 spectrum illumination at an intensity of 1 sun. The evolution of device metrics during extended light soaking is shown in **Figures 5.9(a)-(d)** whilst **(e)** and **(f)** show common changes in current density against voltage characteristics due to light soaking. The light soaking procedure was found to both increase PCE and reduce its spread, effects which arise predominantly due to increases in J_{SC} and V_{OC} together with a reduction in the spread of FF and, in particular, V_{OC} values.

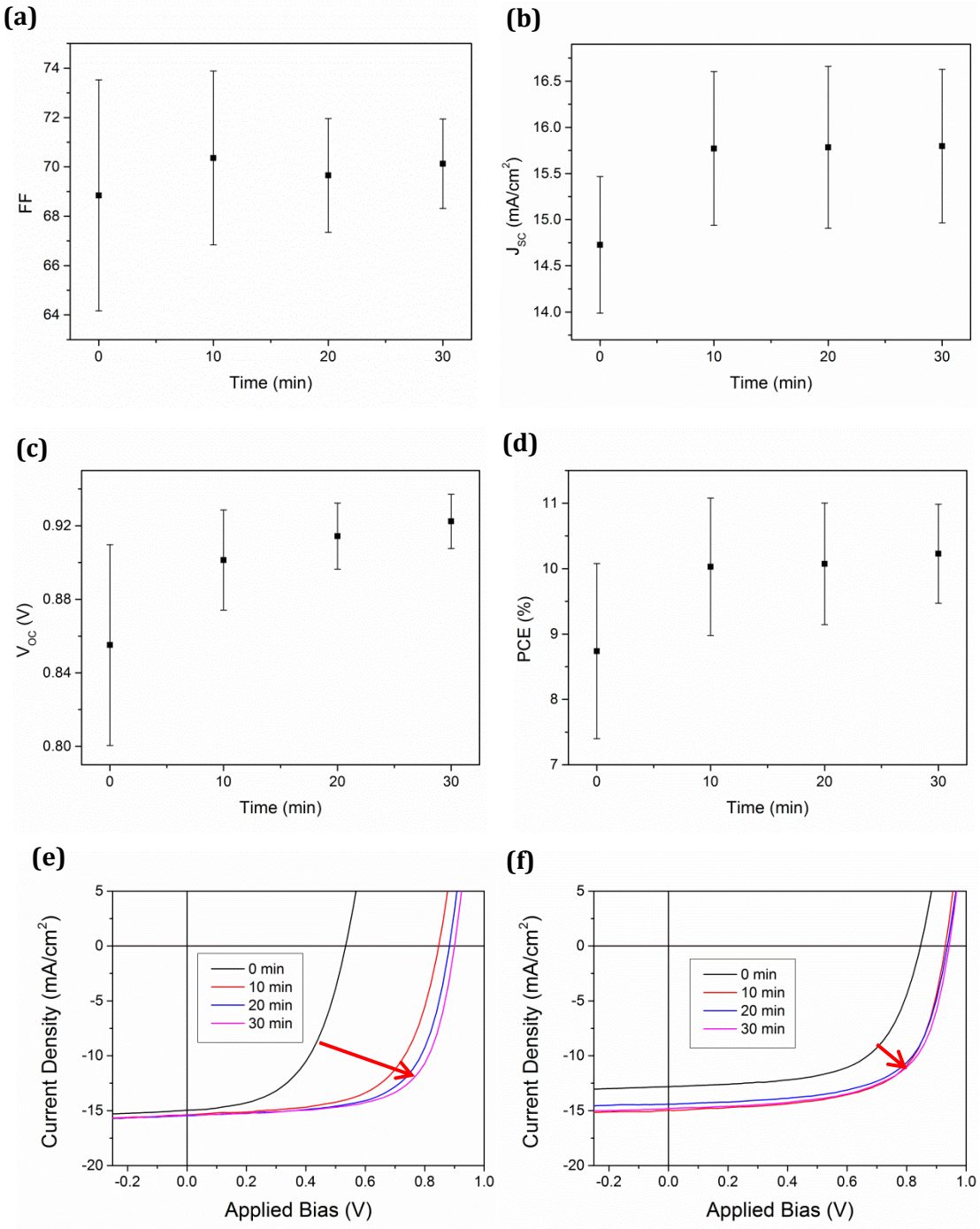

Figure 5.9 Evolution of device metrics during light soaking under 1 sun illumination with an AM1.5 spectrum solar simulator: FF **(a)**, J_{SC} **(b)**, V_{OC} **(c)** and PCE **(d)**. Data is presented for the 6 highest performing devices in the final device experiment. Examples of how light soaking can typically change the current density against voltage characteristics of devices are shown in **(e)** and **(f)**.

The enhancement in device performance observed after light soaking is likely to be attributable to the filling of traps by photogenerated charges or effects relating to ion

migration. A recent study on this phenomenon attributed the enhancement to both filling of positively charged traps in the bulk of the perovskite film and to a reduction in charge accumulation at the interfaces of the device, an effect arising due to passivation of interface defects and/or ion migration and which leads to a large enhancement in V_{OC} [27]. The hypothesis that the filling of trap states is important in enhancing device performance is consistent with results obtained from devices which have undergone a second thermal anneal following the deposition of the $PC_{60}BM$ layer. **Table 5.5** presents PCE data for a batch of spray-coated solar cells in which a number of devices have been subjected to a thermal anneal at 100°C (in a nitrogen glovebox) after deposition of the $PC_{60}BM$ layer. Whilst devices which had undergone no thermal annealing after PCBM deposition exhibited a notable increase in PCE following 20 minutes of light soaking under 1 sun illumination (from 6.04 to 7.86%), devices which have undergone a thermal annealing process showed higher initial efficiencies and did not show a marked increase in PCE upon light soaking. After light soaking, PCEs are comparable between the different procedures. Passivation of trap states in perovskite solar cells by PCBM has since been reported [28], and indeed an increase in device performance upon annealing after the deposition of the PCBM layer has been reported elsewhere [29]. This efficiency enhancement was attributed to diffusion of the PCBM along grain boundaries during the annealing process, leading to passivation of trap states at grain boundaries within the perovskite film as well as at the surface of the layer. In combination with these reports, the observations presented here thus lend weight to the idea that the efficiency enhancement observed here under light soaking may, at least to some extent, be related to trap filling. A full exploration of the observed light soaking effect would, however, be necessary in order to investigate this further and confirm its origin.

Thermal Anneal	**$PCE_{No\ light\ soak}$ (%) (max)**	**$PCE_{20\ min\ light\ soak}$ (%) (max)**
No anneal	6.04 ± 0.26 (6.28)	7.86 ± 0.18 (8.23)
100°C for 15 min	7.27 ± 0.22 (7.49)	7.45 ± 0.16 (7.75)
100°C for 60min	7.72 ± 0.26 (7.92)	7.79 ± 0.17 (8.14)

Table 5.5 Average power conversion efficiencies of devices with and without a thermal anneal following deposition of the $PC_{60}BM$ layer and before deposition of the metal cathode. 3 substrates, (containing a total of 12 devices) were fabricated per annealing condition. Relative humidity during device fabrication was ~50%. Errors given are standard deviations.

5.4.3 Hysteresis

As discussed in **Section 2.5.9**, hysteresis has been observed in the current density against voltage characteristics of perovskite solar cells with a variety of device architectures [30,31]. In order to investigate the magnitude of any such effect on the spray-coated perovskite solar cells fabricated here, *JV* measurements were taken in both the 'forward' (negative bias to positive bias) and 'reverse' (positive bias to negative bias) scan directions at a variety of scan rates. The resulting *JV* curves for a typical device are presented in **Figure 5.10**, where it can be seen that minimal hysteresis is observed for all scan rates investigated. The highest scan rate (2.0 V/s, shown in **Figure 5.10(d)**) results in the greatest hysteresis, however even at this scan speed the reverse scan still only results in a 0.5% (absolute) reduction in PCE in comparison to the forwards scan. Under the scan rate used as standard in this work (0.5 V/s, shown in **Figure 5.10(b)**) the difference in device performance observed between forward and reverse scans is in fact within the error observed for repeat testing of the same pixel under identical scan conditions following light soaking (± 0.1% absolute PCE). Note that unless otherwise stated, device metrics and current density against voltage relationships presented in this Chapter have been determined using a forward scan at a scan rate of 0.5 V/s.

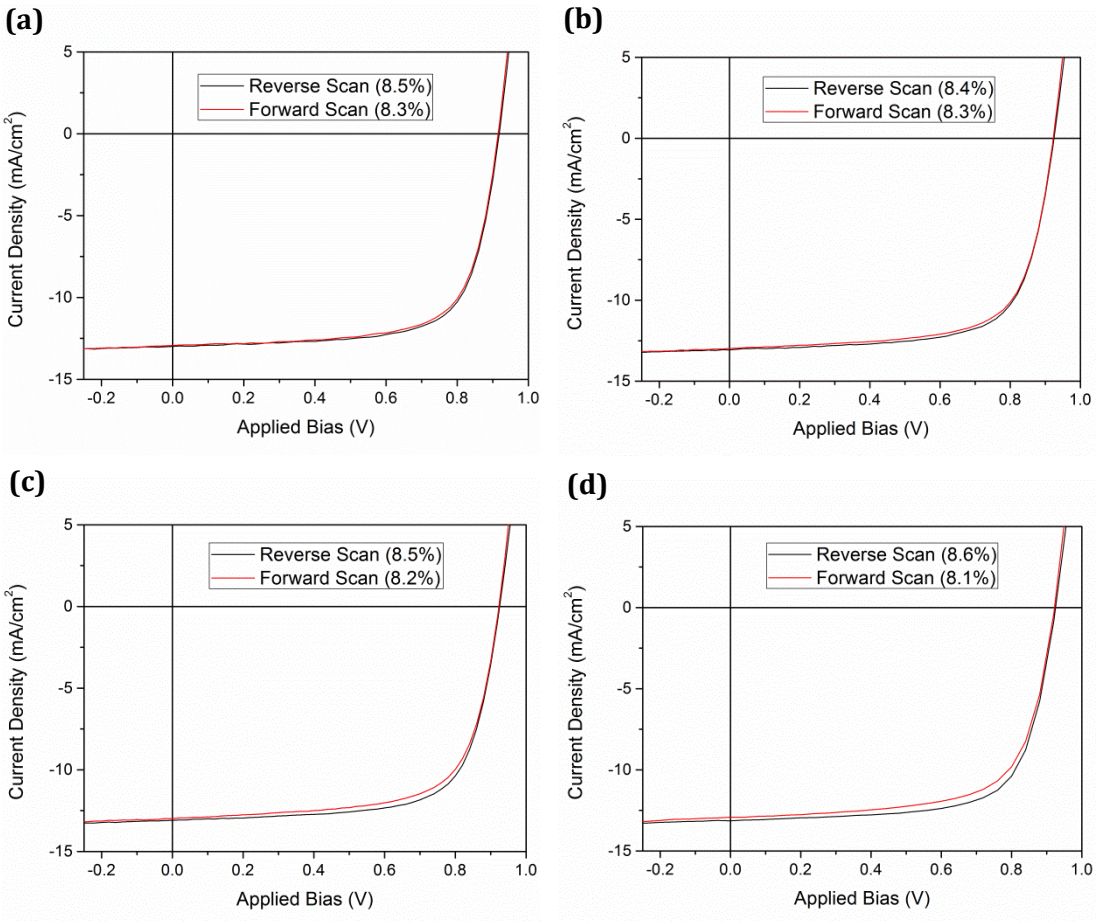

Figure 5.10 Current density against voltage curves for a spray-coated perovskite solar cell tested under different scan rates and scan directions. Scan rates used were: 0.3 V/s **(a)**, 0.5 V/s **(b)**, 1.0 V/s **(c)** and 2.0 V/s **(d)**. Device PCE for the stated scan conditions is given in brackets in each case.

5.4.4 Comparison to Spin-Coated Devices

In order to compare spin-coated and spray-coated devices, it was necessary to first make an attempt at optimising the perovskite spin-coating procedure. In line with some other early reports [32–34], a 'hot' spin coating procedure has been used in order to enhance surface coverage. Here 'hot' deposition refers to the solution and substrate being held on hotplates at temperatures of 70°C and 90°C respectively immediately prior to spin-coating whilst the 'cold' deposition procedure involves both substrate and solution being at room temperature during spin-coating. Optical microscopy and atomic force microscopy images for 'cold' and 'hot' spun perovskite films are shown in **Figure 5.11**, where it can be seen that the hot spin-coating procedure leads to an

increased surface coverage. Given this observation, the hot spin-coating procedure was chosen for device fabrication. Whilst devices metrics arising from the hot and cold procedures were not compared at this time, subsequent work has determined that the hot spin-coating procedure does indeed lead to enhanced device efficiency and the results of this later work are presented in **Table 5.6**.

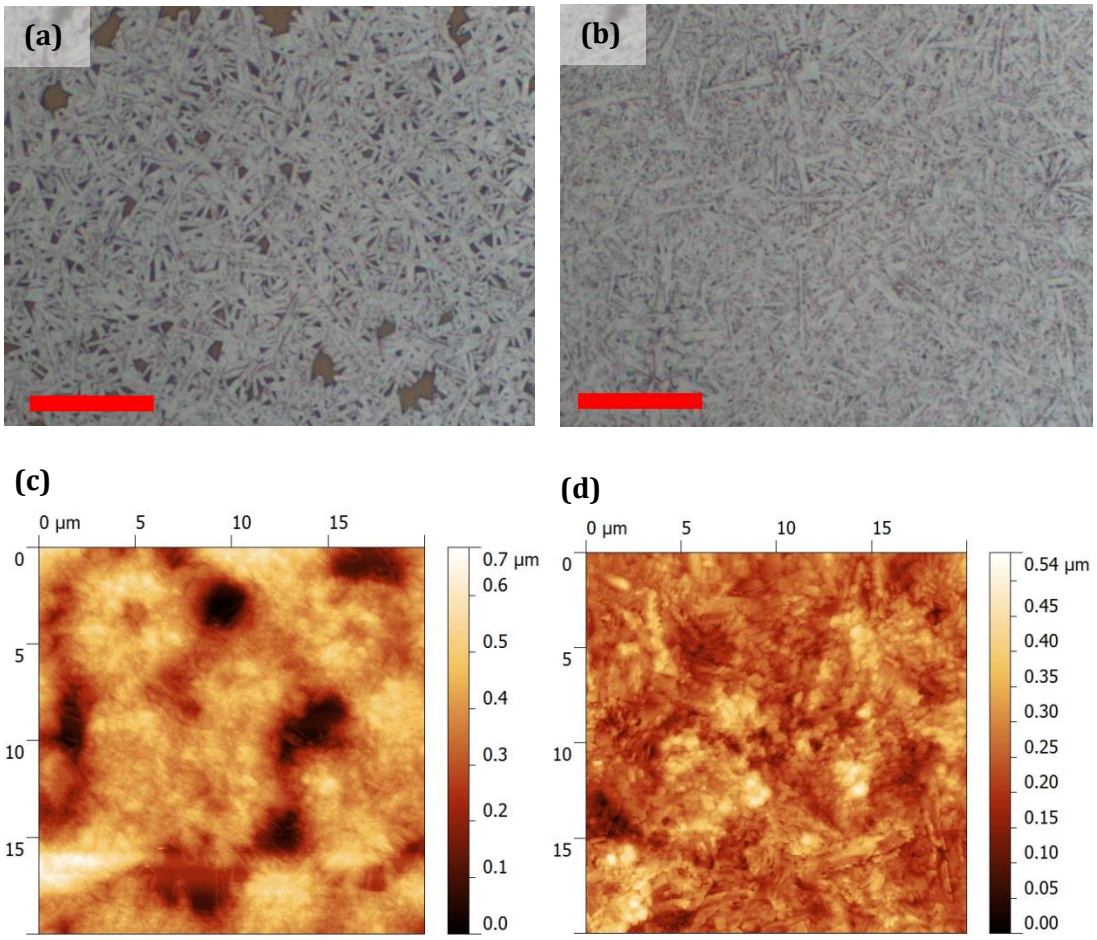

Figure 5.11 Optical microscopy and atomic force microscopy images of perovskite films deposited via spin-coating. Parts **(a)** and **(c)** correspond to 'cold' deposition whilst part **(b)** and **(d)** correspond to 'hot' deposition. Red scale bars on optical microscopy images correspond to 20 µm.

	PCE (%) (max)	J_{SC} (mA/cm²)	V_{OC} (V)	FF (%)
Hot spin-coating	12.2 ± 0.3 (12.7)	17.8 ± 0.2	0.918 ± 0.014	75.0 ± 0.5
Cold spin-coating	10.3 ± 0.1 (10.6)	15.5 ± 0.2	0.909 ± 0.010	73.2 ± 0.5

Table 5.6 Average device metrics for hot and cold spin-coating procedures. Note that devices were fabricated in a relative humidity of ~30% and with a different batch of materials to those employed in this chapter. Errors given are standard deviations. For PCE the maximum value is also given in brackets.

Scanning electron microscopy images of spin-coated (hot deposition procedure) and spray-coated perovskite films are shown in **Figure 5.12**. Films from each deposition procedure appear similar and can be seen to be polycrystalline in nature with comparable grain sizes and high and comparable surface coverage.

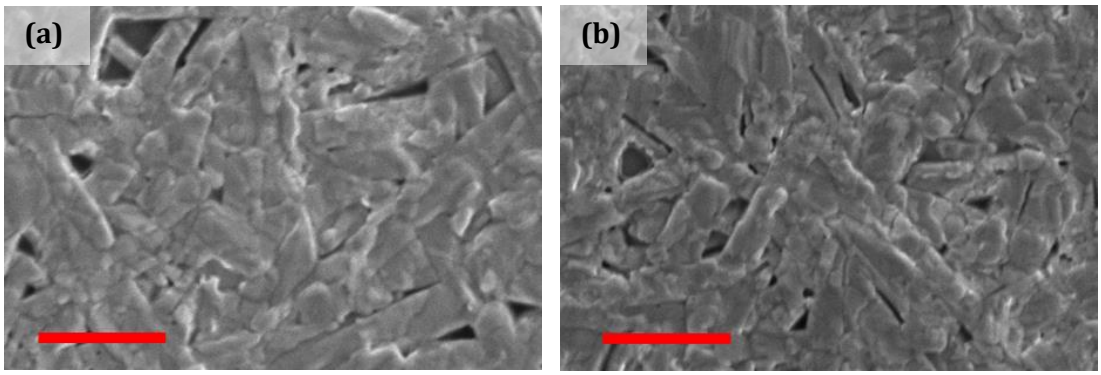

Figure 5.12 Scanning electron microscopy images of spin-coated **(a)** and spray-coated **(b)** perovskite films on glass/ITO/PEDOT:PSS substrates. Red scale bars correspond to 2 μm.

During the final optimised spray-coating device experiment 28 spin-coated devices (spread over 7 different substrates) were also fabricated; the thickness of the spun and sprayed perovskite layers were (400 ± 10) nm and (330 ± 40) nm respectively. Device metrics are presented in **Table 5.7** where it can be seen that average device PCE is similar between the two fabrication methods, being 7.8% in both cases. Whilst spray-cast devices lead to a larger efficiency spread they also produced the highest performing solar cell having an efficiency of 11.1% as compared to 8.3% for the best performing cell based on a spin-cast perovskite layer. From this initial work it thus seems that spray-coating of the perovskite layer does not lead to a reduction in device

performance as compared to spin-coating. Typical current density against voltage curves for spray-coated and spin-coated devices are presented in **Figure 5.13**.

	PCE (%) (max)	J_{SC} (mA/cm²)	V_{OC} (V)	FF (%)
Spray-coated	7.82 ± 1.62 (11.1)	14.9 ± 1.5	0.842 ± 0.051	63.4 ± 4.1
Spin-coated	7.79 ± 0.33 (8.32)	13.8 ± 0.4	0.851 ± 0.020	66.6 ± 2.2

Table 5.7 Average device metrics for perovskite solar cells with spray-coated and spin-coated perovskite active layers. Results are from the standard testing protocol described above, following 20 minutes of light soaking. Errors given are standard deviations. For PCE the maximum value is also given in brackets.

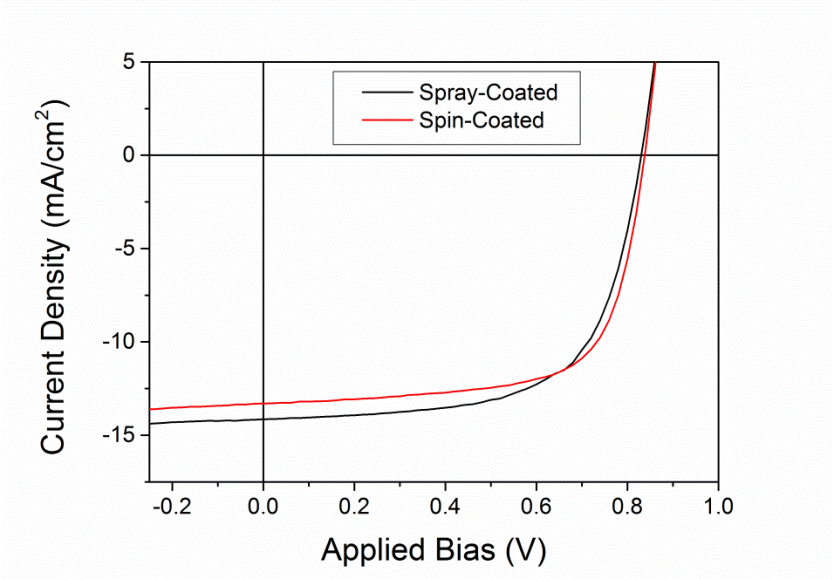

Figure 5.13 Current density against voltage characteristics for typical spray-coated and spin-coated perovskite solar cells.

5.5 Spray-Deposition of a PEDOT:PSS Hole Transport Layer

The commonly used hole transport layer PEDOT:PSS is typically deposited via spin-coating from an aqueous dispersion. Due to the high surface tension of water, however, this formulation provides challenges for spray-deposition due to the tendency of the liquid to form individual droplets on the substrate surface rather than for droplets to coalesce and thence form a uniform wet layer and subsequent film. In order to

overcome this issue, isopropanol (IPA) can be added to the PEDOT:PSS dispersion to reduce the surface tension of the mixture [2]. The PEDOT:PSS formulation used herein was developed by Dr Jonathan Griffin and consists of a 1:8:1 ratio by volume of PEDOT:PSS dispersion:IPA:ethylene glycol; in addition it contained 0.015 mg/ml of 7M Mw polyethylene glycol (PEG) in chlorobenzene (from a 1 mg/ml solution of PEG in chlorobenzene). The IPA reduces the surface tension of the solvent mixture, ensuring good instantaneous wetting during initial spray-coating. During subsequent film drying the IPA will evaporate at a faster rate than water due to its lower boiling point (83°C as compared to 100°C) leading to the risk of dewetting as the mixture becomes predominantly aqueous. Incorporation of ethylene glycol (boiling point 193°C) and polyethylene glycol into the formulation provides a route to overcoming this by increasing the viscosity of the solution, ensuring that dwetting is minimised during the period where little IPA remains in the film but water is still present. It should be noted that the addition of ethylene glycol and PEG into PEDOT:PSS dispersions has also previously been found to increase the conductivity of the resultant film, attributed to phase separation and reorganisation of the PEDOT and PSS chains [35–37].

After spray-coating of the PEDOT:PSS dispersion onto substrates held at 45°C and subsequent film drying, a 150°C thermal anneal was applied for 5 minutes in order to remove the ethylene glycol, although the PEG can be expected to remain within the film. Substrates were then held on a 120°C hotplate for 30 minutes along with the spin-coated PEDOT:PSS samples. Atomic force microscopy (AFM) was undertaken in order to investigate the surface roughness of the PEDOT:PSS layers deposited by both spin-coating and spray-coating. AFM images for each sample are presented in **Figure 5.14**. Root mean squared surface roughness is 1.2 nm for the spin-coated layer and 3.6 nm for the spray-coated layer, both of which are low values, especially when considering the high thickness of the photoactive perovskite layer used in solar cells.

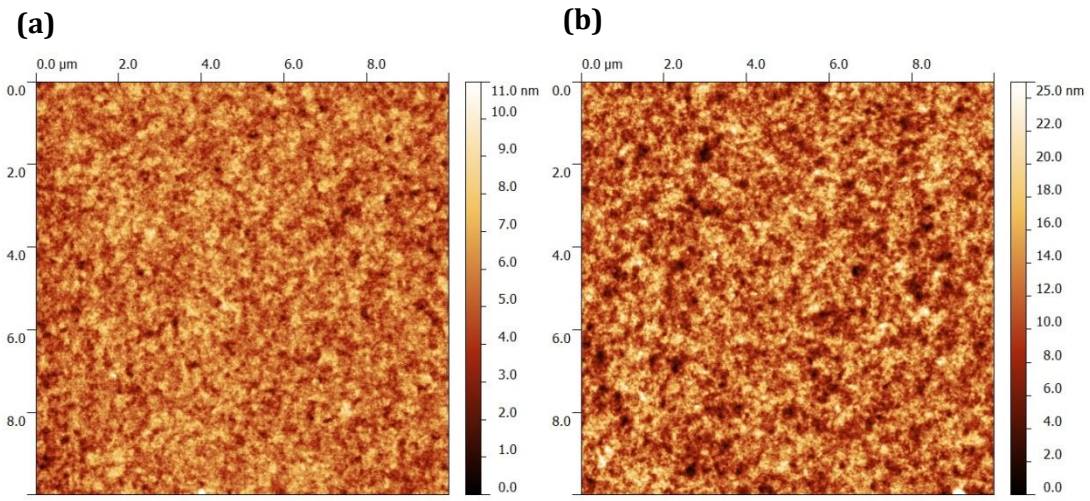

Figure 5.14 Atomic force microscopy images of spin-coated **(a)** and spray-coated **(b)** PEDOT:PSS layers on glass/ITO substrates. RMS roughness values are 1.2 and 3.6 nm respectively.

In order to demonstrate the practical application of this processing route, perovskite solar cells were fabricated on both spin-coated and spray-coated PEDOT:PSS films. Glass/ITO substrates were coated with the PEDOT:PSS film before a perovskite ($CH_3NH_3PbI_{3-x}Cl_x$) active layer was deposited via the spray-coating procedure described earlier in this Chapter. 4 substrates (containing a total of 16 devices) were fabricated for each deposition method. Devices were completed as described previously – a $PC_{60}BM$ electron transport layer was deposited via spin-coating and a Ca/Al cathode was deposited via thermal evaporation. Device metrics for the fabricated solar cells, are presented in **Table 5.8**. It can be seen that the spray-coated and spin-coated PEDOT:PSS layers lead to comparable average device efficiencies of 7.1% and 7.0% respectively. As with the comparison between spray-coated and spin-coated perovskite layers, the spray-coated PEDOT:PSS layer leads to an increased spread of results but also gives rise to the highest efficiency device in the test, with a maximum PCE of 8.7% as compared to 7.4% for the champion device based on a spin-coated PEDOT:PSS layer. *JV* curves for typical and champion devices for each deposition method are presented in **Figures 5.15(a)** and **(b)** respectively.

PEDOT:PSS Deposition	PCE (%) (max)	J_{SC} (mA/cm²)	V_{OC} (V)	FF (%)
Spin-coated	7.02 ± 0.24 (7.36)	13.0 ± 0.5	0.911 ± 0.033	59.1 ± 1.9
Spray-coated	7.12 ± 0.74 (8.66)	13.0 ± 0.8	0.930 ± 0.018	58.9 ± 4.9

Table 5.8 Average device metrics for solar cells fabricated using spin-coated and spray-coated PEDOT:PSS layers. The photoactive layer has been deposited via spray-coating in both cases. Relative humidity was ~50% during device fabrication. Errors given are standard deviations. For PCE the maximum value is also given in brackets.

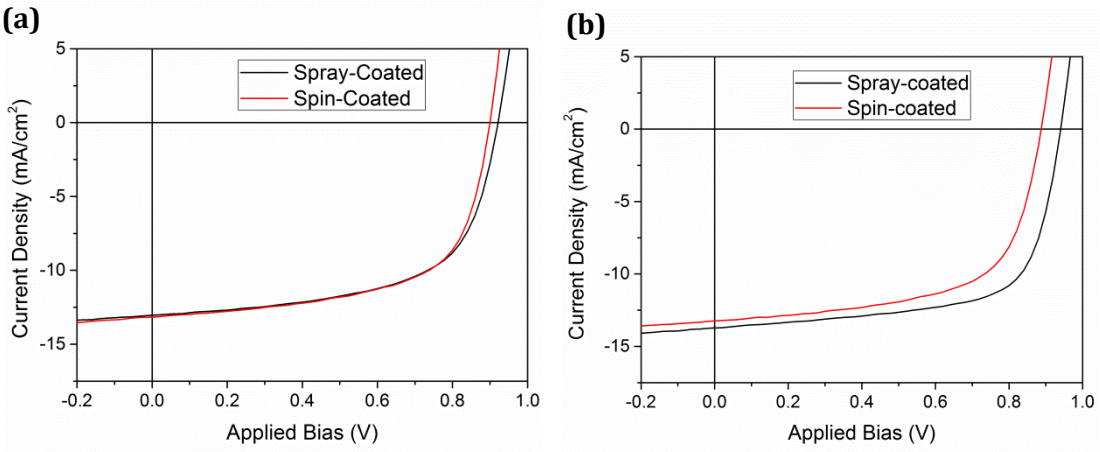

Figure 5.15 Current density against voltage characteristics for typical **(a)** and champion **(b)** perovskite solar cells based on spray-coated and spin-coated PEDOT:PSS hole transport layers, together with a spray-coated perovskite layer.

The successful spray-deposition of the PEDOT:PSS hole transport layer is a promising step towards a fully spray-coated device. That said, it is important that these results can be reproduced with higher efficiency devices, and this is a current project for others in the research group who are continuing with this work.

5.6 Spray-Deposition of a PCBM Electron Transport Layer

In order to move towards a fully roll-to-roll compatible device, the spray-deposition of the PCBM electron transport layer (ETL) has been attempted. Around this time two reports were published in which the replacement of $PC_{60}BM$ by $PC_{70}BM$ resulted in an

approximately 3% absolute (30–40% relative) increase in PCE in perovskite solar cells with similar architectures to those investigated here [9,38]. In one report this was predominantly due to an increased FF whilst in the other it arose largely due to an enhanced J_{SC}, though no detailed investigation of this effect was undertaken in either case. Here a similar experiment was performed on spin-coated perovskite solar cells in order to establish if this reported improvement in PCE could be reproduced. 3 substrates (containing a total of 12 devices) were fabricated per PCBM derivative. The resultant device metrics are presented in **Table 5.9** where it can be seen that the replacement of $PC_{60}BM$ by $PC_{70}BM$ as the electron transport layer results in a 17% relative enhancement in average PCE, from 7.7% to 9.0%, an effect arising due to an increase in V_{OC} and FF. Given the results of this experiment it was decided that further investigations would involve the application of $PC_{70}BM$ as the electron transporting material.

ETL	PCE (%) (max)	J_{SC} (mA/cm²)	V_{OC} (V)	FF (%)
$PC_{70}BM$	9.00 ± 0.16 (9.11)	14.6 ± 0.2	0.861 ± 0.004	71.5 ± 0.6
$PC_{60}BM$	7.73 ± 0.12 (7.89)	15.0 ± 0.2	0.761 ± 0.011	67.7 ± 1.8

Table 5.9 Average device metrics for spin-coated perovskite solar cells with different electron transport layers (ETLs). Errors given are standard deviations. For PCE the maximum value is also given in brackets.

Initial attempts to deposit both $PC_{60}BM$ and $PC_{70}BM$ by ultrasonic spray-coating from a solution of chlorobenzene resulted in non-uniform films which displayed clear local thickness variations as can be seen in **Figure 5.16**. Here the PCBM layer was deposited onto a glass or glass/ITO substrate in order to aid evaluation of layer quality and thickness. Note however that when fabricating complete solar cell devices the PCBM layer was deposited onto the perovskite itself. Attempts to resolve the issue of non-uniformity via varying solution concentration, substrate temperature, spray-head height and spray-head speed were unsuccessful.

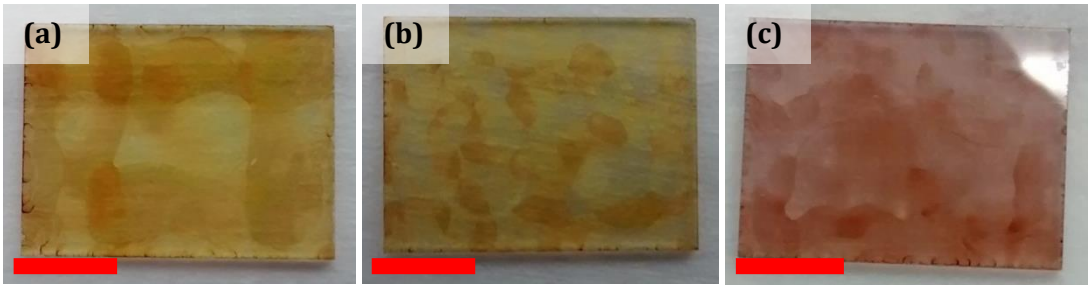

Figure 5.16 $PC_{60}BM$ films spray-cast from chlorobenzene onto substrates held at 25°C **(a)** and 45°C **(b)** together with a $PC_{70}BM$ film spray-cast onto a substrate held at 25°C **(c)**. All solution concentrations were 10 mg/ml. Red scale bars correspond to 5 mm.

The most uniform layers were typically observed for the faster drying films, however increases in substrate temperature were unable to remove the pattern of non-uniformities. For this reason a more volatile solvent system was explored. Work by other members of the research group has previously found that spray-deposition from low boiling point (b.p.) solvents such as chloroform produces poor film quality due to a tendency of individual droplets to dry before forming into a uniform film [1]. A mixture of the solvents chlorobenzene (b.p. ~130°C) and chloroform (b.p. ~60°C) was thus chosen, noting also that two solvent systems have been used successfully in previous report on spray-coating [2]. By dissolving $PC_{70}BM$ in a mixture of chlorobenzene (CB) and chloroform (CF) at a 2:1 volume ratio it was possible to produce apparently uniform $PC_{70}BM$ films of thicknesses up to ~75 nm using a solution concentration of 10 mg/ml. Increasing film thickness, however, whether by increasing solution concentration or changing spray-coater parameters, lead to the return of non-uniformity. By altering the solvent mixture to a 1:1 ratio of CB:CF it then became possible to produce uniform films over a range of thicknesses from ~70–170 nm using a solution of concentration 15 mg/ml and with a substrate temperature of 20°C as can be seen in **Figure 5.17**. Using this approach it is likely that significantly thinner or thicker films could also be deposited without a loss of thickness uniformity.

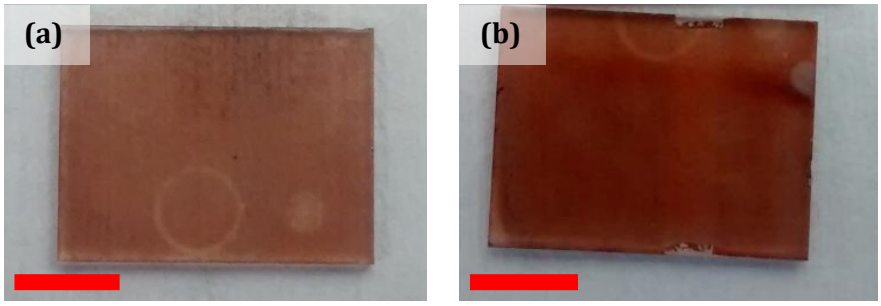

Figure 5.17 $PC_{70}BM$ films spray-cast from a solution of 1:1 CB:CF at 15 mg/ml at different spray-head speeds giving film thicknesses of (72 ± 10) nm **(a)** and (174 ± 7) nm **(b)**. Red scale bars correspond to 5 mm.

Having successfully used spray-coating for the deposition of uniform PCBM films of an appropriate thickness, this technique was then used to deposit such films in perovskite solar cell devices. Note that PEDOT:PSS and perovskite layers were both deposited via spin-coating in air in these devices. $PC_{70}BM$ films were then deposited via spray-coating in ambient conditions whilst reference devices employed $PC_{70}BM$ films spin-coated either in air or in a nitrogen glovebox. 4 substrates (containing a total of 16 devices) were fabricated per condition. Spin-coated films had thickness (110 ± 6) nm whilst spray-coated films had a comparable thickness of (107 ± 11) nm; the resulting device metrics are presented in **Table 5.10** whilst typical *JV* curves are shown in **Figure 5.18**.

PCBM Deposition	PCE (%) (max)	J_{SC} (mA/cm²)	V_{OC} (V)	FF (%)
Spin-coating, N_2	8.45 ± 0.22 (8.81)	14.0 ± 0.2	0.925 ± 0.004	65.5 ± 1.3
Spin-coating, air	0.83 ± 0.06 (0.91)	4.5 ± 0.2	0.909 ± 0.022	20.6 ± 0.4
Spray-coating, air	1.88 ± 0.43 (2.86)	8.0 ± 1.0	0.892 ± 0.085	26.1 ± 3.4

Table 5.10 Average device metrics for perovskite solar cells in which the $PC_{70}BM$ layer was deposited by spin-coating in nitrogen glovebox spin-coating in air or spray-coating in air. Relative humidity was ~35% during device fabrication. Errors given are standard deviations. For PCE the maximum value is also given in brackets.

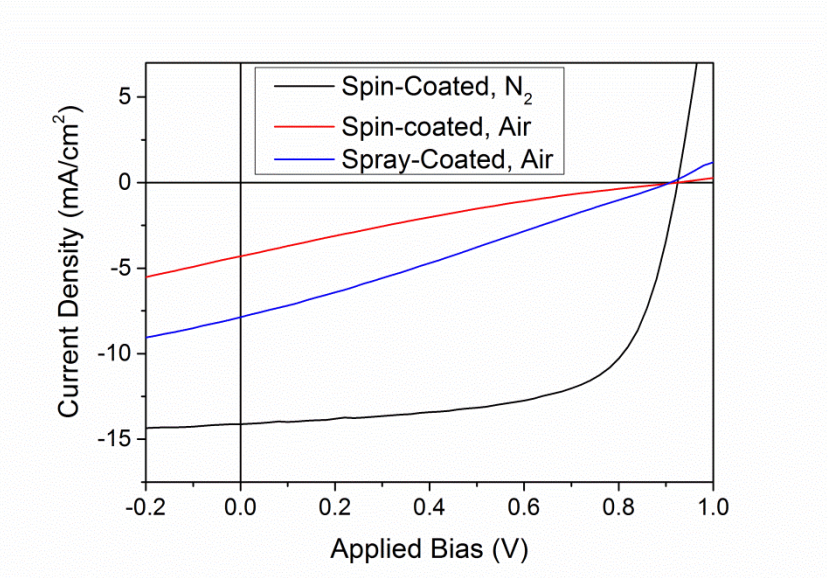

Figure 5.18 Current density against voltage characteristics for typical perovskite solar cells fabricated using different deposition methods for the PCBM electron transport layer.

Whilst $PC_{70}BM$ layers spin-coated in nitrogen lead to solar cell devices with an average PCE of 8.5%, it was found that air deposited $PC_{70}BM$ resulted in very poor PCEs of 0.8% and 1.9% respectively in the case of spin-coating and spray-coating. The major reduction in PCE with air processed $PC_{70}BM$ arises due to large reductions in both FF and J_{SC} whilst V_{OC} is only very slightly reduced. In particular, the current density against voltage characteristics shown in **Figure 5.18** suggest a very large series resistance for devices employing air processed $PC_{70}BM$. The decrease in device performance does not appear to be a result of the spray-coating process since it is also observed for air processed of $PC_{70}BM$ where spin-coating has been employed as the deposition method. Note that the slightly reduced device performance of samples spin-coated in air as compared to those spray-coated in air likely results from a longer air exposure time for the former.

In order to investigate these effects further, an experiment was performed in which devices were fabricated with the $PC_{70}BM$ layer deposited by spin-coating in either air or a nitrogen glovebox. The air deposited samples were immediately transferred to the nitrogen glovebox and subsequently either used in their as-cast state or treated with a 120°C anneal. In addition, a number of samples employing glovebox processed $PC_{70}BM$ were removed from the nitrogen atmosphere and exposed to air for a period of time

following deposition of this layer. Finally, in order to rule out any reaction between the solvent and the perovskite under ambient conditions as being the cause of device degradation, a set of devices were fabricated where chlorobenzene was spin-cast onto the perovskite layer in air before PCBM was deposited in the glovebox. 3 substrates (containing a total of 12 devices) were fabricated per condition. Device metrics for this experiment, following 20 min light soaking, are shown in **Table 5.11**.

PCBM Deposition Environment and Post-Deposition Treatment	**PCE (%)**	**J_{SC} (mA/cm^2)**	**V_{OC} (V)**	**FF (%)**
Glovebox, no treatment	7.14 ± 0.58	13.4 ± 0.5	0.885 ± 0.017	60.1 ± 1.8
Glovebox, exposed to air for 5 min	4.49 ± 0.10	11.8 ± 0.2	0.914 ± 0.010	41.8 ± 1.2
Glovebox, exposed to air for 30 min	3.01 ± 0.06	9.7 ± 0.1	0.943 ± 0.006	32.7 ± 0.6
Glovebox, CB spun on in air first	6.48 ± 0.20	12.5 ± 0.1	0.875 ± 0.013	59.2 ± 2.0
Air, no treatment	3.27 ± 0.08	10.5 ± 0.3	0.931 ± 0.005	33.6 ± 0.8
Air, 120°C anneal for 5 min	2.87 ± 0.14	9.4 ± 0.4	0.931 ± 0.015	32.8 ± 0.7
Air, 120°C anneal for 30 min	3.54 ± 0.22	10.9 ± 0.3	0.921 ± 0.004	35.2 ± 1.4
Air, 120°C anneal for 60 min	5.24 ± 0.25	13.3 ± 0.2	0.860 ± 0.006	45.7 ± 1.8

Table 5.11 Average device metrics for perovskite solar cells in which the $PC_{70}BM$ ETL has been deposited by spin-coating either in air (relative humidity ≈ 45%) or in a nitrogen glovebox and various post-deposition treatments have been applied. Errors given are standard deviations. For PCE the maximum value is also given in brackets.

It can be seen that glovebox processed $PC_{70}BM$ layers result in devices having an average efficiency of 7.1%, whilst air processed $PC_{70}BM$ layers give a significantly lower average PCE of 3.3%. The smaller reduction in PCE for the devices incorporating air processed $PC_{70}BM$ in comparison to in the previous experiment (discussed above) is

likely due to a reduced period of exposure to air in this later work. Exposure of the part finished devices to air lead to reduced PCEs of 4.5% and 3.0% respectively in the cases of 5 minute and 30 minute exposure times, with this reduction in efficiency again arising due to reductions in J_{SC} and FF. This result indicates that the decrease in device performance for air processed $PC_{70}BM$ layers does not likely arise due to the formation of an inferior perovskite/$PC_{70}BM$ interface when $PC_{70}BM$ is deposited under ambient conditions, but rather due to degradation of the $PC_{70}BM$ layer itself or the influence of absorbed moisture and/or oxygen on the highly reactive metal cathode which is subsequently deposited onto the layer by evaporation. Devices in which chlorobenzene (CB) was spun onto the perovskite layer in air before deposition of $PC_{70}BM$ in glovebox had an average PCE of 6.5%, a value that is only a small reduction in comparison to the devices without this treatment (PCE = 7.1%). Any effect that the solvent has when spun onto the perovskite layer in air thus does not seem to be the main reason for the reduced device performance seen with air processed $PC_{70}BM$.

When air processed $PC_{70}BM$ layers are subject to a thermal anneal under a nitrogen atmosphere at 120°C for periods of 5 and 15 minutes, PCE of the resulting devices is not recovered. When this annealing period is extended to 60 min, however, a notable increase in FF and J_{SC} leads to the recovery of a proportion of the efficiency lost due to air processing of the $PC_{70}BM$ layer, giving an average PCE of 5.2%. The lack of full recovery of device efficiency may arise due to irreversible degradation of the $PC_{70}BM$ layer when processed in air, or due to detrimental morphological changes in the perovskite layer during this extended annealing treatment. Further attempts to recover PCE by replacing the highly reactive calcium interlayer with TiO_2, PEI (polyethyleneimine) or BPhen (4,7-diphenyl-1,10-phenanthroline) did not meet with success, indicating that the efficiency loss with air processed $PC_{70}BM$ is likely to arise from degradation of the $PC_{70}BM$ layer itself, though clearly further investigation would be needed to confirm this hypothesis. It should be noted that perovskite devices employing thinner PCBM layers and polymer:PCBM solar cells using the same device architecture as is used here have both previously been successfully fabricated in air [1,8,15]. The large thickness of the PCBM layer used here may well explain the difference between those reports and the reduction in device performance observed in this work. Exposure of C_{60} films to oxygen has previously been shown to lead to significant reductions in electron mobility together with the generation of trap states, whilst processing of P3HT:$PC_{60}BM$ bulk heterojunctions in air has been shown to lead to lower electron mobility in the PCBM than when such junctions are processed in inert

atmospheres [39–41]. Indeed a post-deposition thermal anneal was found to lead to an improvement in device performance, a result also observed here. This effect was attributed to a reduction in the oxygen content of the film and an associated reduction in charge trap density of air-processed P3HT:$PC_{60}BM$ layers. With such thick PCBM layers as those used here it is possible that a decrease in mobility could cause a large increase in series resistance, leading to the observed decrease in device performance. If this is indeed the case then until a smoother perovskite layer can be fabricated, allowing use of a thinner electron transport layer, spray-coating of PCBM in ambient conditions is likely to result in poor device performance.

5.7 Fabrication of Perovskite Layers via a Two-Step Process

As described in **Section 2.5.7** in addition to the 'one-step' fabrication route for perovskite used in the above work, a 'two-step' process has been used elsewhere with much success [42]. The two-step approach typically relies upon the deposition of a PbI_2 layer via spin-coating before exposure of this layer to methylammonium iodide (MAI), resulting in conversion to the $CH_3NH_3PbI_3$ perovskite. Exposure of the lead salt to MAI in this second step is typically achieved by immersion ('dipping') into a solution of MAI dissolved in isopropyl alcohol (IPA). The fabrication of perovskite solar cells via a two-step process based on a layer of lead (II) chloride ($PbCl_2$) rather than lead (II) iodide (PbI_2) is relatively unexplored in the literature, perhaps partly owing to the low solubility of $PbCl_2$ as compared to PbI_2 [43]. Since spray-coating allows for film fabrication using lower concentration solutions than employed in the spin-coating of equal thickness films it offers an interesting opportunity to explore a two-step process based on spray-cast $PbCl_2$. Here a two-step 'spin-dip' process was chosen for investigation, in which the second step occurred via a dipping process in MAI solution.

Initial attempts to spray-cast $PbCl_2$ from a solution of dimethylformamide (DMF) were successful in fabricating apparently uniform thin films with thickness ~50–100 nm. Uniform films with higher thickness, however, could not be obtained due to poor solubility restricting the solution concentration to around only 40 mg/ml. In order to overcome this, the solvent dimethyl sulphoxide (DMSO) (in which $PbCl_2$ has a higher solubility) was tried as a replacement for DMF. A solution concentration of 100 mg/ml gave more promising results than either lower or higher concentrations, and so this

was investigated. Unfortunately, it did not prove possible to achieve uniform films from DMSO due to the slow drying nature of the film which arises due to the high boiling point (b.p.) of DMSO. Adjustment of substrate temperature and other spray-coating parameters was unable to eliminate the non-uniform nature of the films, and so a two solvent approach was tried. Here a blend of DMSO (b.p. ~190°C) and DMF (b.p. ~150°C) was used in a 2:1 volume ratio which proved more successful in producing uniform films of an appropriate thickness, as can be seen in **Figure 5.19(a)**.

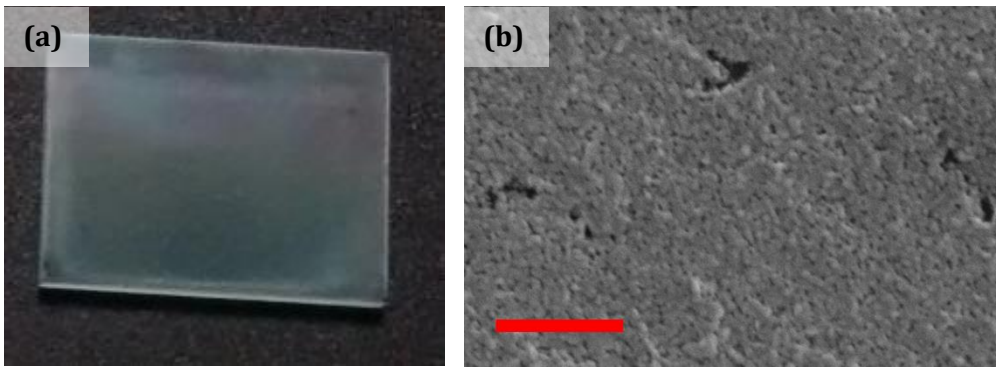

Figure 5.19 Photograph **(a)** and scanning electron microscopy image **(b)** of a $PbCl_2$ film of thickness (260 ± 20) nm spray-coated from a 2:1 DMSO:DMF blend onto a substrate held at 80°C. The red scale bar corresponds to 2 μm.

In order to investigate the effect of substrate temperature on film formation, optical microscopy images were taken of films deposited at substrate temperatures ranging from 40–100°C. As can be seen from **Figures 5.20(a)-(d)**, intermediate deposition temperatures produced the most uniform films with the optimum apparently being at around 60°C. From the optical micrographs shown in **Figures 5.20(e)-(h)** it is clear that a change in film morphology occurs at deposition temperatures between 60°C and 80°C, with the formation of large crystal grains occurring at high temperatures.

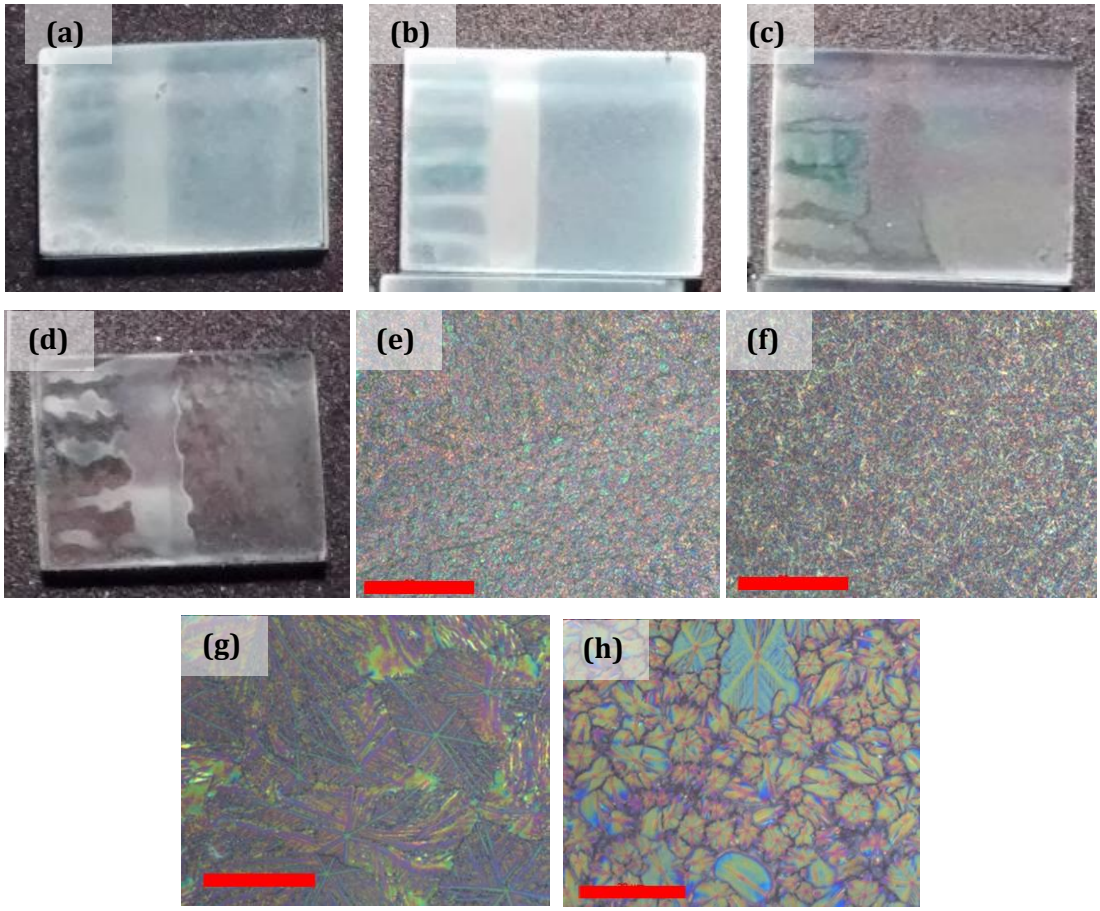

Figure 5.20 Photographs and optical microscopy images of $PbCl_2$ films deposited from a 2:1 DMSO:DMF solvent blend onto substrates held at 40°C **(a)** and **(e)**; 60°C **(b)** and **(f)**; 80°C **(c)** and **(g)**; 100°C **(d)** and **(h)**. Red scale bars correspond to 20 microns

An initial optimisation procedure was undertaken to explore the parameter space related to the two-step procedure. Initially $PbCl_2$ layers of thickness ~200 nm were spray-cast from a solution of concentration 100 mg/ml in a 2:1 DMSO:DMF mixture onto glass/ITO/PEDOT:PSS substrates. Whilst the films deposited at substrate temperatures of 60°C appear the most uniform, given the change in film morphology observed for higher temperatures $PbCl_2$ films deposited at both 60°C and 80°C were investigated. $PbCl_2$ layers deposited at these temperatures were dipped into an MAI solution in IPA (10 mg/ml) held on a 60°C hotplate for lengths of time from 10 seconds to 5 min. Upon removal from the solution the films were dried with compressed nitrogen and did not undergo any annealing treatment, before being finished into complete devices by spin-coating (in glovebox) of a $PC_{70}BM$ electron transport layer and thermal evaporation of a Ca/Al cathode. 2 substrates (containing a total of 8 devices) were fabricated per condition. PCEs from this experiment are shown in **Figure**

5.21(a) where it can be seen that devices fabricated using $PbCl_2$ layers deposited at 60°C notably outperform those deposited at 80°C across a range of dipping times. For this reason all further work on the two-step spray-dip processing route used $PbCl_2$ layers spray-cast at 60°C. For both deposition temperatures the photovoltaic response of devices in which layers had undergone a 10 second dipping was minimal and increased with longer dipping times to reach a maximum PCE for a dipping time of 2 minutes. Typical *JV* curves for devices employing layers in which the $PbCl_2$ films had been deposited onto substrates held at 60°C and subsequently undergone different dip times are shown in **Figure 5.21(c)**. Notably, light soaking reduced device performance for two-step spin-dip processed devices and all results presented here are thus without any light soaking applied.

A further experiment was performed in which $PbCl_2$ layers were dipped into either warm (held on a 60°C hotplate) or cold (room temperature) MAI solution before being finished into complete devices. Whilst the warm-dipped layers achieved an average PCE of (4.23 ± 0.56)%, the cold-dipped devices exhibited limited colour change, minimal photovoltaic response and had an average PCE of (0.1 ± 0.1)% indicating that conversion to perovskite was very much incomplete. MAI dipping solutions were thus held on a 60°C hotplate in all further experiments. In order to investigate the effect of annealing protocols on the devices, $PbCl_2$ films were subjected to 2 min dipping times before being dried with compressed nitrogen and either left without any annealing treatment or undergoing to thermal anneals at 60°C, 90°C or 110°C before being employed in solar cell devices. PCEs for this experiment are presented in **Figure 5.21(b)**. Samples annealed at 110°C exhibited a colour change to yellow during the anneal, likely indicating a decomposition to lead iodide, and the resulting devices exhibited no photovoltaic response. In all cases a thermal anneal was found to reduce device efficiency in comparison to unannealed films, with the reduction being exacerbated by higher annealing temperatures and longer annealing times. Typical *JV* curves for devices having undergone a 90°C anneal are shown in **Figure 5.21(d)**.

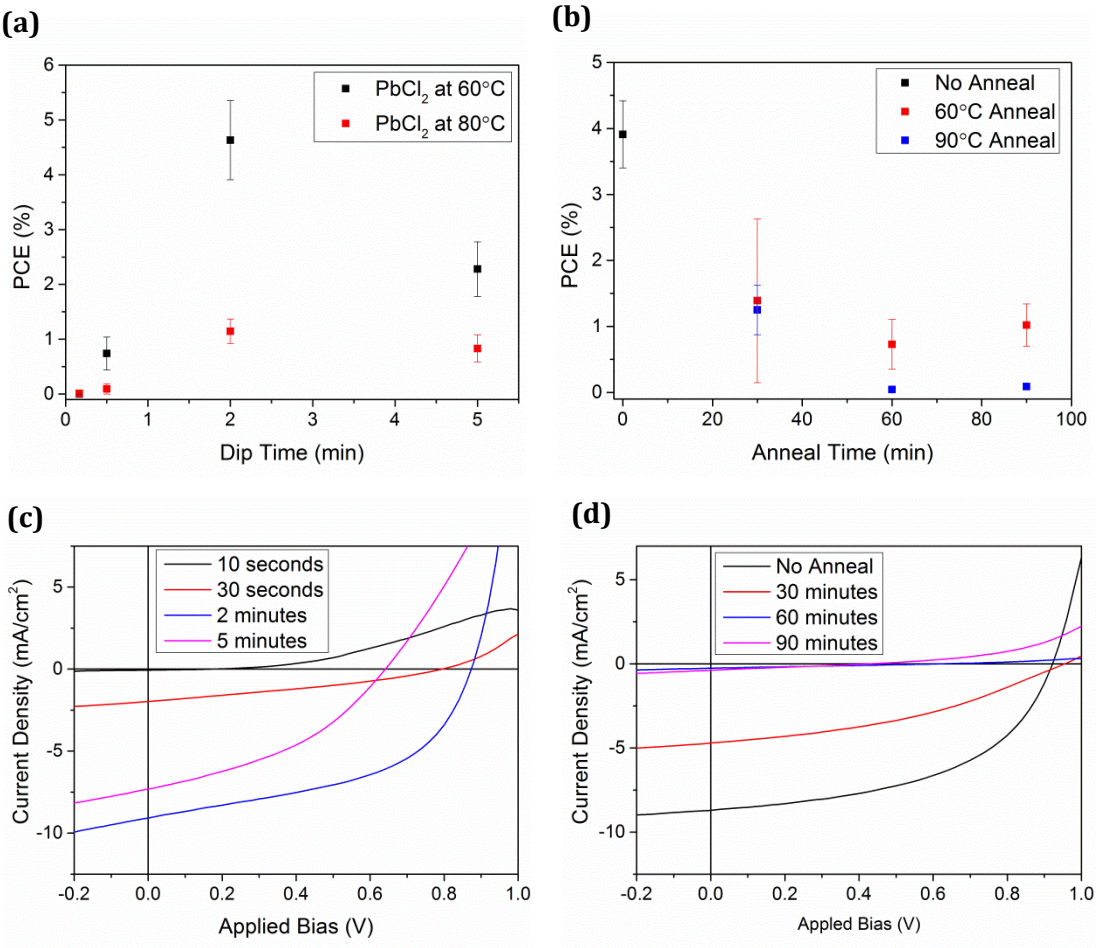

Figure 5.21 Power conversion efficiencies of perovskite solar cells fabricated using a two-step spin-dip approach with different deposition temperatures and dipping times **(a)** and different annealing conditions **(b)**. Typical current-density against voltage curves are shown for devices employing $PbCl_2$ layers deposited at 60°C and subjected to different dipping times **(c)** as well as devices with 2 minute dip times which have undergone a 90°C thermal anneal for differing lengths of time **(d)**.

At his time a report was published on the effect of incorporation of $PbCl_2$ into spin-cast PbI_2 films for subsequent use in a two-step fabrication procedure for perovskite solar cells [23]. This report found that the addition of a small amount of $PbCl_2$ (10 mol%) to the lead salt solution resulted in a slight increase in PCE, attributed to improved film coverage. Increasing the $PbCl_2$ content to 50 or 75 mol%, however, resulted in a notable decrease in PCE due to a reduction in FF, attributed to an increased resistivity of the perovskite film. Notably, a poor FF is a significant problem for the devices fabricated in this work. In addition to this report, during an informal talk with Pablo Docamapo it emerged that his research group at Ludwig Maximillian University of

Munich had attempted a two-step fabrication process based on $PbCl_2$ films and had also been unsuccessful in the fabrication of high efficiency solar cells (data unpublished). Given the above published and unpublished information, and having failed to achieve average device efficiencies in excess of 5% it was decided that the two-step spray-dip fabrication technique based on spray-coated $PbCl_2$ layers did not seem a promising route to enhancing solar cell PCE and this work was thus discontinued. Device metrics for average and champion solar cells from the highest efficiency batch fabricated using this method are shown in **Table 5.12**. For these devices the thicknesses of the initial $PbCl_2$ layer and converted perovskite layer were (240 ± 30) nm and (470 ± 50) nm respectively

	PCE (%)	**J_{SC} (mA/cm²)**	**V_{OC} (V)**	**FF (%)**
Average	4.45 ± 0.68	9.18 ± 1.31	0.864 ± 0.060	56.8 ± 7.46
Champion	5.35	11.3	0.948	50.0

Table 5.12 Average and champion device metrics for the best batch of perovskite solar cells fabricated using a two-step spray-dip processing method based on $PbCl_2$ layers. Relative humidity during this experiment was ~40%. Errors given are standard deviations.

5.8 Conclusions

This work has successfully demonstrated that organometal halide perovskite solar cells can be fabricated using the roll-to-roll compatible technique of ultrasonic spray-coating for deposition of the perovskite layer. Films were spray-cast from a solution of MAI:$PbCl_2$ at a 3:1 molar ratio, dissolved in the solvent DMF, onto substrates held at 75°C (i.e. a 'one-step' process). A thermal anneal at 90°C for 90 minutes was then applied in order to convert the precursor film to a perovskite layer with good uniformity and high surface coverage, albeit with high surface roughness. Such films were then incorporated into solar cells with an inverted architecture. These devices had an average power conversion efficiency of 7.8% and a maximum efficiency of 11.1% after a 20 minute light soaking period during which V_{OC} in particular was enhanced. Minimal hysteresis in current density against voltage characteristics was observed at scan rates from 0.3–2 V/s. Average efficiency was comparable to reference

devices employing spin-cast perovskite layers, although the spread of device performance was notably larger for spray-deposited films. No substantial differences between spun and sprayed perovskite films are observed under scanning electron microscopy or wide angle x-ray scattering.

Ultrasonic spray-deposition of the PEDOT:PSS hole transport layer in solar cells which employed spray-cast perovskite photoactive layers has also been successfully demonstrated, with no loss in average PCE in comparison to spin-cast PEDOT:PSS. A two-solvent approach allowed uniform $PC_{70}BM$ electron transport layers to be deposited via spray-coating, however it was not possible to successfully incorporate these into high performance solar cells due to large reductions in J_{SC} and FF when thick (>100 nm) PCBM layers, whether sprayed or spun, were processed in air. Whilst this effect could somewhat be mitigated by applying thermal annealing protocols in a nitrogen atmosphere after PCBM deposition, full efficiency could not be recovered. Finally, a two-step perovskite fabrication procedure based on the immersion of spray-coated $PbCl_2$ layers into MAI solutions was able to produce working solar cell devices, however average efficiencies did not exceed 5%.

5.9 References

[1] T. Wang, N.W. Scarratt, H. Yi, A.D.F. Dunbar, A.J. Pearson, D.C. Watters, et al., Fabricating High Performance, Donor-Acceptor Copolymer Solar Cells by Spray-Coating in Air, Adv. Energy Mater. 3 (2013) 505–512.

[2] C. Girotto, D. Moia, B.P. Rand, P. Heremans, High-Performance Organic Solar Cells with Spray-Coated Hole-Transport and Active Layers, Adv. Funct. Mater. 21 (2011) 64–72.

[3] V. Gonzalez-Pedro, E.J. Juarez-Perez, W.-S. Arsyad, E.M. Barea, F. Fabregat-Santiago, I. Mora-Sero, et al., General Working Principles of $CH_3NH_3PbX_3$ Perovskite Solar Cells., Nano Lett. 14 (2014) 888–893.

[4] E. Edri, S. Kirmayer, A. Henning, S. Mukhopadhyay, K. Gartsman, Y. Rosenwaks, et al., Why lead methylammonium tri-iodide perovskite-based solar cells require a mesoporous electron transporting scaffold (but not necessarily a hole conductor), Nano Lett. 14 (2014) 1000–1004.

[5] M.M. Lee, J. Teuscher, T. Miyasaka, T.N. Murakami, H.J. Snaith, Efficient hybrid solar cells based on meso-superstructured organometal halide perovskites, Science. 338 (2012) 643–647.

[6] H. Gao, C. Bao, F. Li, T. Yu, J. Yang, W. Zhu, et al., Nucleation and Crystal Growth of Organic-Inorganic Lead Halide Perovskites under Different Relative Humidity, ACS Appl. Mater. Interfaces. 7 (2015) 9110–9117.

[7] Z. Xiao, B. Cheng, Y. Shao, Q. Dong, Q. Wang, Y. Yongbo, et al., Efficient, High Yield Perovskite Photovoltaic Devices Grown by Interdiffusion of Solution-Processed Precursor Stacking Layers, Energy Environ. Sci. 7 (2014) 2619–2623.

[8] J.H. Heo, H.J. Han, D. Kim, T.K. Ahn, S.H. Im, Hysteresis-less inverted $CH_3NH_3PbI_3$ planar perovskite hybrid solar cells with 18.1% power conversion efficiency, Energy Environ. Sci. 8 (2015) 1602–1608.

[9] C.-G. Wu, C.-H. Chiang, Z.-L. Tseng, Planar Heterojunction Perovskite/PC71BM Solar Cells with enhanced open-circuit voltage via (2/1)-step Spin-coating Process, J. Mater. Chem. A. 2 (2014) 15897–15903.

[10] G.E. Eperon, V.M. Burlakov, P. Docampo, A. Goriely, H.J. Snaith, Morphological Control for High Performance, Solution-Processed Planar Heterojunction Perovskite Solar Cells, Adv. Funct. Mater. 24 (2014) 151–157.

[11] M. Liu, M.B. Johnston, H.J. Snaith, Efficient planar heterojunction perovskite solar cells by vapour deposition, Nature. 501 (2013) 395–398.

[12] K.W. Tan, D.T. Moore, M. Saliba, H. Sai, L.A. Estroff, T. Hanrath, et al., Thermally Induced Structural Evolution and Performance of Mesoporous Block Copolymer-Directed Alumina Perovskite Solar Cells, ACS Nano. 8 (2014) 4730–4739.

[13] A. Dualeh, N. Tétreault, T. Moehl, P. Gao, M.K. Nazeeruddin, M. Grätzel, Effect of Annealing Temperature on Film Morphology of Organic-Inorganic Hybrid Pervoskite Solid-State Solar Cells, Adv. Funct. Mater. 24 (2014) 3250–3258.

[14] S. Colella, E. Mosconi, P. Fedeli, A. Listorti, F. Gazza, F. Orlandi, et al., $MAPbI_{3-x}Cl_x$ Mixed Halide Perovskite for Hybrid Solar Cells : The Role of Chloride as Dopant on the Transport and Structural Properties, Chem. Mater. 25 (2013) 4613–4618.

[15] P. Docampo, J. Ball, M. Darwich, G. Eperon, H.J. Snaith, Efficient organometal trihalide perovskite planar-heterojunction solar cells for flexible polymer substrates, Nat. Commun. 4 (2013) 2761.

[16] B. Conings, L. Baeten, C. De Dobbelaere, J. D'Haen, J. Manca, H.-G. Boyen, Perovskite-Based Hybrid Solar Cells Exceeding 10% Efficiency with High Reproducibility Using a Thin Film Sandwich Approach, Adv. Mater. 26 (2014) 2041–2046.

[17] J. You, Z. Hong, Y.M. Yang, Q. Chen, M. Cai, T. Song, et al., Perovskite Solar Cells with High Efficiency and Flexibility, (2014).

[18] C. Bi, Q. Wang, Y. Shao, Y. Yuan, Z. Xiao, J. Huang, Non-wetting surface-driven high-aspect-ratio crystalline grain growth for efficient hybrid perovskite solar cells, Nat. Commun. 6 (2015) 7747.

[19] C. Wehrenfennig, G.E. Eperon, M.B. Johnston, H.J. Snaith, L.M. Herz, High Charge Carrier Mobilities and Lifetimes in Organolead Trihalide Perovskites, Adv. Mater. 26 (2013) 1584–1589.

[20] S.D. Stranks, G.E. Eperon, G. Grancini, C. Menelaou, M.J.P. Alcocer, T. Leijtens, et al., Electron-hole diffusion lengths exceeding 1 micrometer in an organometal trihalide perovskite absorber., Science. 342 (2013) 341–344.

[21] Q. Wang, Y. Shao, Q. Dong, Z. Xiao, Y. Yuan, H. Jinsong, Large Fill Factor Bilayer Iodine Perovskite Solar Cells Fabricated by Low-Temperature Solution-Process, Energy Environ. Sci. 7 (2014) 2359–2365.

[22] K. Liang, D.B. Mitzi, M.T. Prikas, Synthesis and Characterization of Organic–Inorganic Perovskite Thin Films Prepared Using a Versatile Two-Step Dipping Technique, Chem. Mater. 10 (1998) 403–411.

[23] D. Sabba, H.A. Dewi, R.R. Prabhakar, T. Baikie, S. Chen, Y. Du, et al., Incorporation of Cl in sequentially deposited lead halide perovskite films for highly efficient mesoporous solar cells., Nanoscale. 6 (2014) 13854–13860.

[24] C.C. Stoumpos, C.D. Malliakas, M.G. Kanatzidis, Semiconducting tin and lead iodide perovskites with organic cations: Phase transitions, high mobilities, and near-infrared photoluminescent properties, Inorg. Chem. 52 (2013) 9019–9038.

[25] A. Barrows, A. Pearson, C. Kwak, A. Dunbar, A. Buckley, D. Lidzey, Efficient planar heterojunction mixed-halide perovskite solar cells deposited via spray-deposition, Energy Environ. Sci. 7 (2014) 2944–2950.

[26] S. Das, B. Yang, G. Gu, P.C. Joshi, I.N. Ivanov, C.M. Rouleau, et al., High-Performance Flexible Perovskite Solar Cells by Using a Combination of

Ultrasonic Spray-Coating and Low Thermal Budget Photonic Curing, ACS Photonics. 2 (2015) 680–686.

[27] C. Zhao, B. Chen, X. Qiao, L. Luan, K. Lu, B. Hu, Revealing Underlying Processes Involved in Light Soaking Effects and Hysteresis Phenomena in Perovskite Solar Cells, Adv. Energy Mater. 5 (2015) 1500279.

[28] J. Xu, A. Buin, A.H. Ip, W. Li, O. Voznyy, R. Comin, et al., Perovskite–fullerene hybrid materials suppress hysteresis in planar diodes, Nat. Commun. 6 (2015) 7081.

[29] Y. Shao, Z. Xiao, C. Bi, Y. Yuan, J. Huang, Origin and elimination of photocurrent hysteresis by fullerene passivation in $CH_3NH_3PbI_3$ planar heterojunction solar cells, Nat. Commun. 5 (2014) 5784.

[30] H.J. Snaith, A. Abate, J.M. Ball, G.E. Eperon, T. Leijtens, N. Kimberly, et al., Anomalous Hysteresis in Perovskite Solar Cells, J. Phys. Chem. Lett. 5 (2014) 1511–1515.

[31] A. Dualeh, T. Moehl, N. Tetreult, J. Teuscher, P. Gao, M.K. Nazeeruddin, et al., Impednce Spectroscopic Analysis of Lead Iodide Perovskite-Sensitized Solid-State Solar Cells, ACS Nano. 8 (2014) 362–373.

[32] J.-Y. Jeng, Y.-F. Chiang, M.-H. Lee, S.-R. Peng, T.-F. Guo, P. Chen, et al., $CH_3NH_3PbI_3$ perovskite/fullerene planar-heterojunction hybrid solar cells, Adv. Mater. 25 (2013) 3727–3732.

[33] J.T.-W. Wang, J.M. Ball, E.M. Barea, A. Abate, J. a Alexander-Webber, J. Huang, et al., Low-Temperature Processed Electron Collection Layers of Graphene/TiO2 Nanocomposites in Thin Film Perovskite Solar Cells, Nano Lett. 14 (2014) 724–730.

[34] A. Yella, L.-P. Heiniger, P. Gao, M.K. Nazeeruddin, M. Grätzel, Nanocrystalline rutile electron extraction layer enables low temperature solution processed perovskite photovoltaics with 13.7% efficiency., Nano Lett. 14 (2014) 2591–2596.

[35] D. Alemu Mengistie, P.-C. Wang, C.-W. Chu, Effect of molecular weight of additives on the conductivity of PEDOT:PSS and efficiency for ITO-free organic solar cells, J. Mater. Chem. A. 1 (2013) 9907–9915.

[36] E.C.S. Transactions, T.E. Society, D. A. Mengistie, P.-C. Wang, C.-W. Chu, Highly

Conductive PEDOT: PSS Electrode Treated with Polyethylene Glycol for ITO-Free Polymer Solar Cells, ECS Trans. 58 (2013) 49–56.

[37] Q. Wei, M. Mukaida, Y. Naitoh, T. Ishida, Morphological Change and Mobility Enhancement in PEDOT:PSS by Adding Co-solvents, Adv. Mater. 25 (2013) 2831–2836.

[38] S. Paek, N. Cho, H. Choi, H. Jeong, J.S. Lim, J. Hwang, Improved External Quantum Efficiency from Solution-Processed $(CH_3NH_3)PbI_3$ Perovskite/$PC_{71}BM$ Planar Heterojunction for High Efficiency Hybrid Solar Cells, J. Phys. Chem. C. 118 (2014) 25899–25905.

[39] A. Tapponnier, I. Biaggio, P. Günter, Ultrapure C60 field-effect transistors and the effects of oxygen exposure, Appl. Phys. Lett. 86 (2005) 112114.

[40] R. Könenkamp, G. Priebe, B. Pietzak, Carrier mobilities and influence of oxygen in C60 films, Phys. Rev. B. 60 (1999) 11804–11808.

[41] C.-Y. Nam, D. Su, C.T. Black, High-Performance Air-Processed Polymer-Fullerene Bulk Heterojunction Solar Cells, Adv. Funct. Mater. 19 (2009) 3552–3559.

[42] J. Burschka, N. Pellet, S.-J. Moon, R. Humphry-Baker, P. Gao, M.K. Nazeeruddin, et al., Sequential deposition as a route to high-performance perovskite-sensitized solar cells, Nature. 499 (2013) 316–319.

[43] Y. Tidhar, E. Edri, H. Weissman, D. Zohar, G. Hodes, D. Cahen, et al., Crystallization of methyl ammonium lead halide perovskites: implications for photovoltaic applications., J. Am. Chem. Soc. 136 (2014) 13249–13256.

Chapter 6: Characterizing the Formation of $CH_3NH_3PbI_{3-x}Cl_x$ Perovskite Films During Thermal Annealing

6.1 Introduction

As discussed in **Chapter 2**, recent years have seen an unprecedented increase in the power conversion efficiencies (PCEs) of perovskite solar cells together with notable progress in their fabrication via commercially viable large-scale fabrication techniques [1,2]. In parallel with these advances, there has been significant improvement in our understanding of the underlying properties of these materials. This Chapter aims to expand on this understanding by characterising the formation of the perovskite $CH_3NH_3PbI_{3-x}Cl_x$ during the thermal annealing in air of a precursor film deposited using a 'one-step' spin-coating procedure. Both 2D grazing incidence wide angle and small angle X-ray scattering (GIWAXS and GISAXS) measurements have been employed to monitor the evolution of the film during in-situ annealing, providing access to the dynamics of structural changes in the film over three orders of magnitude in length scales. Ex-situ scanning electron microscopy (SEM) and device data from planar solar cells employing nominally identical films are also presented.

In-situ 2D GIWAXS and 1D XRD have previously been used to investigate the dynamics of both the two-step and one-step deposition methods in planar and mesoporous architectures [3–6]. Planar layers deposited onto PEDOT:PSS have not, however, been investigated via in-situ GIWAXS or XRD before. Thus far there has been limited use of GISAXS to study the crystallization of organometal halide perovskites. Schlipf et al. reported a detailed ex-situ GISAXS investigation of two-step fabrication of planar $CH_3NH_3PbI_{3-x}Cl_x$ films, concluding that length scales in the final perovskite films were very similar to those of the initial PbI_2 film and thus that controlling PbI_2 morphology is crucial in controlling the morphology of the final perovskite film [7]. Liao et al. used ex-situ GISAXS to investigate $CH_3NH_3PbI_3$ deposited via both one-step and two-step methods [8], observing evidence of pores within the perovskite crystal grains which could subsequently be filled by the electron transporting material or hole transporting material deposited onto the perovskite film. Their devices based on perovskite films

fabricated by the one-step process, however, displayed average PCEs of only 2.2% owing to poor surface coverage. Since GISAXS is concerned with probing structure on a length scale relevant to film morphology and coverage (nanometres to hundreds of nanometres) it is likely that their conclusions may not extend to the more uniform films required for high performance devices. The work presented here is thought to be the first in-situ GISAXS study for perovskite crystallization, as well as the first report of GISAXS for one-step fabricated perovskite films capable of producing high efficiency solar cells with average PCEs in excess of 10%.

6.2 In-Situ Grazing Incidence Wide Angle X-Ray Scattering (GIWAXS)

Firstly the evolution in film structure as characterised by in-situ GIWAXS measurements is considered. An MAI:$PbCl_2$ precursor ink (3:1 molar ratio in DMF) was deposited via a hot spin-coating process under ambient conditions (relative humidity RH ≈ 40–45%) onto Si/PEDOT:PSS substrates. The PEDOT:PSS layer was employed to ensure that perovskite nucleation conditions were the same in both solar cells and X-ray scattering samples, since it constitutes the hole transport layer in the inverted architecture devices fabricated herein. Perovskite films had a thickness of ~400 nm. Following spin-coating, the precursor films were immediately transferred to a sample chamber for GIWAXS measurement and a single diffraction pattern was recorded at room temperature as a reference (t = 0 min). Note that there was approximately a 2 minute (min) delay between spin-coating and the acquisition of this first image. After acquisition of the initial image the hotplate temperature was raised to the desired value (80°C, 90°C or 110°C) and films were heated in-situ for a period of up to 3 hours. The hotplate experienced an overshoot of approximately 10°C upon heating, with its measured temperature exceeding the target value within one minute for target temperatures of 80°C and 90°C and within two minutes for a target temperature of 110°C. In all cases the measured temperature dropped to its intended value within 10 minutes of the acquisition of the first image. Further details of this temperature overshoot are provided in **Section 6.3** where the crystallization kinetics of the film are explored.

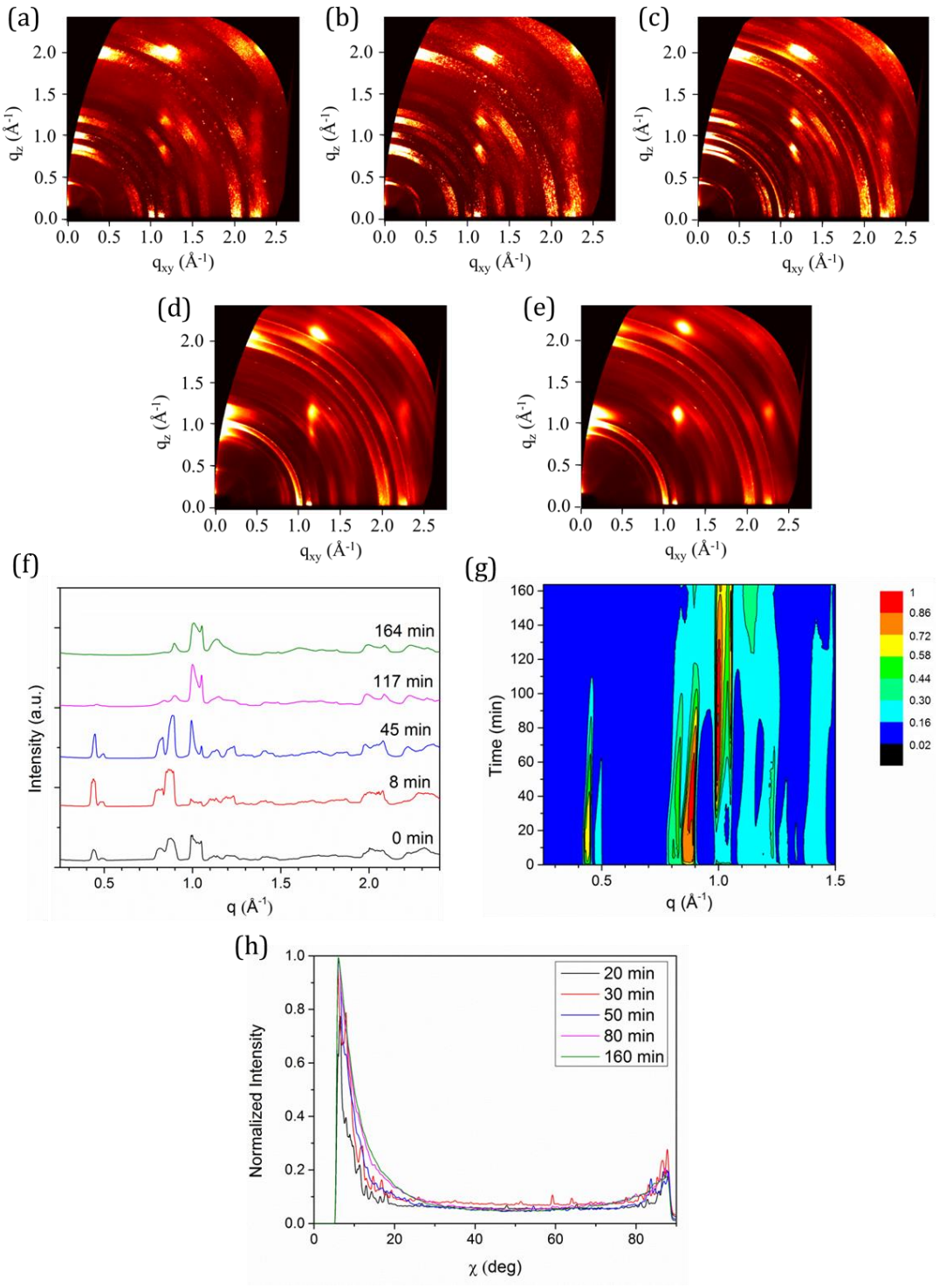

Figure 6.1 2D GIWAXS patterns recorded during an anneal at 80°C. Images are presented at t = 0 min **(a)**, 8 min **(b)**, 45 min **(c)**, 117 min **(d)** and 164 min **(e)**. Part **(f)** presents azimuthally integrated intensity profiles determined at these times. Part **(g)** shows the evolution of the GIWAXS spectrum through the annealing process as a contour plot of (normalized) azimuthally integrated intensity. Part **(h)** plots azimuthal profiles for the q ≈ 1 Å^{-1} diffraction peak during the anneal; a 5 point moving average has been used in order to smooth the data.

In **Figure 6.1** a summary of the in-situ GIWAXS data for the 80°C annealing process is presented. GIWAXS patterns are shown for t = 0 (part **(a)**) as well as at the lowest integrated intensity of the $q \approx 1$ Å^{-1} perovskite scattering ring (8 min, part **(b)**), at 50% of the maximum integrated intensity of this peak (45 min, part **(c)**), at the maximum integrated intensity of this peak (117 min, part **(d)**) and at the end of the annealing experiment (164 min, part **(e)**).

From **Figures 6.1(a)** and **(b)** it can be seen that the GIWAXS pattern for the precursor film at early annealing times is characterised by a large number of diffraction rings having a non-uniform intensity distribution in the azimuthal direction, indicative of a polycrystalline sample with some degree of crystallite orientation present. In line with previous reports, an unidentified crystalline precursor phase can be identified during the early stages of the annealing process, as shown by the rings located around q ≈ 0.45 Å^{-1} and q ≈ 0.8-0.9 Å^{-1} [4,6]. As noted in **Chapter 5**, the diffraction peak at q ≈ 1 Å^{-1} is widely attributed to the (110) plane of the tetragonal phase of the perovskite $CH_3NH_3PbI_{3-x}Cl_x$, although the (002) plane of the same structure, being located at q = 0.99 Å^{-1}, may also provide a contribution to this feature [5,9–11]. It is apparent that this broad feature having maximum intensity at q ≈ 1.00 Å^{-1} is in fact composed of a number of narrower peaks, with peaks evident at both q = 1.00 and 1.05 Å^{-1}. This observation is consistent with the existence of a series of crystallites within the film having different lattice constants, perhaps due to the coexistence of multiple perovskite phases [12,13]. At this point it is worth noting that the material commonly denoted $CH_3NH_3PbI_{3-x}Cl_x$ actually appears to be structurally similar to $CH_3NH_3PbI_3$, as discussed briefly in **Chapter 2** [14,15].

Due to the relatively high ambient humidity in the experimental environment (RH ≈ 40–45%), the yellow precursor film rapidly changed colour to grey during and immediately after spin-coating. This colour change can be attributed to the formation of perovskite upon exposure of the rapidly cooling precursor film to the ambient atmosphere, as has been reported previously in the supplementary information of ref [6]**.** Upon heating, the film returned to the bright yellow colour whilst, as can be seen in **Figures 6.1(a)**, **(b)**, and **(f)**, the intensity of the (110)-(002) diffraction ring dropped to a minimum at t = 8 min and the intensity of the precursor peaks increased, indicating a return to the precursor phase. As the thermal anneal proceeded the intensity of the perovskite (110)-(002) diffraction ring then increased, reaching a maximum integrated intensity at t = 117 min. This was accompanied by a simultaneous reduction in the

intensity of the peaks attributed to the crystalline precursor phase, indicating transformation of the precursors into $CH_3NH_3PbI_{3-x}Cl_x$. In **Figure 6.1(g)** it can be clearly seen that the precursor peak at q ≈ 0.45 $Å^{-1}$ has all but disappeared by ~115 min, an observation also seen in the radial profile of the diffraction measurement at 117 min shown in **Figure 6.1(f)**. At the longest annealing times a new peak attributed to PbI_2 emerges at q ≈ 0.9 $Å^{-1}$ [4,16,17]. Due to the overlap of this peak with the precursor peaks it is difficult to quantify the exact time at which it emerges. The growth of this feature occurs alongside a relative reduction in intensity of the peak at q ≈ 1 $Å^{-1}$, suggesting that decomposition of the $CH_3NH_3PbI_{3-x}Cl_x$ is taking place. Whilst this effect is relatively limited for the 80°C anneal, it is more evident at the higher annealing temperatures of 90°C and 110°C for which GIWAXS data is shown in **Figures 6.3** and **6.4**. In particular, the application of a 110°C anneal for 187 min leads to almost complete decomposition of the perovskite, as can be seen in **Figures 6.4(f)** and **(g)**. The relatively prompt onset of perovskite decomposition observed here is likely attributable to the high relative humidity during the experiment (RH ≈ 40-45%) [4]. Although the effect of beam damage accelerating this process has not been ruled out, it is notable that similar experiments performed under a dry nitrogen atmosphere do not lead to such rapid degradation. Evidence of this can be observed in **Figure 6.2** where, after a 170 minute anneal at a temperature of 90°C, a film annealed in air can be seen to have decomposed significantly, as evidenced by the large PbI_2 peak at q ≈ 0.9 $Å^{-1}$ whilst only a small peak remains at q ≈ 1 $Å^{-1}$. Meanwhile, a comparable sample annealed under nitrogen shows only a small lead iodide peak with most material remaining as perovskite.

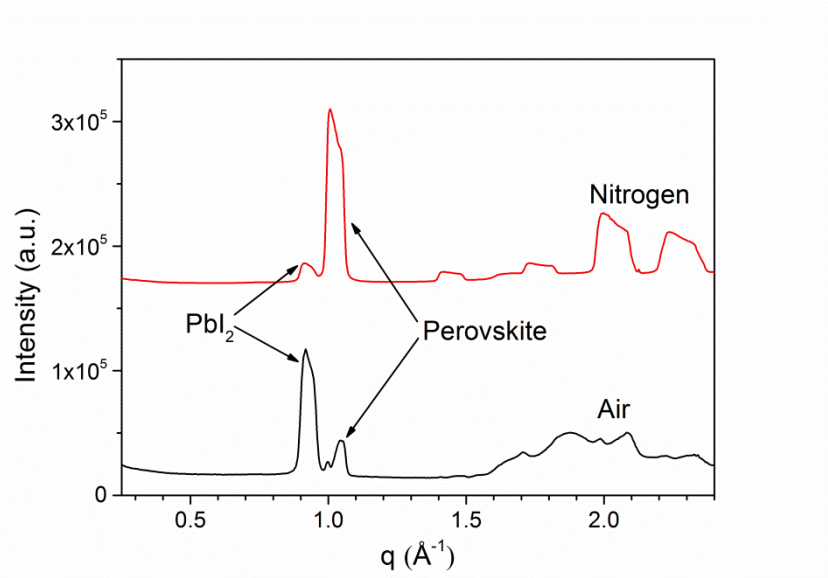

Figure 6.2 Azimuthally integrated radial profiles at an annealing time of 170 min for an annealing temperature of 90°C where the anneal has been undertaken in either air (RH ≈ 40-45%) or under dry nitrogen.

By comparing **Figure 6.1(a)** with **6.1(d)** it can be seen that some of the preferential crystallite orientation observed at early times persists throughout the annealing treatment. To determine the extent of this observation, **Figure 6.1(h)** presents azimuthal profiles of the X-ray scattering intensity for the feature at q ≈ 1 $Å^{-1}$ (i.e. intensity vs azimuth χ, where χ is the azimuth of q_z and q_{xy} in scattering vector polar coordinates with $\chi = 0°$ at positive q_z and $\chi = 90°$ at positive q_{xy} [18]). Data is presented at various times during the annealing process, with each trace normalised to its maximum intensity (at $\chi \approx 6°$). The scattering intensity is initially observed to be greater close to $\chi = 0°$, indicating preferential orientation of the (110) and (002) perovskite planes in the out-of-plane direction. Note however, that a relatively small population of $CH_3NH_3PbI_{3-x}Cl_x$ crystallites show in-plane orientation, as evidenced by the intensity of X-ray scatter close to $\chi = 90°$. During the annealing process the preferential orientation persists largely unchanged, although X-ray scattering intensity does increase slightly at intermediate angles of χ, implying that the annealing drives a slightly wider distribution of crystallite orientations relative to the structures formed during preparation of the precursor film. Preferential out-of-plane orientation of the (110)-(002) diffraction ring has previously been observed for planar $CH_3NH_3PbI_3$ and $CH_3NH_3PbI_{3-x}Cl_x$ films on compact TiO_2 and PEDOT:PSS respectively [19,20]. In

contrast, preferential in-plane orientation has been observed for $CH_3NH_3PbI_{3-x}Cl_x$ films fabricated on mesoporous Al_2O_3 scaffolds [21].

Similarly to **Figure 6.1**, **Figures 6.3** and **6.4** present summaries of the in-situ GIWAXS data for the 90°C and 110°C annealing processes respectively. In both cases GIWAXS images are presented at t = 0 min as well as at times corresponding to the lowest integrated intensity of the $q \approx 1$ Å^{-1} perovskite scattering ring, 50% of the maximum integrated intensity of this feature, the maximum integrated intensity of this feature and the end of the annealing experiment. By making a comparison between these Figures, and in particular between parts **(f)** and **(g)** it can be seen that, unsurprisingly, the transformation from precursor to perovskite proceeds significantly faster at higher temperatures. In addition, the subsequent degradation of the perovskite is accelerated at higher annealing temperatures. Preferential out-of-plane orientation for the (110)-(002) feature is observed at all temperatures, although at 110°C the level of preferential in-plane orientation is increased and there is no increase in scattering intensity at intermediate angles as the anneal proceeds.

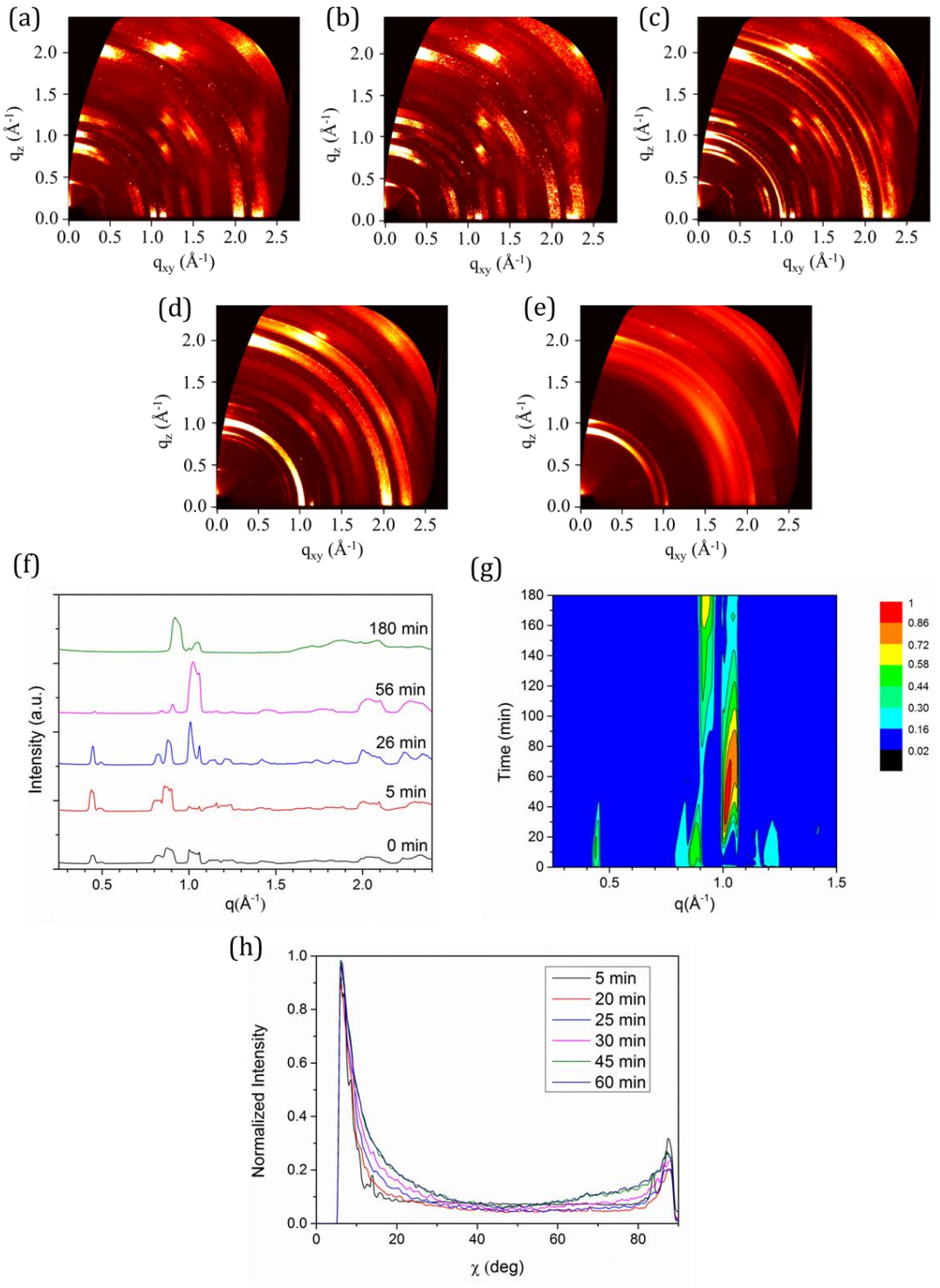

Figure 6.3 2D GIWAXS patterns for a 90°C anneal. Images are presented at t = 0 min **(a)**, 5 min **(b)**, 26 min **(c)**, 56 min **(d)** and 180 min **(e)**. Part **(f)** presents azimuthally integrated intensity profiles at these times. Part **(g)** shows the evolution of the GIWAXS spectrum through the annealing process as a contour plot of (normalized) azimuthally integrated intensity. Part **(h)** plots azimuthal profiles for the q ≈ 1 Å^{-1} diffraction peak during annealing, a 5 point moving average has been used in order to smooth the data.

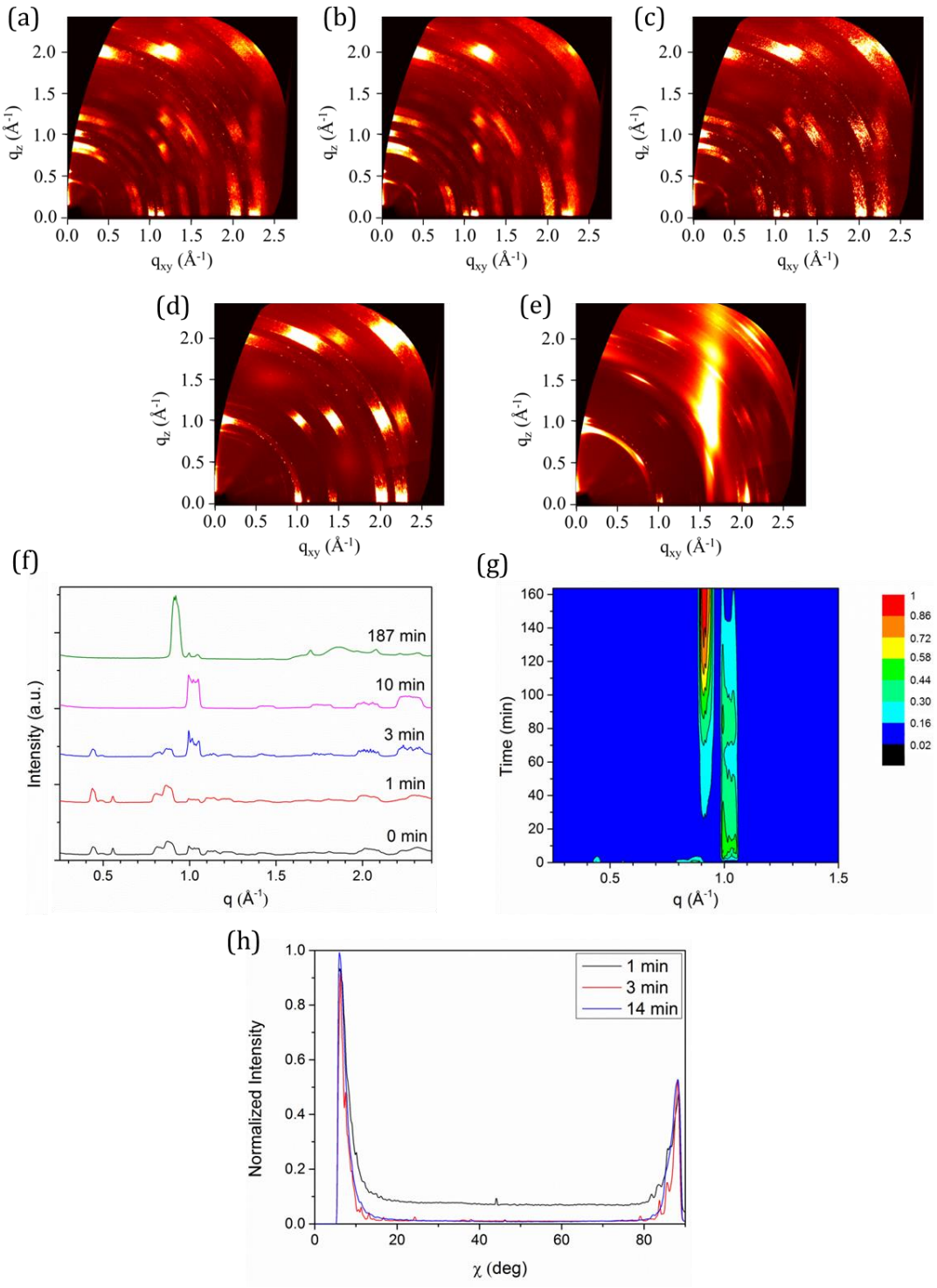

Figure 6.4 2D GIWAXS patterns for a 110°C anneal. Images are presented at t = 0 min **(a)**, 1 min **(b)**, 3 min **(c)**, 10 min **(d)** and 187 min **(e)**. Part **(f)** presents azimuthally integrated intensity profiles at these times. Part **(g)** shows the evolution of the GIWAXS spectrum through the annealing process as a contour plot of (normalized) azimuthally integrated intensity. Part **(h)** plots azimuthal profiles for the q ≈ 1 Å^{-1} diffraction peak during annealing, a 5 point moving average has been used in order to smooth the data.

6.3 Crystallization Kinetics

Following the approach of Moore et al. [5], it is possible to determine the activation energy E_A for $CH_3NH_3PbI_{3-x}Cl_x$ formation due to isothermal annealing of an MAI:$PbCl_2$ precursor film. Films were annealed at the three different target temperatures (80°C, 90°C and 110°C) and monitored via in-situ GIWAXS measurements. Relative changes in integrated intensity of the $q \approx 1$ Å^{-1} diffraction peak observed in the GIWAXS measurements were used to gauge the fraction of material transformed into the perovskite structure. The scattering ring at $q \approx 1$ Å^{-1} was used as a measure of this since it is by far the most intense peak arising from the perovskite material as well as being clearly distinguishable from the PbI_2 and precursor peaks. First it is necessary to define the fraction of material transformed into perovskite at a given time t as $x(t)$. Defining $x(t) = 1$ to occur at the maximum integrated intensity, the value of integrated intensity at other times is then normalised to this. For each diffraction measurement the integrated intensity of the q ≈ 1 Å^{-1} peak was calculated by peak fitting using four Gaussians.

Making the assumption that the transformation from precursor to perovskite is a direct, solid state transition the activation energy for an isothermal process can be determined using equation {1} [22]:

$$\ln(t_{x2} - t_{x1}) = \frac{E_a}{RT} - \ln k_0 + \ln(\beta_{x2} - \beta_{x1}) \qquad \{1\}$$

where t_{xn} is the time at which the transformed fraction is x_n, E_a is the effective activation energy for the transformation, R is the ideal gas constant, T is the temperature, k_0 is known as the "rate constant prefactor" or "pre-exponential factor" and β_{xn} is a property which depends upon the transformed fraction of the film (it is a monotonic function of x) which is invariant with time/temperature. The final two terms on the right of equation {1} are constants, thus by plotting $\ln(t_{x2}\text{-}t_{x1})$ against $1/RT$ one can expect to find a linear slope of gradient E_a. Here values of $x_1 = 0.2$ and $x_2 = 0.8$ were used, since these incorporate the bulk of the transformation whilst excluding the noisiest data. It should be noted that in this experiment the transformations were in fact not quite isothermal due to an overshoot on the hotplate as the temperature is raised. In order to account for this, the calculations presented here have used the average recorded temperature during the relevant time period, that is during the time

period from t_{x1} to t_{x2} where x_1 = 0.2 and x_2 = 0.8. For target temperatures of 80°C and 90°C these average values are the same as the target value due to the long annealing times (slow transformation from precursor to perovskite). For the target value of 110°C, however, this average temperature during the transition was in fact 119°C.

Despite the imperfect experimental procedure arising from the overshoot of the hotplate, particularly in the case of the highest temperature anneal, fitting to the data extracted from the GIWAXS measurements gives an activation energy of (85 ± 9) kJ/mol, a value very similar to the (86 ± 6) kJ/mol found by Moore et al. for the same material system. The plot used for the determination of E_a can be seen in **Figure 6.5(a)**.

The value of E_a calculated above can then be used to fit an appropriate model to the data. The Avrami equation, also known at the Johnson-Mehl-Avrami equation, is commonly used to describe isothermal transformations and is applied here in the common form

$$x(t) = 1 - e^{-\beta^n} \quad \{2\}$$

where n is the growth exponent (which relates to the dimensionality of growth) and β is the rate constant for the transformation [23][24]. Application of an Arrhenius-type equation for the rate constant in a simple rate equation, as is standard, then gives [22]

$$\beta = k(T)t = k_0 e^{\left(\frac{-E_a}{RT}\right)}t \quad \{3\}$$

Combining equations {2} and {3} one finds

$$x(t) = 1 - e^{-(k_0 e^{\left(\frac{-E_a}{RT}\right)}t)^n} \quad \{4\}$$

By treating n and k_0 as constants which can be adjusted as fitting parameters, equation {4} can be fitted to the $x(t)$ data extracted from the GIWAXS measurements. The results of this fitting are presented in **Figure 6.5(b)** and **Table 6.1**. As is common for such transformations an 'S'-shaped curve is observed on graphs of $x(t)$ against $\log(t)$. This can be rationalised by considering the initial low rate of transformation to correspond to a period of nucleation, which is then followed by rapid growth before the transformation rate again drops off once the majority of the material has been

converted. As can be seen in **Figure 6.5(b)** there is a good fit between model and data, in particular in the case of the 90°C annealing temperature.

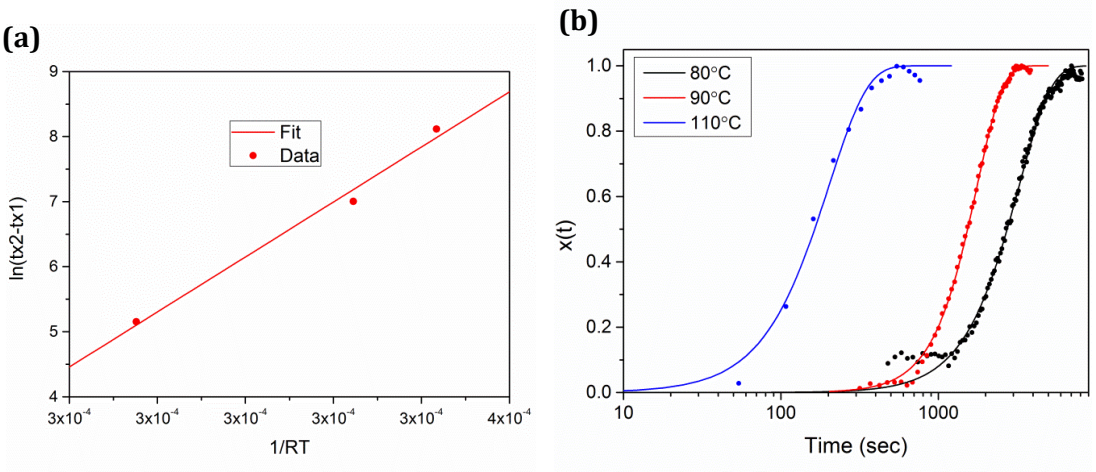

Figure 6.5 A graph for determination of activation energy **(a).** Part **(b)** presents the fit of the model to the data for all temperatures; filled circles are experimental data points whilst lines show the results of the model. Note that the '110°C' data has been labelled as such for consistency but the average temperature during the transformation period was actually 119°C, as discussed in the main text.

Anneal Temperature (°C)	**n**	**k_0**
80	2.10 ± 0.10	(1.10 ± 0.10) x 10^9
90	2.63 ± 0.06	(9.15 ± 0.05) x 10^8
110	1.76 ± 0.28	(9.94 ± 0.61) x 10^8

Table 6.1 Best fit parameters for the different annealing temperatures. For comparison, Moore reported values of n = 2.43 and k_0 = 4.1x10^{10}.

Having introduced the concept of the transformed fraction of material at a given time, $x(t)$, it is now possible to present a more comprehensive demonstration of the accelerated decomposition of the perovskite film when annealed under air as opposed to under nitrogen (as discussed earlier with reference to **Figure 6.2**). **Figure 6.6** presents a plot of $x(t)$ against annealing time for both air and nitrogen annealing

environments, where the accelerated degradation under ambient conditions can very clearly be seen.

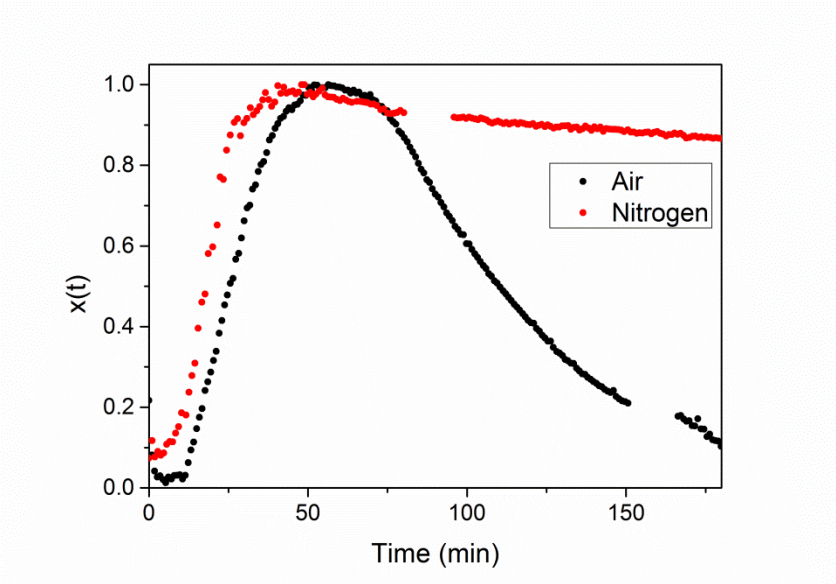

Figure 6.6 A plot of the transformed fraction of material, $x(t)$, against annealing time for an annealing temperature of 90°C under different environmental conditions.

6.4 In-Situ Grazing Incidence Small Angle X-Ray Scattering (GISAXS) and Ex-Situ Scanning Electron Microscopy (SEM)

The use of GISAXS measurements to monitor the evolution in film structure during thermal annealing complements the wide angle dataset by characterising the sample at q values as low as 10^{-3} Å^{-1}. In real space this corresponds to length scales as large as ~400 nm, a size that is potentially commensurate with that of individual perovskite grains [25–29]. Measurements were performed under nominally identical conditions to the GIWAXS measurements, although relative humidity was slightly higher (RH ≈ 45–50% as opposed to 40–45% during the GIWAXS experiments). Perovskite films were spin-cast onto glass/ITO/PEDOT:PSS substrates before being immediately transferred to the hotplate which was already at the setpoint temperature. There was approximately a 90 second delay between spin-coating and the acquisition of the first image (t = 0 min).

Quantitative analysis of GISAXS measurements is typically undertaken by modelling the data using the Distorted Wave Born Approximation (DWBA) to simulate scattering from periodic features in the film under investigation [30]. An attempt at modelling the data presented herein was undertaken by Dr David Babonneau at Université de Poitiers, France. Unfortunately, due to the irregular shape and large size distribution of grains in the films (as can be seen in the SEM images of nominally identical films shown in **Figures 6.8** and **6.9**) it was not possible to achieve a good fit to the data at low q values. Nevertheless, whilst a quantitative analysis has not been possible, a qualitative analysis can still provide useful information on the evolution of the film during the annealing process. Assistance in this qualitative analysis was kindly provided by Dr Babonneau.

Line profiles in q_y were taken at the Yoneda Peak for each image [31]. The evolution of the GISAXS scattering intensity in q_y during a thermal anneal at 80°C is shown in **Figure 6.7(a)**. It can be seen that for annealing times longer than around 60 minutes there is an increase in intensity at lower q values, although the shape of the spectrum remains quite similar throughout the process. By plotting the data in terms of the change in scattering intensity relative to that recorded at t = 0 min, it is possible to more easily observe changes in the scattering spectrum as a function of time during thermal annealing, as shown in **Figure 6.7(b)**. It can be seen that during the first 30 min of annealing, the intensity at all q_y values is slightly lower than that observed at t = 0, and that no clear features can be identified. At t > 40 min, there is an increase in intensity at q_y values below ~0.02 $Å^{-1}$, corresponding to length scales greater than ~30 nm. This increase in intensity gradually manifests itself as a peak in the spectrum centred at ~0.005 $Å^{-1}$, corresponding to a length scale of ~130 nm. Note that the lower bound of the data presented here is at $q_y = 1.54 \times 10^{-3}$ $Å^{-1}$, corresponding to a length scale of approximately 400 nm. These measurements thus suggest that as the perovskite is formed from the crystalline precursor phase, there is an increase in the fraction and number of structures within the film having length scales in the range 30 to 400 nm, and in particular an increase in the number of structures having length scales between 100 and 150 nm.

Plotting the logarithm of scattering intensity against q^2 at low q values (known as a Guinier analysis) allows for further qualitative analysis [30]. This is shown for q_y in **Figure 6.7(c)**, whilst **Figure 6.7(d)** presents a similar plot for q_z (taken at q_y = 0.003 $Å^{-1}$). As the annealing process proceeds, the slope of the curve close to q_y = 0 (**Figure**

6.7(c)) decreases, a feature attributable to a decrease in the average (lateral) diameter of the scatterers in the film. Similarly, an increase in the slope after the Yoneda peak in q_z, as seen in **Figure 6.7(d)**, indicates an increase in the average height of the grains. Together, these observations suggest a change in the aspect ratio of crystal grains during the annealing and transformation process. Finally, the shift of the Yoneda peak towards larger q_z values can be attributed to an increase in the density of the film.

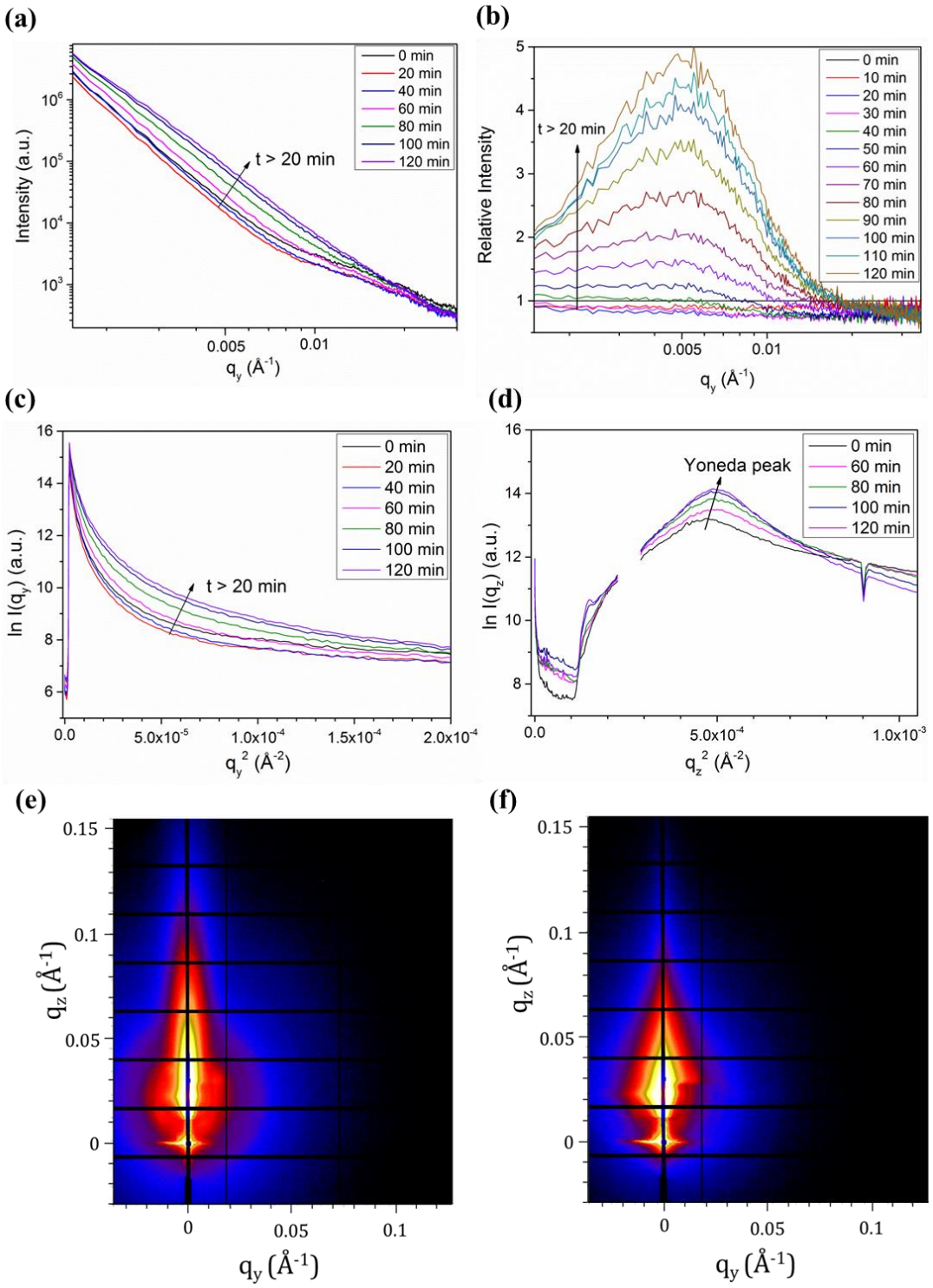

Figure 6.7 Evolution of the GISAXS data slice in q_y during an 80°C thermal anneal **(a)** and the same data presented as a relative intensity as compared to the data at 0 minutes **(b)**. The Guinier analysis for data slices in q_y and q_z are shown respectively in parts **(c)** and **(d)**. Parts **(e)** and **(f)** respectively show detector data for annealing times of 0 min and 120 min; the slight shading on the right side of the feature is due to the beam-stop, data was thus taken from the left side of the scattering feature.

In order to further investigate these changes in length scales, nominally identical films were annealed at 80°C for various lengths of time under a relative humidity of ~45% before being imaged via scanning electron microscopy (SEM) and atomic force microscopy (AFM). From the SEM images presented in **Figures 6.8** and **6.9** it can be seen that as the annealing time is increased from 60 to 120 min the film morphology evolves from one dominated by large micron sized grains separated by significant voids to one composed of many features at smaller length scales (hundreds of nm). At annealing times longer than 120 min the film morphology appears to stabilise and remains comparatively unchanged with further annealing. The decrease in apparent grain size and increase in the quantity of features with length scales of hundreds of nm during the period from t = 60 to 120 min is commensurate with the qualitative analysis of the GISAXS measurements described above. Atomic force microscopy images of the perovskite surface, as shown in **Figures 6.10** and **6.11**, further confirm this evolution in length scales within the perovskite film during annealing. Note that films annealed for times of less than 60 minutes were not sufficiently stable to be imaged via SEM or AFM.

The change in length scales during the period from t = 60 to 120 min is accompanied by an increase in the film surface coverage from ~80% to ~95%. This process is of particular importance due to the necessity of high surface coverage for the fabrication of high performance solar cells. Low surface coverage due to large voids in the perovskite film can be expected to lead to a reduced efficiency in solar cells due to both reduced light absorption (reduced J_{SC}) and additional leakage paths resulting in a reduction in shunt resistance (reduced V_{OC} and FF) [32,10]. The evolution of the film to the more continuous morphology as observed at longer annealing times appears to be linked to the change in length scales as evidenced by the GISAXS data. In particular, the largest changes in GISAXS data and observed film morphology both occur in the period from $t \approx 60$ to 100 min. This evolution is likely to be critical in the formation of the continuous and uniform films necessary for high performance perovskite solar cells prepared using a one-step process.

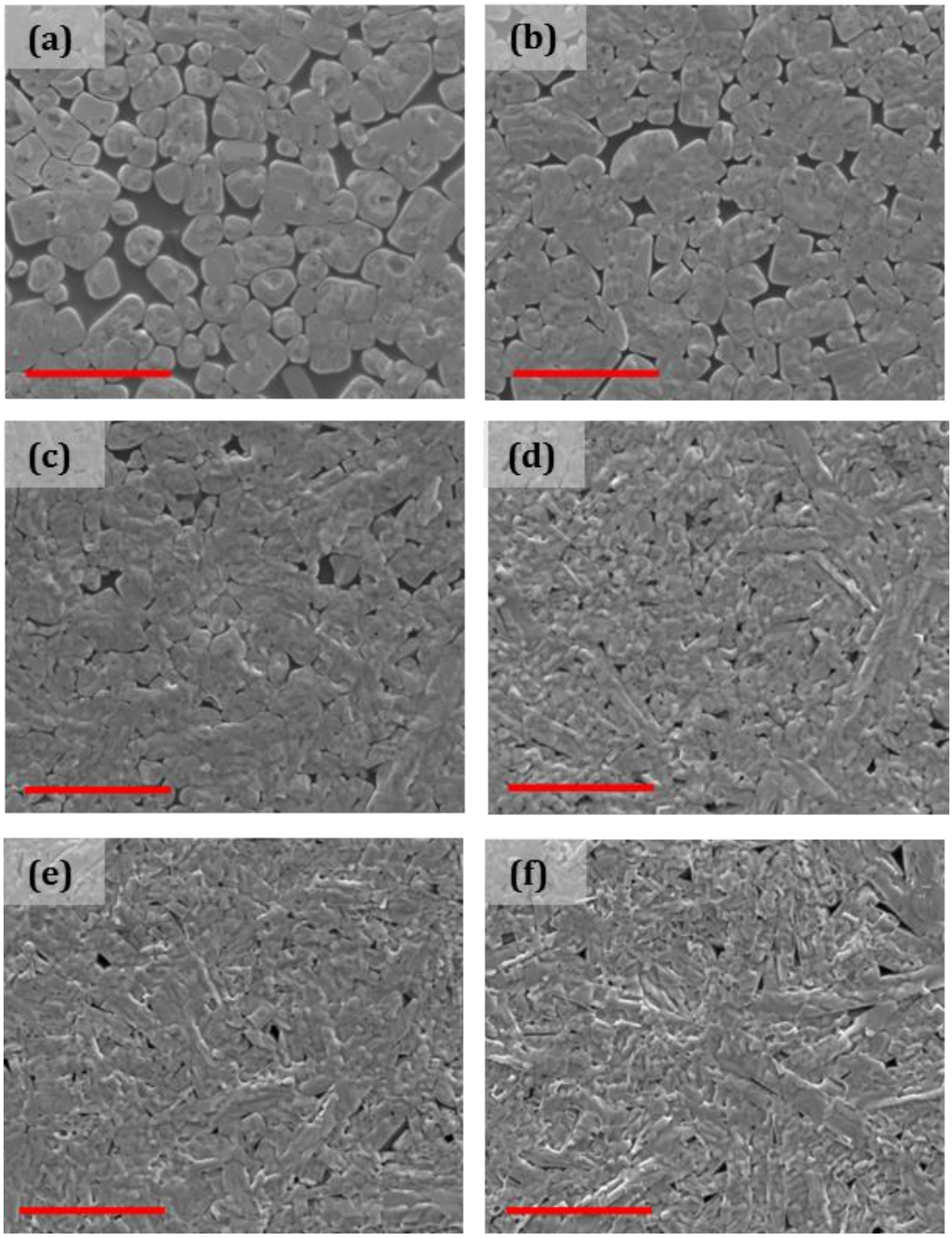

Figure 6.8 Scanning electron microscopy images of films annealed at 80°C for periods of 60 **(a)**, 80 **(b)**, 100 **(c)**, 120 **(d)**, 140 **(e)** and 180 **(f)** min. Red scale bars correspond to 5 μm.

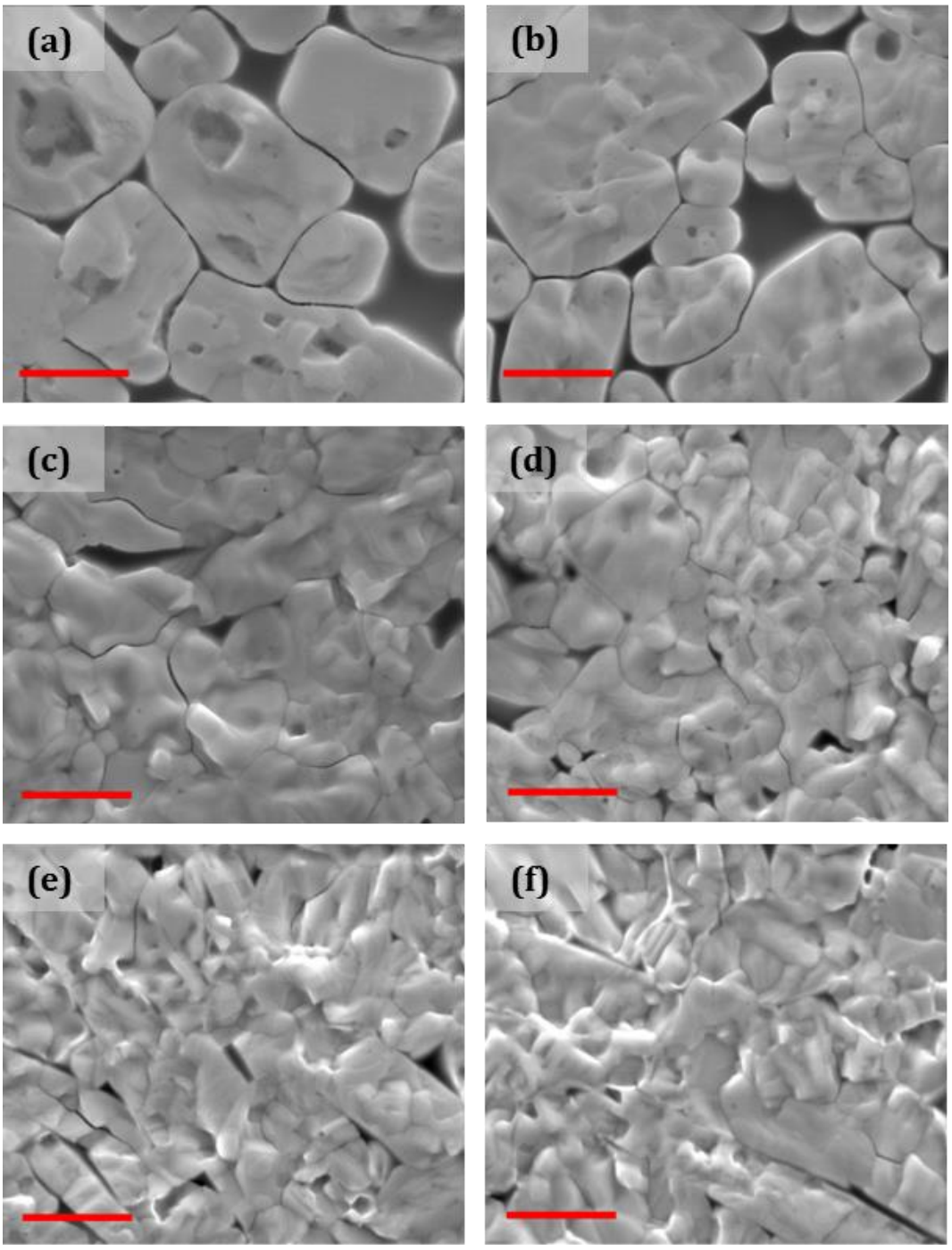

Figure 6.9 High magnification scanning electron microscopy images of films annealed for periods of 60 **(a)**, 80 **(b)**, 100 **(c)**, 120 **(d)**, 140 **(e)** and 180 **(f)** min. Red scale bars correspond to 1 μm.

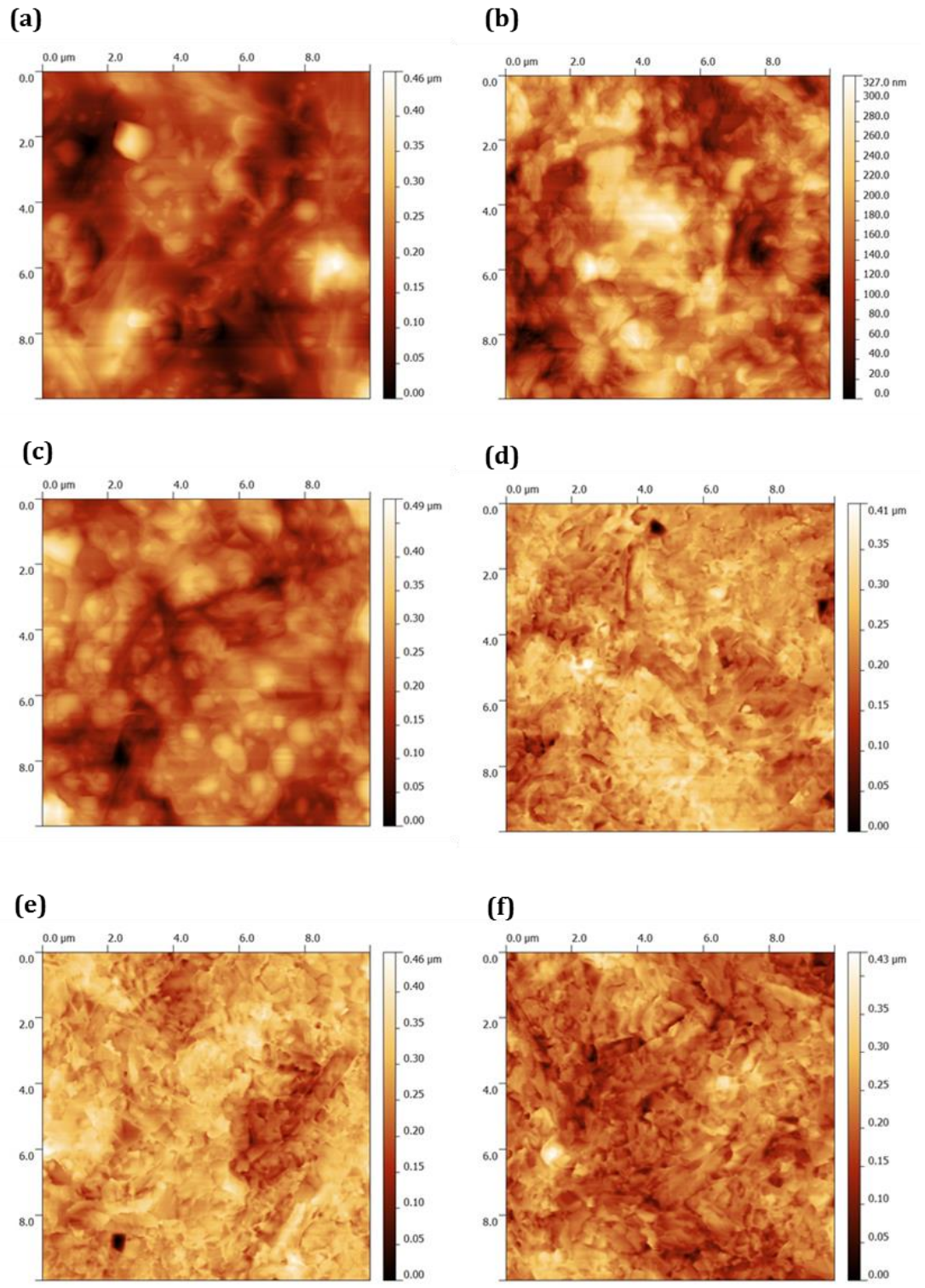

Figure 6.10 Atomic force microscopy images of films annealed at 80°C for periods of 60 **(a)**, 80 **(b)**, 100 **(c)**, 120 **(d)**, 140 **(e)** and 180 **(f)** min. Root mean squared surface roughness values for the measurements are 68, 51, 58, 42, 47 and 47 nm respectively.

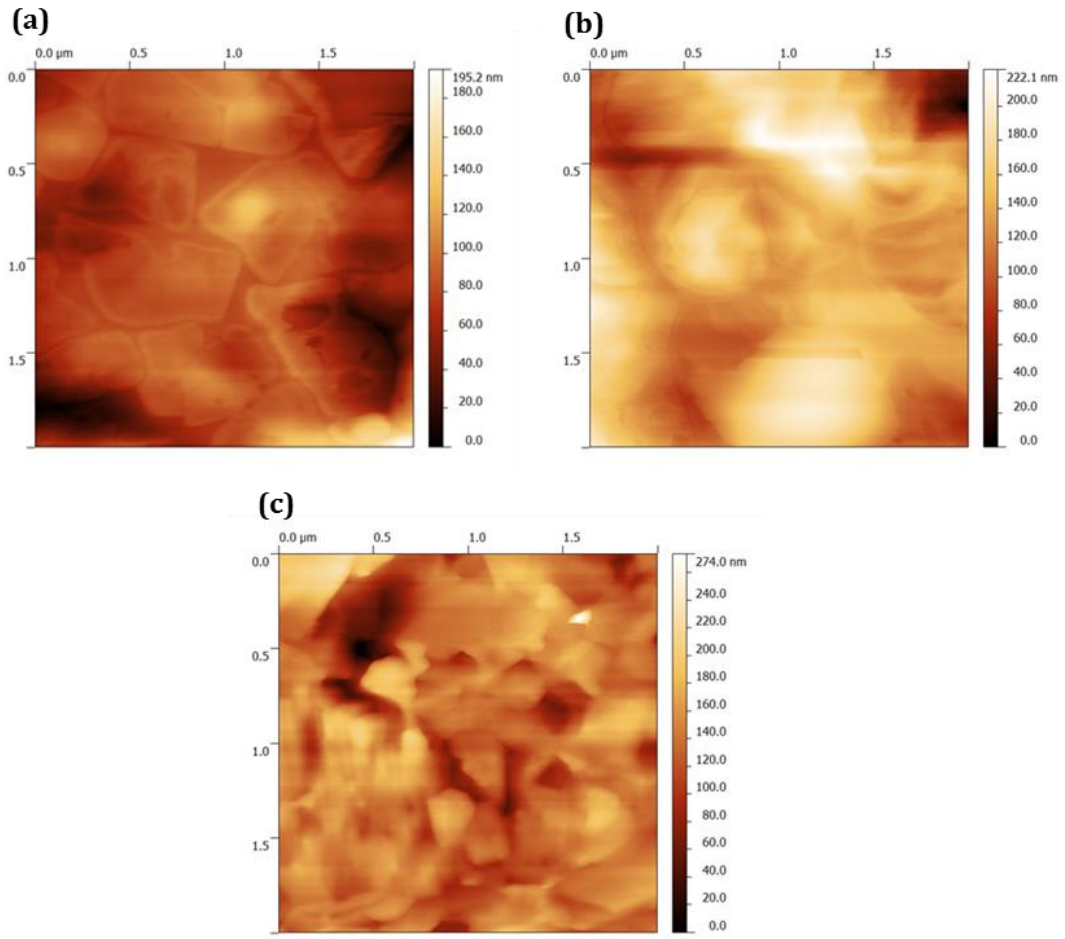

Figure 6.11 Atomic force microscopy images of films annealed at 80°C for periods of 80 **(a)**, 100 **(b)** and 120 **(c)** min.

In comparison to the results obtained during an anneal of the precursor film at 80°C, a higher annealing temperature produces a more marked change in the shape of the scattering spectrum. This can be seen in **Figure 6.12** which shows the scattering intensity at various times during an anneal at 115°C. Large changes in the scattering spectrum at early annealing times can be attributed to the rapid transformation of the film from precursor to perovskite at an elevated temperature, as observed from the GIWAXS measurements. The morphology of such films, however, is characterised by significant voids at all annealing times, as can be seen in SEM images of nominally identical ex-situ samples (presented in **Figure 6.13**). These films can thus be expected to lead to poor efficiencies when utilised in solar cells, and, as detailed in **Chapter 5**, previous reports have found that annealing temperatures in excess of ~100°C do indeed lead to reduced solar cell performance [16,32].

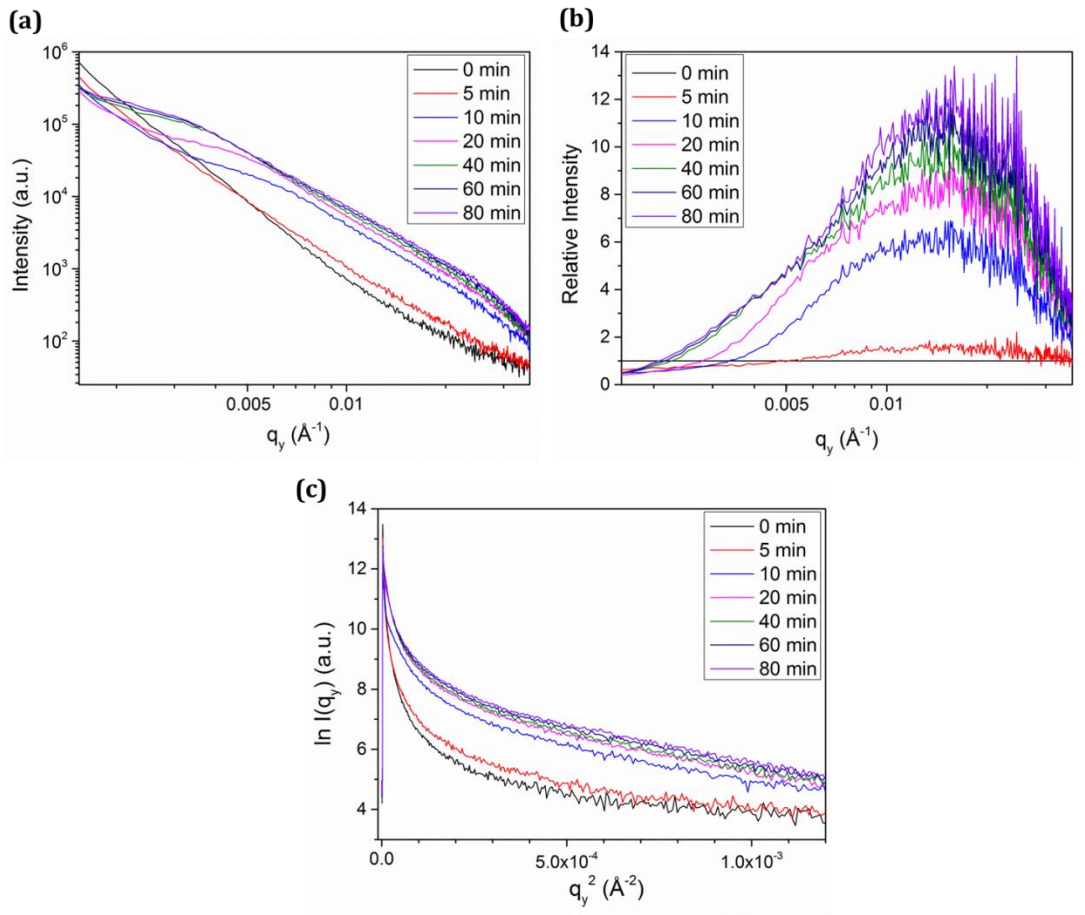

Figure 6.12 Evolution of the GISAXS data slice in q_y during a 115°C thermal anneal **(a)** and the same data presented as a relative intensity as compared to the data at 0 minutes **(b)** and as a Guinier plot **(c)**.

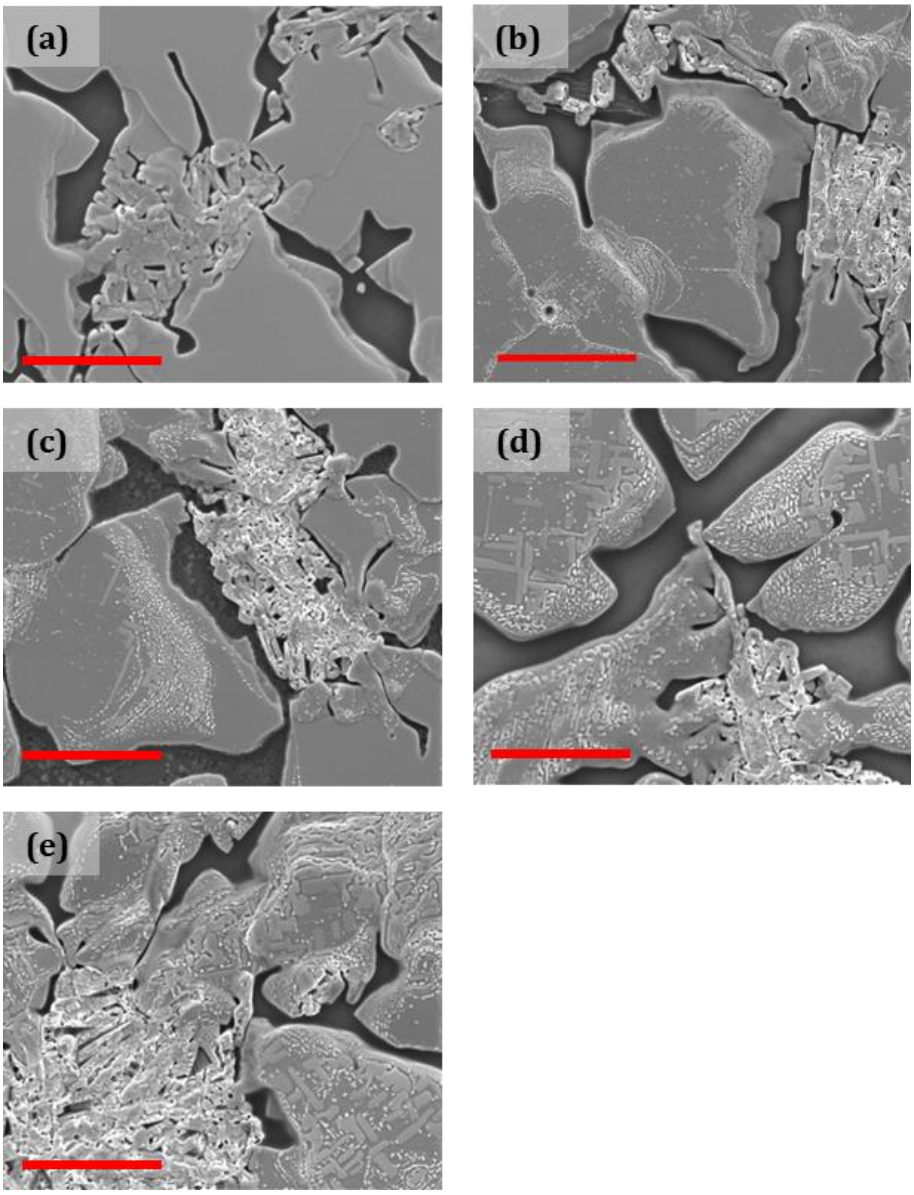

Figure 6.13 Scanning electron microscopy images of films annealed at 115°C for periods of 10 **(a)**, 20 **(b)**, 40 **(c)**, 60 **(d)**, and 80 **(e)**. Red scale bars correspond to 5 μm.

6.5 The Role of Annealing Treatments on Device Performance

In order to correlate solar cell performance with the evolution of perovskite films during the annealing process, films nominally identical to those used for the X-ray scattering measurements were fabricated into complete perovskite solar cells having the structure ITO/PEDOT:PSS/$CH_3NH_3PbI_{3-x}Cl_x$/$PC_{70}BM$/Ca/Al. Perovskite films were annealed at 80°C under a relative humidity of ~45% for lengths of time varying from 80 to 180 min. 3 substrates (containing a total of 12 devices) were fabricated for each

annealing time. Results shown are from a reverse *JV* scan at a scan rate of 0.5 V/s; no light soaking was used as it was not found to improve the performance of the devices. Device metrics for the resulting solar cells are presented in **Table 6.2**. Histograms showing the spread of device performance for each annealing condition are presented in **Figure 6.14(a)** whilst current-density against voltage curves for typical devices are shown in **Figure 6.14(b)**. Films annealed for less than 80 min could be seen by eye to have not fully converted to perovskite and can thus be expected to exhibit poor device performance as well as limited device lifetime. As the annealing time increased from 80 to 100 and then 120 min, average device power conversion efficiency (PCE) increased from 7.8% to 10.7% and finally 12.2%. This improved efficiency arises due to an increase in short circuit current density (J_{SC}) from 15.8 to 17.2 and finally 18.4 mA/cm^2, and an increase in fill factor (FF) from 50.6 to 64.0 and then 68.8%. At annealing times longer than 120 min, PCE began to reduce with all device metrics undergoing a reduction.

The observed trends in device performance can be understood with reference to the GISAXS, GIWAXS and SEM data presented above. Initial increases in performance can be attributed to the combined effect of two processes. Firstly, the increased annealing time leads to an increase in surface coverage and a reduced number of voids and pinholes in the film, resulting in an enhanced J_{SC} and FF. Concurrently there is a more complete conversion of precursor materials to the perovskite, and indeed the maximum efficiency of devices corresponds closely to the annealing time at which the integrated intensity of the q ≈ 1 Å^{-1} GIWAXS diffraction peak takes its maximum integrated value (117 min). This correspondence is confirmed in **Figure 6.13(c)**, where PCE and *x(t)* (the fraction of transformed material as defined in **Section 6.3**) are presented as a function of annealing time. Finally, at long annealing times the perovskite begins to undergo decomposition into various products including lead iodide, as observed via the in-situ GIWAXS data, leading to a reduction in device performance as might be expected.

Annealing Time (min)	PCE (%) (max)	J_{SC} (mA/cm²)	V_{OC} (V)	FF (%)
80	7.8 ± 1.0 (9.2)	15.8 ± 0.9	0.979 ± 0.006	50.6 ± 3.7
100	10.7 ± 0.5 (11.3)	17.2 ± 0.3	0.972 ± 0.004	64.0 ± 3.0
120	12.2 ± 0.3 (12.7)	18.4 ± 0.1	0.966 ± 0.004	68.8 ± 1.2
140	11.9 ± 0.2 (12.2)	18.3 ± 0.1	0.951 ± 0.005	68.4 ± 0.7
180	8.8 ± 0.5 (9.4)	17.5 ± 0.2	0.893 ± 0.012	56.7 ± 3.2

Table 6.2 Solar cell performance for devices employing perovskite layers annealed at 80°C for lengths of time from 80-180 minutes.

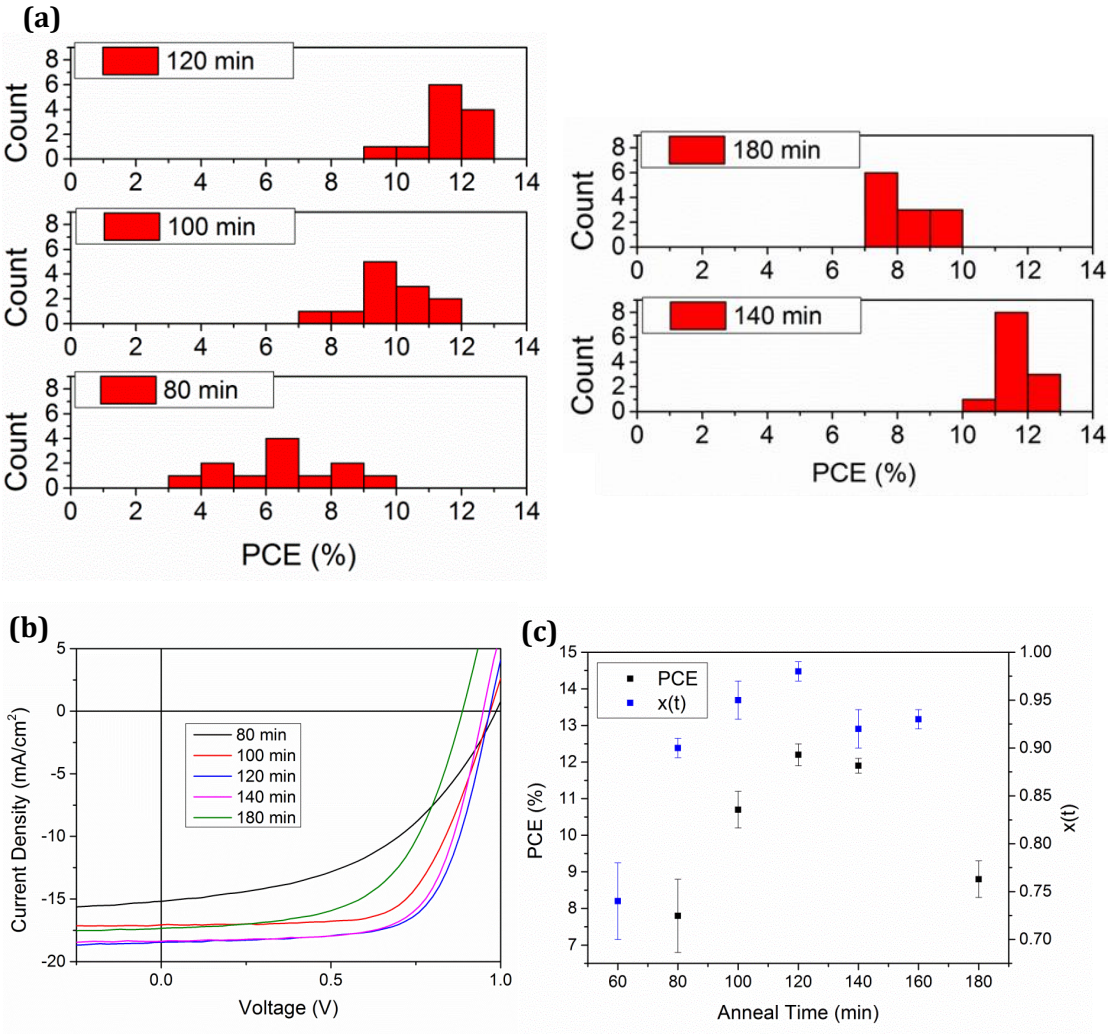

Figure 6.14 Histograms of solar cell power conversion efficiency for devices employing perovskite layers annealed at 80°C for lengths of time from 80-180 minutes **(a)** and current-density against voltage curves for typical devices **(b)**. Part **(c)** shows PCE and $x(t)$ as functions of annealing time.

In order to confirm that no significant hysteresis is observed in the current density against voltage characteristics for these devices, forward and reverse scans were performed on a typical pixel annealed for a period of 120 min. As can be seen in **Figure 6.15** the device exhibits minimal hysteresis for the scan rate used (0.5 V/s).

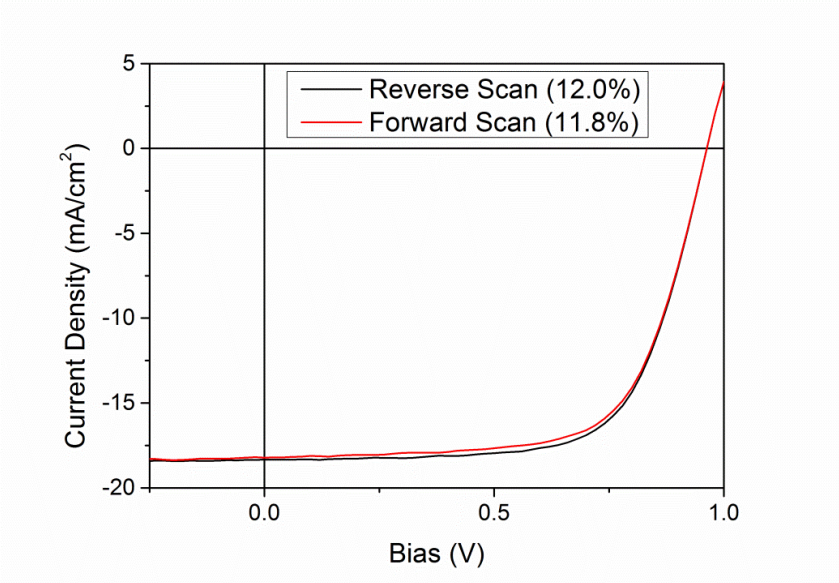

Figure 6.15 Forward and reverse scans of a typical perovskite solar cell in which the perovskite layer has been thermally annealed at 80°C for 120 minutes.

6.6 Conclusions

A variety of in-situ and ex-situ techniques have been utilised in order to characterise the formation of the perovskite $CH_3NH_3PbI_{3-x}Cl_x$ during the thermal annealing in air of a precursor film deposited using a 'one-step' spin-coating procedure. Through in-situ GIWAXS measurements the evolution of a crystalline precursor film into the perovskite structure and the subsequent decomposition of the perovskite could be monitored. The activation energy for the transformation from precursor to perovskite has been calculated to be (85 ± 9) kJ/mol, a value in line with a recent report on the subject. Preferential orientation in the out-of-plane direction is observed throughout the annealing process at all annealing temperatures investigated. In-situ GISAXS measurements show that during a thermal anneal at 80°C there is an evolution in length scales within the film, with a large increase in features having size in the

range 30-400 nm. Concurrently there is a change in the aspect ratio of grains due to a decrease in lateral diameter and an increase in height, as well as an increase in the density of the film. This evolution in length scales is correlated with an increase in film surface coverage which is known to lead to improved device efficiency. Devices fabricated using perovskite films annealed at 80°C for lengths of time from 80 to 180 min show efficiencies which can be explained on the basis of in-situ X-ray scattering and ex-situ SEM measurements with an optimised annealing time resulting in devices having an average PCE of 12.2%.

6.7 References

[1] M.A. Green, K. Emery, Y. Hishikawa, W. Warta, E.D. Dunlop, Solar cell efficiency tables (version 46), Prog. Photovoltaics Res. Appl. 23 (2015) 805–812.

[2] A. Barrows, A. Pearson, C. Kwak, A. Dunbar, A. Buckley, D. Lidzey, Efficient planar heterojunction mixed-halide perovskite solar cells deposited via spray-deposition, Energy Environ. Sci. 7 (2014) 2944–2950.

[3] T. Miyadera, Y. Shibata, T. Koganezawa, T.N. Murakami, T. Sugita, N. Tanigaki, et al., Crystallization Dynamics of Organolead Halide Perovskite by Real-Time X-ray Diffraction, Nano Lett. 15 (2015) 5630–5634.

[4] K.W. Tan, D.T. Moore, M. Saliba, H. Sai, L.A. Estroff, T. Hanrath, et al., Thermally Induced Structural Evolution and Performance of Mesoporous Block Copolymer-Directed Alumina Perovskite Solar Cells, ACS Nano. 8 (2014) 4730–4739.

[5] D.T. Moore, H. Sai, K.W. Tan, D. Smilgies, W. Zhang, H.J. Snaith, et al., Crystallization kinetics of organic-inorganic trihalide perovskites and the role of the lead anion in crystal growth, J. Am. Chem. Soc. 137 (2015) 2350–2358.

[6] E.L. Unger, A.R. Bowring, C.J. Tassone, V.L. Pool, A. Gold-parker, R. Cheacharoen, et al., Chloride in Lead Chloride-Derived Organo-Metal Halides for Perovskite-Absorber Solar Cells, Chem. Mater. 26 (2014) 7158–7165.

[7] J. Schlipf, P. Docampo, C.J. Schaffer, V. Körstgens, L. Bießmann, F.C. Hanusch, et al., A Closer Look into 2-Step Perovskite Conversion with X-Ray Scattering, J. Phys. Chem. Lett. 6 (2015) 1265–1269.

[8] H.-C. Liao, C.-S. Tsao, M.-H. Jao, J.-J. Shyue, C.-P. Hsu, Y.-C. Huang, et al., Hierarchical i–p and i–n porous heterojunction in planar perovskite solar cells, J. Mater. Chem. A. 3 (2015) 10526–10535.

[9] M.M. Lee, J. Teuscher, T. Miyasaka, T.N. Murakami, H.J. Snaith, Efficient hybrid solar cells based on meso-superstructured organometal halide perovskites, Science. 338 (2012) 643–647.

[10] M. Liu, M.B. Johnston, H.J. Snaith, Efficient planar heterojunction perovskite solar cells by vapour deposition, Nature. 501 (2013) 395–398.

[11] K. Liang, D.B. Mitzi, M.T. Prikas, Synthesis and Characterization of Organic–Inorganic Perovskite Thin Films Prepared Using a Versatile Two-Step Dipping Technique, Chem. Mater. 10 (1998) 403–411.

[12] K. Wu, A. Bera, C. Ma, Y. Du, Y. Yang, L. Li, et al., Temperature-dependent excitonic photoluminescence of hybrid organometal halide perovskite films, Phys. Chem. Chem. Phys. 16 (2014) 22476–22481.

[13] T. Baikie, Y. Fang, J.M. Kadro, M. Schreyer, F. Wei, S.G. Mhaisalkar, et al., Synthesis and crystal chemistry of the hybrid perovskite $(CH_3NH_3)PbI_3$ for solid-state sensitised solar cell applications, J. Mater. Chem. A. 1 (2013) 5628.

[14] H. Yu, F. Wang, F. Xie, W. Li, J. Chen, N. Zhao, The Role of Chlorine in the Formation Process of "$CH_3NH_3PbI_{3-x}Cl_x$" Perovskite, Adv. Funct. Mater. 24 (2014) 7102–7108.

[15] M.I. Dar, N. Arora, P. Gao, S. Ahmad, M. Grätzel, M.K. Nazeeruddin, Investigation Regarding the Role of Chloride in Organic-Inorganic Halide Perovskites Obtained from Chloride Containing Precursors, Nano Lett. 14 (2014) 6991–6996.

[16] A. Dualeh, N. Tétreault, T. Moehl, P. Gao, M.K. Nazeeruddin, M. Grätzel, Effect of Annealing Temperature on Film Morphology of Organic-Inorganic Hybrid Pervoskite Solid-State Solar Cells, Adv. Funct. Mater. 24 (2014) 3250–3258.

[17] S. Colella, E. Mosconi, P. Fedeli, A. Listorti, F. Gazza, F. Orlandi, et al., $MAPbI_{3-x}Cl_x$ Mixed Halide Perovskite for Hybrid Solar Cells : The Role of Chloride as Dopant on the Transport and Structural Properties, Chem. Mater. 25 (2013) 4613–4618.

[18] S. Lilliu, T. Agostinelli, E. Verploegen, E. Pires, M. Hampton, M. Al-Hashimi, et al., Effects of thermal annealing upon the nanomorphology of poly(3-

hexylselenophene)-PCBM blends, Macromol. Rapid Commun. 32 (2011) 1454–1460.

[19] Y.-C. Huang, C.-S. Tsao, Y.-J. Cho, K.-C. Chen, K.-M. Chiang, S.-Y. Hsiao, et al., Insight into Evolution, Processing and Performance of Multi-length-scale Structures in Planar Heterojunction Perovskite Solar Cells, Sci. Rep. 5 (2015) 13657.

[20] W. Huang, F. Huang, E. Gann, Y. Cheng, C.R. Mcneill, Probing Molecular and Crystalline Orientation in Solution-Processed Perovskite Solar Cells, Adv. Funct. Mater. 25 (2015) 5529–5536.

[21] M. Saliba, K.W. Tan, H. Sai, D.T. Moore, T. Scott, W. Zhang, et al., The Influence of Thermal Processing Protocol upon the Crystallization and Photovoltaic Performance of Organic-Inorganic Lead Trihalide Perovskites, J. Phys. Chem. C. 118 (2014) 17171–17177.

[22] E.J. Mittemeijer, Analysis of the kinetics of phase transformations, J. Mat. Sci. 27 (1992) 3977–3987.

[23] M. Avrami, Kinetics of Phase Change. II - Transformation-Time Relations for Random Distribution of Nuclei, J. Chem. Phys. 8 (1940) 212–224.

[24] T. Wang, a D.F. Dunbar, P. a Staniec, a J. Pearson, P.E. Hopkinson, J.E. MacDonald, et al., The development of nanoscale morphology in polymer: fullerene photovoltaic blends during solvent casting, Soft Matter. 6 (2010) 4128–4134.

[25] S.T. Williams, F. Zuo, C.-C. Chueh, C.-Y. Liao, P.-W. Liang, A.K.-Y. Jen, Role of chloride in the morphological evolution of organo-lead halide perovskite thin films, ACS Nano. 8 (2014) 10640–10654.

[26] O. Malinkiewicz, C. Roldán-Carmona, A. Soriano, E. Bandiello, L. Camacho, M.K. Nazeeruddin, et al., Metal-Oxide-Free Methylammonium Lead Iodide Perovskite-Based Solar Cells: the Influence of Organic Charge Transport Layers, Adv. Energy Mater. 4 (2014) 1400345.

[27] E. Edri, S. Kirmayer, A. Henning, S. Mukhopadhyay, K. Gartsman, Y. Rosenwaks, et al., Why lead methylammonium tri-iodide perovskite-based solar cells require a mesoporous electron transporting scaffold (but not necessarily a hole conductor), Nano Lett. 14 (2014) 1000–1004.

[28] J. Xiong, B. Yang, R. Wu, C. Cao, Y. Huang, C. Liu, et al., Efficient and non-hysteresis CH3NH3PbI3/PCBM planar heterojunction solar cells, Org. Electron. 24 (2015) 106–112.

[29] P. Löper, M. Stuckelberger, B. Niesen, J. Werner, M. Filipič, S.-J. Moon, et al., Complex Refractive Index Spectra of CH3NH3PbI3 Perovskite Thin Films Determined by Spectroscopic Ellipsometry and Spectrophotometry, J. Phys. Chem. Lett. 6 (2015) 66–71.

[30] G. Renaud, R. Lazzari, F. Leroy, Probing surface and interface morphology with Grazing Incidence Small Angle X-Ray Scattering, Surf. Sci. Rep. 64 (2009) 255–380.

[31] Y. Yoneda, Anomalous Surface Reflection of X Rays, Phys. Rev. 131 (1963) 2010–2013.

[32] G.E. Eperon, V.M. Burlakov, P. Docampo, A. Goriely, H.J. Snaith, Morphological Control for High Performance, Solution-Processed Planar Heterojunction Perovskite Solar Cells, Adv. Funct. Mater. 24 (2014) 151–157.

Chapter 7: Conclusions and Further Work

7.1 Conclusions of Work Undertaken

Whilst many advances have been made in the field of solution processed solar cells, there is still much work to be done if they are to fulfil their potential and reduce the cost of commercial photovoltaic devices. A number of barriers exist to the commercialization of these devices, including the costly and mechanically brittle nature of the electrode material indium tin oxide, the use of solution deposition techniques which are not compatible with large-scale roll-to-roll production, and a lack of understanding of the physical properties of promising new semiconducting materials such as organometal halide perovskites as well as how such properties relate to PV device performance. Here I have attempted to explore solutions to these issues.

In **Chapter 4** multilayer oxide/metal/oxide semi-transparent electrodes were investigated as a replacement for indium tin oxide, with TeO_2/Ag/MoO_3 (TAM) and MoO_3/Ag/MoO_3 (MAM) multilayer electrodes being fabricated. At low thicknesses of the silver film the TAM electrodes exhibit significantly higher transmittance as well as a lower sheet resistance than their MAM counterparts, attributable to the formation of a more continuous silver film on the TeO_2 seed layer. Due to this effect, the percolation threshold for the TAM structures occurs at 8 nm as compared to 10 nm for the MAM structures. The optimised TAM electrodes thus have an average transmittance of 77.1% over the wavelength range 350–700 nm whilst the optimised MAM electrodes have a reduced average transmittance of 71.7% over the same range. When applied as the transparent front electrode in PCDTBT:$PC_{70}BM$ polymer solar cells, the higher transmittance of the TAM electrode leads to an enhanced J_{SC} and thus an enhanced PCE, although both indium-free electrodes are outperformed by their ITO counterpart.

Chapter 5 presented the first published work on employing a solution-processing roll-to-roll compatible deposition technique for the fabrication of the photoactive layer of a perovskite solar cell. Following an optimisation process, such devices exhibited average power conversion efficiencies of 7.8%, a value comparable with spin-coated reference devices. Maximum power conversion efficiency was 11.1%, the highest

reported PCE for a spray-coated solar cell at that time. Devices exhibited a light soaking effect which enhanced PCE largely due to an increased V_{OC}. No substantial differences between spun and sprayed perovskite films were observed under scanning electron microscopy or wide angle X-ray scattering. Ultrasonic spray-deposition of the PEDOT:PSS hole transport layer in solar cells which employed spray-cast perovskite layers was also successfully demonstrated, with no loss in average PCE in comparison to spin-cast PEDOT:PSS. A two-solvent approach allowed uniform $PC_{70}BM$ electron transport layers to be deposited via spray-coating, however it was not possible to successfully incorporate these into high performance solar cells due to large reductions in J_{SC} and FF when thick (>100 nm) PCBM layers were processed in air. Finally, a two-step perovskite fabrication procedure based on the immersion of spray-coated $PbCl_2$ layers into an MAI solution was able to produce working solar cell devices, however average efficiencies did not exceed 5%.

In **Chapter 6** a variety of in-situ and ex-situ techniques were employed in order to study the formation of $CH_3NH_3PbI_{3-x}Cl_x$ during the thermal annealing in air of a precursor film deposited using a one-step spin-coating technique. In-situ GIWAXS measurements allowed the evolution from crystalline precursor to perovskite to be studied and for the activation energy of this transformation to be determined as (85 ± 9) kJ/mol. Preferential out-of-plane orientation was observed for both the precursor and perovskite crystallites and persisted throughout the annealing process. In-situ GISAXS measurements showed that during a thermal anneal at 80°C there is an evolution in length scales within the film, with a large increase in crystallites having sizes in the range 30 to 400 nm. Concurrently the average height of such crystallites appears to increase. This evolution in length scales is correlated with an increase in film surface coverage, as evidenced by scanning electron microscopy images, which is known to lead to improved device efficiency. Devices fabricated using perovskite films annealed at 80°C for lengths of time from 80 to 180 min showed efficiencies which can be explained by the in-situ X-ray scattering and ex-situ SEM measurements. An optimised annealing time for such films lead to an average efficiency of (12.2 ± 0.3)%.

7.2 Further Work

A clear extension of the work in **Chapter 4** would be to undertake an investigation of the origin of the V_{OC} loss which was observed in polymer solar cells employing indium-free multilayer electrodes. It is hoped that this would allow for a reduction in the V_{OC} loss, leading to a notable enhancement in PCE for the indium-free devices. Another obvious and worthwhile extension of this work would be to utilise flexible substrates for fabrication of the electrodes, and to undertake a test of their performance after repeated bending cycles at different bending radii. Finally, the application of these electrodes to other polymer:fullerene blends that exhibit higher PCEs could be undertaken, and the fabrication of spray-coated perovskite solar cells on flexible, indium-free electrodes would provide a very nice link to the work on perovskite devices presented in **Chapter 5**.

Within the scope of applying ultrasonic spray-coating to the fabrication of perovskite solar cells, as discussed in **Chapter 5**, there are a myriad of further investigations to be undertaken, many of which are currently underway at Sheffield. An improvement in device PCE for the one-step process is a clear objective, for example by utilising higher purity materials. More thorough optimisation of annealing temperature and PCBM thickness may also lead to enhancements in efficiency. More significantly, a transition to the normal, rather than inverted, architecture might well increase PCE and would certainly be worthwhile as a proof of concept in any case. A detailed investigation of the effect of humidity on film formation and device performance could also prove interesting owing to the particulars of the film formation processes. There are also a wide variety of novel processes used in recent literature on spin-coated devices which could potentially be transferred to spray-coated devices to improve their efficiencies. Such processes include the addition of additives such as HI or DIO to the precursor solution [1], the application of novel perovskite materials such as formamidinium lead trihalides [2], alternative annealing procedures such as vacuum-assisted annealing and 'flash' annealing [3,4], the application of solvent annealing [5,6], Lewis-base passivation [7] and so forth.

More directly related to the work presented here, further investigations to uncover the causes of the observed light soaking effect for spray-cast perovskite solar cells as well as the loss of performance for air processed $PC_{70}BM$ would be of interest. Any improvement in the smoothness of the perovskite layer may also reopen the possibility

of the successful deposition of PCBM via spray-coating in air by allowing the use of a thinner PCBM film. Finally, transfer of the ultrasonic spray-coating procedure to a nitrogen environment would be advantageous in allowing exploration of materials which require processing under an inert environment.

With regards to further in-situ X-ray scattering work as extensions to **Chapter 6**, it would be interesting to investigate the very earliest stages of the film formation during different deposition procedures. In-situ deposition via spray-coating whilst performing X-ray scattering would, for example, allow characterisation of the film during its drying phase and the initial formation of the precursor structure. An attempt at this experiment was in fact made during the course of this work, using a simple pneumatic nozzle rather than the ultrasonic system employed in **Chapter 5**. Unfortunately however, a number of experimental issues were encountered with the set-up including excessive movement of the substrate during solution deposition as well as contamination and clogging problems with the spray-head, and a repeat of this experiment with improved methods has yet to be undertaken.

7.3 References

[1] P.-W. Liang, C.-Y. Liao, C.-C. Chueh, F. Zuo, S.T. Williams, X.-K. Xin, et al., Additive Enhanced Crystallization of Solution-Processed Perovskite for Highly Efficient Planar-Heterojunction Solar Cells, Adv. Mater. 26 (2014) 3748–3754.

[2] G.E. Eperon, S.D. Stranks, C. Menelaou, M.B. Johnston, L.M. Herz, H.J. Snaith, Formamidinium lead trihalide: a broadly tunable perovskite for efficient planar heterojunction solar cells, Energy Environ. Sci. 7 (2014) 982.

[3] M. Saliba, K.W. Tan, H. Sai, D.T. Moore, T. Scott, W. Zhang, et al., The Influence of Thermal Processing Protocol upon the Crystallization and Photovoltaic Performance of Organic-Inorganic Lead Trihalide Perovskites, J. Phys. Chem. C. 118 (2014) 17171–17177.

[4] F.X. Xie, D. Zhang, H. Su, X. Ren, K.S. Wong, M. Gra, Vacuum-Assisted Thermal Annealing of $CH_3NH_3PbI_3$ for Highly Stable and Efficient Perovskite Solar Cells, ACS Nano. 9 (2015) 639–646.

[5] Z. Xiao, Q. Dong, C. Bi, Y. Shao, Y. Yuan, J. Huang, Solvent Annealing of

Perovskite-Induced Crystal Growth for Photovoltaic-Device Efficiency Enhancement, Adv. Mater. 26 (2014) 6503–6509.

[6] W. Zhu, T. Yu, F. Li, C. Bao, H. Gao, Y. Yi, et al., A Facile Solvent Vapor Fumigation Induced Self-repair Recrystallization of $CH_3NH_3PbI_3$ Films for High Performance Perovskite Solar Cells, Nanoscale. 7 (2015) 5427–5434.

[7] N.K. Noel, A. Abate, S.D. Stranks, E.S. Parrott, V.M. Burlakov, A. Goriely, et al., Enhanced Photoluminescence and Solar Cell Performance via Lewis Base Passivation of Organic-Inorganic Lead Halide Perovskites, ACS Nano. 8 (2014) 9815–9821.